ABSTRACT

Title of dissertation: TURBULENT SHEAR FLOW
IN A RAPIDLY ROTATING
SPHERICAL ANNULUS

Daniel S. Zimmerman, Doctor of Philosophy, 2010

Dissertation directed by: Professor Daniel P. Lathrop
Department of Physics

This dissertation presents experimental measurements of torque, wall shear stress, pressure, and velocity in the boundary-driven turbulent flow of water between concentric, independently rotating spheres, commonly known as spherical Couette flow. The spheres' radius ratio is 0.35, geometrically similar to that of Earth's core. The measurements are performed at unprecedented Reynolds number for this geometry, as high as fifty-six million. The role of rapid overall rotation on the turbulence is investigated. A number of different turbulent flow states are possible, selected by the Rossby number, a dimensionless measure of the differential rotation. In certain ranges of the Rossby number near state borders, bistable co-existence of states is possible. In these ranges the flow undergoes intermittent transitions between neighboring states. At fixed Rossby number, the flow properties vary with Reynolds number in a way similar to that of other turbulent flows.

At most parameters investigated, the large scales of the turbulent flow are characterized by system-wide spatial and temporal correlations that co-exist with

intense broadband velocity fluctuations. Some of these wave-like motions are identifiable as inertial modes. All waves are consistent with slowly drifting large scale patterns of vorticity, which include Rossby waves and inertial modes as a subset. The observed waves are generally very energetic, and imply significant inhomogeneity in the turbulent flow. Increasing rapidity of rotation as the Ekman number is lowered intensifies those waves identified as inertial modes with respect to other velocity fluctuations.

The turbulent scaling of the torque on inner sphere is a focus of this dissertation. The Rossby-number dependence of the torque is complicated. We normalize the torque at a given Reynolds number in the rotating states by that when the outer sphere is stationary. We find that this normalized quantity can be considered a Rossby-dependent friction factor that expresses the effect of the self-organized flow geometry on the turbulent drag. We predict that this Rossby-dependence will change considerably in different physical geometries, but should be an important quantity in expressing the parameter dependence of other rapidly rotating shear flows.

TURBULENT SHEAR FLOW IN A RAPIDLY ROTATING SPHERICAL ANNULUS

by

Daniel S. Zimmerman

Dissertation submitted to the Faculty of the Graduate School of the
University of Maryland, College Park in partial fulfillment
of the requirements for the degree of
Doctor of Philosophy
2010

Advisory Committee:
Professor Daniel P. Lathrop, Chair/Advisor
Professor Peter Olson
Professor William Dorland
Professor Saswata Hier-Majumder
Professor James Duncan

Dedication

Dedicated to my wife, Jess, who has accompanied me through the latter half of my extended graduate career with patience, encouragement, and interest in my work.

Acknowledgments

First and foremost, I must acknowledge our core experimental team, consisting of my advisor, Dan Lathrop, my fellow graduate student Santiago Andrés Triana, and technical supervisor Don Martin, who has most certainly earned his unofficial lab title of "Ubërtechnician." A well known turbulence experimentalist, upon visiting our lab and seeing our experiment for the first time, asked, before anything else, how large our technical staff was. At this time the permanent technical staff for the three meter experiment then consisted solely of the four of us. We have spent years together, starting when the experimental space was full of other experiments. We have brainstormed, sketched, engineered, and constructed together, and we are all rightfully proud of the machine we've built.

However, while each of us has assumed many roles, we could not do it ourselves. I'd like to acknowledge Jim Weldon, a long time acquaintance of Dan Lathrop's and indispensable engineering consult on the design of rapidly rotating equipment, and Allen Selz of Pressure Sciences Incorporated in Richardson, TX, whose stress analysis of the outer sphere gives us confidence that we may safely reach our design speed goals. Furthermore, I would like to acknowledge the fine fabrication job done on the outer sphere by Central Fabricators in Cincinnati, OH, and the efforts of the other machine and fabrication shops, especially Motion Systems in Warren, MI who built our large, custom pulley and Chesapeake Machine in Baltimore, MD who were responsible for the fabrication of many large parts.

I'd like to acknowledge the great crew of young scientists that Dan Lathrop

has assembled here at the University of Maryland over the years. I have enjoyed working with and learning from Woodrow Shew, Dan Sisan, Barbara Brawn, Nicolas Mujica and others on various smaller experiments. I'd like to especially thank Doug Kelley and Matthew Adams, who are respectively the previous and current researchers on the 60 cm experiment , without whom the insights from magnetic data would not be possible, and Matt Paoletti who was undertaking a similar program of torque measurement in Taylor-Couette flow, and with whom I had several helpful discussions. Thanks to IREAP technician Jay Pyle for additional technical support and machining advice, and also to Dr. John Rodgers, who provides much insight into the issues of taking good data in a noisy world.

I'd like to acknowledge all of those who have tirelessly supported my scientific leanings throughout my life, especially my mother Nancy and her late father, John D. Sipple. When I was young, he gave me a hefty science encyclopedia. This single volume was nearly more than I could lift at the time, probably nine inches thick, and bound with steel bolts. Perhaps that influenced my eventual choice of Ph.D. project. And last, I cannot thank my wife Jess enough. Two years ago, when we were married after several years together, we requested that the guests take it easy with physical gifts since "Dan was going to get his Ph.D. soon," and we expected to relocating. Jess has been patient, understanding, encouraging, and constantly interested in what I do, helping me through the inevitable frustrations of this long project.

CONTENTS

LIST OF TABLES

LIST OF FIGURES

List of Abbreviations

β	Coriolis force dependence with latitude in the linearized vorticity equation
δ	Ekman boundary layer thickness
ϵ	Energy dissipation
ζ	Vertical vorticity
η	Radius ratio, $r_\mathrm{i}/r_\mathrm{o}$
η_m	Magnetic diffusivity
θ_c	Critical latitude
μ	Magnetic permeability
μm	Micrometer
ν	Kinematic viscosity
ρ	Fluid density
σ	Electrical conductivity, (Dimensionless half frequency, App. A)
σ_u	Standard deviation of u, similar for other quantities
τ,τ_w	Wall shear stress
τ_∞	Predicted shear stress as a function of Re when $Ro = \infty$
ϕ	Cylindrical azimuthal coordinate
ω	Angular frequency (dimensionless in Ch. 1)
ω_{lab}	Angular frequency measured from lab (nonrotating) frame
ω'	Dimensionless angular frequency (Ch. 6)
Ω	Characteristic angular velocity (In electronics context, Ohms)
$\mathbf{\Omega}$	Angular velocity vector
Ω_o	Outer sphere rotation rate
Ω_i	Inner sphere rotation rate
$\Omega(s)$	Angular velocity as a function of cylindrical radius
∂_t	Partial derivative with respect to time
2D	two-dimensional
3D	three-dimensional
AC	Alternating current
ADC	Analog to digital converter
AISI	American Iron and Steel Institute
B	"Bursty" torque state label
$\mathbf{B}$	Magnetic field, vector
B_0	Applied magnetic field
B_ind	Induced magnetic field
$\mathbf{c}_g$	Wave group velocity
c	Wave phase speed
cm	Centimeters
C	Capacitance
CTA	Constant temperature anemometry, Constant temperature anemometer

DAQ	Data acquisition
dB	Decibel
DC	Direct current
E	Ekman number, herein based on gap width ℓ
E_{R}	Ekman number based on outer sphere radius r_{o}
$E(k)$	Energy density in wavenumber space
E	"Ekman layer modified" torque state
f	Frequency
f_{c}	Filter cutoff frequency, usually -3dB
f_o	Natural resonant frequency
$\mathbf{F}$	Force, vector
g31	l=3 m=1 Gauss coefficient, similar for other l and m
G	Dimensionless torque on the inner sphere
G_{o}	Dimensionless torque on the outer sphere
G_∞	Dimensionless torque as a function of Re with $Ro = \infty$
G_{net}	Net torque, $G + G_{\mathrm{o}}$
GHz	Gigahertz
h	Helicity density
H	"High torque" state
Hz	Hertz
in.	Inches
I	Moment of inertia
$\mathbf{k}$	Vector wavenumber
k	Wavenumber magnitude
k_z	Z-component of wavenumber
k_f	Forcing wavenumber
kg	Kilogram
kHz	Kilohertz
kN	Kilonewton
kPa	Kilopascal
kW	Kilowatt
l	Polar wavenumber, spherical harmonic degree
ℓ	Spherical Couette fluid gap width, $r_{\mathrm{o}} - r_{\mathrm{i}}$
L	Generic characteristic length, angular momentum, inductance
L	"Low torque" state
LL	"Lower than low" torque state
lb.	Pounds
LED	Light emitting diode
m	Meters
m	Azimuthal wavenumber, spherical harmonic order

MHz	Megahertz
MOSFET	Metal oxide silicon field effect transistor
N	Newton
NOAA	National Oceanic and Atmospheric Administration
OSHA	Occupational Safety and Health Administration
P	Pressure
p	Dimensionless reduced pressure, incl. centrifugal pressure gradient.
$P_{\omega'}$	Dimensionless spectral power
Pa	Pascal
P_m	Magnetic Prandtl number
PSD	Power Spectral Density
psi	Pounds per square inch
$\mathbf{r}$	Position vector (also $\mathbf{x}$)
Re	Reynolds number
Re_δ	Reynolds number based on Ekman boundary layer thickness
Re_i	Reynolds number based on inner sphere radius and angular speed
r_i	Inner sphere radius
R_m	Magnetic Reynolds Number
Ro	Rossby number
Ro_jet	Zonal flow mean Rossby number
Ro_R	Rayleigh line Rossby number
r_o	Outer sphere radius
RF	Radio frequency
RMS	Root mean square
RTD	Resistive temperature detector
s	Cylindrical radial coordinate
$S(\omega)$	Power Spectral Density
$S'(\omega')$	Dimensionless Power Spectral Density
SPI	Serial peripheral interface
T	Dimensional torque
TTL	Transistor-transistor logic
$\mathbf{u}$	Velocity vector
u'	Velocity normalized by outer sphere tangential velocity
u_ϕ	Azimuthal velocity
u_e	Envelope velocity (Ch. 6)
u_s	Cylindrical radial velocity
u_w	Band pass filtered inertial wave velocity
u_z	Vertical velocity
u_Z	Zonal velocity
U	Characteristic velocity

$\mathbf{U}_0$	Inertial wave amplitude vector
USB	Universal serial bus
UVP	Ultrasound velocity profile
V	Volume
V	Volt
y'	Dimensionless distance along ultrasound beam
z	Cylindrical vertical coordinate

1. INTRODUCTION AND THEORETICAL BACKGROUND

1.1 Turbulence

1.1.1 The Problem With Turbulence

The spatiotemporal complexity of the motion of flowing fluids has provided both intriguing possibilities and vexing difficulties for scientists and mathematicians for hundreds of years. Posing the problem, though, is simple enough. Assuming a continuum of infinitesimal parcels of fluid, conservation of mass requires a continuity equation for the fluid density ρ as the fluid moves in space with velocity $\mathbf{u}$,

$$\frac{\partial \rho}{\partial t} + \nabla \cdot \rho \mathbf{u} = 0. \tag{1.1}$$

Assuming that the fluid flow is incompressible reduces the above to $\nabla \cdot \mathbf{u} = 0$. Conservation of momentum density $\rho\mathbf{u}$, is described by the Navier-Stokes momentum equation with the pressure P and kinematic viscosity ν:

$$\frac{\partial \mathbf{u}}{\partial t} + (\mathbf{u} \cdot \nabla)\mathbf{u} = -\frac{\nabla P}{\rho} + \nu \nabla^2 \mathbf{u} + \mathbf{F}. \tag{1.2}$$

This partial differential equation describes fluid acceleration due to advection, pressure forces, viscous drag, and external forces $\mathbf{F}$. If we adopt a velocity scale U, length scale L, pressure scale ρU^2, and time scale L/U, we may recast Eq. 1.2 (without

external forces) in dimensionless form:

$$\frac{\partial \mathbf{u}}{\partial t} + (\mathbf{u} \cdot \nabla)\mathbf{u} = -\nabla P + \frac{1}{Re}\nabla^2 \mathbf{u}. \tag{1.3}$$

In the above, all quantities are dimensionless; dimensional quantities are formed by multiplying the dimensionless variables by the chosen scales. The sole adjustable dimensionless parameter, the Reynolds number,

$$Re = \frac{UL}{\nu}, \tag{1.4}$$

describes the relative importance of inertia to viscous drag. In the experiments described herein, we are interested in high Reynolds number flows, with Reynolds number ranging from a quarter million up to sixty million.

Our knowledge of the correct equations of motion[1] does not imply knowledge of all possible solutions. Non-trivial exact nonlinear solutions to Eq. 1.3 are hard to come by. Some of the most interesting and important fluid motions in nature and industry, those of turbulent fluid flow at high Reynolds number, certainly are not described by known solutions. As computing power has grown, it has become practical to numerically seek closely approximate solutions to Eq. 1.3 for turbulent flows. It is now possible to use a fine enough grid in space and time to resolve the wide range of spatial and temporal scales in somewhat high Reynolds number turbulence for short times. Direct numerical simulation, as this procedure is called, provides a important tool to test theories of turbulence and to closely predict weakly

[1] Certainty on this point requires that the thermodynamic degrees of freedom completely decorrelate with the hydrodynamic fluctuations. This may not be the case [1, 2], but this is far beyond the scope of this dissertation.

turbulent flow in some useful situations.

However, even the state of the computational art at the time of this writing has not obviated the need for a predictive theory of turbulent motions. Many geophysical and astrophysical applications will remain beyond direct numerical simulation for many decades at least. And it is only fairly recently that we can compute turbulent velocity fields at all. Modern turbulence theory has likely been shaped by the impossibility of computing solutions to Eq. 1.3. Much of the productive theory of the 20th century starts from a statistical description of turbulent motions and correlations rather than an attempt to predict the fluid motions in any detail.

1.1.2 Homogeneity, Isotropy, and Universality of Statistics

In 1941, A.N. Kolmogorov advanced a statistical theory of fluid turbulence with important and far-reaching predictions about the properties of three-dimensional, spatially homogeneous and isotropic flows. His predictions, often called K41 theory, still inform our understanding of turbulent flows nearly 70 years later. This is due in part to the success of the predictions and in part to their elegance. The ease of the dimensional analysis needed to re-derive some of Kolmogorov's predictions and the conceptual simplicity of a local-in-wavenumber "cascade" of turbulent kinetic energy provides a convenient entry point into a study of the theory of turbulence. One such result predicts the distribution of the fluid specific kinetic energy $\frac{1}{2}\,\mathbf{u}\cdot\mathbf{u}$ across the wide range of spatial scales in a turbulent flow. Starting from the assumption that the only quantities important for sufficiently high Reynolds number turbulent flow are the energy dissipation per unit mass per unit volume ϵ and the

spatial wavenumber k, one can write down the energy spectrum for an intermediate range of scales (the inertial range) on dimensional grounds:

$$E(k) = C\epsilon^{2/3}\ k^{-5/3}. \tag{1.5}$$

The role of the assumptions of homogeneity and isotropy in the above result must not be neglected. Any statistical theory of the distribution of energy across the spatial scales of a turbulent flow must consider an ensemble average over all possible realizations of the turbulent velocity field. The assumption of spatial homogeneity (and large extent) allows the replacement of this ensemble average with a spatial average, assuming, in a sense, that everything that *can* happen *will* happen somewhere in the flow:

$$\frac{1}{2}\langle \mathbf{u}\cdot\mathbf{u}\rangle = \frac{1}{2V}\int \mathbf{u}(\mathbf{x})\cdot\mathbf{u}(\mathbf{x})\ d^3\mathbf{x}. \tag{1.6}$$

If a system is homogenous throughout space and infinitely extended it is also reasonable to use a spectral decomposition of the above, with an energy spectrum $E(\mathbf{k})$. With the assumption of isotropy, it becomes reasonable to expect that the properties of the turbulence at scales of size $2\pi/k$ to depend only on the magnitude of the wavenumber. In an anistropic flow, one must consider the distribution of energy in different directions in wavenumber space and how the equilibrium transfer among the different directions might proceed.

The restrictions of homogeneity and isotropy can never be precisely true for real flows, which are often bounded and usually subject to inhomogeneous and anisotropic forcing. Flow near boundaries and energy-injecting stirrers can be different from that in regions that are more remote. Isotropy is easily broken: large

scale shear, fluid buoyancy effects, magnetic fields, and overall rotation all impart direction on the fluid as a whole. Such effects are extremely important in geophysical, astrophysical, and industrial applications, and the particular physics of rotating flow will be discussed in detail later in this dissertation.

There is an often expressed hope that we may find a region of the fluid where we observe *only* the generic properties of turbulence if we look far enough from walls or stirrers. But as we perform increasingly more sophisticated investigations, it is clear that the influence of the "non-universal large scales"[3] persist in the statistics of the even the smallest scales of the flow. Turbulence that is forced inhomogenously or anisotropically does not appear to homogenize and isotropize at any scales. Systems in nature that provide homogenous, isotropic forcing are rare, so homogenous, isotropic turbulence may also be quite rare.

This is not diminish the value of the large body of existing research on homogeneous, isotropic turbulence. Nor is it to suggest that the problem of anisotropic and inhomogeneous turbulence is a neglected area of study. It is merely that our ability to predict the turbulent motion and associated material transport in many important flows must extend to anisotropic and inhomogeneous *systems* with realistic forcing, boundary conditions, and body forces. It is not only the common behaviors of turbulent fluid motions that are of interest. We also need to understand the possible non-universal behaviors of entire systems.

1.2 Outline of the Dissertation

This dissertation will focus on a series of experimental measurements of the anisotropic and inhomogeneous turbulent shear flow between concentric, rapidly rotating spherical boundaries. At approximately 3 m outer diameter and 1 m inner diameter, the University of Maryland three-meter device is by far the largest spherical Couette apparatus ever built. A substantial fraction of the device was designed and built by the author. This device clearly demonstrates the strong influence of the differential and overall rotation, boundary geometry, and boundary layer flow on high Reynolds number turbulence. In the remainder of Chapter 1, we will review some of the relevant concepts and literature on the effects of rotation, shear, boundary geometry, and boundary layers on turbulent flows. In Chapter 2, we will motivate our interest in rapidly rotating turbulent flow in the context of geophysics, and briefly review a few relevant aspects of the prior work in spherical Couette flow. Chapter 3 will describe the experimental apparatus in detail. It will also discuss the design process in the context of our motivations, and detail some of the engineering and instrumentation contributions of the author. Chapter 4 will present a broad view of turbulent flow states observed throughout the parameter range explored in the experimental campaign in water. Chapter 5 will focus in detail on one particular turbulent flow transition and attendant bistable behavior in the transition region. Chapter 6 will discuss scaling of torque and turbulent fluctuations as a function of the relevant dimensionless parameters, and will propose a particular picture of the overall dynamics based on these scalings. Chapter 7 will summarize the dissertation

and advance some speculative ideas regarding our observations. Finally, we will look at the prognosis for our original experimental goal of generating self-excited magnetic fields in an Earthlike geometry, and propose a few ideas for future experimental work to further illuminate the findings of this dissertation and test the predictions we make herein.

1.3 Rotating Fluid Flow

1.3.1 Equations of Motion

Fluid flow with significant overall rotation can often be more conveniently described in a frame rotating with an angular velocity, $\mathbf{\Omega} = \Omega\hat{\mathbf{z}}$. The choice of $+\hat{\mathbf{z}}$ for the overall rotation vector is a typical convention. The equations of motion in the rotating frame can be deduced by noting that $\partial_t \mathbf{u} = \partial_t^2 \mathbf{r}$ and replacing ∂_t with $\partial_t + \mathbf{\Omega}\times$. The result is:

$$\frac{\partial \mathbf{u}}{\partial t} + (\mathbf{u}\cdot\nabla)\mathbf{u} + 2\mathbf{\Omega}\times\mathbf{u} + \mathbf{\Omega}\times\mathbf{\Omega}\times\mathbf{r} = -\frac{1}{\rho}\nabla P + \nu\nabla^2\mathbf{u}. \tag{1.7}$$

The term $\mathbf{\Omega}\times\mathbf{\Omega}\times\mathbf{r}$ is the centrifugal force. A static pressure gradient set up when the fluid is retained by walls balances part of the centrifugal force, keeping fluid from being flung outward. As this is a prerequisite for studying contained fluid, the static pressure gradient that holds the fluid in the container is often implicit in the "reduced pressure" $p = P + \frac{1}{2}\rho\Omega^2 r^2$. Differentially rotating fluid regions, like the flow near differentially rotating walls, may feel a centrifugal force that is out of balance with the gradient of the pressure, and in this case, the centrifugal term will result in flow. The term $2\,\mathbf{\Omega}\times\mathbf{u}$ is the Coriolis force and is responsible for many

interesting effects in rotating fluid flow.

The velocity field $\mathbf{u} = \mathbf{\Omega} \times \mathbf{r}$ is a solution to the nonlinear equations of motion in the inertial frame. In the rotating frame, this corresponds to $\mathbf{u} = 0$, and any small perturbation to the solid body state is subject only to pressure force, the Coriolis force, and viscous force. The pressure force is conservative, the Coriolis force can do no work and the viscous drag is dissipative, so the fate of otherwise unforced perturbations is to decay. Solid body rotation is, therefore, an energy stable steady state. Furthermore, it satisfies the boundary conditions on any rigidly rotating set of bounding surfaces, independent of shape. In the absence of additional forces, flow in any rotating container will eventually decay to solid body rotation.

It is clear from Eq. 1.7 and Eq. 1.3 that the relative strength of the Coriolis force is what separates rotating flow from nonrotating flow. We can make this clearer by writing Eq. 1.7 in dimensionless form. In a frame rotating with angular velocity $\mathbf{\Omega} = \Omega\hat{\mathbf{z}}$, we adopt a time scale of $1/\Omega$, a length scale L, a relative velocity scale in the rotating frame U, and a pressure scale $\rho\Omega LU$. This pressure scale will also be used as the expected wall shear stress scale in Chapter 6. These choices make the Coriolis term of order unity, and transform Eq. 1.7 to

$$\frac{\partial \mathbf{u}}{\partial t} + Ro\,(\mathbf{u}\cdot\nabla)\mathbf{u} + 2\hat{\mathbf{z}}\times\mathbf{u} = -\nabla p + E\,\nabla^2\mathbf{u} \tag{1.8}$$

We now have two dimensionless parameters. The Rossby number,

$$Ro = \frac{U}{\Omega L}, \tag{1.9}$$

characterizes the importance of nonlinear interactions of velocities in the rotating

frame relative to the Coriolis force. The Ekman number, defined as

$$E = \frac{\nu}{\Omega L^2}, \tag{1.10}$$

is the dimensionless ratio of the viscous drag force to the Coriolis force. Note that with these definitions we can still define a Reynolds number dependent on the two dimensionless parameters,

$$Re = \frac{Ro}{E} = \frac{U\Omega L^2}{\Omega L \nu} = \frac{UL}{\nu}. \tag{1.11}$$

Geophysical and astrophysical work will often adopt Ro and E, as does prior work on rapidly rotating spherical Couette flow. Work on general rotating turbulence, both in experiment and numerics, seems to prefer Ro and Re, perhaps to compare to nonrotating turbulence at the same Reynolds number. The use of Ro and Re will turn out to be a natural choice for certain aspects of this work. However, where use of Ro and Re is not particularly called for, Ro and E will be used.

Fluid flow is considered rapidly rotating when E is low and Ro is not too large. If Ro is so large that the nonlinear term in Eq. 1.8 dominates the Coriolis term *everywhere* in the flow at all times, we would expect the dynamics to reduce to those described by Eq. 1.3 with $Re = Ro/E$. This is a regime of essentially non-rotating turbulence. When E is small and Ro is extremely small, a variety of interesting behaviors can be noted by looking at linear or weakly nonlinear perturbations to rapid solid body rotation. Flows in this regime expose some of the phenomena that seem to be important to rapidly rotating turbulence.

When Ro is increased and nonlinearity becomes significant, it is important to look not only at the dimensionless prefactors of the terms but their behavior in space

and time. When a system-size length scale is chosen in Eq. 1.9, the Coriolis force is important at larger, slower scales in the flow, where weak large-scale velocity gradients and small accelerations ensure that the Coriolis term dominates. With steep velocity gradients and large accelerations due to pressure forces, the Coriolis force can be negligible. A ready example is found in Earth's atmosphere. Large scale weather systems, like tropical cyclones and hurricanes, are shaped by the Coriolis force but small-scale ordinary thunderstorms and tornadoes with similar[2] planetary Rossby number are not.

1.3.2 Two-Dimensionality

One of the most well-appreciated effects of rapid rotation is a tendency for the flow to become apparently two-dimensional, with fluid motions in columns aligned with the axis of rotation. This effect is easily demonstrated even in relatively small tanks of water rotating once every few seconds, with Ekman number perhaps 10^{-4} or 10^{-5}, so it is a popular classroom demonstration. The Taylor-Proudman theorem states that steady flow at low Rossby number will be two-dimensional. Mathematically, steady flow $\partial_t \mathbf{u} = 0$ in the limit $Ro, E \to 0$ requires that the Coriolis force exactly balance with the gradient of the reduced pressure:

$$2\hat{\mathbf{z}} \times \mathbf{u} = -\nabla p. \tag{1.12}$$

Taking the curl of the above equation and invoking incompressibility, we arrive at

$$(\hat{\mathbf{z}} \cdot \nabla)\mathbf{u} = 0. \tag{1.13}$$

[2] The non-tornadic wind speed record of about 113 m/s was set in 1996 in Australia by Tropical Cyclone Olivia [4]. This corresponds to a planetary Rossby number of about 0.25.

The gradient of the velocity along the rotation axis (in this case, $\hat{\mathbf{z}}$) must be zero for steady flow. Often Eq. 1.13 is usefully used in an approximate sense for slow flow where $\partial_t \mathbf{u} << 0$. Care must be taken in conceptually applying this theorem to flows where accelerations and nonlinearity are *not* negligible. In Sec. 1.4.1 we will further discuss the role of the Taylor-Proudman theorem in turbulent flows, where $\partial_t \mathbf{u}$ is non-negligible.

1.3.3 Inertial Waves

The Taylor-Proudman theorem is arrived at by neglecting fluid acceleration in the Navier-Stokes equations. Keeping the acceleration in the limit $Ro, E \to 0$ exposes other interesting linear dynamics. In this case,

$$\frac{\partial \mathbf{u}}{\partial t} + 2\hat{\mathbf{z}} \times \mathbf{u} = -\nabla p. \tag{1.14}$$

We may again take the curl of the above to eliminate the gradient of pressure, and after some manipulation we arrive at

$$\frac{\partial}{\partial t} \nabla \times \mathbf{u} = 2(\hat{\mathbf{z}} \cdot \nabla)\mathbf{u}. \tag{1.15}$$

In an unbounded fluid, it is reasonable to insert a plane wave ansatz into Eq. 1.15,

$$\mathbf{u} = \mathbf{U_0} e^{\mathrm{i}(\mathbf{k}\cdot\mathbf{r} - \omega t)} \tag{1.16}$$

with $\mathbf{U_0}$ a constant vector. The dispersion relation for plane inertial waves that can be deduced from Eq. 1.15 is

$$\omega = \frac{2k_z}{|\mathbf{k}|} = 2\cos\theta, \tag{1.17}$$

where θ is the angle of the wavevector from the vertical and ω is a dimensionless frequency in the interval $(0, 2)$. The dimensional frequency is $\omega\Omega$. At dimensional frequencies exceeding 2Ω, the governing equation changes character and no wave motions are possible. Plane inertial waves are circularly polarized transverse waves as depicted schematically in Fig. 1.1.

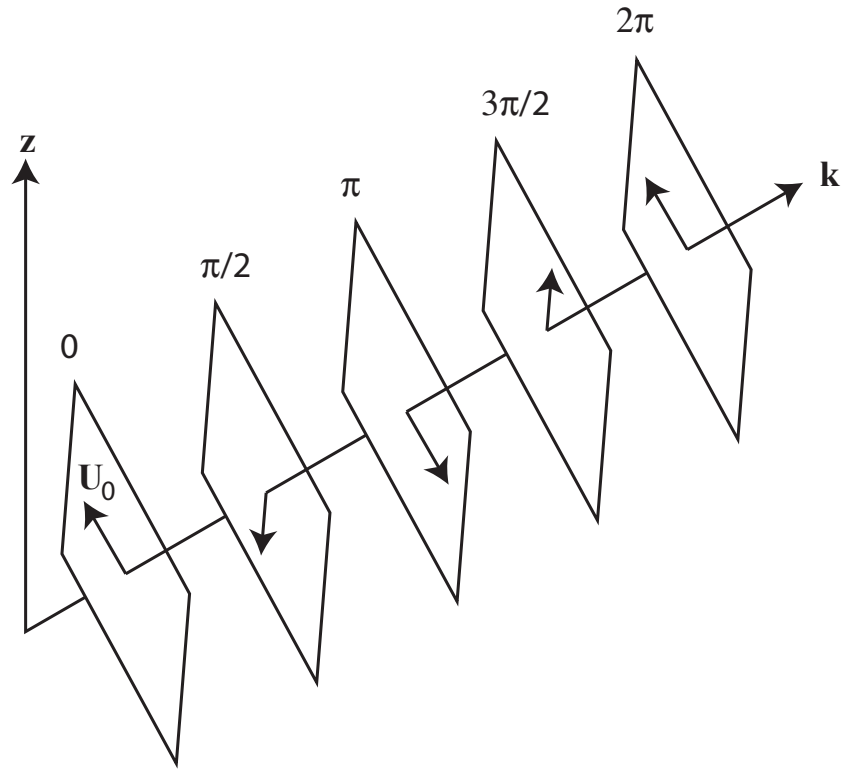

Fig. 1.1: Plane inertial wave in an unbounded fluid. Planes of constant phase extend infinitely far transverse to the wavevector **k**. In each plane, fluid moves with speed U_0, with direction changing as the wave passes.

As the wave passes a point in space, the velocity vector rotates at a frequency given by Eq. 1.17 and fluid parcels trace out circular paths in planes perpendicular to **k**. Unlike many common waves, the wave frequency of plane inertial waves does not depend on the wavelength. The dispersion relation of Eq. 1.17 depends only on the

direction of wave propagation, not the magnitude of the wavevector. Furthermore, the group velocity of these waves [5],

$$\mathbf{c}_g = \frac{\mathbf{k} \times (2\hat{\mathbf{z}} \times \mathbf{k})}{k^3}, \tag{1.18}$$

is perpendicular to the phase velocity.

The independence of wave frequency and wavelength allows the construction of purely monochromatic wavepackets, localized in space and consisting only of fluid motions at a single frequency. Since energy propagates in the direction of the group velocity, it does not spread in the direction of the wavevector. A typical observation of "plane" inertial waves, then, generally consists of a frequency-monochromatic packet with only a few crests and troughs in the direction of $\mathbf{k}$ with a dominant wavelength of about the size of the forcing device. Experiments have used a small vertically oscillating disc in a rotating cylindrical tank to excite a conical wavepacket. The localized forcing radiates a superposition of plane waves with horizontal wavevectors in all directions, forming a conical layer, across which several wave crests and troughs are observed. Older examples as well as a full treatment of inertial waves can be found in Greenspan's 1968 monograph [6]. Messio *et al.* [5] provide modern particle image velocimetry measurements of these conical inertial wave excitations at low Ro, as well as introducing the physical picture of these waves in a particularly clear way.

1.3.4 Inertial Modes

The previously discussed fluid dynamics in the presence of rotation did not discuss realistic boundary conditions on the flow. Provided that *Ro* is very low and accelerations are small, the Taylor-Proudman theorem holds generally outside the boundary layers in the presence of walls. Wave beams that behave more or less as plane inertial waves may be excited in a bounded fluid provided that they are generated in a short wavelength limit and dissipate before any closed trajectories are completed. However, contained rotating fluids also exhibit normal modes of oscillation involving global coherent motions of the fluid. These modes also obey Eq. 1.15, but must additionally satisfy the boundary conditions on the container. In cylindrical coordinates (s, ϕ, z) in axisymmetric containers we may use an ansatz

$$\mathbf{u} = \mathbf{U}(s, z)\ e^{\mathrm{i}(m\phi + \omega t)} \tag{1.19}$$

where $\mathbf{U}(s, z)$ is a complex amplitude as a function of position. Solutions to Eq. 1.15 consistent with boundary conditions in a given container can be difficult to find. However, analytical solutions in some geometries are known. Solutions are known in the interior of a sphere or spheroid subject to no-penetration boundary conditions ($U_n = 0$, where n denotes the wall-normal direction). In the context of rotating spheres or spheroids, Eq. 1.15 is called the Poincaré equation, after Poincaré 1885 [7]. Bryan [8] found implicit solutions. Greenspan [6] and Kudlick [9] found explicit solutions for some modes as polynomials in s and z. Zhang *et al.* found explicit solutions for every mode in a sphere [10] and a spheroid [11].

Nonaxisymmetric inertial modes in a sphere are three-dimensional traveling

waves. As with plane inertial waves, the motion of fluid parcels is everywhere sinusoidal with dimensionless frequency $0 < \omega < 2$. However, the phase and amplitude pattern $\mathbf{U}(s,z)e^{im\phi}$ for a given mode is generally fairly complicated. One mode is depicted in Fig. 1.2. A series of papers by Kelley and collaborators [12–15] establish that inertial modes similar to those in the full sphere can be excited in spherical Couette flow.

The non-slip boundary conditions and existence of the inner core in the experiment are significant departures from the full sphere, free-slip conditions of the theoretical mode calculation. Solutions for the spherical shell are not known in general. In a spherical shell with free-slip and non-slip boundary conditions, numerical calculations [16–18] show interesting behavior like wave attractors, ray focusing and internal shear layers. However, despite the presence of a core and non-slip boundary conditions of the experiments, the modes observed so far in spherical Couette flow show good agreement with the inviscid eigenmodes of Zhang *et al.*. In the special case where a full sphere mode has identically zero spherical radial velocity, it will trivially satisfy no-penetration boundary conditions. Modes that fit this criterion are among those observed [12], but this condition does not fully describe the observed modes. Inertial oscillations satisfying the boundary conditions of the spherical shell, their relation to those in the full sphere, and the weakly nonlinear behavior of inertial modes are a topic of considerable active study [16–21], as these modes are thought to be important in the low-viscosity fluid cores and atmospheres of planets and wholly fluid stars.

It is important to establish to what extent modes like those of the full sphere

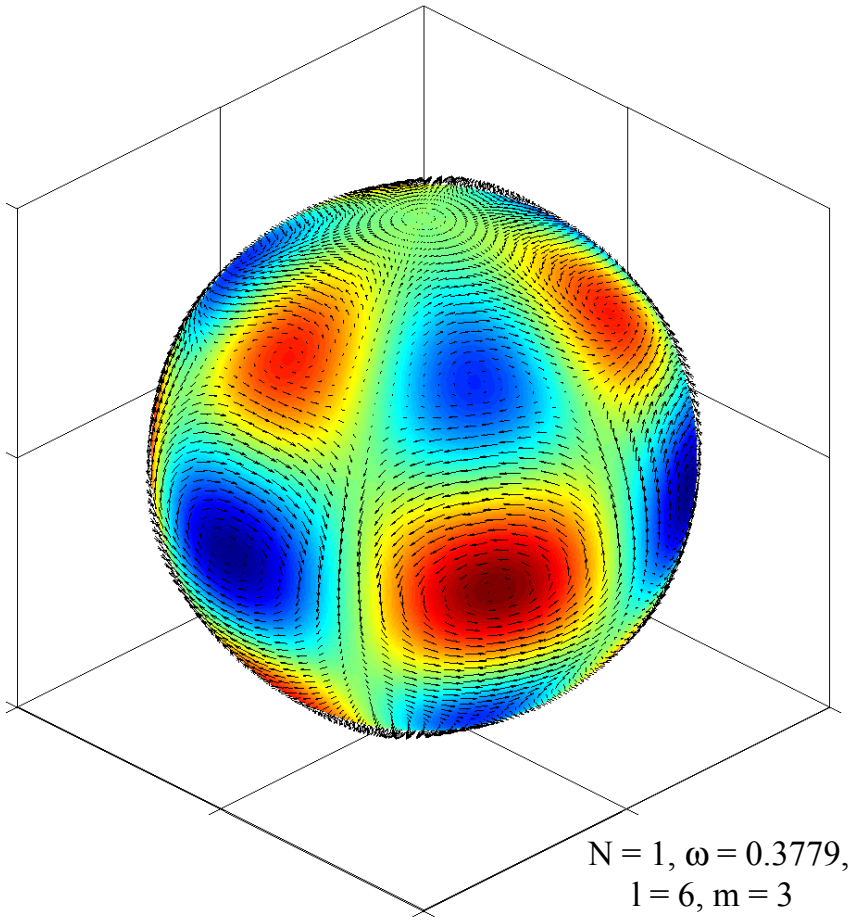

Fig. 1.2: Velocity (arrows) and spherical radial component of vorticity (color, see Appendix A) on a surface near the outer sphere boundary (0.95 r_o) for a particular inertial mode. This mode, according to the classification of Zhang *et al.* [10], has subclass $N = 1$, azimuthal wavenumber $m = 3$, and dimensionless frequency $\omega = 0.3779$. Greenspan [6], points out that on the surface of the sphere, a mode has the polar angular dependence of a single associated Legendre polynomial, $P_l^m(\cos\theta)$. This mode is also, then, uniquely determined by (l, m, ω). For this mode, $l = 6$. This mode is one observed by Kelley *et al.* [12]

play a role in spherical shells in general under a wide variety of forcing methods, as the existence of analytical solutions is a powerful theoretical tool. Zhang *et al.* have established, for example, the relevance of inertial modes to rapidly rotating convection in a spherical shell [22]. Some of the convective modes in an Earthlike geometry ($r_\mathrm{i} = 0.35\, r_\mathrm{o}$) have nearly vanishing velocity near the inner core. Therefore, they should be weakly affected by its presence. However, it does not seem from the experiments of Kelley *et al.* [12–15] that this is a necessary property either, at least for forcing by differential rotation.

Inertial modes are an orthogonal set of velocity modes in a rotating sphere, but it is not known if they form a complete set [23]. If the inertial modes are complete, then any velocity field consisting of motions with frequencies less than 2Ω in the rotating frame could be written as a superposition of these modes. Liao and Zhang [23] point out that truncated approximations based on inertial modes may lead to a great computational savings in predicting the flow inside rotating spheres. It is also worth mentioning here another recent paper [24] by Liao and Zhang on a new set of orthogonal polynomials useful for expanding the geostrophic motions, that is, the axisymmetric steady ($\omega = 0$) motions. It is important to investigate the applicability of all of these results to rotating turbulence in a spherical annulus, as already a good deal of insight has been gained through knowledge of the analytical inertial eigenmodes in a sphere.

1.3.5 Rossby Waves

In a 1939 paper [25], Carl-Gustaf Rossby deduced that waves could propagate on a zonal flow in a rapidly rotating thin atmosphere on a planet, starting from the principle of conservation of absolute vorticity[3]. The sum of the relative vorticity on the sphere surface, ζ, and the component of planetary vorticity normal to the surface, $2\,\Omega\,\sin\,\theta$, must be constant. Here, θ is the latitude. Rossby used cartesian coordinates to model two-dimensional flow in a thin latitudinal band, with $\hat{\mathbf{x}}$ to the East (prograde direction) and $\hat{\mathbf{y}}$ to the North. The conservation of total vorticity normal to the planet surface reads:

$$\zeta + 2\,\Omega\,\sin\,\theta = 0 \tag{1.20}$$

Differentiating with respect to time and introducing u and v, the relative velocity components in the $\hat{\mathbf{x}}$ and $\hat{\mathbf{y}}$ directions respectively, one arrives at an equation for the evolution of the vorticity in the rotating frame:

$$\frac{\partial \zeta}{\partial t} = -\beta v. \tag{1.21}$$

In the above, $\zeta = \partial_x v - \partial_y u$ and $\beta = 2\,\Omega\,\cos\,\theta/R$, where R is the planetary radius. If flow in a narrow latitudinal band is of interest, the θ-dependence of β can be neglected and β taken to be a constant. This is the beta-plane approximation, and solutions to Eq. 1.21 are often called "flow on the beta plane." Using Eq. 1.21, with $u = U + u'$ and $v = v'$, Rossby sought perturbations u' and v' that propagated without change of shape and constant velocity c. Perturbations of the form $v' =$

[3] This can be derived by applying Stokes' theorem to the the Kelvin circulation theorem.

sin $k(x - ct)$ are solutions, with the phase speed c given by

$$c = U - \frac{\beta}{k^2}. \tag{1.22}$$

The dispersion relation shows that long, low wavenumber waves with $k < \sqrt{\beta/U}$ propagate in the negative $\hat{\mathbf{x}}$ (West, retrograde) direction, while waves with $k > \sqrt{\beta/U}$ propagate in the positive $\hat{\mathbf{x}}$ (East, prograde) direction.

Rossby waves are important to flow in Earth's atmosphere, and indeed, this is the original motivation of Rossby's work. The wavy form of the jet stream is an important example. These Rossby waves grow to large amplitude and break, leaving behind isolated high and low pressure systems (anticyclonic and cyclonic vorticity, respectively). Many large-scale weather patterns depend on Rossby wave propagation and breaking, and their generation by and pinning to surface topography. Some good reviews of the role of Rossby waves in the atmosphere and oceans are Dickinson 1978 [26] and Rhines 1979 [27].

A number of experiments study, in particular, turbulence on the beta-plane by use of a sloping bottom in an annular rotating channel. See, for example, Tian *et al.* [28], Baroud and collaborators [29–31], and Read *et al.* [32]. The β-effect in such experiments arises as the variation of height with the radial coordinate stretches or compresses regions of relative vorticity as they move inward or outward on a uniform background vorticity. The sign of this geometrical β-effect and the resultant direction of propagation of Rossby waves depends on whether or not height increases or decreases with increasing radius. If the height H decreases with radius, as is the case in the interior of a sphere, the long wavelength Rossby waves should propagate

Eastward (prograde) and the short wavelength waves should propagate Westward (retrograde). Rossby waves in the interior of a sphere have been addressed numerically by Schaeffer and Cardin [33] in a sphere with differentially rotating endcaps. They identify the turbulence in their quasi-geostrophic, depth-averaged model as Rossby wave turbulence. We expect that Rossby waves will be important to turbulence in a spherical annulus, but with an additional effect. In this geometry, the height increases with radius for radii inside a cylinder tangent to the inner sphere, but decreases with radius outside the tangent cylinder. This important feature with regard to Rossby wave propagation is depicted in Fig 1.3 (a).

There is a connection between Rossby waves in the interior of the sphere and inertial modes. According to Busse, Zhang, and Liao [34], certain slow inertial modes in the sphere, those that have the lowest frequency for their subclass and azimuthal wavenumber, are indistinguishable from Rossby waves. These slow inertial modes are nearly two-dimensional. The Rossby-like inertial modes discussed by Busse *et al.* propagate only in the prograde direction, while Rossby's waves propagated in both. However, Rossby's initial derivation included a prograde zonal flow. When $U = 0$, all waves would be retrograde. So it seems it is merely the zonal flow that allows prograde Rossby waves in the β-plane. The propagation is always retrograde to the zonal flow. With the reversal of the sign of the β-effect in the sphere, in the absence of a zonal flow, we only expect prograde Rossby waves outside the tangent cylinder.

Furthermore, since the inertial modes are not known for the spherical annulus, it is also not known what effect the inner core will have in the sense of Fig. 1.3 (a).

Even if Rossby waves in the region outside the tangent cylinder are described by the analytical formulas of Zhang *et al* [10], those inside and their interactions with the outer region are not known. Further, it is not clear that experimentally observed waves in shear flow are well described by slow inertial modes. Schaeffer and Cardin [35] find that the varying β-effect with radius results in a spiralling Rossby wave instability of the Stewartson layer. No single inertial mode has a spiral structure, as all azimuthal variation in the known inertial modes are described by a single multiplicative $e^{\mathrm{i}m\phi}$ factor. It is possible that a coherent superposition of modes could describe this, however.

We must account for the role of zonal flow, because we generally drive differential rotation. Rossby's original 1939 paper assumed a relative eastward wind velocity U. The inertial modes of the sphere propagate on a background of pure solid body rotation, but there are probably also modes that propagate on sheared profiles. A few exact nonlinear solutions are known for flow on the beta plane. A review by Barcilon and Drazin [36] collects a number of nonlinear solutions relevant for different zonal flow profiles. The implication of the nonlinear solutions is that the waves may exist at high amplitudes on background shear. This could make them robust features even in strong rotating turbulence. The existence of such nonlinear solutions to the beta-plane equations and the analogy drawn between inertial modes and Rossby waves raises the question of nonlinear solutions to the Poincaré equation, perhaps as sums of inertial modes, inertial modes plus shear profiles, or single special inertial modes.

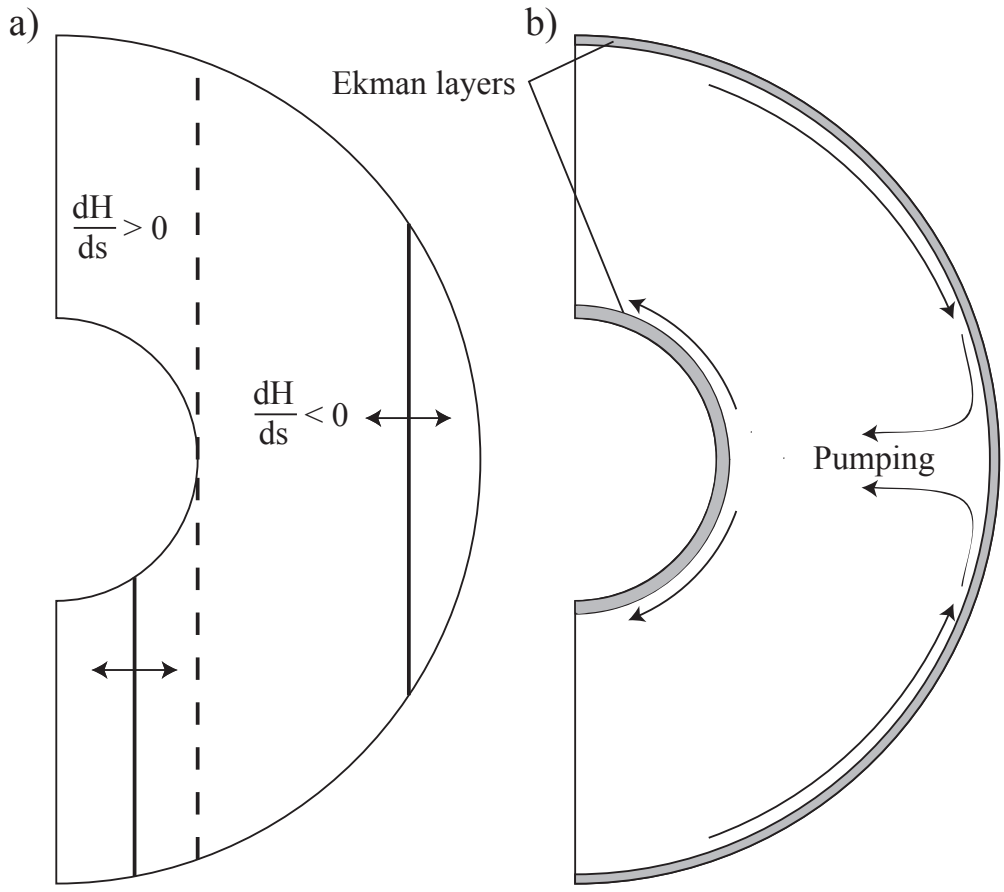

Fig. 1.3: (a) The direction of propagation of Rossby waves in a spherical annulus depends on the sign of dH/ds. Inside the tangent cylinder, long wavelength Rossby waves should propagate the opposite direction of those outside the tangent cylinder. In (b), Ekman layers and Ekman pumping will always be present on sloping boundaries in this geometry whenever fluid is rotating differentially with respect to the walls.

1.3.6 Ekman Layers: Pumping and Stability

In many real turbulent flows of interest in nature, and certainly for those that we can study in the laboratory, fluid is contained within walls on which it must satisfy non-slip boundary conditions. Even in high Reynolds number flow where much of the bulk fluid dynamics can be well described as inviscid, the tangential stresses at the boundaries will have a substantial effect on the flow. If the flow is, as in the present experimental investigation, driven by relative motion of relatively smooth[4] walls, then energy injection and momentum exchange take place entirely through the action of the boundary layers. This can be the case even without a solid boundary, as in the forcing of ocean currents by surface wind stresses.

It is this problem in particular that spurred the initial work of V. Walfrid Ekman. Fridtjof Nansen, a Norwegian explorer and oceanographer, had observed that icebergs did not drift in the direction of the wind, but rather at an angle to it. In 1905, Ekman established [37] mathematically that a rotation of the ocean current direction with depth should be expected from a balance of shear stresses and the Coriolis force near the surface of the ocean. Ekman's work assumed a uniform turbulent momentum diffusion, as molecular viscous shear stresses in balance with the Coriolis force would lead to "the absurd result" of an oceanic boundary layer only a few tens of centimeters thick. However, Ekman's name is also associated

[4] If the walls are rough enough compared to the smallest scales of the turbulence, then pressure gradients across roughness elements can dominate the momentum exchange with the walls. In this situation, the viscous sublayer near the wall is irrelevant. Otherwise, viscous stresses are always important in a thin layer at the wall.

with a laminar layer in which viscous shear stress is balanced by the Coriolis force. In laboratory experiments on turbulent flow, the Ekman boundary layers are not necessarily turbulent.

In the ocean, there can be sources of turbulent motion near the surface that are unrelated to that generated by an unstable laminar Ekman layer. For example, wave motion causes turbulent mixing in the near-surface ocean. This will probably be the case in many geophysical and experimental situations of interest, but we should also consider the stability of an Ekman layer resulting from the relative motion of fluid near a wall. The Reynolds number threshold for instability and transition to turbulence in a laminar Ekman layer is typically given in terms of a Reynolds number based on the Ekman layer thickness $\delta = \sqrt{\nu/\Omega}$,

$$Re_\delta = \frac{U\delta}{\nu}. \tag{1.23}$$

Leibovich and Lele [38] establish that the critical Re_δ for instability of the Ekman layer on the surface of a sphere is a complicated function of both the relative local direction of the velocity in the bulk and the latitude on the sphere. Typically, Re_δ for initial instability to rolls in the Ekman layer is low, a few tens. In terms of the experiments presented here, this will generally be exceeded except in the case of regions in the flow that happen to be quiet because of the constraints of rotation. But even if the Ekman layer is everywhere unstable, the complicated spatial dependence of the instability could have consequences to the global flow on the interior of the sphere, as the boundary layers could be rather inhomogeneous.

Matters may be simplified if the Ekman layers were everywhere fully turbu-

lent. However, it is not clear that this should always be the case in the experiments presented here. A number of papers, including Aelbrecht *et al.* [39] put the critical Re_δ for sustained turbulence in the vicinity of 400-500. Noir *et al.* report a value greater than $Re_\delta = 120$ for sustained boundary turbulence near the equator of a librating[5] sphere. Furthermore at large libration amplitudes, the latitudinal extent of the observed turbulence saturates, covering most but not all of the whole boundary up to $Re_\delta = 400$ or so. In the experiments here, where typical parameters are $\Omega/2\pi \sim 1$ Hz and $U \sim 1$ m/s, we expect $Re_\delta = 325$. Whether or not to expect fully turbulent boundary layers everywhere on the surface is not clear, despite the enormous free stream Reynolds number.

Furthermore, the experimental investigation by Aelbrecht *et al.* demonstrates a curious property of Ekman layer stability when the outer flow is oscillatory. For Re_δ up to several hundred, the oscillatory Ekman layer always showed laminar flow near the maximum velocity portion of the cycle. At the velocity minima as the flow was reversing, however, the layer would become turbulent. The extent of the laminar and turbulent portions of the oscillation cycle was a function not only of Re_δ but of the ratio of oscillation frequency to rotation frequency. This peculiar behavior has important consequences to the present experimental work. The question of damping of large scale coherent wave motions like Rossby waves and inertial modes hinges partially on whether or not the boundary layers are turbulent where the waves are strong. Zhang *et al.* [10] establish that the inertial modes all have zero internal dissipation in the case of free-slip boundaries. There is some internal dissipation due

[5] Rotating with a modulated rotational speed.

to internal shear layers in the case of non-slip boundaries, but boundary dissipation is still the most important source of damping. This is addressed for laminar boundary layers in Liao *et al.* [40]. It would be expected that turbulent boundary layers would increase modal damping rates. However, the finding of Aelbrecht *et al.* for oscillatory layers raises the question of whether instability would happen for inertial modes' boundary layers. The behavior of the Ekman layers in this case has not, to our knowledge, been established. Perhaps there is a turbulent bursting phase, but at wave nodes instead of wave maxima.

Additional Ekman layer effects are relevant to inertial waves and modes in particular. At critical latitudes in the spherical shell, given in terms of the dimensionless frequency, ω, by

$$\theta_c = \cos^{-1} \frac{\omega}{2}, \tag{1.24}$$

the Ekman boundary layers erupt and radiate inertial wave shear layers into the flow [12]. These internal shear layers spawned from the Ekman layer are the viscous resolution of an inviscid singularity in the flow field [16, 17, 41]. The energy carried to the boundary by the inertial modes at the critical latitudes is not reflected back to the flow, but instead stays in the boundary layer there, and this leads to a breakdown and eruption of the Ekman layer flow [41]. The shear layers driven by Ekman layer breakdown can be strong and the nonlinear self-interaction of the shear layers can transport angular momentum by generating zonal flows. [21, 41].

One final property of the boundary layers in a rotating system needs to be addressed, one that depends on the centrifugal term of Eq. 1.7. When a boundary

is differentially rotating with respect to the bulk fluid, the fluid inside the boundary layer will experience a greater or smaller centrifugal force. The pressure, however, cannot change significantly over the small thickness of the boundary layer. So the greater or lesser centrifugal force in the boundary layer will not be balanced by the gradient of the pressure, and fluid near any horizontal or sloping surface will be accelerated in the direction of the net force resulting from this imbalance. This effect is known as Ekman pumping and it will always be present on every boundary of the spherical annulus when the fluid is not strictly rotating rigidly with the boundary.

An example circulation pattern set up by Ekman pumping is depicted in Fig. 1.3 (b). The pattern depicted might be expected for flow driven by sub-rotating the inner sphere. The outer boundary rotates fastest of all, and fluid is pumped out from the poles down toward the equator. The fluid from the lower hemisphere meets that from the upper at the equator and is injected into the bulk. Near the inner sphere, the fluid near the more slowly rotating inner sphere is pumped by the pressure gradient of the bulk fluid from the equator of the inner sphere to the poles. Ekman pumping is also likely the most important sources of dissipation for the large scale vortices in rotating systems. In rapidly rotating turbulence, which we will discuss next, energy tends to undergo a cascade to large scales. Boundary friction at these large scales resulting from Ekman pumping is a significant contributor to the total dissipation. In three-dimensional isotropic turbulence, the energy is cascaded to small scales and dissipated in intense shear events in the bulk. Dissipation in the boundary layers is a less important effect there.

1.4 Rotating Turbulence

1.4.1 Rotating vs. 2D Turbulence

The tendency toward two-dimensional flow introduced by the Taylor-Proudman constraint has important consequences in the turbulent flow of rotating fluids. In a 1967 paper [42], Robert Kraichnan derived the expected scaling for the inertial range in strictly two-dimensional turbulence. In inviscid two-dimensional flow, where vortex stretching by fluid strain is impossible, both energy and mean-squared vorticity (also called enstrophy) are conserved. The enstrophy is constrained by other physical considerations to cascade toward smaller scales. Then, to conserve energy, there must be a net energy transfer toward larger scales. This "inverse cascade" of energy to the large scales of the flow is observed in exactly two-dimensional flows in numerics [43, 44], and in nearly two-dimensional experiments using, for example, soap films or other thin fluid layers [45, 46]. An up-scale transfer of energy is observed in rotating turbulence as well, expected due to its tendency toward two-dimensionality. However, it is important to keep a clear distinction between truly two-dimensional turbulence and rapidly rotating turbulence. Indeed, Kraichnan writes [42]:

> "The result is not directly applicable to meteorological flows because the constraints that render the latter two-dimensional break down at sufficiently high [wavenumber] k."

The Coriolis force acts weakly in proportion to advection and pressure forces at small scales, as discussed in Sec. 1.3.1, and this breaks the small-scale two-dimensionality in rotating turbulence. Furthermore, even in linear theory, any accelerations in

rotating flow must be associated with three-dimensional motion, in accordance with Eq. 1.15. This is in contrast to more strictly 2D flows, such as soap films, in which velocities in the thin third direction can never become important. Even though the constraint of rotation is broken primarily for small scale motions, the differences between two-dimensional turbulence and rotating turbulence persist to the large scales. One notable example is that of cyclone-anticyclone asymmetry in rotating turbulence. In experiment and simulation of strictly two-dimensional turbulence forced at intermediate or small scales, there are about as many vortices of positive vorticity as of negative [47, 48]. In experiments and numerics of rapidly rotating turbulence forced three-dimensionally at small scales, cyclones are preferentially excited [47, 49–51] and isolated cyclones in rotating tanks have different stability properties than anticyclones [52–54].

Phenomenologically, a tendency toward two-dimensionalization *is* noted in fairly low Rossby number rotating turbulence. Relatively recent theoretical work attempts to extend the Taylor-Proudman theorem to low Rossby number turbulent flow. Chen *et al.* [55] build on the work of Waleffe [56] and others to establish the dynamics of the the "slow modes" in rotating periodic box turbulence. The normal modes of a periodic box can be described in Fourier space, each with wavevector $\mathbf{k}$. In a weakly nonlinear system, modes with purely horizontal wavenumbers $k_z \equiv 0$, decouple to first order from the "fast modes" which have $k_z \neq 0$. In this situation, the dynamics of the large scale purely two-dimensional modes obey Eq. 1.13 while the three-dimensional fast modes evolve independently according to Eq. 1.8. In the words of Chen *et al.*

> "Notice that it is not implied by this result that the flow under rapid rotation will become two-dimensional, but it does mean that the dynamics will contain an independent two-dimensional subdynamics, to leading order."

Chen *et al.* present wavenumber spectra conditioned on k_z from a turbulence model forced with three-dimensional isotropic forcing at an intermediate single scale. The energy spectra show that the three-dimensional fast modes contain a good fraction of the total energy. Even the developed statistically steady flow is actually far from two-dimensional.

This work may help explain the observation in experiment that rotating turbulence appears to weakly depart from columnar structure. This often explained simply by invoking the Taylor-Proudman theorem despite obvious accelerations in the rotating frame. The two-dimensional subdynamics will result in long range vertical correlations at fairly energetic and likely easy-to-observe scales. However, this does not mean that the flow is actually two-dimensional even for rotating turbulence that is fairly weak. Therefore, it is not always appropriate to take the Taylor-Proudman constraint too literally when the flow is turbulent.

1.4.2 Inertial Waves in Turbulence: Linear Propagation

If we supply a three-dimensional perturbation to a rapidly rotating flow, Eq. 1.13 cannot hold. In the linear theory of rapidly rotating flow, we must look at Eq. 1.15, noting that a small three dimensonal perturbation $\mathbf{u}$ will lead to time varying vorticity ($\nabla \times \mathbf{u}$). If we restrict the problem to an infinite rotating space,

we may decompose a three-dimensional velocity perturbation into a sum of plane inertial waves, as they form an orthonormal basis [47]. The subsequent evolution of the perturbation may then be described as radiation of inertial waves. This process can be complicated when a spatially compact initial perturbation is considered, as such a perturbation necessarily contains a wide spectrum in both wavelength and direction. Radiation of energy away from the perturbation will proceed at the group velocity (Eq. 1.18). The group velocity $\mathbf{c}_g \sim k^{-1}$, so the energy in the long wavelength Fourier components will radiate away fastest.

In a pair of papers, Davidson, Staplehurst, and Dalziel [49, 57] consider the role of linear inertial wave propagation in the evolution of small three-dimensional eddies in a rotating turbulent flow using both inviscid theory and experiment. Davidson *et al.* [57] note that in the inviscid limit, the axial component of the angular momentum, linear momentum, and vorticity of the original eddy must always remain inside a cylinder tangent to it and aligned with the rotation axis. Energy can radiate in all directions under the action of inertial waves. Davidson *et al.* show that a spherical vortex of diameter d evolving according to Eq. 1.15 will form a pair of increasingly elongated vortices with centers spaced a distance $2d\Omega t$ apart. This is consistent with the dispersive propagation of energy implied by Eq. 1.18. This process provides a way for a sea of small three-dimensional eddies to rapidly evolve toward an anisotropic, vertically elongated flow even in the absence of nonlinear interactions. The process is depicted in Fig. 1.4.

Staplehurst *et al.* present empirical evidence that this linear propagation process is important to the vertical elongation of vortices in realistic rapidly rotating

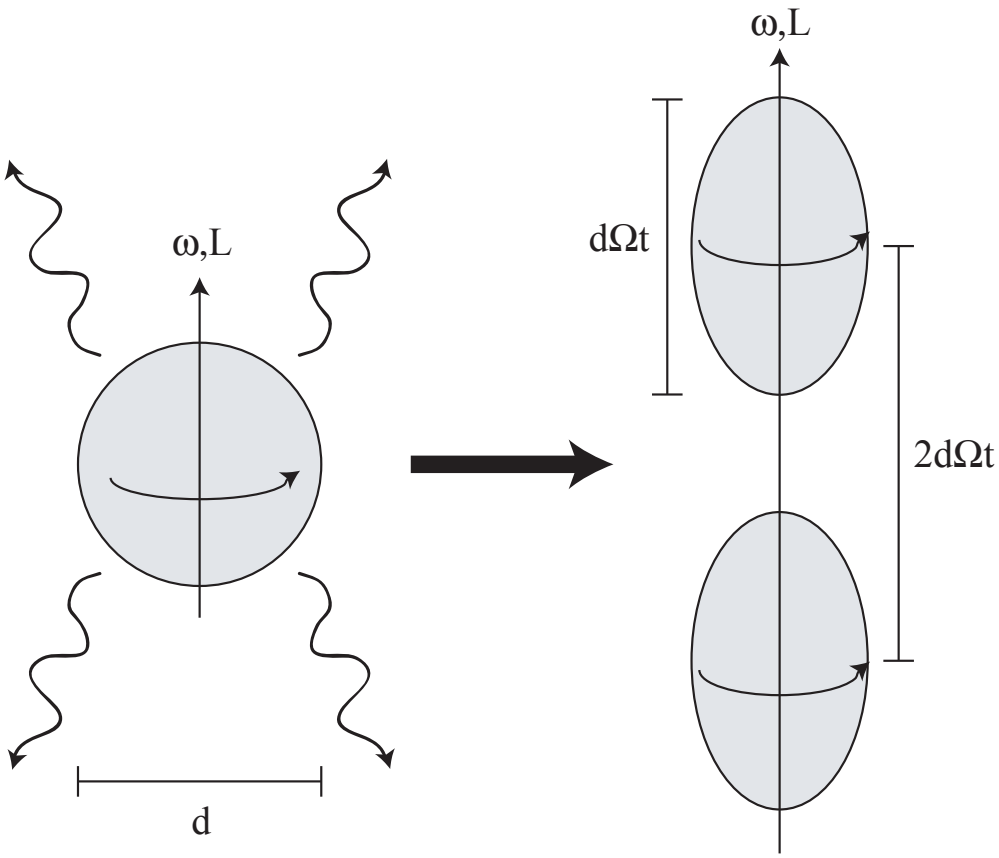

Fig. 1.4: An initially spherical isolated vortex evolves into a pair of vertically elongated vortices by inertial wave radiation, according to Davidson *et al.* [57] and Staplehurst *et al.* [49]. The separation and vertical extent of these vortices are consistent with a spreading of energy at the inertial wave group velocity, given in Eq. 1.18. The vorticity ω and angular momentum L inside a cylinder tangent to the original blob must remain there in the inviscid limit of Eq. 1.15, but energy can radiate in all directions.

turbulence by studying two-point correlations in decaying grid turbulence in a rotating tank. Davidson, Staplehurst, and Dalziel emphasize the role of phase coherence among the component inertial waves making up an initial three-dimensional perturbation: in the linear dynamics, the energy spectrum of the original vortex blob is forever identical to that of the subsequently evolving flow, because the energy spectrum does not retain phase information. Vertical elongation is not a general feature of a random sea of linear, noninteracting inertial waves, but rather a specific property of the particular phase-coherent superpositions needed to describe compact three-dimensional initial conditions.

Kolvin *et al.* [58] establish the importance of inertial wave propagation to the transient evolution of rotating turbulence by forcing an initially quiescent rotating tank from the bottom using turbulent, three-dimensional source-sink flow. The instantaneous horizontal power spectrum in a sheet near the top of the tank is measured using particle image velocimetry. Despite the three-dimensional forcing with a broadband distribution of length and timescales, energy in long wavelengths arrives first at the measurement plane, consistent with propagation at the group velocity of inertial waves, Eq. 1.18. The initial evolution from quiescent rotation to turbulence is well described by fronts of inertial waves arriving after a time $H/\mathbf{c}_g$, with H the height from the bottom forcing to the the measurement plane. The experiment is depicted schematically in Fig. 1.5 At later times, a buildup of energy at long scales is observed, consistent with a nonlinear inverse cascade of additional energy from small scales to large. An important observation of Kolvin *et al.* is that the slow group speed of the short wavelength (large k) inertial wavefronts results in

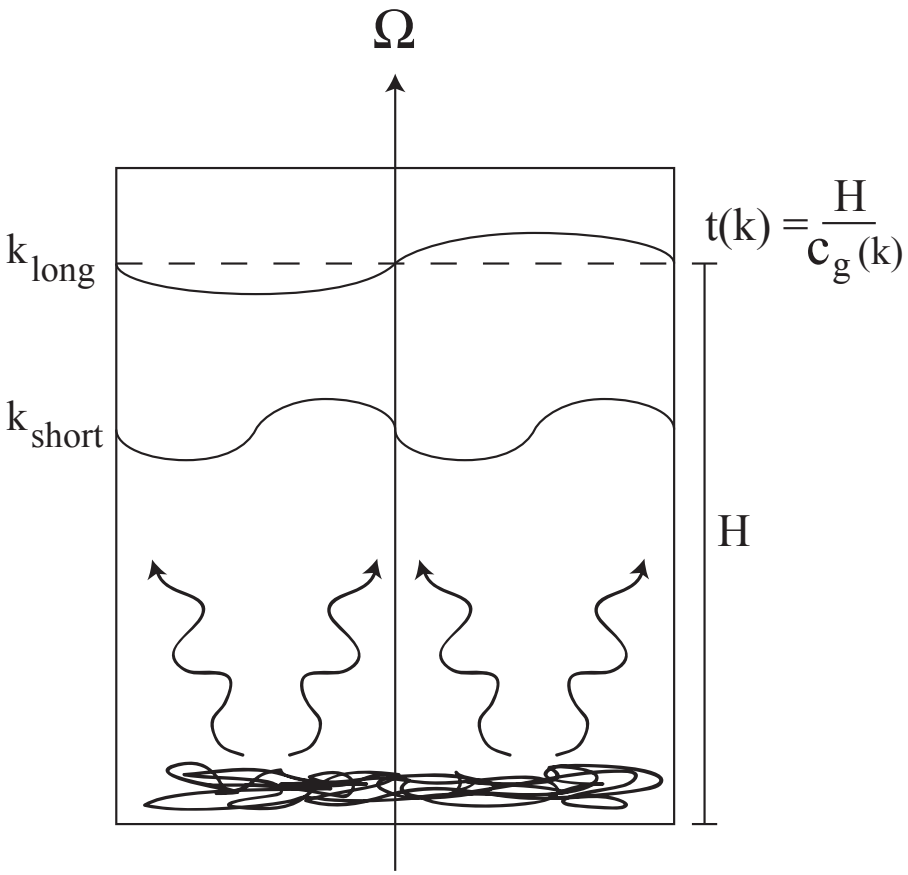

Fig. 1.5: Schematic of the experiment of Kolvin *et al.* [58]. Three-dimensional turbulence is excited at the bottom of an initially quiescent rotating tank by source-sink flow. Velocity energy spectra are measured in a plane a height H from the bottom of the tank. It is observed that the longest wavelength disturbances arrive first, followed by shorter and shorter wavelengths. The arrival time of motions with wavenumber k is consistent with the dispersive propagation of inertial waves at the group speed $c_g(k) \propto \frac{2\Omega}{k}$, as in Eq. 1.18. In the experiment, the shorter wavelength waves are observed to propagate through a turbulent background, suggesting that they are a relatively robust feature of moderate *Ro* turbulence.

their arrival at the measurement plane well after nonlinear effects have started to cascade intermediate scale energy to large scales.

The short wavelength inertial waves continue to arrive in in a manner well described by linear theory despite their propagation through established rotating turbulence. The implication is that inertial waves are robust to nonlinear advection in the rotating frame, and are important to energy transport even through a turbulent background. As Kolvin *et al.* put it,

> "These waves can, therefore, not be regarded as small and slow perturbations to a static fluid, but as a more general mode of energy transport."

The fragility of inertial waves and inertial modes under the action of other turbulent motions is a matter of some contention, as the derivation of both assumes small amplitude perturbations to solid body rotation. However, the "linear propagation" of inertial waves is, when viewed in the inertial frame, already a significantly nonlinear effect. In the inertial frame, there is no Coriolis term, and it is the rapid advection by the fast azimuthal velocity (a high Reynolds number flow) that is responsible for the aforementioned effects of rotation. When the azimuthal velocity of solid body rotation is large compared to the velocities in a frame rotating with it (when Ro is low), the mathematics in the rotating frame are significantly simplified by truly negligible *additional* nonlinearity. However, as Ro is increased, the exact role of the nonlinear term is always a matter of great difficulty for both calculation and intuition. It should not be assumed *a priori* that its only role is to decohere and tear apart motions that are derived using linear analysis. The certainty of nonlinear

interaction of large amplitude inertial waves does not preclude observation of the "linear" effects.

1.4.3 Inertial Waves in Turbulence: Nonlinear Interaction

The observation of linear wave propagation in rotating turbulence does not minimize the importance of nonlinear interactions. However, inertial waves have a role to play here too. The nonlinear interactions of inertial waves are some of the first nonlinear effects to become relevant for three-dimensional forcing as Ro is increased. Smith and Waleffe [59] discuss the importance of resonant wave triads in low Rossby number turbulence. Non-resonant triads are also first-order nonlinear interactions among inertial waves, but the strength of the interaction of triads depends on time as $e^{\mathrm{i}(\omega_1+\omega_2+\omega_3)t/Ro}$. When Ro is small, this phase factor will oscillate rapidly in time unless $(\omega_1 + \omega_2 + \omega_3) = 0$. The time-averaged interaction is therefore heavily dominated by resonant triads.

According to Smith and Waleffe, the role of the inertial wave triads is that they transfer energy from strongly three-dimensional motions (those with large $(\hat{\mathbf{z}}\cdot\nabla)\mathbf{u}$) to more nearly two-dimensional ones. At low Ro, inertial waves with wavevectors and frequencies that add to zero tend to transfer energy to the wave with the more nearly horizontal wavevector, those with small values of $k_z/\left|\mathbf{k}\right|$. At first order, fluid motions with $k_z \equiv 0$, which can be Rossby waves or other geostrophic motions, decouple from the motions with $k_z \neq 0$ [55, 59]. Higher order interactions such as resonant quartets are needed transfer energy from the small k_z inertial waves into the purely two-dimensional flow. The two-dimensional large scales in rotating turbulence are

energetic scales, and nonlinear interactions among them can also be important, in the manner of an inverse cascade discussed in Sec. 1.4.1. It appears, however, that these interactions can be of secondary importance in low Ro turbulence.

Smith and Lee [47] investigate this by comparing simulations including inertial wave triad interactions to those with 3D interactions suppressed. The latter is equivalent to the 2D inverse cascade. In both cases, energy is injected at intermediate scales around k_f. If Ro is low enough, both the 3D and the 2D simulation result in the generation of energetic, nearly two-dimensional large scales. However, the purely two-dimensional nonlinear evolution results in a dramatically slower buildup of energy in the large scales than that afforded by the three-dimensional inertial wave interactions. Furthermore, the 2D inverse cascade process ends (at the termination of the simulation) with nearly symmetric distribution of cyclones and anticyclones, while the 3D cascade process results in a significant asymmetry in favor of cyclones.

Inertial waves' role in the cascade of energy to large-scale, nearly two-dimensional motion is similar to the ideas of Davidson, Staplehurst and Dalziel [49, 57]. However, the mechanism proposed by Smith and Lee is nonlinear where that of Davidson, Staplehurst and Dalziel is not. Davidson, Staplehurst and Dalziel suggest that the linear mechanism of Fig. 1.4 may be important where the forcing method results in a large number of small three-dimensional eddies, like von Kármán vortices shed behind an oscillating grid. It may be that both effects generally co-exist. As Ro becomes larger, off-resonant triads and higher order nonlinear interactions will become more and more important. These two mechanisms are simply examples that elucidate different aspects of the evolution of rapidly rotating turbulence.

1.4.4 Inertial Modes and Rossby Waves in Turbulence

The discussion so far of inertial waves' role in rotating turbulence has not made explicit mention of modes of containers or other system-scale waves like Rossby waves. Experimental work in rapidly rotating tanks [49, 58] could possibly (should probably?) result in excitation of these modes. The constraint placed on possible large scale inertial wave motions by the boundary conditions is not necessarily particularly restrictive. However, the spectrum of allowable large scale modes in certain frequency ranges can have a significant role in shaping the overall flow. The experiments of Kelley *et al.* [12–14] find that the power spectrum of induced linear magnetic field fluctuations near a turbulent spherical Couette experiment is dominated by a single inertial mode with a spectral power perhaps 10^4 times larger than the induction by any other fluid motion. The external induced magnetic field in such experiments and comparison with the external linear induction predicted for a pure inertial mode velocity field are shown in Fig. 1.6 (a). The modes are excited by differential rotation at Reynolds numbers exceeding 10^6. The physical mechanism of excitation of inertial modes in spherical Couette flow appears to be over-reflection [12, 14], wherein wave-induced ripples on a shear layer moving faster than the phase speed of the wave transfer energy to the wave. This dissertation will extend the results regarding inertial modes in spherical Couette flow somewhat by establishing some of the directly measured flow properties of the turbulent flow states associated with inertial mode excitation. In particular, we will present scaling of driving torque and flow fluctuations.

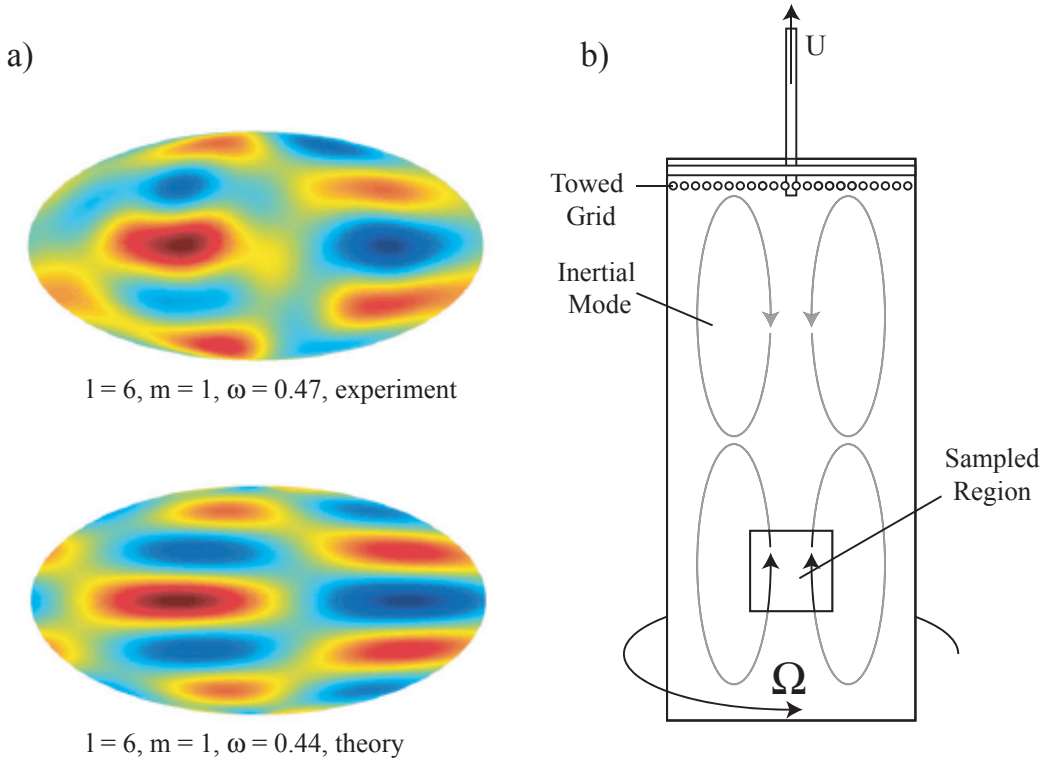

Fig. 1.6: Inertial modes in turbulent flows result in global flow correlations and inhomogeneity. At (a), a Mollweide projection of the external induced magnetic field (top) in rapidly rotating turbulent spherical Couette flow with weak axial applied field is compared with the induction predicted for that expected from a single matching inertial mode (bottom). The experimental measurements of Kelley *et al.* [14] show a strong signature of the identified mode along with additional fluctuating induction. At (b), a schematic depiction of the results of Bewley *et al.* [60]. Inertial modes excited by a towed grid in rotating, decaying turbulence result in oscillatory flows at large scales with respect to the measurement volume. Several inertial modes are observed as the turbulence decays. Excerpted images from Kelley *et al.*, 2007 [14] reproduced here with permission from Taylor and Francis Group, Ltd.

Bewley *et al.* [60] observe the strong excitation of several modes of rotating channels (cylindrical and square) throughout the decay of rapidly rotating grid turbulence. The kinetic energy in a small measurement volume does not decay as a power law in time, but rather undergoes large fluctuations at frequencies consistent with known inertial modes of the container. These inertial modes excited by grid turbulence are a strong source of inhomogeneity in the flow, as a few oscillatory system-scale motions dominate the kinetic energy in a given measurement volume, as depicted schematically in Fig 1.6 (b).

A few experimental groups report magneto-Coriolis waves of system-wide scale in hydromagnetic systems. These waves are the combined result of restoration by Coriolis and Lorentz forces and their fast branch, with forces acting in concert on the fluid[6], shares features in common with Alfvèn waves and inertial waves. Large scale wave motions identified with magneto-Coriolis waves in a cylinder are reported by Nornberg *et al.* [61]. Magneto-inertial waves are identified in magnetized spherical Couette flow by Schmitt *et al.* [62]. These latter two do not attempt to compare directly with predicted modes of the containers, although the addition of magnetic field as a restoring force complicates that comparison.

Observation of large scale motions in rotating turbulent flows specifically ascribed to inertial modes of the container are relatively scarce, though the results we are aware of suggest that modes of containers are robust components of the large scale motions if a mechanism exists to excite them, and perhaps they are not often identified. In experiments, this may be due partially to the difficulty of global mea-

[6] The slow branch has Coriolis and Lorentz forces in opposition.

surements that expose system-wide correlations like those available for the induced magnetic field in the experiments of Kelley *et al.*. In numerics, it is probably due to the difficulty of performing three-dimensional calculations at low enough Ekman numbers even in the absence of other turbulence. Quasi-geostrophic numerics such as those by Schaeffer and Cardin [33], while they can reach low Ekman number, are incapable of showing inertial modes, as they are limited to strictly two-dimensional motions.

The role of Rossby waves in turbulence is more well established, especially in geophysical contexts. Rhines has written a good review on the role of Rossby waves in oceanic and atmospheric turbulence [27]. Rossby waves dominate the motion at long length scales in geophysical turbulence, and the wave "steepness" controls the nonlinearity at large scales. That is, long wavelength waves must grow to much larger amplitude than shorter wavelength Rossby waves for nonlinearity to be important. Rossby wave motions cause significant non-locality in the evolution of β-plane turbulence: waves can radiate energy into previously quiet regions of fluid. Turbulent straining and mixing coexists with propagating waves on the large scales of rotating turbulence. Rossby wave breaking (where a wave motion is wrapped up by its own vorticity) and interaction with zonal flows are phenomena of primary importance for planetary-scale transport in Earth's stratosphere [63–65].

The quasi-geostrophic simulations of Schaeffer and Cardin and comparison with experiment [33, 35] demonstrate the importance of Rossby waves to extremely low *Ro* turbulence in a rapidly rotating sphere. Tian *et al.* [28] study flow transitions between Rossby wave flow states in a turbulent rotating annulus, and Baroud *et*

al. [30] measure the scaling properties of Rossby-type turbulence in a similar experimental geometry. Read *et al.* [32] demonstrate generation of banded zonal flows by rapidly rotating convection on the β-plane.

1.5 Summary

The preceding review of theory relevant to rotating turbulence and review of the literature on rotating flows is not comprehensive, but it touches on a number of phenomena that we may expect to be relevant. Rotating turbulent flows have a tendency toward two-dimensional correlations and vertical coherence. However, only those flows where fluid accelerations are unimportant and where forcing is predominantly two-dimensional will be described well by the theory of two-dimensional turbulence. Real rotating turbulence will be extremely anisotropic, but will still have a great deal of the energy contained in three-dimensional motions.

Three-dimensional rotating turbulence is dominated by inertial waves. The linear propagation of inertial waves and Rossby waves quickly radiate energy into otherwise quiescent regions of rotating fluid, but this non-local transport of energy is also robust to pre-existing turbulent flows and so is not limited to energy transport into quiet regions. Linear propagation of inertial waves and nonlinear interaction thereof both help to efficiently cascade energy to the two-dimensional large scales, which retain significant memory of the forcing method. In bounded flows, a few large scale inertial modes (or Rossby waves) can be an important component of the velocity field, resulting in system-wide coherence and strongly inhomogeneous

turbulent flow.

The boundary layers in rotating turbulent flow may be complicated, especially where inertial modes, Rossby waves, or other oscillatory flows interact with boundaries in relatively quiet regions of inhomogenous rotating turbulent flows. The effect of the boundary layer dynamics on rotating flows can be especially significant, as the tendency for an inverse cascade results in energy piling up in the otherwise nearly inviscid large scales. Boundary friction is likely to be the most important energy dissipation mechanism for the energy in many rapidly rotating flows. Tight nonlocal coupling of the bulk fluid to the boundaries can arise from the "fluid elasticity" evidenced by Rossby waves, inertial waves, and a tendency toward two-dimensional flow. Instabilities and boundary inhomogeneity as the Ekman layers are modulated by inertial modes or Rossby waves could provide system-wide feedback on overall energy dissipation and transport. Boundary layer eruptions as the resolution of inertial mode singularities can result in strong zonal circulations and may therefore significantly affect transport of angular momentum in the bulk.

Rotating turbulence is anisotropic, inhomogeneous, wavy, and tightly coupled to boundaries. It is also commonplace in real physical systems, and as such, there is much to be gained from a solid predictive theory that incorporates all of these effects in a realistic way. Moreover, we find in rotating turbulence, as Lord Kelvin wrote [66] regarding the motions of a rotating column of fluid:

"Crowds of exceedingly interesting cases present themselves."

2. MOTIVATION AND PRIOR WORK

2.1 Earth's Dynamo

The magnetic fields of Earth and the Sun have significant influence on humankind. Dynamics of the magnetic field of the sun are responsible for accelerating charged particles toward Earth, and the Earth's field acts as a shield for this energetic charged particle radiation. The shield afforded by our magnetosphere is important for life on Earth and increasingly important as we expand technologically into near space. In 1919, Joseph Larmor hypothesized [67] that the magnetic field of the sun was due to the motion of the electrically conducting fluid thereof. Like the sun, the Earth has a magnetic field because of the flow of conducting fluid. In the case of the Earth, this flow is that of its liquid iron outer core, depicted in Fig. 2.1, along with the solid inner core and mantle. This dynamo process is a sort of continuous electrical generator resulting from a self organizing turbulent flow.

The evolution of Earth's field is slow, and it is arguably of more immediate importance to have good predictions for the Sun's magnetic field dynamics. However, we have access to long historical records of Earth's field dynamics in the form of magnetized lava flows and sediment deposition, and we can map Earth's modern field in great detail with satellite magnetometers. Understanding Earth's field is a

key to unlocking more general predictions for planetary and stellar dynamos.

Earth's magnetic field is dominated by a dipolar component tilted slightly with respect to Earth's rotation axis. The higher-order multipole moments of the field that we can measure are equal in strength when extrapolated to the core-mantle boundary. [68]. The dipole is a factor of ten stronger than the apparently white spectrum of higher multipoles. Earth's field is a dynamical quantity. Changes are observed on a wide range of time scales. Most notable, perhaps, are the erratic reversals evident in the paleomagnetic record. Deposited sediments and lava record the direction and strength of Earth's magnetic field in the distant past, and it is observed that the dipole component of the magnetic field changes polarity on irregular intervals from a few tens of thousands of years to fifty million years [69]. The dipole reversals are only one component of the variations of Earth's field. The smaller deviations, known as the secular variation, have been of interest to humankind for as long as we have used compasses, and for centuries we have recorded the local direction of the magnetic field across much of the globe with respect to true North, in the interest of navigation [70].

The generation of magnetic field by a velocity field $\mathbf{u}$ is described by the induction equation, which can be arrived at from combining Maxwell's equations in a moving conductor with Ohm's law. In dimensionless form, the induction equation is

$$\frac{\partial \mathbf{B}}{\partial t} = \nabla \times (\mathbf{u} \times \mathbf{B}) + \frac{1}{R_m} \nabla^2 \mathbf{B} \tag{2.1}$$

To fully describe the nonlinear dynamo process in a rotating planet, one must also

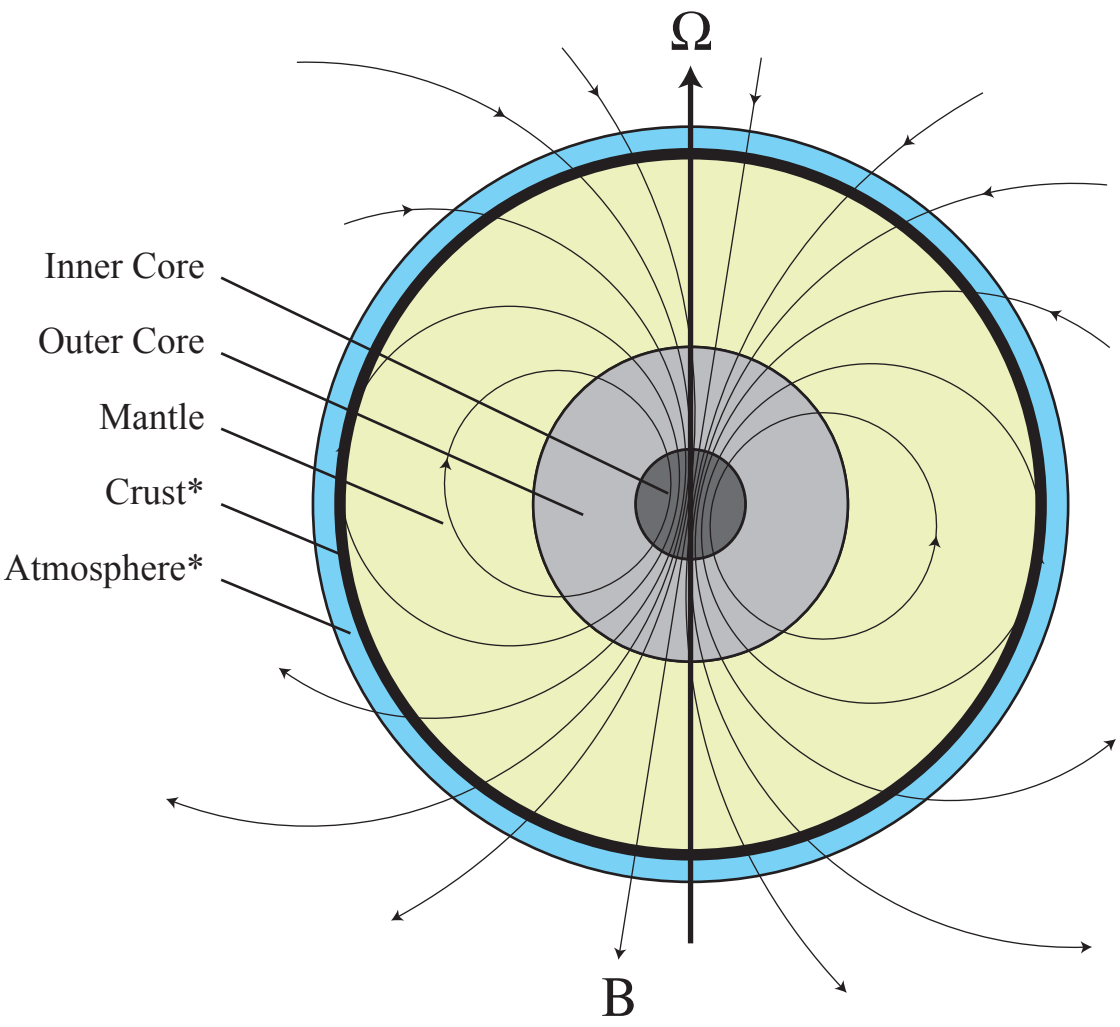

Fig. 2.1: The dipole-dominated magnetic field of the earth is generated by turbulent flow in the outer core. The inner core of the Earth is thought to be nearly pure solid iron with a radius 0.35 times that of the outer core. The outer core a liquid mix of iron and lighter metallic elements. The mantle is rock, very weakly conducting and slow flowing. The thin rocky crust and atmosphere are drawn much thicker than to scale (*). Dynamics in the core are greatly influenced Earth's rotation, and many of the results discussed in Sec. 1.3 should be relevant there.

include a Lorentz force term in in the Navier-Stokes equations, Eq. 1.8. This feedback of magnetic field on the velocity field is responsible for nonlinear saturation of dynamos.

The magnetic Reynolds number of Eq. 2.1 expresses the strength of the diffusion of magnetic field by ohmic dissipation of currents. With length scale L, velocity U and magnetic diffusivity $\eta_m = (\mu\sigma)-1$ the magnetic Reynolds number is defined as

$$R_m = \frac{UL}{\eta_m} \tag{2.2}$$

In any fluid dynamo, the flow $\mathbf{u}$ must be sufficiently vigorous to overcome the action of diffusion. However, the critical value of R_m required for any particular flow field to show a growing ($\partial_t \mathbf{B} > 0$) magnetic field is a complicated matter of the flow geometry.

Some analytical results for growing field solutions of Eq. 2.1 for prescribed flows of homogeneous, incompressible fluid were presented by Bullard and Gellman [71]. Magnetic field generation by a velocity field where Lorentz forces are negligible is called a kinematic dynamo process, and is important for the start-up phase of a self-excited magnetic dynamo. It is likely that subcritical bifurcations to dynamo action can exist in nature when a nearby object supplies sufficiently strong field. Some simple model flows are known to be subcritical dynamos [72]. However, to produce a field initially from a dynamically insignificant seed field requires a kinematic dynamo phase. Inspired by particular mathematical flows known to be kinematic dynamos, a number of experiments have been performed, with only a few showing dynamo

action. The Riga, Latvia dynamo involves a helical downflow of liquid sodium and straight return flow in a large, rotating concentric tube apparatus [73]. This apparatus was inspired by the Ponomarenko dynamo [74], a theoretical kinematic dynamo where a cylinder rotates and translates in an infinite conducting medium. An experiment in Karlsruhe, Germany [75] pumped liquid sodium through a lattice of oppositely-signed helical baffles. Although they were successful dynamos, both of these experiments placed fairly rigid constraints on the geometry of the fluid flow. The prescribed velocity fields chosen in much of the early work on kinematic dynamos were not consistent with solutions to the Navier-Stokes equations with any particular forcing or boundary conditions. This resulted in a need to build the right flow geometry out of stainless steel.

A difficulty in achieving self-organizing dynamos is that sufficiently high magnetic Reynolds number using liquid metals requires strongly turbulent flow. The magnetic Prandtl number,

$$P_m = \frac{\nu}{\eta_m} = \frac{R_m}{Re} \tag{2.3}$$

for liquid metals is on the order of 10^{-5} or 10^{-6}, and the critical magnetic Reynolds number for dynamo flows is at least one, if not tens or hundreds. Therefore, there is no hope in a liquid metal experiment of generating a dynamo in a laminar flow, as the required hydrodynamic Reynolds number will be in the millions. The large velocity fluctuations in a turbulent flow make it difficult to predict whether a particular apparatus will be a dynamo.

High magnetic Reynolds number with sufficiently self-organized flow appears

to be easily achieved in the liquid metal cores of planets and the plasma of stars. In experiment, turbulence greatly confounds analysis and experimental design, and the search for a turbulent laboratory free from the tightly constrained flows of the Riga and Karlsruhe experiments has proven difficult. A recent experiment in Von-Kármán shear flow (counter-rotating disks at either end of a cylinder) in Caderache, France exhibited a self-excited and dynamically interesting magnetic field, replete with reversals [76, 77]. This is a turbulent dynamo in perhaps the most open geometry used to date, allowing Lorentz forces to restructure the flow. It is a step toward a self-organizing turbulent flow free from strong boundary constraints on the flow. However, this experiment so far has only generated a field when ferromagnetic impellers are used. This raises doubts to the validity of the results for planetary and stellar dynamos, which are too hot to support ferromagnetism.

Numerical simulations have done better than laboratory dynamos in producing earth-like dynamics. Glatzmaier and Roberts [78] were among the first to find a dipolar reversing solution in rapidly rotating convection in an earth-like geometry. Reversing dipoles are a common feature of modern geodynamo models [79], but they are not the only possibility. Christensen, Olson, and Glatzmaier [80] find that in the range of numerically accessible parameters, many dynamo solutions can be found. A new review by Christensen *et al.* [81] collects a number of numerical dynamo models that are "earth-like" in relative dipole strength and reversal frequency. Most geodynamo numerics focus on convectively driven flows, though it has been postulated that the precession of Earth's axis could be an alternative candidate for forcing the core flow. Tilgner [82] has demonstrated that self-consistent flow driven

by precession of the rotation axis can result in a dynamo.

However, despite the Earthlike behavior of these dynamo models, a mystery remains. None of the geodynamo numerics come close to matching the dimensionless parameters of planetary or stellar dynamos. The Ekman number is as much as nine orders of magnitude too large and the magnetic Prandtl number P_m in the numerical simulations is rarely lower than 0.1 or 0.01, with many simulations run near $P_m = 1$. Serious computational limitations exist in the ability to push toward more Earthlike parameters, and when attempts are made to do so, the long-time evolution of the resulting models can rarely be studied, as time evolution is traded for spatial resolution. Furthermore, Christensen *et al.* [81] note that the more the parameters are tuned toward those of the Earth, the *less* the resultant dynamo behavior agrees with the observations of Earth's magnetic field. The success of numerical models in capturing some of the salient features of the geodynamo must eventually be reconciled with the self-consistent turbulent flow at realistic parameters.

While no experiment or numerics will reach Earthlike parameters in any of our lifetimes, a great deal could be learned about these unusual observations by comparing a self-excited laboratory dynamo with numerical models. It is suggested that perhaps turbulent momentum diffusion resolves the vast discrepancy in the actual geodynamo Ekman number and the model Ekman number. This is similar to how the oceanic Ekman spiral of Section 1.3.6 is more consistent with a momentum diffusion hundreds of times the molecular value. This seems to be a reasonable hypothesis, but to build predictive models of the geodynamo, we will need to establish a solid understanding of turbulent momentum transport in a rapidly rotating system

with similar geometry, and test any predictions in situ. The University of Maryland three meter experiment is the latest in a series of turbulent sodium experiments aimed at better understanding the geodynamo problem.

As will be described more fully in Section 3.2, our experiment is designed to capture some of the important ingredients of the geodynamo. In particular, it will have high magnetic Reynolds number, turbulent flow, rapid rotation, and a geometry that matches the inner and outer core depicted in Fig 2.1, with the outer rotating tank representing the core-mantle boundary. The experiment still does not reach an Earthlike Ekman number[1], but if it successfully produces a dynamo, it will come closer to Earthlike parameters and, possibly, Earthlike dynamics than any other to date. It will also present a testbed for numerical models that reproduces many of the difficult conditions that keep us from *predicting* the behavior of planetary dynamos in simulations. It is a rapid rotator, highly turbulent, and filled with low magnetic Prandtl number fluid with a familiar geometry. If this device shows dynamo action, working to predict its dynamics with an eye toward realistically and consistently parameterizing the effects of the rapidly rotating, magnetized turbulence will be fruitful in the more general problem of predicting planetary and stellar dynamos.

[1] It is likely that this is literally impossible in a non-self-gravitating object without significant advances in materials science.

2.2 Atmospheric Turbulence

As it turns out, no hydromagnetic[2] data will be presented in this dissertation. However, the mechanically complete experiment was filled with water and the hydrodynamic flow therein has yielded a good deal of interesting science, which forms the scientific content of this work. These results are all relevant as a purely hydrodynamic base case that can be compared with numerics in the interest of studying core flows. However, rapidly rotating purely hydrodynamic flow bears on other geophysical problems. The complicated turbulent circulation of the atmosphere is something of a *post-hoc* motivation for the experiments we have conducted.

Few turbulent fluid flows have more direct effect on humankind[3] than the motions of the Earth's atmosphere. Intense weather events like hurricanes and tornado-spawning squall lines carve wide swaths of destruction. The general pattern of the transport of moisture is critical to the food and water supply for our populace. Our ability to predict the short-term weather is reasonably good in a practical sense. Good short-term prediction of intense storms and sophisticated real-time tracking of them helps to limit the loss of life and property by allowing people time to prepare and find shelter well before a large storm arrives. However, the prediction horizon for atmospheric motions is not long enough to predict long-term trends in the weather. In recent decades, there has been a keen interest in climate prediction. We would like to understand how rising temperatures may change the familiar long-term averages of energy transport and material transport in Earth's atmosphere and oceans.

[2] We prefer hydromagnetic to magnetohydrodynamic or the acronym MHD.

[3] With exceptions for the blood pumping through our veins [83] and the air in our lungs [84].

Climate prediction is a thicket of interacting feedback loops of energy inputs and sinks, turbulent flows, chemical and phase changes, and biological responses. While an incompressible, unstratified experiment cannot capture most of these aspects, it does appear to have some relevance to a specific problem in climate prediction. The world's structure of population centers, farmland, and uninhabited areas is largely contingent on the very long-term, persistent behavior of the turbulent flow of our atmosphere and oceans. The general circulation of the air mass on the Earth has profound consequences on the zones of habitability of our planet. A schematic cross section of the layers of the atmosphere and its general circulation are depicted in Fig. 2.2. Strongly three-dimensional turbulence tends to be localized in a thin

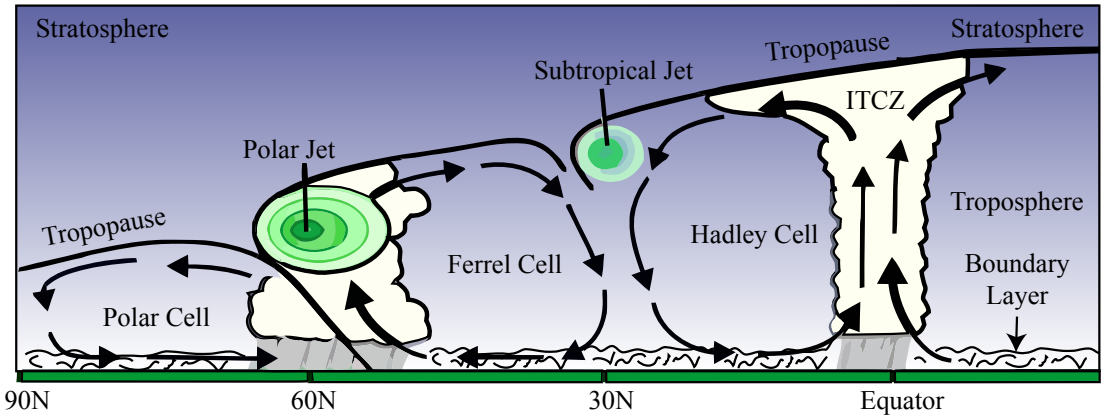

Fig. 2.2: Schematic view of Earth's general circulation and layered structure. Convective upwellings in the inter-tropical convergence zone and the midlatitudes large-scale recirculations, which are deflected in and out of the page by the Coriolis force. Jet streams are strong azimuthal motions resulting from this process. Instabilities of the the jet streams feed back strongly on the convective energy release. This figure is adapted from a public domain image at http://www.srh.weather.gov/srh/jetstream/global/jet.htm, thanks to NOAA.

boundary layer near the ground on the order of 1 km thick [85]. This layer is well

mixed and vigorously turbulent, with a Reynolds number approaching 10^{10}, but is capped by stably stratified fluid above, which damps turbulent fluctuations. The thickness of the well mixed boundary layer is a strong function of other factors. The troposphere is an often stably-stratified region of the atmosphere that may be unstable to three-dimensional turbulence depending on the exact local conditions. The troposphere is strongly turbulent as well, but the turbulence there is typically closer to two-dimensional. The onset of vigorous moist convection results in thunderstorms which can extend up to the depth of the troposphere, up to 8-15 km and occasionally into the stratosphere. The stratosphere, lying beyond the tropopause is tenuous and strongly stratified as it is in radiative equilibrium. Typically, little mass is exchanged between the troposphere and stratosphere [86]. The stratosphere has only weak direct fluid effects on the troposphere, and so will not be discussed here.

The wavy, slowly evolving character of the upper tropospheric turbulence seems to provoke atmospheric scientists into calling the three-dimensional boundary layer motions "turbulence" and the large-scale more nearly geostrophic motions a "mean flow" when studying the velocity fluctuations near the surface [85]. Nevertheless, flow in the upper troposphere is generally nonlinear and aperiodic, and exerts an influence on the details of the boundary layer turbulence [87]. So the turbulence in the troposphere could reasonably be described as strongly anisotropic, inhomogeneous turbulence.

The general circulation of the earth is organized into several poloidal cells. The Hadley cells in Fig. 2.2 exist on on either side of the equator to around 30° N and

are essentially simple convective recirculations driven by a steady supply of vigorous thunderstorm activity in the inter-tropical convergence zone at low latitudes [88, 89]. All the circulation cells are significantly deflected by the Coriolis force resulting in the large-scale mean wind patterns near the surface in the troposphere[4]. The subtropical jet stream is a rapid region of meandering but largely azimuthal flow the upper troposphere at the downflow boundaries of the Hadley cells, caused largely by angular momentum conservation as fluid is pumped from the equator to that region. The polar and Ferrel cells have a more complicated relationship to the convective processes that drive the atmospheric circulation. The polar jet stream is driven largely by turbulent eddy momentum transport in the midlatitudes as familiar weather systems like midlatitude cyclones form and mature [88, 89]. The two jet streams are fed by convective motions but exert a strong feedback on the convection. Rossby waves that form, grow, and break on the jet streams strongly influence the development of all large-scale convective weather systems. The mid-latitude energy release and momentum transfer to the jet streams is especially sensitive to the meandering and the pressure systems associated with them. So the upper level, slow, tropospheric turbulence, is coupled in a rather tight feedback with the processes that sustains it. Furthermore, the upper level tropospheric winds are acted upon by a turbulent boundary layer drag and even at enormous Reynolds numbers, this turbulence does not appear to become free of the influence of the mean shear and strong anisotropy aloft [3, 85, 87].

It rains a great deal near the equator and in the midlatitudes but it is rather

[4] The trade winds, for example.

hot and dry near the downflow of the Ferrel and Hadley cells depicted in Fig. 2.2. This is an important factor in how we have structured our global population centers and farmland. However, the number of cells and jet streams is probably not predictable solely by simple arguments regarding force and energy balances, especially since the polar jet heavily depends on rotationally organized turbulent transport of momentum. Detailed predictions of momentum transport in a turbulent atmosphere are likely needed for fully predictive climate models. It would be a vast oversimplification to suggest that our experiment could serve as a climate model, as it is free from many of the detailed energy transports and feedback loops of energy and moisture by processes other than fluid transport. However, we will present results that suggest that the "global circulation" in the experiment, the large-scale pattern of zonal flows and waves, is a rather sensitive function of the experimental parameters even in unstratified, non-convecting shear turbulence. Angular momentum transport away from the inner sphere and and large-scale flow patterns in the system are robust across broad ranges of the Rossby number defined in Eq.1.9. In these ranges of Ro, the flow patterns remain the same, simply strengthening with increasing Ro. At critical values of Ro, however, there are abrupt transitions to other turbulent flow regimes. The ratio of measured azimuthal velocities to the outer sphere tangential velocity in the ranges Ro where multiple stability are experimentally observed are comparable to the ratio observed jet stream velocities (60 m/s) [88] to the tangential velocity of the Earth. The Ekman number of the experiment, while two orders of magnitude higher than that of Earth, is still extremely low. In each case, the rotation should be of great importance. A comparison is shown in Table 2.1.

Tab. 2.1: Comparison of the dimensionless parameters of Earth's atmosphere and those of the experiment. The Ekman number is based on the thickness of the fluid layer in both cases, using Earth's maximum troposphere depth of 15km [88]. A value of 1.5×10^{-5} m^2/s is used for the kinematic viscosity of air [90]. In each case the Rossby number is defined as $U/(\Omega R)$. The Rossby number, in the atmospheric case is based on the maximum observed jet stream velocity of 60 m/s [88]. In the experimental case, it is defined based on measured mean zonal velocity observed in one particular turbulent flow state out of multiple stable states observed in the experiment.

Parameter	Earth	Experiment
E	10^{-9}	10^{-7}
Ro_{jet}	0.2	0.2

This is not to suggest that we are *close* to a switch of the jet stream behaviors or global circulation patterns, but rather it seems that Ro is a critical parameter in rapidly rotating systems that can exhibit multiple stable turbulent states. Understanding the flow regime switches in a simple system free from the extra complications of the convecting, stratified atmosphere could be instructive in some way, much as Rossby's simplified dynamical model described in section 1.3.5 remains useful in our understanding of the jet streams' tendency to meander.

2.3 Prior work on Spherical Couette

2.3.1 Differential Rotation vs. Convection

Neither the rapidly rotating core of the Earth nor Earth's atmosphere have strong boundary differential rotation[5]. The forcing in Earth's core comes from buoy-

[5] It should be mentioned that spherical Couette flow can produce dynamo action. For example, see Guervilly and Cardin [91]

ancy driven convection or precessional torques as discussed in Sec. 2.1. Rotating shear flow, however, is in some ways not so different from rotating convectively driven flow. A strong analogy can be drawn between the turbulent shear flow between between concentric cylinders and thermal convection [92, 93]. The Reynolds stresses[6] associated with a wide variety of fluid motions in rotating systems generate differential rotation in the form of zonal flows (axisymmetric and vertically invariant azimuthal flows). Convection in rapidly rotating systems often causes differential rotation in both theoretical studies [94–96] and experiment [32, 97]. The nonlinear interaction of inertial modes or other waves in a shell can drive strong differential rotation [21, 98]. Such waves can be excited by precession or convection. Even generically forced homogenous turbulence in a rotating, sheared system exhibits Reynolds stresses that generate zonal motion [99]. Indeed, strong differential rotation is a common feature of rapidly rotating turbulence. So, despite the seemingly more direct forcing of differential rotation by the differentially rotating boundaries, spherical Couette might not be such a bad model for vigorously nonlinear rapidly rotating flows. It will be shown later that the observed differential rotation is not simply related to the strength of the "applied" differential rotation based on the boundary angular velocities. The effects of strong zonal flows on the energy and momentum transport may be more important than how they are set up in the first place.

[6] Advective forces resulting from persistent velocity correlations.

2.3.2 Non-Rotating Laminar States

Curiously, much of the prior work in the shear flow between rotating spheres is not particularly relevant to the current work. There are few experiments or simulations addressing the turbulent regime. The Chapter 1 review on inertial waves, inertial modes, Ekman layers, and other topics on rotating flow and turbulence is perhaps of more importance. With a few exceptions that will be noted at the end of this section, experiments in the spherical Couette geometry have focused largely on laminar mode transitions, up to the transition to chaos, using small devices. When turbulent flow is achieved, the transition threshold is noted, and the turbulence is not characterized further. Simulations have been largely focused on investigating the same laminar parameter regime as the experiments, and it is still not possible to reach our experimental parameters using three-dimensional direct numerical simulations. It is useful to review a few instructive examples and clear, systematic studies to elucidate some of the basic laminar flow states from both experiment and simulation. A few results in similar geometries may be relevant, and will be discussed here, as well as the few turbulent spherical Couette results that have been published.

In the ensuing discussion, it is useful to use some typical spherical-Couette-specific definitions of the Ekman and Rossby numbers. The Ekman number used from here on without other qualification will be defined using the gap width $\ell = r_\mathrm{i} - r_\mathrm{o}$ and the outer sphere rotation rate Ω_o as

$$E = \frac{\nu}{\Omega_\mathrm{o} \ell^2} \tag{2.4}$$

and the Rossby number will be defined using a dimensionless velocity scale based on the boundary differential angular velocity and the length scale, $U = (\Omega_\mathrm{i} - \Omega_\mathrm{o})\ell$. With these choices, the Rossby number of Eq. 1.9 becomes a dimensionless differential angular speed:

$$Ro = \frac{\Omega_\mathrm{i} - \Omega_\mathrm{o}}{\Omega_\mathrm{o}} \tag{2.5}$$

When the outer sphere rotation is zero, neither the Ekman nor the Rossby number is defined, but the Reynolds number based on their quotient,

$$Re = \frac{Ro}{E} = \frac{(\Omega_\mathrm{i} - \Omega_\mathrm{o})\ell^2}{\nu}, \tag{2.6}$$

is always defined and we will adopt this definition of Re throughout the parameter plane. For completeness, we note that the radius ratio,

$$\eta = \frac{r_\mathrm{i}}{r_\mathrm{o}} \tag{2.7}$$

is an important dimensionless parameter[7] in spherical Couette flow. Many authors use the dimensionless gap width instead, usually denoted β

$$\beta = \frac{r_\mathrm{i} - r_\mathrm{o}}{r_\mathrm{i}}. \tag{2.8}$$

For reference, in our experiment $\beta = 1.86$. It is more typical to use the inner sphere tangential speed instead of the velocity $(\Omega_\mathrm{i} - \Omega_\mathrm{o})\ell$ in the definition of Re, but the choices above appear to be most relevant to the final experimental results, and the definition of $Re = Ro/E$ for every Ro and E simplifies the comparison of experiments where the outer boundary rotates and those where it does not. It is common in the literature to define E in terms of the outer sphere radius r_o, and

[7] Again, η=0.35 for the three meter experiment.

sometimes to have an extra factor of two in the denominator. We note that some care should be used in comparing to other work and among other papers, as the choices for the external experimental parameters have various definitions. It is easy to convert, provided explicit definitions are provided.

Other researchers have taken an interest in laminar spherical Couette flow to understand the routes to chaos therein. It turns out that an enormous variety of laminar flow patterns can be found as a function of the dimensionless parameters in Eqns. 2.4-2.7. The basic state of laminar spherical Couette flow with the outer sphere stationary for small enough radius ratio η is a simple recirculation as shown in Fig. 2.3(a), though with a laminar and equatorially symmetric outflow jet at the equator. The jet as sketched is deflected and turbulent.

Fluid is subject to Ekman pumping near the inner sphere boundary, and fluid on the upper and lower halves gets pumped to the equator, emerging as a jet. For low enough Re, this jet is equatorially symmetric and axisymmetric, and a large-scale meridional circulation completes the fluid circuit [100, 101, 104]. Along with this is an axisymmetric azimuthal velocity profile throughout the fluid, leading to a fully three-dimensional axisymmetric circulation. Despite the simple geometry and axisymmetric flow, the fully three-dimensional base state is more difficult to work with theoretically. According to Wulf *et al.* [101], spherical Couette flow is a prototype for systems where the possible dynamical instabilities vary continuously in space. Certainly, a great number of laminar states are possible as η and Re are varied. Wulf *et al.* map the laminar bifurcations as a function of Re for two different radius ratios with the outer sphere stationary.

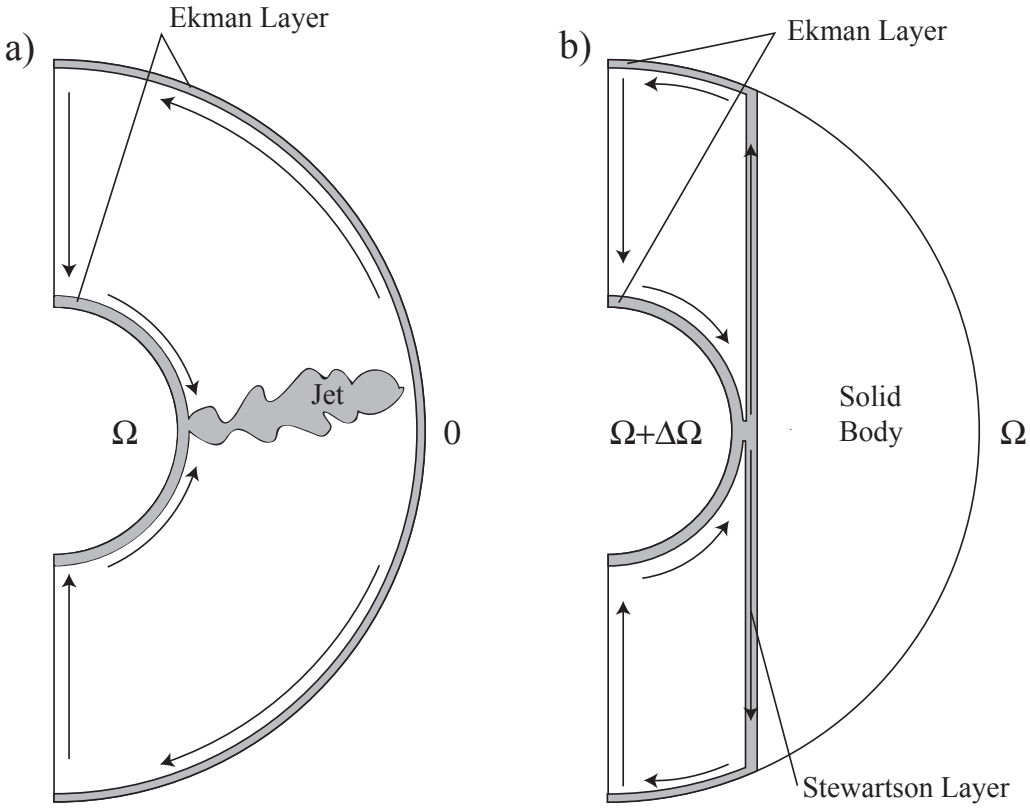

Fig. 2.3: The general circulation patterns for the special cases when the outer sphere is stationary (a) and rapidly rotating (b). At (a), when the inner sphere revolves faster than the outer, the Ekman layer on the inner sphere pumps fluid toward the equator, where it erupts in a jet, with a global two cell poloidal recirculation. This jet is steady, planar, and axisymmetric in the laminar basic state flow, but develops wavy instabilities at higher Re [100, 101]. This jet persists and becomes turbulent at high enough Re. At (b), the basic state with rapid overall rotation (low E and nearly vanishing Ro) consists of motions confined near and inside the cylinder tangent to the inner sphere. The Ekman layers on the inner and outer spheres are connected by a steady, nested free shear layer called the Stewartson layer after Keith Stewartson who derived its structure [102, 103]. The Stewartson layer resolves the velocity jump between the differentially rotating fluid inside the layer and the fluid rotating with the outer cylinder.

The first bifurcations from the two-cell recirculation state in laminar spherical Couette flow, even leaving the outer sphere stationary, depend on the radius ratio and Reynolds number in a complex fashion. As Re is increased, the flow bifurcates from the axisymmetric two cell recirculation to a nonaxisymmetric rotating wave. Hollerbach *et al.* [100] systematically studied a wide range of radius ratios, from the narrow gap case of $\eta = 0.91$ to a very wide gap with $\eta = 0.09$, and found strong and unusual[8] dependence on radius ratio. Hollerbach *et al.* establish that the the nonaxisymmetric wave is an instability of the equatorial outflow jet for all but the smallest radius ratios, where the instability is in the inflow near the poles. In the two cases considered that straddle our radius ratio, the instability is to a low azimuthal wavenumber ($m = 2$ or $m = 3$) slowly traveling wave. The low Re associated with these flow states is impossible to achieve in our experiment, but the idea of a wavy outflow jet may still have some relevance.

2.3.3 Turbulent Equatorial Jet

If the inner sphere has an outflow jet in our experiment, that jet must be turbulent due to the large[9] Reynolds numbers at which we operate. A turbulent outflow jet as depicted in Fig 2.3(b) is not a feature that seems to be established by a published direct observation in high Re spherical Couette flow, though it is established for related cases. Bowden and Lord [105] present a Schlieren visualization of a likely turbulent jet ejected from the equator of a magnetically levitating, rapidly

[8] For example, a mode transition involving two *different* m = 6 waves

[9] Up to 6×10^7.

rotating sphere in a large container. Hollerbach *et al.*[106] observe a turbulent jet from the equator of a periodically oscillating sphere starting at $Re = 200$. Kohama and Kobayashi [107] study the boundary layer on a rapidly rotating sphere in a large volume and report a turbulent jet and turbulent boundary layer below some critical latitude, which is about 40° at their highest Reynolds number[10]. A turbulent equatorial jet in spherical Couette flow has been visually established in a small apparatus here at $Re \sim 200,000$, but no satisfactory visual record has been worked out in the short time this was attempted. The outflow jet is a basic consequence of the imbalanced centrifugal forces near the sphere surface, and so should be robust at all Re.

A boundary such as the inner sphere will always act as a centrifugal pump and drive an outflow when it is rotating more rapidly than the fluid around it. This pumping and equatorial jet is therefore likely to be significant to many of our results. The jet almost certainly exists throughout a large region in parameter space, and may play a role in rotating turbulent states when the inner sphere is super-rotating. We might also consider a similar process at the *outer* sphere equator when the fluid is rotating more slowly than the wall. This undoubtedly causes Ekman pumping down toward the equator as depicted in Fig. 1.3(b). This is the basic mechanism of Ekman spin up from rest [6]. However, to our knowledge, the possibility of a concentrated and turbulent radially inward jet at the outer sphere equator has not been addressed, as it does not correspond to any numerically or experimentally accessible flow.

[10] Less than 2×10^5 based on the sphere radius and tangential velocity.

2.3.4 *Stewartson Layer and Instabilities*

There is another laminar limiting case of interest of flow at low velocities in spherical Couette flow. The circulation at low Ro and low Ekman number, very near solid body rotation, is depicted schematically in Fig. 2.3(b). Stewartson [103] derived a steady solution to the flow between concentric spheres for rapid overall rotation and infinitesimal differential rotation. In some sense, this solution is the resolution of the equatorial outflow consistent with the Taylor-Proudman theorem of Eq. 1.13, which must hold except in the boundary layers for vanishing Ro. The solution consists of nested shear layers near the cylindrical surface tangent to the inner sphere. The outer layer at largest radius scales in thickness[11] as $E^{1/4}$, and resolves the azimuthal velocity discontinuity. It also transports mass and angular momentum from the faster sphere to the slower, as per the arrows in Fig. 2.3(b). The outer layer at the smallest radius scales differently, as $E^{2/7}$ and is required to smoothly join the internal shear layer with the boundary layers. This layer has some reversed mass flux, the balance circulating in a less concentrated return flow in the region inside the tangent cylinder. The innermost layer, scaling as $E^{1/3}$ is needed to resolve a 2nd derivative discontinuity that the other layers cannot. The Stewartson layer is a striking example of the effects of rapid rotation, but as with the Taylor-Proudman theorem in general, the range of validity of the concept to rotating turbulence is limited. Stewartson stated the conditions for validity of the solution as $RoE^{-1/3} \ll 1$. Even if we interpret "much less than" generously and fix

[11] This layer would be a few centimeters thick in our experiment, could we reach sufficiently low Ro

it at 1, the solution ceases to be valid at $Ro = 0.003$ at the lowest Ekman number we will present here. Our minimum achievable Ro is approximately seventeen times that, $Ro_{\min} = \pm 0.05$. Stewartson's validity threshold is consistent with extrapolation from the experimental studies of Hide and Titman [108] and Schaeffer and Cardin [35] on instabilities of the Stewartson layer. Hollerbach *et al.* [109] studied supercritical mode transitions in comparison between theory and experiment in a spherical Couette apparatus, but again this work is much less strongly rotating, with E in the simulation four orders of magnitude higher than that in our experiment. At our Ekman number, using a quasigeostrophic model, Schaeffer and Cardin report Rossby wave turbulence at a Rossby number less than half of our lowest accessible Ro. So while the Stewartson layer and instabilities thereof are conceptually useful, the existence of such a layer consistent with Stewartson's original solution should not be expected in any of our experiments.

2.3.5 Turbulent Sodium Spherical Couette

As far as we know, there are three spherical Couette devices worldwide that operate in a strongly turbulent regime. The desire to perform hydromagnetic experiments in planetary geometries and the need for more vigorous forcing than that afforded by convection makes spherical Couette flow attractive, and any experiment that reaches an interesting value of R_m using liquid metals will be necessarily turbulent. Therefore, the other high Re devices are all liquid sodium experiments. The DTS[12] experiment in Grenoble, France is a sodium flow with a permanent

[12] Derviche Tourneur Sodium

magnet dipole inner core and therefore has a core region of highly magnetized fluid [62, 110, 111]. It is a large device, about 42 cm in diameter, capable of Re up to probably 10^7, but the permanent magnet core confounds direct comparison of results in weakly magnetized flows. This device exhibits interesting hydromagnetic waves and future work to understand the similarities and differences to turbulent spherical Couette without strong magnetic field could prove fruitful.

The other two highly turbulent devices are housed at our lab, and the author has assisted with experiments in both devices. The 30 cm device used by Sisan *et al.* [112] has a fixed outer sphere, a rotating, conducting inner core, and strong applied axial magnetic field. Sisan *et al.* studied primarily hydromagnetic instabilities of the turbulent base state. The hydromagnetic instabilities were identified with the magnetorotational instability, a phenomenon that is a matter of some intense research in the astrophysical community. This device has a peak Re as defined by Eq. 2.6 of about 4.4×10^6, but is incapable of outer sphere rotation. The 60 cm diameter device used in the inertial mode studies of Kelley *et al.* [12, 14] is capable of Re up to about 1.6×10^7 and the 3m device has reached 5.6×10^7 in the experiments presented here. The rapidly rotating 60 cm device and the newly constructed three meter device have a significant region of overlap in Rossby and Ekman and in this region they can complement each other. The three meter experiment has direct flow measurements in the rotating frame to allow directly access to turbulent fluctuations and mean flows, while the 60 cm experiment allows the use of weak magnetic field as a passive flow tracer to infer the global large-scale velocity field using magnetic field induction. The hydromagnetic three meter experiment with liquid sodium will

exceed the maximum R_m of the 60 cm device by about a factor of ten, the purpose for which it was originally constructed. It is also capable of much more rapid inner sphere super-rotation, achieving higher positive Ro for a given E. This region of parameter space is home to the most novel turbulent flow states presented herein. A few new results regarding the turbulent flows in the overlapping parameter space will also be reported here, with comparison of both direct flow and magnetic field measurements.

3. EXPERIMENTAL APPARATUS

3.1 Introduction

The design and construction of the experimental apparatus represents a significant contribution to the experimental study of rotating hydrodynamic and, eventually, hydromagnetic turbulence. The majority of the time spent[1] on this dissertation work was in the preparation of the device, and the author's contribution to the success of this massive experimental undertaking is significant. This description of the experiment's engineering and construction will be detailed in a way that is not called for on purely scientific grounds. The author leaves behind the usual lab notebooks and repositories of drawings and design files. However, the complexity of the device warrants a more structured description of the author's contribution to the mechanical, control, and instrumentation systems. Persistent and easily accessible documentation of various design elements is critical for future researchers in our lab, as well as possible international collaboration efforts. The detailed description in this chapter is intended to collect engineering information into something of a users' manual to help other researchers throughout the hopefully long life of the University of Maryland three-meter device. Those interested primarily in the scientific content

[1] A large amount, but worthwhile and enjoyable.

of this dissertation may skip to the relatively terse overview of the geometry and capabilities of the finished device provided in Appendix B, and then resume with the scientific results, starting with Chapter 4.

Section 3.2 of this chapter will discuss the design goals for the experiment in the context of the original motivation of obtaining dynamo action in an earth-like laboratory experiment. This is of some importance, as the experiment was not designed for purely hydrodynamic experiments with water as a working fluid. Some of the design choices may seem overly restrictive for the experiments presented in this dissertation. The remainder of the chapter will be structured to provide a complete overview of the engineering and design of the device, while dwelling in more detail on the contributions of the author. This device is a collaboration, and many hours were spent by our design team on all aspects of the experiment. Major subsystems designed largely by other members of the team will be discussed in the interest of completeness and continuity, but it will be made clear who was responsible for the largest portion of the engineering and/or construction thereof. Further detail on the contributions made by Santiago Andrés Triana throughout the course of the design process will be available in his forthcoming dissertation.

3.2 Design Motivation

3.2.1 Dimensionless Parameter Goals

The original experimental goal of dynamo action in an Earthlike system led to design choices specifically aimed toward safely conducting hydromagnetic ex-

periments at high magnetic Reynolds number and low Ekman number in a device geometrically similar to Earth's core. Fig. 3.1 schematically depicts the basic experimental apparatus, which consists of outer and inner stainless steel spheres with radius ratio $\eta = 0.35$, making the fluid volume the same shape as Earth's fluid outer core.

The Earth's inner core is thought to be nearly pure solid iron, so it is electrically conducting[2]. Several solid metallic inner sphere designs were considered but ultimately rejected as too costly, too heavy, or too far beyond the abilities of reasonable manufacturing processes to be feasible. We chose instead to approximate insulating electromagnetic boundary conditions by installing a thin, hollow stainless steel shell. The inner shell is essentially transparent to fluctuating magnetic fields at frequencies we might expect to encounter, becoming one electromagnetic skin depth ($\delta = \sqrt{2/\sigma\mu\omega}$) thick at a frequency of 7 kHz. The thicker outer shell is one skin depth thick at a frequency of about 280 Hz, which should be transparent to all except the induction at fast small scales. This boundary condition is fairly Earth-like, with the mantle and core mantle transition zone thought to be weakly conducting[3].

The goal of achieving high magnetic Reynolds number,

$$R_m = \frac{UL}{\eta_m} \tag{3.1}$$

demands a large apparatus capable of driving high velocity flows in a working fluid with low magnetic diffusivity. The magnetic diffusivity, $\eta_m = (\mu\sigma)^{-1}$ is a material

[2] But not ferromagnetic, as the core exceeds the Curie temperature for iron.

[3] Though possibly heterogeneously so [113].

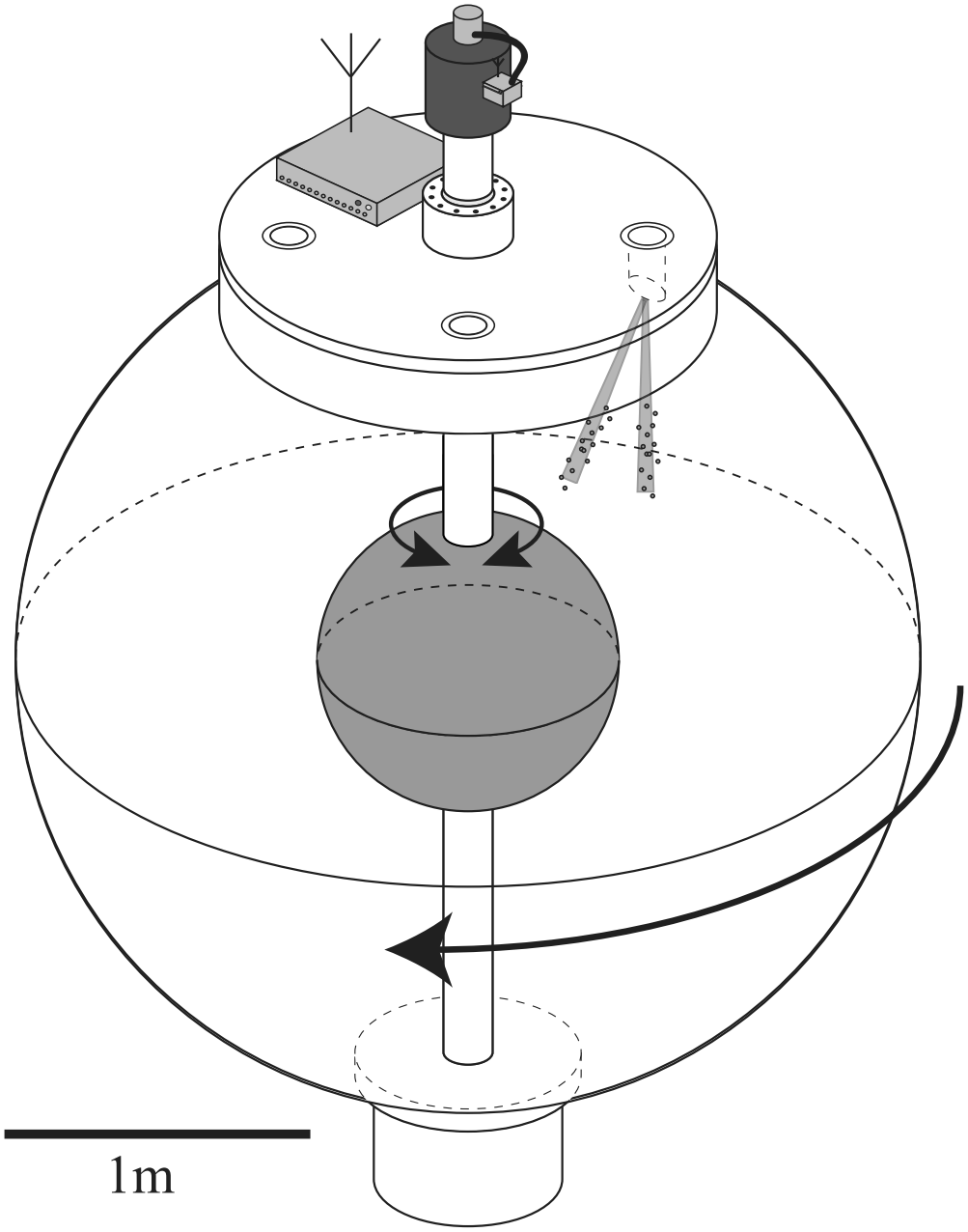

Fig. 3.1: Brief schematic overview of the experiment. The spherical boundaries are free to revolve independently. The ratio of their radii, $r_\mathrm{i}/r_\mathrm{o} = 0.35$, is the same as the radius ratio of Earth's fluid outer core to its solid inner core.

property of the working fluid. Though the magnetic permeability, μ, of liquid sodium is close to that of free space, μ_0, it is one of the best fluid electrical conductors, with an electrical conductivity σ only five and a half times less than pure copper. Therefore, it is a good choice for high magnetic Reynolds number experiments. There are further advantages to sodium in large hydromagnetic experiments. It has a fairly low melting point, around 98° C. It is produced easily via the electrolysis of salt, so it is rather inexpensive. The density of liquid sodium is low, 0.93 kg m^{-3} , slightly less than that of water. Other groups have used mercury or gallium metal in smaller experiments, however, both of these metals are significantly more dense and expensive. As the three-meter experiment already contains 13,500 kg of working fluid at the density of water, this is not an insignificant issue. Furthermore, other liquid metals in common use are less electrically conductive than sodium, requiring larger experiments or higher speeds to produce the same magnetic Reynolds number. Sodium is, then, nearly the only choice for a large scale hydromagnetic experiment like this one.

Once the magnetic diffusivity of the working fluid has been made as low as possible, further improvements in magnetic Reynolds number come from increasing the size and the flow velocities of the apparatus. The scaling of the power required to drive a turbulent shear flow apparatus is approximately

$$\mathcal{P} \propto \rho U^3 L^2. \tag{3.2}$$

Thus, the achievable flow velocity scales as the cube root of the input power. Power supply and cooling can be difficult for a large apparatus like this one. The installed

electrical infrastructure for the experiment as designed was one of the single most significant budget items. A major difficulty in smaller apparatus is an issue of power density. Ultimately, all of the mechanical power supplied to the apparatus is dissipated as heat in the fluid. The cooling requirements for a small apparatus can be extremely stringent, and every predecessor of the three-meter apparatus at the University of Maryland has ultimately had R_m limited by the impossibility of providing sufficient cooling, rather than other design considerations.

To achieve high enough Rm while avoiding power density problems, it is best to make the apparatus as large as possible. The major design constraint in this regard is the available laboratory space and access to it. The three-meter experiment is housed in a large high-bay laboratory with an overhead crane. Access from the outside to this laboratory space is by means of a large rolling door at one end, which is 10 feet (3.05 m) wide. The frame of this door is of heavy I-beam post and lintel construction, a load-bearing structure. The cost to enlarge this door was estimated early on to be a significant fraction of the total budget. The nominally three meter size of this experiment is simply the largest sphere that would fit through the door. The finished vessel cleared the door's width by approximately 16 mm (5/8").

The three-meter experiment is driven by a pair of 250 kW motors However, as the speed of the outer boundary is limited to a fraction of the maximum speed of the inner sphere, and, as the torques on the two spheres must balance, it is impossible for the outer motor to develop full rated power. The absolute upper bound on the mechanical power input for the three-meter apparatus is 320 kW based on the motor torque and the allowable boundary speed. The actual fluid power demand,

however, is a property of the turbulent flow state as a function of inner and outer sphere rotation speeds. It is impossible to predict the power input required at a given Ro and E. Similarly, it is not possible to predict the actual flow velocities. We will discuss magnetic Reynolds number estimates based on measured flows in Chapter 7, where we give a brief prognosis of the prospects for dynamo action based on our hydrodynamic results.

We may, however, estimate a maximum magnetic Reynolds number here. Using a velocity scale that is an estimate of the maximum achievable tangential boundary velocity of the inner sphere and a length scale of the radius of the outer sphere, we have

$$R_m = \frac{\Omega_\mathrm{i} r_\mathrm{i} r_\mathrm{o}}{\eta_m}. \tag{3.3}$$

Based on a estimate of the limiting speed of the differential boundary rotation taken from experiments conducted in water, the maximum possible Reynolds number in the three meter experiment is about 700.

We are also interested in attempting model a dynamo such as that which arises in the Earth's rapidly rotating core. The dynamo simulations discussed in Chapter 2 seem to rely on the flow organization afforded by the rapid rotation. Such a low Ekman number (Eq. 1.10) as that in Earth's core, $E \sim 10^{-15}$, is impossible to achieve in experiments. However, we can study rotating turbulence at modest Rossby number at an Ekman number considerably lower than that which can be achieved in simulation. The Ekman number defined using the maximum design

rotation rate and outer sphere radius

$$E_{\mathrm{R}} = \frac{\nu}{\Omega_{\mathrm{o}} r_{\mathrm{o}}^2} \tag{3.4}$$

can be as low as 1.25×10^{-8}. We denote this as E_{R} here, as later chapters will use the fluid gap width, not the outer sphere radius, as the relevant length scale, and we do not wish to cause confusion. The definition using the core-mantle boundary radius (equivalent to our outer sphere radius) is common in the geophysical literature, so E_{R} is more appropriate to the current discussion. Table 3.1 compares the dimensionless parameters achievable in the three meter experiment vs. what is estimated for Earth's core.

Tab. 3.1: Comparison of the relevant dimensionless parameters, Ekman and Magnetic Reynolds, of Earth's core and the design goal parameters of the experiment.

Parameter	Earth	Experiment
E_{R}	10^{-15} [114]	10^{-8}
R_m	300-500 [115]	700

Sodium metal is a good choice as a working fluid for rapidly rotating hydromagnetic experiments. It has a low viscosity (7×10^{-7} m^2/s, 70% that of water), and its low density compared to other commonly used liquid metals reduces the centrifugal load on the experimental device, allowing more rapid rotation. Ultimately, the lowest Ekman number that can be achieved is limited by the maximum allowable centrifugal stresses in the outer shell. This sets our highest rotational speed limit of 4 Hz, corresponding to our lowest Ekman number, $E_{\mathrm{R}} \sim 10^{-8}$.

3.2.2 Experiment Limitations

While sodium metal is the clear choice to achieve the highest possible magnetic Reynolds number, and a good choice for reaching low Ekman number, it is not without its hazards, as it reacts violently with water and burns readily in air if it comes in contact with an ignition source[4]. The sodium oxide produced by burning or otherwise oxidizing sodium dissolves in water (damp skin, throat, eyes, mucous membranes) to form sodium hydroxide, which in low concentrations is an irritant and can cause severe caustic burns in high concentrations. Sodium fires are difficult to extinguish. The best prevention of all possible sodium hazards is to attempt to eliminate the possibility of any large scale leaks. In a rapidly rotating experiment such as this one, the high centrifugal pressures developed at large cylindrical radius are of serious concern. Even small orifices can leak significant mass in a short time. A three centimeter hole opening near the equator with the outer sphere rotating at maximum design speed could release a thousand kilograms or more of sodium in the few minutes before the sphere could be brought to a halt. Additionally, when the sphere is at rest, any opening far from the top of the experiment has the potential to leak a large amount of sodium slowly if the leak goes unnoticed for some time. In the interest of minimizing the possibility of large scale leaks of either sort, it was decided that the outer spherical vessel would have openings only at the top. A large cylindrical flanged opening 1.5 m (5 feet) in diameter provides access to the interior of the outer vessel. This allows easy insertion and removal of a variety of internal

[4] At the temperatures we intend to run the experiment, around 105° C, liquid sodium does not auto-ignite in air. However, if sprayed into air at significantly higher temperatures it will.

forcing systems, but significantly limits the amount of sodium that can leak out gravitationally. A centrifugal leak could still be significant, but the modest pressure at the lid rim (about 1.7 atmospheres at maximum speed) can be sealed effectively without any special techniques.

The prohibition of openings below the lid rim is not particularly limiting for the planned hydromagnetic experiments. As discussed in Sec. 3.2.1, the wall of the outer vessel is nearly transparent to magnetic fields, as long as they are fluctuating more slowly than a few hundred Hertz. A great deal of information can be deduced from magnetic field measurements external to the outer vessel. In regions of parameter space where the experiment does not generate its own magnetic field, applying a magnetic field and observing the induced field can still be instructive. It is scientifically useful to have some direct flow measurements, pressure, velocity, and so forth to corroborate the magnetic field measurements. However, measurements of the magnetic field can serve as a primary diagnostic. For the purely hydrodynamic flows that will be presented in this dissertation, the limitation of access to the flow solely through the top lid (coupled with limited space for instrumentation) does prove to be something of a hindrance. Some seemingly rather basic quantities relevant to a rotating, turbulent shear flow, such as mean velocity profiles, may seem conspicuously absent.

3.3 Machinery Overview

3.3.1 Rotating Frame

We will begin the description of the experimental device with a mechanical and power system overview describing the major mechanical and drive subsystems. We will leave instrumentation until Sec. 3.5. Figure 3.2 is an annotated cross section of the apparatus, and Fig 3.3 is an annotated photograph of the exterior. The outer sphere, Fig. 3.3 (a), has an inner boundary diameter of 2.92 ± 0.005 m (115 in.)[5] and 2.54 cm (1 in.) wall thickness. The entire rotating mass is supported by a load spreading base, Fig. 3.2 (A). The cylindrical section of the base is welded to a half inch thick stainless steel plate, and strong struts help spread the load. The plate, base, and struts, and lower portion of the frame, Fig. 3.3 (b), are a welded assembly that rests on the laboratory floor. The weight of the rotating mass (about 21 tons) is borne by a spherical roller thrust bearing, Fig. 3.2 (B), which fits into a seat in the cylindrical base. A part called the bottom head, Fig. 3.2 (C), fits into the bottom bearing inner race and bolts to the bottom sphere flange Fig. 3.2 (D). The original design called for an alignment pin in this location, but the manufacturer was unable to adequately align the hole in the vessel bottom flange with the vessel's rotation axis. Therefore, spacer plates allow a range of radial adjustment for centering the bottom of the sphere on the rotation axis. In addition to its mechanical function, the bottom head conveys heat transfer oil from a concentric-flow rotary fluid union,

[5] Dimensions relevant to scientific results will be given in metric and Imperial units. Those that are engineering details will only be given in Imperial, as was used in the design process.

Fig. 3.2 (E), to inlet and outlet manifolds, Fig. 3.2 (F), which distribute fluid to a spiral wound half-pipe heat transfer jacket that covers much of the outer sphere surface.

A 1.52 m (5 ft.) diameter flanged cylindrical opening in the top of the outer sphere allows installation and extraction of the interior forcing package and allows access to the fluid for making flow measurements. This opening is capped by a thick stainless steel lid, Fig. 3.2 (G), the lower surface of which completes the outer spherical boundary. The lid is located with respect to the sphere flange by two large location pins diametrically opposite on the 65 in. diameter bolt circle. A short shaft integral with the lid mates with the inner race of the outer sphere top bearing, Fig. 3.2 (H). The outer race of this bearing is held by a housing Fig. 3.2 (I) which bolts to the outer support frame seen in Fig. 3.3. The bearing (H) is free to move axially on the shaft of lid (G) to allow for thermal expansion of the vessel when it is brought to operating temperature for sodium experiments. The outer sphere is driven by a timing belt drive with a 25:3 reduction ratio. A large toothed pulley, Fig. 3.2 (J), bolts to the top lid and is centered on the rotation axis using a dial indicator. Four instrumentation ports, Fig. 3.2 (K), each 12.7cm (5 in.) in diameter allow direct measurement of flow quantities. These ports are located at 60 cm (23.625 in.) from the rotation axis. Removable port plugs approximate a flush surface at the outer sphere boundary, and are removable so that instrumentation may be installed in them easily. These port plugs will seal to the top lid with flat graphite seals for the sodium experiments. For water, O-rings were used.

A 16.8 cm (6.6 in.) shaft, Fig. 3.2 (L), concentric with the outer sphere axis

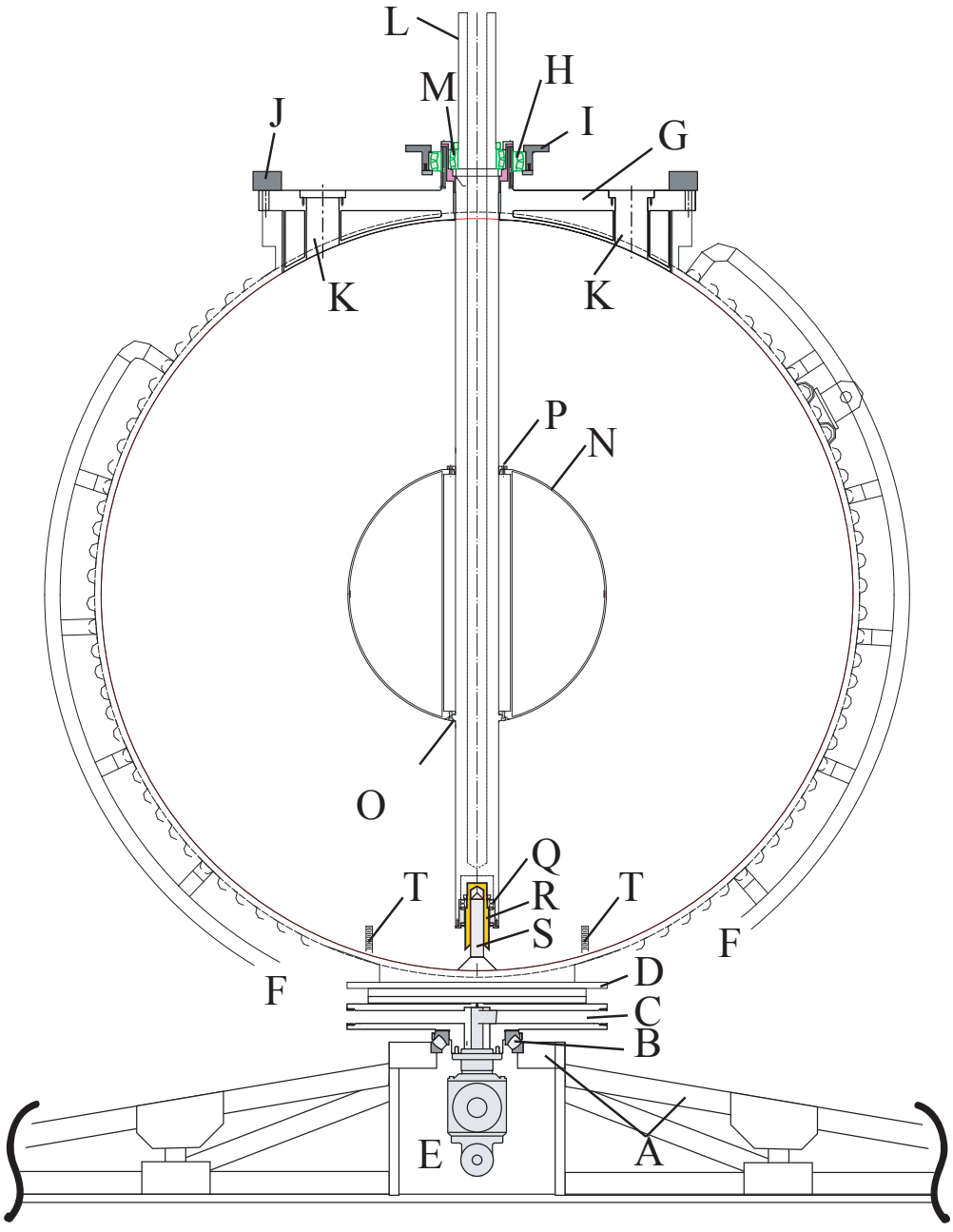

Fig. 3.2: A cross-sectional overview of the experiment mechanical design, excluding supporting structure. *Cont'd next page.*

Fig. 3.2: A) Load spreading base and bottom bearing outer race seat, integral with Fig. 3.3 b.
B) Outer sphere bottom bearing, SKF#29344E.
C) Bottom head.
D) Outer vessel flange, bolts to B.
E) Dual-flow rotary fluid union, Deublin #H107.
F) Outer vessel jacket manifolds.
G) Top lid, bolts to outer vessel flange.
H) Outer sphere top bearing, SKF #ECB 23956 CAC/W33.
I) Outer top bearing housing, bolts to motor subframe, Fig. 3.4(e).
J) Outer sphere pulley.
K) Instrumentation port (4 total).
L) Inner shaft.
M) Inner shaft bearing, SKF#24030 CC/W33, #N030/#W030 locknut/washer, seal CR#64998
N) Inner sphere.
O) Inner sphere bottom flange.
P) Inner sphere top clamp.
Q)Inner sphere bottom bearing, SKF#22216E, locknut #AN16, sealed by CR#36359.
R) "Joe," bottom bearing bayonet mount.
S) Hexagonal bottom bayonet, integral with outer vessel.
T) 3/4"-10 studs (4).

supports and drives the inner sphere. The weight of the inner sphere and shaft is borne by the top lid, with the axial load carried by the inner sphere top bearing and locknut, Fig. 3.2 (M). This bearing is sealed against the fluid by a pair of lip seals directly beneath. The inner sphere top bearing and the seals are nominally replaceable *in situ* without disassembling the experiment due to the design[6] of the outer race housing, allowing prompt recovery from any small leak through the seals. The inner sphere, Fig. 3.2 (N), has 1.02 ± 0.005 m (40.1 in.) outer diameter and a wall thickness of approximately 0.2 in. The inner sphere is hollow and liquid-tight. Axial location of the inner sphere with respect to the top bearing and radial location of the bottom of the sphere is provided by a flange integral to the inner shaft, Fig. 3.2 (O), which bolts into the bottom of the removable inner sphere unit. A clamping ring, Fig. 3.2 (P), radially locates the top of the inner sphere. The bottom flange and top clamping ring are sufficient to transmit the torque. The bottom of the shaft is radially located by a bearing, Fig. 3.2 (Q), and a receptacle[7], Fig. 3.2 (R), which mate with a hexagonal bayonet integral with the bottom of the outer sphere, Fig. 3.2 (S). The tip of this bayonet was adjusted to be concentric with the rotation axis of the bottom bearing (B). The concentricity with the rotation axis was measured by means of projecting a magnified video image of the bottom bayonet onto a whiteboard to measure its runout as the outer sphere was rotated by hand. A hydraulic press was used to slightly slide the sphere flange (D) with respect to the bottom head (C). In this way, the axis of the vessel was aligned with

[6] Detailed drawings in the dissertation of S.A. Triana.

[7] We named it Joe, and don't really know what to call it otherwise.

the bottom bearing to better than 0.4 mm (0.017 in.). Rounding out Fig. 3.2, four 3/4"-10 studs Fig. 3.2 (T) are welded to the bottom of the outer sphere concentric with the four ports in the lid above, in case any baffles or other sorts of forcing or boundary system were to be desired in the future.

The great majority of the design of the vessel and forcing package described above was conducted by S.A. Triana, although the author was responsible for the initial thermal jacket design as part of designing the overall thermal system. In Figure 3.2, the author was responsible for the detailed design of components (A) through (C) as well as parts (I) and (J). S.A. Triana was responsible for the design of the rest of the rotating equipment. The large rotating parts were largely beyond our in-house fabrication capabilities, and were manufactured by outside companies. While it is not a strict demarcation, the author's contribution to the design of the three meter machine was generally in the nonrotating infrastructure: the design of the frame, mechanical drive system, and thermal system. Therefore, the design of some of these systems will be discussed in detail here. For the more detailed design and mechanical drawings of the rotating equipment, the reader is referred to the dissertation of S.A. Triana.

3.3.2 Lab Frame

The exterior of the experiment is depicted with annotations in Fig. 3.3, and a top schematic view of the frame and motor drive system is depicted in Fig. 3.4. A roughly cubical frame in four parts, Fig. 3.3 (b,c,d,e), is primarily a mechanical support for the top outer sphere bearing, Fig. 3.2 (H). The inner dimensions of the

frame are approximately 14 ft. × 14 ft. × 12 ft., 8 in. (4.2 × 4.2 × 3.9 m). The frame is mostly of welded construction. Frame members are 4 in. square beams of AISI 304L non-magnetic stainless steel with 0.25 in wall thickness. The side walls of the cube are divided into two sections. The bottom section, Fig. 3.3 (b), comprises roughly the bottom third of the cube. This portion of the frame is designed as a catch basin with more than sufficient volume to accept the entire sphere's contents in the extremely unlikely event of a catastrophic complete leak. The floor of the bottom portion is 1/2 in. thick stainless steel to help spread the weight of the experiment across the concrete floor of the laboratory, and all seams of this floor are welded to the frame members around the bottom interior. The walls of the bottom section are 0.059 in. thick stainless steel sheet, welded to the frame members around the periphery. All seams of the frame are welded to create a nominally liquid-tight basin. Some areas were more difficult to weld than others, and the seams of this basin will be painted with silicone rubber sealant before sodium fill to help ensure that it is fully liquid-tight.

The removable upper frame section, Fig. 3.3 (c), is bolted to the bottom frame section (b) in twelve locations, with a bolting plate at every frame upright. The upper frame section was installed after the sphere (a) was placed by a professional rigging team. The laboratory space has a crane on the ceiling sufficient to lift 5 tons, but the sphere shell is approximately 7 tons. It was lifted into place by professionals with stronger equipment. Each frame section is designed to weigh safely less than 5 tons. The frame roof, Fig. 3.3 (d), depicted in top view in Fig. 3.4 (d), tops the frame with a framework capable of transferring large radial loads from the rotating

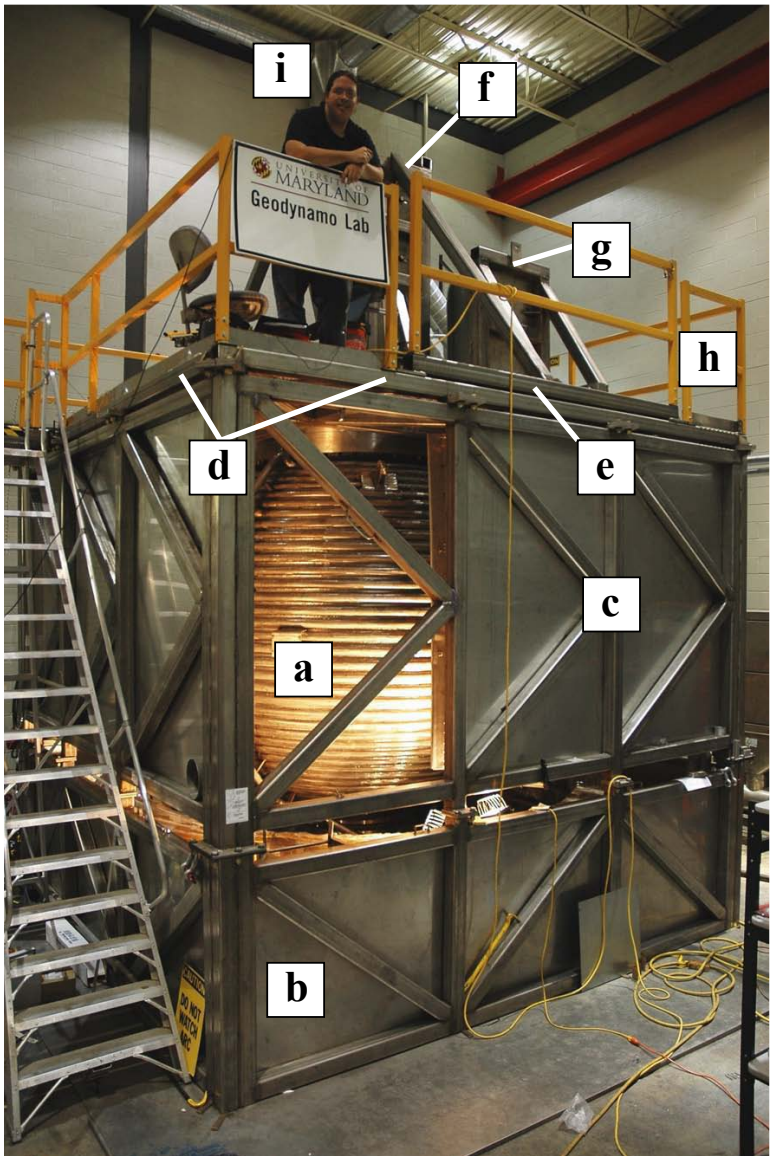

Fig. 3.3: Annotated photograph of the experiment.
a) Outer pressure vessel.
b) Bottom frame section, secondary containment.
c) Middle frame section, shield panels.
d) Frame roof.
e) Motor mount subframe.
f) Inner motor mount.
g) Outer motor mount.
h) OSHA-compliant safety rail.
i) The author, nowhere else referred to as "i."

sphere out to the cube walls. The roof is of the same 4 in. box beam construction, but is covered in expanded metal decking to provide a walking/working surface, and is surrounded by an OSHA-compliant handrail (h). The roof Fig. 3.3 (d) bolts to the upper sidewall section (c) in twelve places, and can be removed to allow insertion and removal of large equipment into the cube. The outer sphere flange protrudes through a square opening in the middle of the roof that is not much bigger than the sphere pulley. In this way, provided that the roof is installed, the outer sphere can not tip more than approximately 1° from the vertical. In ordinary disassembly, even if the roof is not to be removed, the outer sphere is guyed using four steel cables to the corners of the lower frame section (b) before the top bearing is removed. However, if the bearing were removed, the outer sphere pulley would come to rest against the inner surface of the roof opening. This effects a secondary mechanical confinement for the rotating equipment in case of bearing failure.

The motor mount subframe, Fig. 3.3 (e) and Fig. 3.4 (e) bolts to the lid roof and mates with the outer bearing housing Fig. 3.2 (I) to transfer loads from the outer sphere to the roof. The motor mount subframe is the only frame piece that must be removed to allow extraction of the lid Fig. 3.2 (G) and forcing package Fig. 3.2 (L-S) from the outer vessel. Two motors weighing about 1 ton apiece drive the inner and outer sphere respectively. The inner motor is held centered above the inner shaft by the inner motor frame Fig. 3.3 (f) and Fig. 3.4 (f). This frame is actually an integral part of the motor mount subframe, having been welded in place after initial positioning. The tall inner motor mount is stiffened by diagonal struts out to the edges of the motor mount subframe. The outer motor mount Fig. 3.3

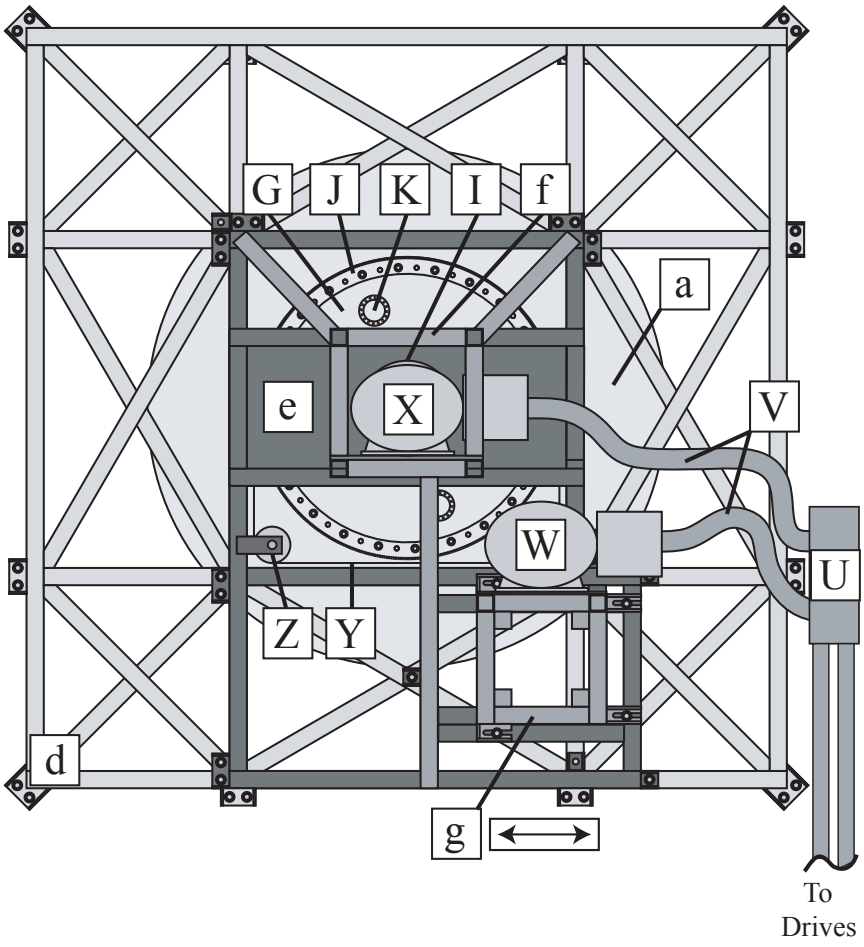

Fig. 3.4: Schematic top view of the experiment.
a) Outer vessel.
d) Frame roof.
e) Motor mount subframe.
f) Inner motor mount.
g) Outer motor mount, movable in direction indicated.
G) Vessel top lid.
I) Outer bearing housing, bolts to (e).
J) Outer sphere pulley.
K) Instrumentation port.
U) Motor power junction box.
V) Motor flex conduits.
W) Outer motor.
X) Inner motor.
Y) Outer drive belt, Gates 6160-14MGT-55.
Z) Outer drive idler pulley.

and Fig. 3.4 (g) bolts to the motor mount subframe and can be freed to translate in the direction indicated by the arrow in Fig. 3.4 to allow adjustment of outer sphere drive belt tension.

3.3.3 Motor Drive System

The rotation of the spherical boundaries is driven by a pair of 250 kW (350HP) induction motors. These 480 V three-phase motors are speed controlled to better than 0.2% by a pair of ABB ACH-550 variable frequency drives. Power from the drives arrives at the edge of the frame through a quartet of conduits terminating in a junction box, Fig. 3.4 (U). This junction box is supported on a beam that attaches only to the lowest frame section, so that most of the frame can be removed simply by disconnecting the cables in the flexible conduits, Fig. 3.4 (V), using quick connects in the junction box. Generally, this is not necessary, but the flex conduits (V) must be disconnected to free the motor mount subframe for sphere access. The inner motor, Fig. 3.4 (X), directly drives the inner sphere shaft through a Lovejoy flexible shaft coupling and a torque sensor to be described later. The outer motor, Fig. 3.4 (W) has a timing pulley mounted on its output shaft. A high horsepower Gates Powergrip timing belt Fig. 3.4 (Y) transmits power from this pulley to the large ring pulley on the outer sphere lid rim, Fig. 3.4 (J). The ratio of this pulley drive system is 25:3. An idler pulley, Fig. 3.4 (Z), ensures that the the belt only wraps around the large ring pulley over an arc of 180°, a design advised by an engineer at Gates. Static belt tension is adjustable by use of a large bolt that pulls and pushes the outer motor mount (g) in the direction of the arrow.

3.4 Mechanical Engineering

Before moving on to the description of the scientific instrumentation and data collection, some detailed design information will be presented regarding the author's contribution to the engineering of the three meter device. The author was responsible for the design engineering and most of the construction of the experiment's outer frame, motor mounts, and mechanical motor drive systems. This detailed description has several motivations. Documentation of these design processes is of use in our upcoming preparation for an operational readiness review as we work toward sodium fill. These design tasks represent substantial contributions of the author to the successful completion of the device, and are worth documenting in that regard. Lastl, the author has received a more comprehensive than usual education in the design and construction of large experimental apparatus, and some exhibition of the mechanical engineering education received while enrolled at the University of Maryland seems appropriate for inclusion here.

3.4.1 Support Frame

The outer cube frame supports and contains approximately 21 tons (19000kg) of rotating mass with over five and a half megajoules of rotational kinetic energy at top design speed. This mass is well balanced and smooth running by itself but a bearing or other failure could result in very large forces applied to the frame as the sphere comes to a halt. Prediction of the strength of the frame and elimination of stress concentrating design elements is important to ensure a robust and long-lived

experiment and the safety of the experimental team. Furthermore, frame vibration is of substantial concern, a lesson learned from many prior rotating experiments in our lab.

An initial goal of frame design was to make it as stiff, light, and strong as possible. However, it is difficult to remove all mechanical resonances from the operating speed band for an experiment of this size and speed. Simple detuning by stiffening or adding mass is not useful with an experimental device that must operate throughout a continuous range of speeds. Furthermore, while many resonances can be practically removed from the operating band, harmonics of the operating frequency can excite higher modes. For those troublesome vibrational modes that lie within the operating speed band, especially those at higher frequencies with more complex structures, prediction of the frame normal mode shapes is useful. This information can be used to place vibration measurement intelligently. It can also be used to decide likely locations for added damping to reduce the amplitude of vibration and subsequent vibrational stresses developed in the frame. To determine the strength of the frame and the vibrational mode shapes, we have used linear stress and mode shape analysis of finite element beam structures to model the cube frame. These analyses served as a guide toward rational assessment of proposed frame structures before we rendered one in stainless steel. Five or six major frame revisions were modeled by the author throughout the design process. It is worth discussing the methods used and the final output of the predicted calculations.

Our proposed frame designs were analyzed using linear stress and mode shape analysis, implemented using Algor, a commercially available professional finite el-

ement analysis software. Our frame is, with a few exceptions, well described by a rigidly connected network of beam elements. In the context of finite element analysis, a beam, depicted schematically in Fig. 3.5 is a linear elastic mechanical element that can support extension and compression, flexure, and torsion when used in a finite element model. The stresses and vibrations of a network of beams can be

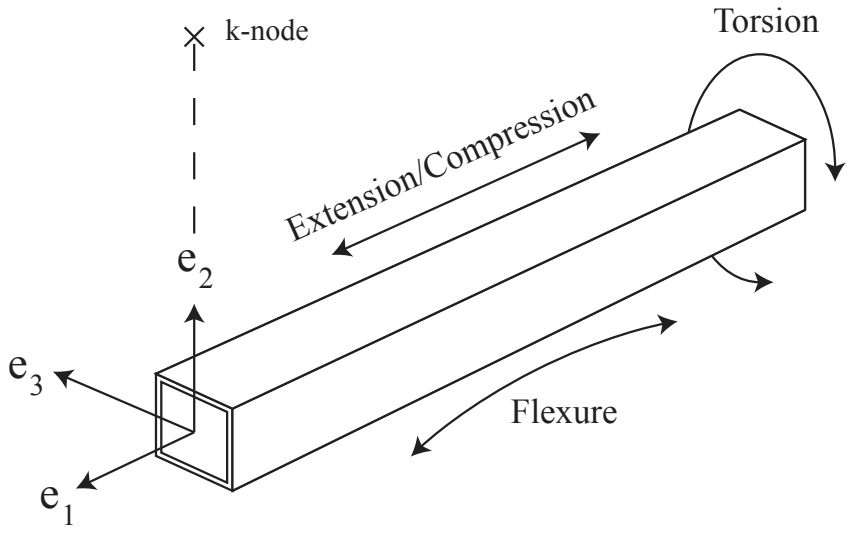

Fig. 3.5: A beam is a mechanical element that can support extension, compression, flexure and torsion. This is in contrast to a simpler truss element, which can only support extension and compression. As beams can be anisotropic with different stiffness in different directions, analysis using beam elements requires knowledge of beam properties referenced to a local coordinate system in each beam.

analyzed by calculating the displacements and rotations of all of the nodes in the network consistent with the elastic response of each element, which are determined for a given beam by the forces and twisting moments at its ends. In beam analysis, the calculation must take into account all three components of the force and the three components of the moment at every node.

The basic idea of the linear finite element methods used here can be understood through the direct stiffness formulation of finite element beam analysis. The equations at all the nodes can be written as one matrix equation,

$$\mathbf{F} = K\mathbf{x} \tag{3.5}$$

where $\mathbf{F}$ is a vector of forces *and* moments, $\mathbf{x}$ is a vector of translational and rotational displacements, and K is called the stiffness matrix, in which is encoded all the beam data: it represents the connectivity among all nodes and the elastic responses of the beams connecting them. The design process of a suitable support frame involves a certain optimization of this stiffness matrix by choosing beam properties and connections intelligently. With applied forces and boundary conditions at certain nodes, Eq. 3.5 can be solved for the forces and displacements everywhere, and the stresses in the beam elements can be calculated afterward from their stress-strain relationships. The mode shapes and frequencies for small amplitude sinusoidal oscillations of a beam network are the solutions to the eigenvalue problem,

$$(K - \omega^2 M)\mathbf{x} = 0, \tag{3.6}$$

where M is the nodal mass matrix expressing the mass loading of each node, either by explicit masses or those of the beams themselves The eigenvectors $\mathbf{x}_n$ give the mode shapes and the eigenvalues ω_n are the corresponding vibrational frequencies.

We must specify the connectivity of all the beams, their lengths, their material properties, and their cross sectional properties so that Algor can formulate the stiffness matrix and solve the problems discussed above for a proposed frame design.

This is the heart of the design process. We iterate through different designs, inspecting the output for troublesome vibrational modes and areas of excessive stress, adding beams and modifying connections to move toward a better design.

The beam material properties are homogenous throughout the frame. We use stainless steel, out of a desire to use nonmagnetic and relatively weakly conducting material in the vicinity of the experiment. A weight density of 0.289 lb/in.^{3} (8 g/cc), Poisson's ratio of 0.3, and elastic modulus of 2.9×10^7 lb.in.^{2} (200GPa) are used throughout, as per values obtained from www.matweb.com for AISI 304L stainless steel[8]. To specify the cross sectional distribution of mass, which determines the stiffness of the beam, several properties of the cross-section must be specified. The beam cross section properties are specified with reference to the coordinate system of Fig. 3.5. Figure 3.6 depicts the two important beam sections required for the frame model.

The square beam of Fig. 3.6 (a) is the basic frame member. The triple corner beam in Fig. 3.6 (b) is simply three square beams welded together. One of these triple composite beams forms each vertical corner of the cube. The area of the cross section is one required sectional property. The centroid of the section is another, as it defines the location of the neutral axis of the beam. When the beam is bent, a plane through the neutral axis separates the metal that is in compression from that in tension. The centroid is the origin of the coordinate system in Figs. 3.5 and 3.6, labeled as "CM" in Fig. 3.6 (b). Higher moments of the area further define the distribution of mass around the centroid. The second moment of the area, called

[8] These material properties vary only modestly across different types of steel.

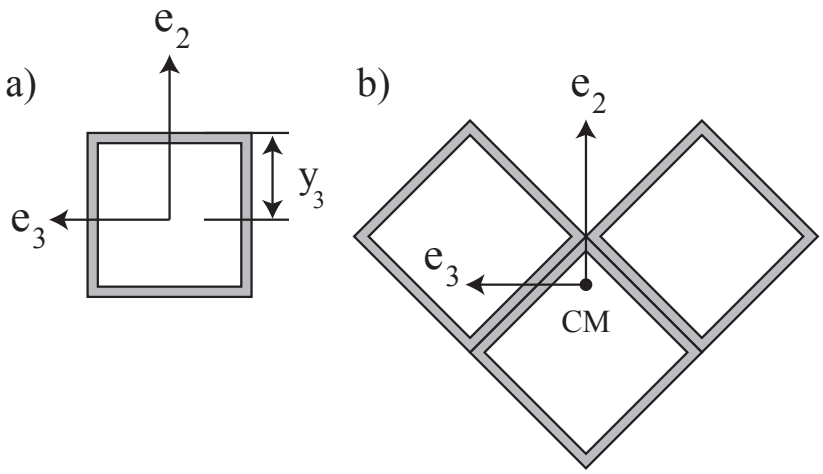

Fig. 3.6: Cross sections of the two beam types needed in our frame model, a square beam (a) and a triple beam as we have in the corners of the frame (b). This schematic shows the 2 and 3 coordinate axes, the extremal distance from the three axis to the beam extremum, y_3, and the centroid of the triple beam, labeled CM. The centroid is the origin of the beam local coordinate system.

the moment of inertia [9] about the $\mathbf{e}_n$ axis, is defined as

$$I_n = \int x^2 dA \tag{3.7}$$

and has units of length to the fourth power. This integral is taken along the axis perpendicular to the n_{th} axis: this is the moment of inertia for the cross sectional shape rotating about the n_{th} axis. The section modulus S_n is defined as

$$S_n = \frac{I_n}{y_n}, \tag{3.8}$$

where y_n is the distance from the n_{th} axis to the most extreme point on the section, as shown in Fig. 3.6. Finally, the torsional stiffness of the beam about the 1-axis, J_1

[9] The second moment of the mass per unit area would give the more familiar moment of inertia in kg m^2. In beam bending, the moment of inertia is a property of the area.

must be known to specify the resistance of the beam to twisting. The expression for the torsional stiffness of a given beam section is too complicated to warrant space here, but formulas for sectional properties for many useful shapes can be found in Roark's Formulas for Stress and Strain [116]. We tabulate the relevant section properties for the two beam sections of Fig. 3.6 in Table 3.2.

Tab. 3.2: Beam sectional properties of the square and corner beams in Fig. 3.6 for input to Algor finite element modeling software. A is the area, I_2 and I_3 are the moments of inertia about the 2 and 3-axes, S_2 and S_3 are the section moduli about the same, and J_1 is the torsional stiffness about the beam 1-axis. J_1 for the corner beam is incorrect, but at worst that makes our calculations a lower bound on strength and stiffness.

Property	Square Beam	Corner Beam
A	3.75 in.^{2}	11.25 in.^{2}
I_2	8.83 in.^{4}	86.47 in.^{4}
I_3	8.83 in.^{4}	63.14 in.^{4}
S_2	4.41 in.^{3}	15.30 in.^{3}
S_3	4.41 in.^{3}	12.65 in.^{3}
J_1	14.9 in.^{4}	14.9 in.^{4}

With beam properties collected, a model can be built. The Algor software provides a graphical user interface to draw a connected wireframe of the beam structure which is parsed into length and connectivity information for the stiffness matrix. Beam joint coordinates in the finished model are connected with beams divided into perhaps five to ten segments between joints for better representation of the mode shapes and deflections. Fig. 3.7 shows the wireframe model in perspective view looking from an elevated vantage point West of the cube.

The cylindrical base is modeled as a set of perfectly rigid constraints in space,

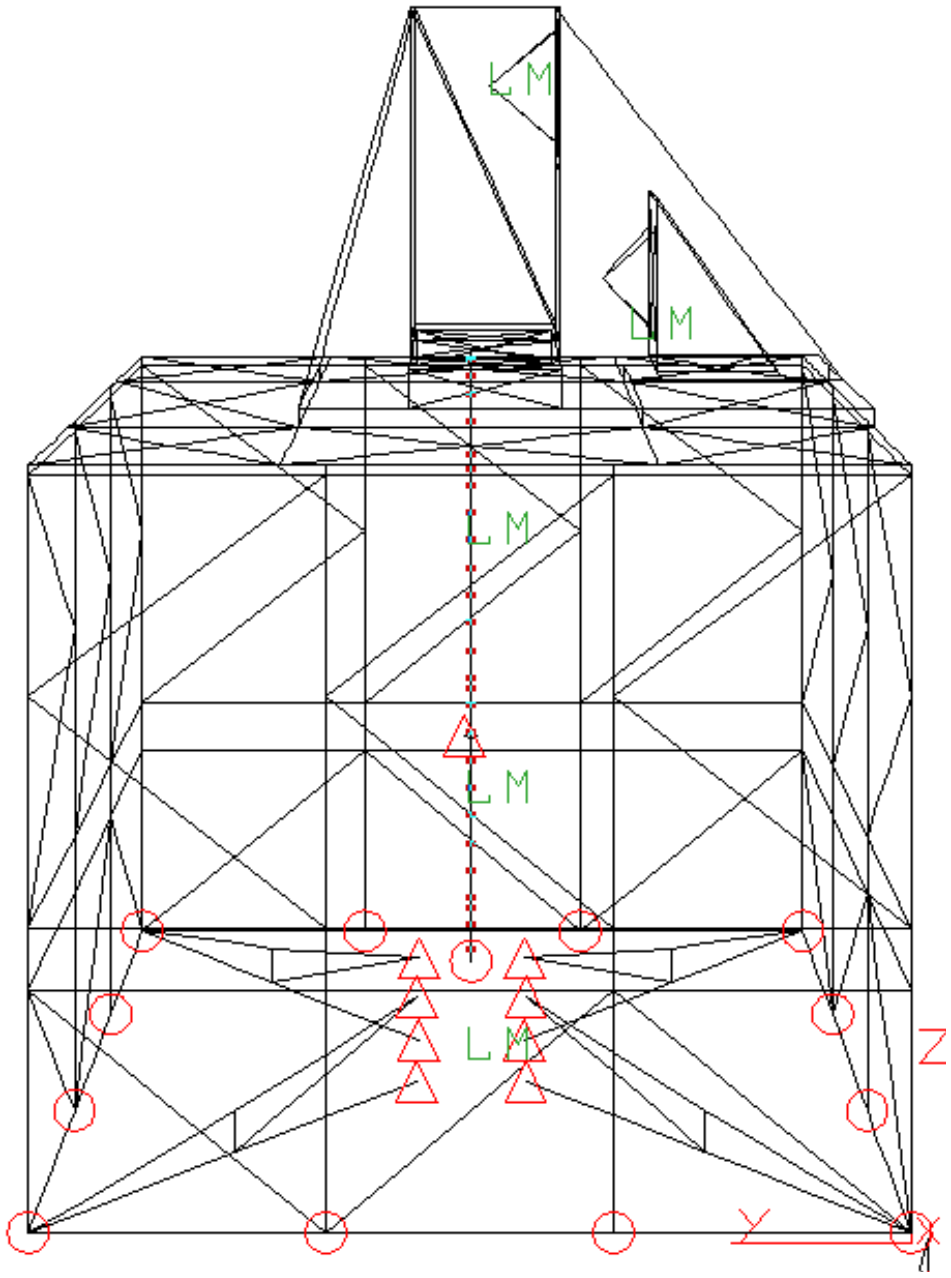

Fig. 3.7: Wireframe frame drawing from the finite element model, west perspective view. Red circles and triangles are boundary condition constraints. Green labels of LM are the locations of lumped masses representing the motor and distributed mass of the sphere. The small red points on the beam in the middle of the frame highlight the sphere model beam. The cube's orientation in the lab has Y to the North and X to the East. The corner closest to the camera in Fig. 3.3 is the Southwest corner.

but the boundary constraints around the bottom edge of the cube are varied to investigate the solutions' dependence on edge boundary conditions. The cube is *not* bolted to the floor. This is intentional, as a sudden development of significant out of balance forces will result in much lower peak stresses on the cube if it can slide slightly with respect to the floor. This will dissipate a great deal of energy and lower the peak forces. However, it makes renders the boundary conditions around the bottom outer edge of the cube somewhat indeterminate. We assume that the center of base will not move under normal operation, so we always constrain it fully[10], but we change the boundary conditions around the edge to compare cases.

Fig. 3.8 shows the locations for constraints for four cases considered in the following text. Typically we prevent translation in the X and Y-directions at least, to model the 1/2in. plate welded inside the bottom frame section that adds a huge amount of stiffness at the bottom edges in the X,Y plane. However, we try different boundary conditions, some of them somewhat unphysical, simply to put bounds on what to expect. All bolted joints are modeled as rigid connections.

For the purpose of accurate modal analysis, especially for modes that involve horizontal oscillations of the top of the frame, we must include a model of the sphere. We model the outer spherical vessel using a stiff, nearly massless beam and three point masses. The two 6400 lb. masses are positioned away from the center of mass such that that the moment of inertia of the spherical shell about the X and Y-axes through the center of mass is correct. The balance of the mass of the fluid is represented by a lumped mass at the center of mass of the sphere model.

[10] In fact there is no base, *per se*, but just a set of eight constraints.

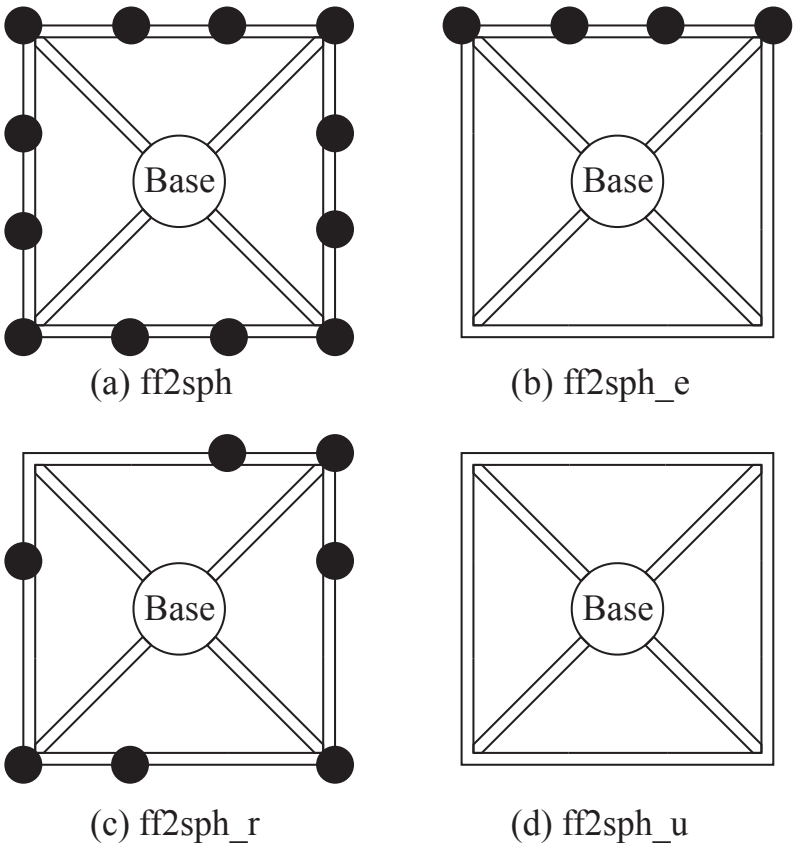

Fig. 3.8: The four constraint cases considered in the text and Fig. 3.13 are pictured here. The base is always modeled by rigid constraints on the inner ends of the support struts. We consider four cases, (a), all twelve edge nodes at the bottom of a vertical beam are constrained. At (b), only the nodes along one edge are constrained. At (c), a random selection with no symmetry is chosen. At (d), we use only the base as a constraint. This is not especially realistic, because the real cube has a 1/2" thick steel floor adding a web between all the struts. However, (d) can be considered a worst case.

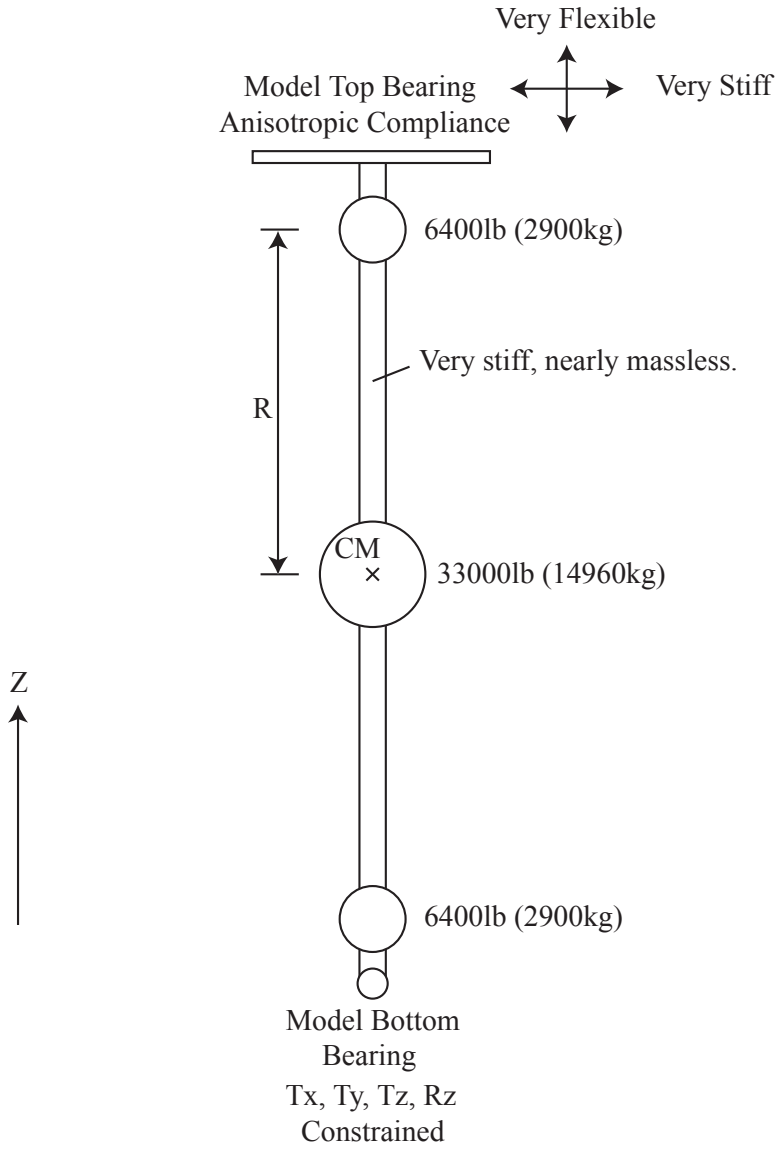

Fig. 3.9: A trio of point masses on a large cross section, extremely light and stiff beam is used to model the vessel. The 6400 lb. masses give the correct moment of inertia of the sphere about the X and Y-axes through the center of mass and the 33,000 lb. mass models the mass of the water, inner sphere, etc. R is the radius of the outer sphere. The bottom bearing is modeled by a spatial constraint that allows the joint to pivot about the X and Y-axes, but disallows translation. R_z, rotation about the Z-axis, is constrained to prevent spurious torsional oscillations of the sphere beam restored by the top bearing model. The top bearing model allows easy displacements with little stress in the Z-direction but is horizontally stiff, modeling in a linear way the ability of the top shaft to slide in the bearing.

Unlike the shell, the fluid moment of inertia is irrelevant for vibration analysis as the boundaries will just slip with respect to the fluid. Pressure, however, will engage the mass of the water.

The main bottom sphere bearing is a spherical roller bearing and is modeled here by a constraint that disallows translation in the the X,Y, and Z directions. It also disallows rotation about the Z-axis[11], but allows the axis to pivot about the X and Y-directions, as is appropriate for a spherical roller bearing. The top bearing, which is axially free to slide on the shaft, is modeled as a set of four beams that will bend easily if Z-directed loads are applied at their midpoint but which are rigid in transmitting horizontal forces to the frame. Without this, the very rigid sphere shaft effectively constrains the motor subframe's distance from the sphere's bottom constraint constraint. This flexibility trick would not work if beam buckling were allowed, as such slender beams would crumple, but the linear analysis performed here can show no such effects. Linear stress analysis does not re-calculate the beam lengths and nodal forces based on the new nodal distances. A more sophisticated model would use some sort of node that allowed local degrees of freedom to slip.

3.4.2 Static Stress Analysis

Static stress analyses were performed on numerous iterations of frame models with loadings corresponding to different operational and accident scenarios. We will present only one example here. In this example, the frame is constrained around

[11] This constraint is required to suppress spurious torsional modes of the model sphere that would arise if it were rotationally constrained by only the anisotropic "top bearing" beams.

the lower edge in twelve places, as depicted in Fig. 3.7 and Fig. 3.8 (a), with full translational constraints at the four corner locations and translational constraints in the wall-normal direction on the eight mid-span nodes. All nodes are free to rotate about all three axes. This constraint and loading is not of a sort that could be arranged precisely in the actual experiment, as the cube is not actually tied down. Even if it were, the concrete floor and tie anchors would not be well modeled by an infinitely rigid constraint. However, this stress model should be reasonably accurate for a radial differential force applied between the experiment base and the bearing housing on the motor subframe. This is a load case we care about substantially, as it is similar to how the rotating sphere might apply radial forces to the frame. Figure 3.10 shows the result of the calculation. With 10,000lb. (44kN) applied force, the peak stress is just over 4100 psi[12] (28 MPa), about 7 to 10 times lower than the yield stress for stainless steel. We use a working number of 30,000 psi for the yield stress of 304L stainless, but much of the steel used in the frame is rated to 40,000 psi as per the specifications received from the supplier.

3.4.3 Vibrational Mode Analysis

A few results for vibrational analysis of the frame are presented here. With sufficiently constrained edges, the lowest vibrational mode of the frame is well above the operating speed range for the outer sphere, though it is still inside the allowable speed band for the inner sphere. To situate us in the discussion of differently constrained cases below, we will refer back to Fig 3.8.

[12] lb./in.^{2}

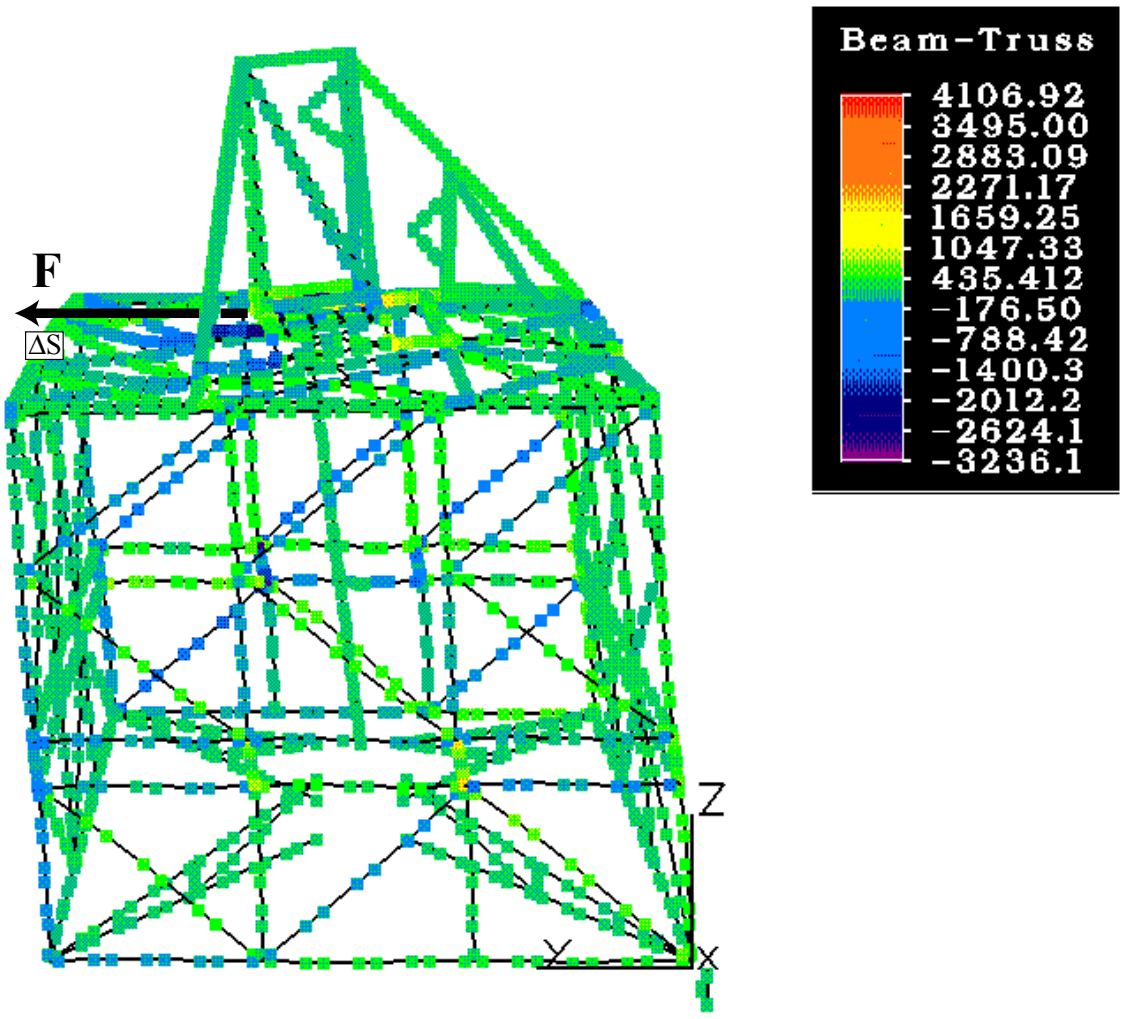

Fig. 3.10: Static stress distribution and 100x exaggerated deflection, with 10,000 lb. (44kN) force applied to the motor subframe near the point where the bearing housing bolts. The load is applied in the Y-direction, as indicated by the arrow. The peak stress is 4100 psi (28MPa), a factor of 7 to 10 lower than the yield stress of AISI 304L stainless steel. Constraints in the four bottom corners are (T_x, T_y, T_z) and in the eight mid-span edges they are (T_x) or (T_y), which prevents the edge from translating in the cube-wall-normal direction, mimicking the effect of the plate. The label ΔS indicates the location of a quantitative displacement inquiry at the top edge of the cube, which displaces about 0.011 in. (0.3 mm). We may use the force and displacement to calculate a spring constant for the cube lid in this loading configuration, 9×10^5 lb./in (1.6×10^8 N/m). Positive stresses here are extensional, negative are compressional.

The lowest vibrational mode with the fullest edge constraints, Fig. 3.8 (a), is depicted in Fig. 3.11 and has a frequency of 10.8 Hz. This mode involves primarily an X-direction[13] tilting of the inner motor mount, Fig. 3.3 and Fig. 3.4 (f). This mode is likely troublesome and some additional struts with dampers could be useful in limiting its amplitude, or rigid struts might raise it sufficiently to move it out of the experimental speed band. Due to time constraints, empirical measurement of the finalized frame's vibration spectrum has not been performed. However, this will done as part of the upcoming transition to sodium.

We consider another vibrational model with only one edge constrained, as in Fig. 3.8 (b). The lowest mode of this constraint case is depicted in Fig. 3.12 and has a frequency of about 5.5 Hz. This may be a slightly more realistic lowest mode, as there will be a tendency for one edge of the cube frame to be on the floor at all times. However, this model does not take into account the membrane elasticity of the 1/2 in. floor plate or the mass loading of the floor plate on the bottom of the lower frame section. The elasticity of this plate is probably more important, and it is likely that this resonant frequency underestimates the true frequency somewhat.

A summary of the effect of boundary conditions on the spectrum of mode frequencies is given in Fig. 3.13. The first thirty lowest vibrational modes were calculated for comparison. The four constraint cases referred to in Fig. 3.13 are pictured in Fig. 3.8.

The unconstrained, Fig. 3.8 (d), and heavily constrained, Fig. 3.8 (a) cases in Fig. 3.13 are probably reasonable upper and lower bounds for the frequencies

[13] East-West in lab coordinates.

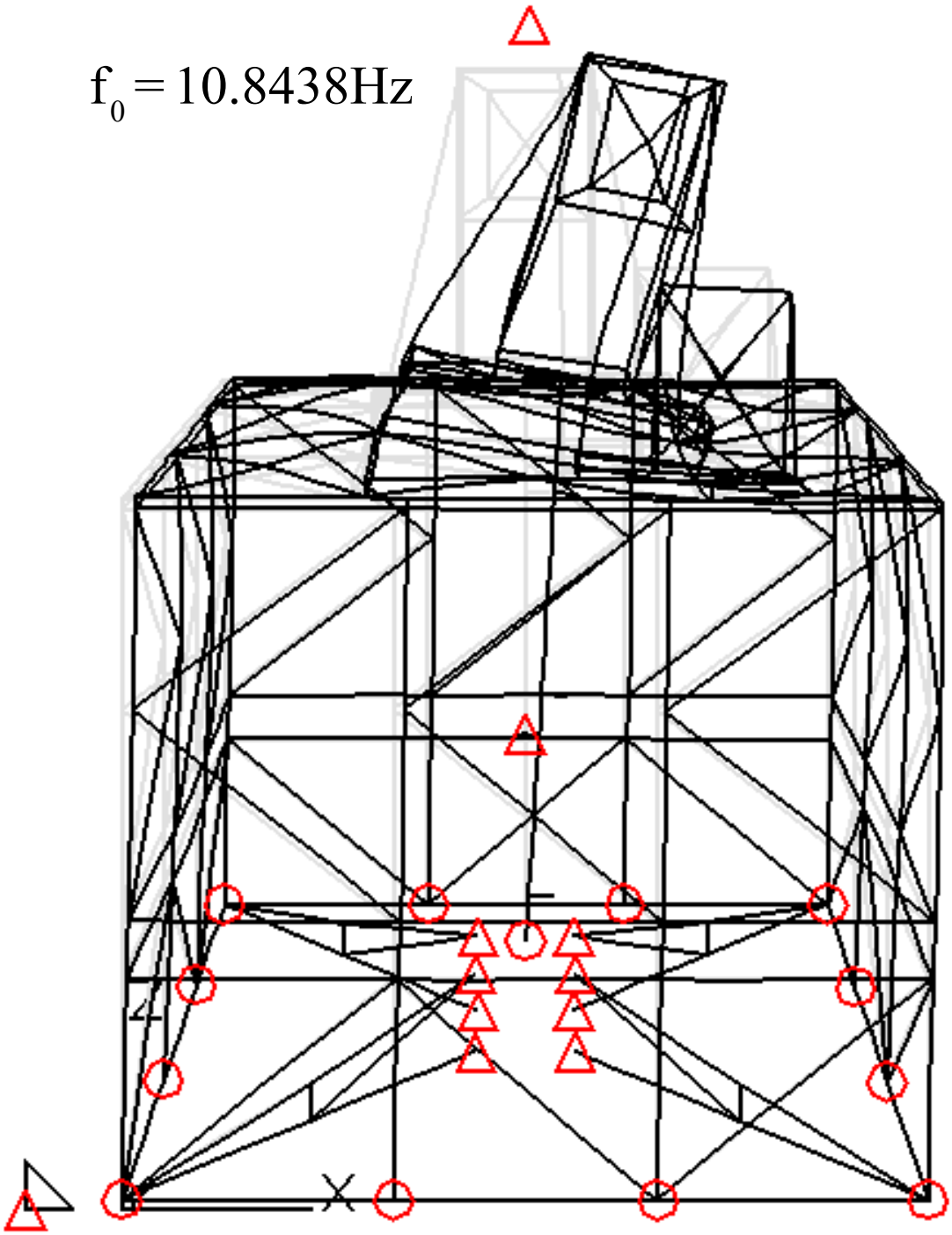

Fig. 3.11: Deflected mode shape, lowest mode with full constraints, model ff2sph. The mode resonant frequency f_0 is 10.8 Hz.

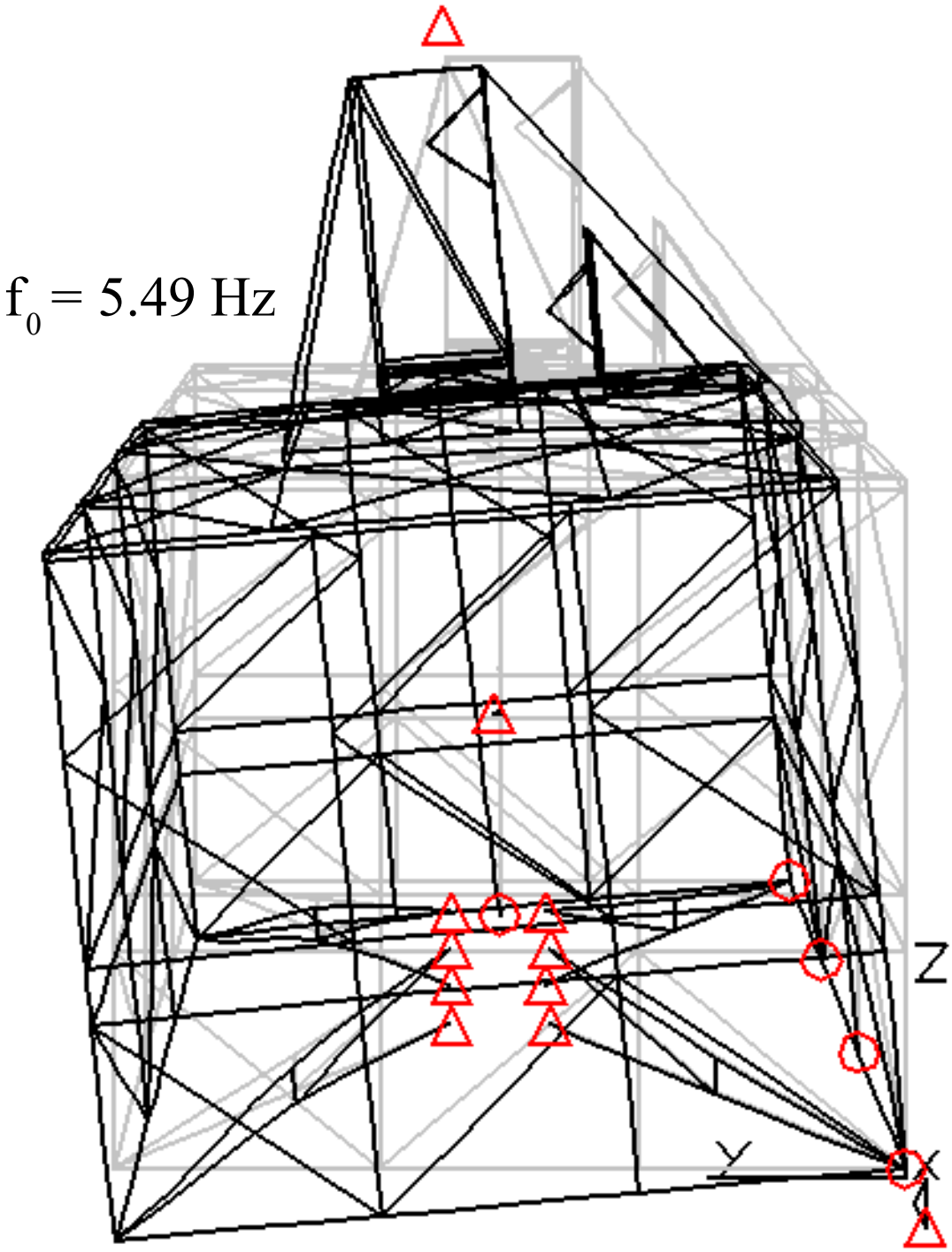

Fig. 3.12: Deflected mode shape, lowest mode with one edge constrained. The mode resonant frequency is probably underestimated as the plate on the bottom of the cube would be stretched in-plane by the mode pattern shown. The added stiffness would probably raise this frequency significantly. The real lowest frequency is probably somewhere between this one and that of the mode shown in Fig. 3.11.

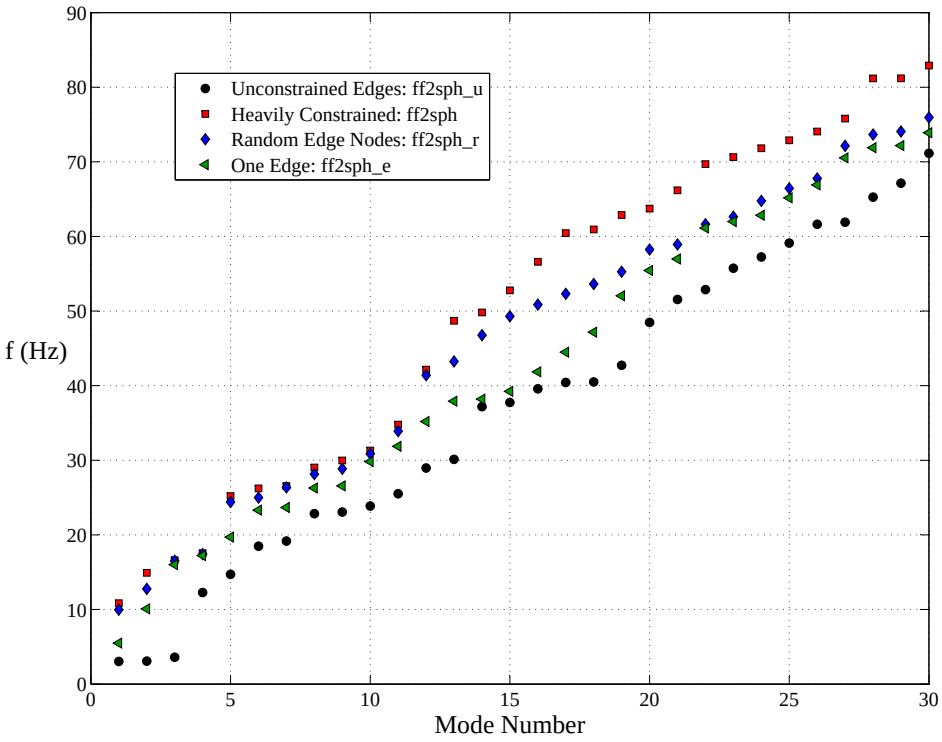

Fig. 3.13: Frequency spectrum of the lowest thirty modes for four different edge constraint choices. Fig. 3.8 depicts the four constraint conditions presented here. These mode spectra show the general effect of the edge constraints on the frequencies. Generally speaking, the lowest five modes or so involve either the cube shearing, the cube and sphere tilting and various combinations of motor mount motion. These modes, in most cases, are in the 10-20 Hz range. The exceptions to that for the one edge constrained and no edges constrained case are unlikely to be particularly realistic, and are likely also to be damped by collisions with the floor and sliding. Modes 6-10 in the 20-30 Hz frequency band tend to be drumhead-type membrane modes of the walls, with various walls oscillating in and out of phase with the others. Higher modes than this tend to incorporate the next-highest modes corresponding to the aforementioned motions. For example, two walls may deflect in a half-wavelength bulge while one wall has a full wavelength across it and deflects into a S-shaped curve. The wall modes in the 20 Hz and above range seem to strongly decouple from the motion of the model sphere.

of all the motions. So the wall-bulge modes will probably all fall into the 20-30 Hz range, roughly, and motor mount modes in the 10-20 Hz range, no matter the real boundary conditions. Cube shearing/tilting modes need to be assessed carefully because it is unlikely that such modes can really be observed as linear vibrational modes. Excitation of such modes will cause boundary condition changes as different cube bottom nodes come in contact with the floor. Some of these motions may be of some concern with the outer sphere rotating rapidly. We have rotated the outer sphere up to $\Omega_o/2\pi \sim 2$ Hz and the inner up to $\Omega_i/2\pi \sim 9$ Hz with few vibrational problems. We intend, however, to finish vibrational measurements of the frame to assess the possibility of low-lying troublesome modes. We have done such measurements on portions of the frame as it was under construction and compared them to a partial frame model for model validation. In this process, we noticed that the actual vibrational spectrum tends toward broad peaks around frequencies corresponding to modes with every permutation and combination of bottom edge boundary conditions. Constraints of time have prevented empirical measurement of the complete frame.

3.4.4 Additional Contributions

To round out the mechanical engineering section of this dissertation, brief mention will be made of some further significant tasks undertaken by the author in the design process of the hardware. The author rounded out the detailed design and produced mechanical drawings of the frame. Furthermore the author engaged in a great deal of heavy construction, assembling much of the frame, cutting out

beams with a bandsaw and plasma torch, and welding and bolting together the frame sections. The author had significant help from the rest of the team for the lower portions of the frame sections. However, by the time the roof and motor mount sections were constructed, they were completed essentially singlehandedly by the author and his trusty torch and welder. Working directly to turn drawings into solid steel structure was a satisfying experience and also an important part of an education in straightforward design of structures that can be easily built.

Space will not be allocated in this dissertation for any mention of the thermal control system, as the great majority of the hydrodynamic experiments in this dissertation were run at sufficiently low power input that passive cooling to the room and the large heat capacity kept the temperature of the fluid nearly constant near room temperature throughout the experimental period. As it was not needed, no attempt was made to finalize the thermal system and get it on line for hydrodynamic experiments. However, much of this system was designed by the author to provide 120 kW of heating for melting the sodium. This system is also capable of cooling 500 kW, which is more than sufficient for steady state operation at maximum power. Much of the thermal system had been installed by the team prior to experiments in water. Similarly, a ventilation system for the sodium experiments occupied a fair amount of time.

Perhaps a year of the author's time was spent on mechanical aspects of the drive system design. The drive requirements for the three meter experiment are rather complicated, as we desired a significant speed reduction on the outer sphere drive, but the unusual speed at which the large apparatus runs and the additional

constraints of the design made this difficult. A pinion and ring gear system was designed but the high tangential speed of the pulley rim resulted in unacceptable predicted wear characteristics. This was only revealed in the final stages of design, after weeks working with professional gearing engineers. Ultimately, the final drive design is simple, motors are mounted on the frame and the outer sphere is driven by a large timing belt reduction drive. A custom-manufactured pulley, depicted in Fig. 3.14 bolts to the experiment lid rim. The pulley has alternate large and small holes, so that the experiment lid may be bolted down with half of the bolts holding the pulley as well. The large holes in the ring pulley give ample clearance to the nuts on the lid bolts. In this way, the lid may be bolted solidly and the experiment can be rotated by hand to adjust the pulley's concentricity with the rotation axis. After the pulley is aligned, it is bolted down tightly. The large ring pulley in Fig. 3.14 was designed by the author and fabricated by Motion Systems of Warren, MI. The pulley is made of 6061-T6 aluminum, hard-coat anodized to help protect it from any caustic residue and to give it long-lasting wear characteristics needed for a high speed belt drive. The other drive system pulleys, the motor pulley and idler, were stocked parts, though the outer motor pulley was modified by D.H. Martin to suit our motor shaft.

The author also did some stress calculations regarding the strength of the inner sphere. The inner sphere design was worked out by S.A. Triana with estimated strength from analytical expressions. However, the finished fabrication of the inner sphere involved welding together two hemispheres supplied by a spun metal manufacturer. An attempt was made to weld the equator and polar regions with full

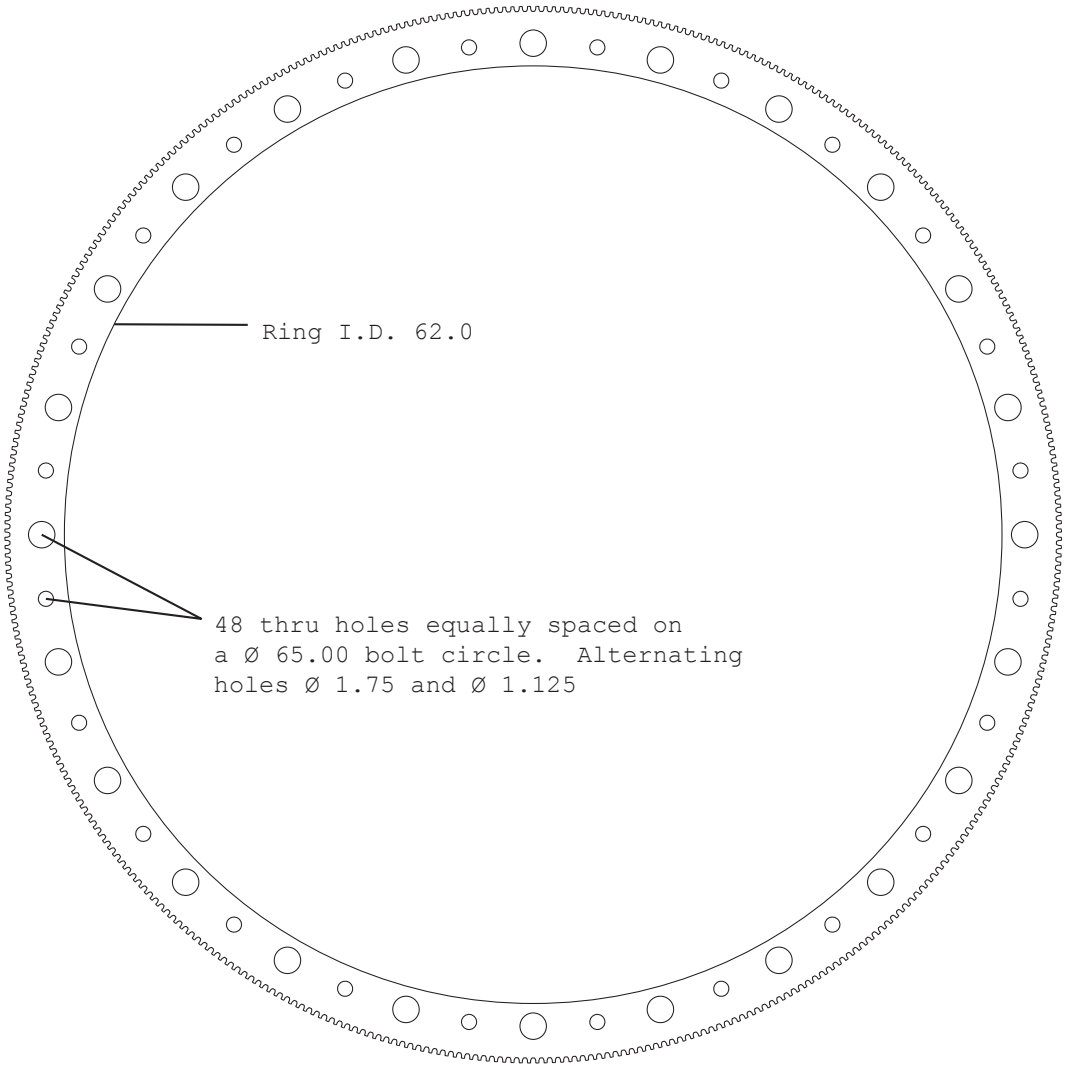

All dimensions in inches
14M Pitch/Gates Power Grip GT2 Teeth
400 Teeth
Face Width:3 inches
Material: 6061-T6 aluminum; hardcoat anodized

Fig. 3.14: Large ring pulley for outer sphere mechanical drive system.

penetration welds. However, there was no way to inspect the inside of the inner sphere to check if this was the case. The inner sphere maximum speed limit set by centrifugal stresses is barely a matter of personnel safety, as the inner sphere could explode with great force inside the outer spherical vessel and literally not make a dent. However, it is important to know the operational limitations of the device. So a finite element model of the inner sphere with centrifugal stresses was undertaken in Algor.

An axisymmetric linear stress analysis with centrifugal loading was performed with several models of fully welded and "cracked" inner sphere, modeling the effects of incomplete weld fusion. The incomplete weld fusion regions are, as expected, stress concentrators. The output of the stress analysis model is shown in Fig. 3.15.

The model above was run at 1800 RPM (30 Hz) and at that speed, the stresses in the inside corner of any stress concentrating incomplete weld fusion regions near the poles are approaching the lower limit yield stress for AISI 304L. An upper speed limit of approximately 20 Hz gives a safety factor of two, and may be considered an upper safe speed. Experiments suggest, however, that this speed will be difficult to achieve due to the torque and power demand of the turbulent flow. It is likely that throughout much of parameter space the inner sphere maximum speed, at least without further speed reduction gearing, will be limited to little more than 12 Hz by the available torque of the motors. This is far from the maximum allowable upper speed. However, the inner sphere should not be run faster than $\Omega_{\rm i}/2\pi$ =20 Hz if that should prove possible in some region of the $(\Omega_{\rm o}, \Omega_{\rm i})$ parameter plane.

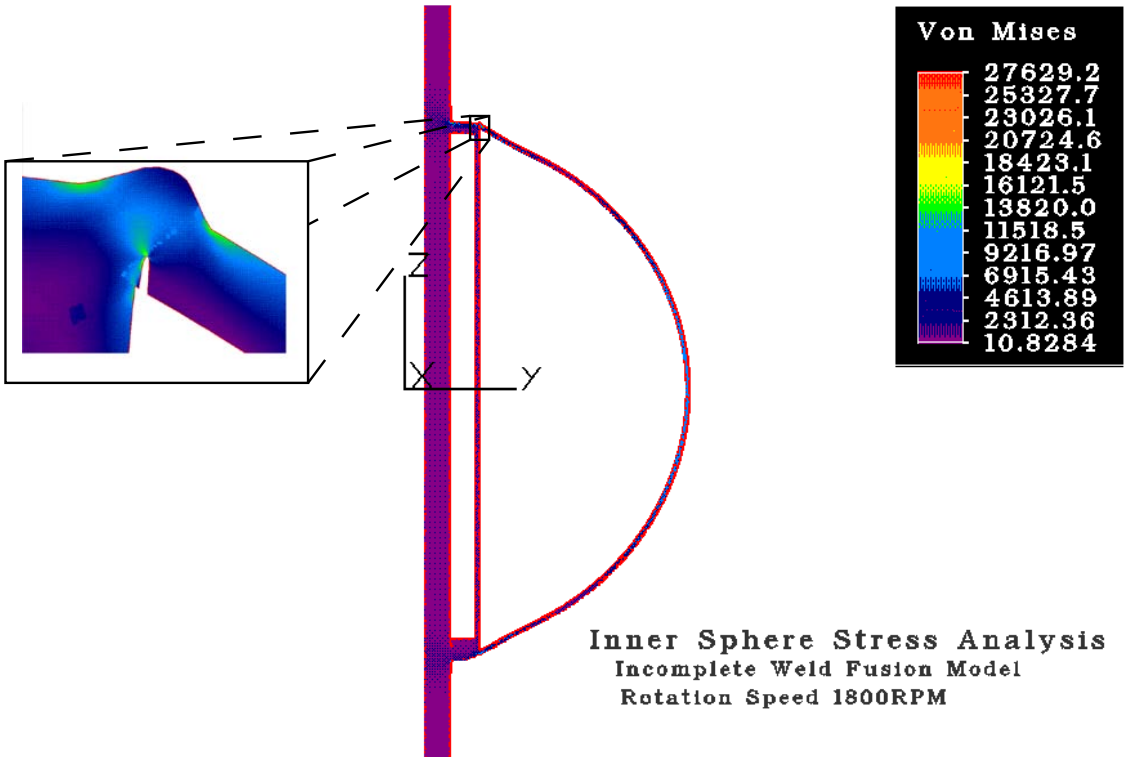

Fig. 3.15: Inner sphere stress analysis for centrifugal loading at a speed of 30 Hz. Inset shows the polar "cracked" region of concern. As expected, the region of highest stress is a small region near the tip of the crack. Based on this analysis, it is unlikely that the maximum speed of the inner sphere will be set by centrifugal stresses. The drive system will probably be torque limited before the maximum safe speed, an allowable value for which may be 20 Hz. This gives a safety factor of 2.25 based on this rather badly fused model.

3.5 Instrumentation and Control

While it is ultimately scientifically useful to study purely hydrodynamic states in a rapidly rotating, highly turbulent system like this one, the decision to do so was done late in the design and construction process. Ultimately, the initial goal of sodium data in this device as a dissertation project was too ambitious. Fill with water and mechanical testing had always been planned, as water has nearly the same hydrodynamic properties (density and viscosity) as liquid sodium, and as such provides a safe and easy way to do mechanical fitness testing of the system. Some instrumentation was to be fielded during this process, partially to do instrument debugging, but the results proved too interesting to pass up the chance to perform a more complete survey of the rapidly rotating hydrodynamics. Furthermore, the author, having spent many years designing and constructing, was excited to examine some scientific results.

However, little instrumentation design had been undertaken as the mechanical system went on line. An attempt was made to initially field instrumentation that would perform measurements in water, but with an eye toward eventual use with sodium. As water data collection progressed, a few water-specific sensors were added. Largely, though, instrument design and choices were made with the intent to minimize wasted work on the longer-ranging project. That is, we looked toward our sodium goal even as we instrumented the device for water. As discussed in Sec. 3.2.2, magnetic field measurements are intended as the primary diagnostic in sodium. We needed direct flow measurements in water, but we largely limited our choices to

those useful in an opaque liquid metal, like ultrasound doppler velocimetry. An exception is made for the wall shear stress array discussed in Sec. 3.5.4.

Although the three meter apparatus has a large rotating lid on which a great deal of instrumentation can be mounted, small vertical clearance, strong centrifugal and Coriolis forces, and a desire to re-use existing equipment required some special instrumentation design and constrained the commercial choices for certain types of instrumentation. Many common pieces of fluid dynamics instrumentation are designed to be rack-mounted and occupy a much larger volume than is necessary for their function. Additionally, the budget for instrumentation, especially for equipment that would only be useful in water, was fairly limited. Therefore, much of the rotating instrumentation was designed and constructed in-house. Additional equipment was added to the rotating frame for the sake of remote control of various rotating systems. The time to spin up the massive volume of water is substantial, so being able to turn equipment on and off remotely and change the position of sensors without stopping the outer sphere is of great value. Some of the instrumentation outgrowth of the experimental campaign in water may be useful to other fluid dynamics researchers, especially those working in tight spaces or with small budgets. Many measurements herein rely on simple equipment that uses inexpensive, commonly available parts. Those pieces of equipment that seem especially useful will be discussed in some detail in the following sections. A general overview of the instrumentation and data collection will be provided for the sake of lasting documentation.

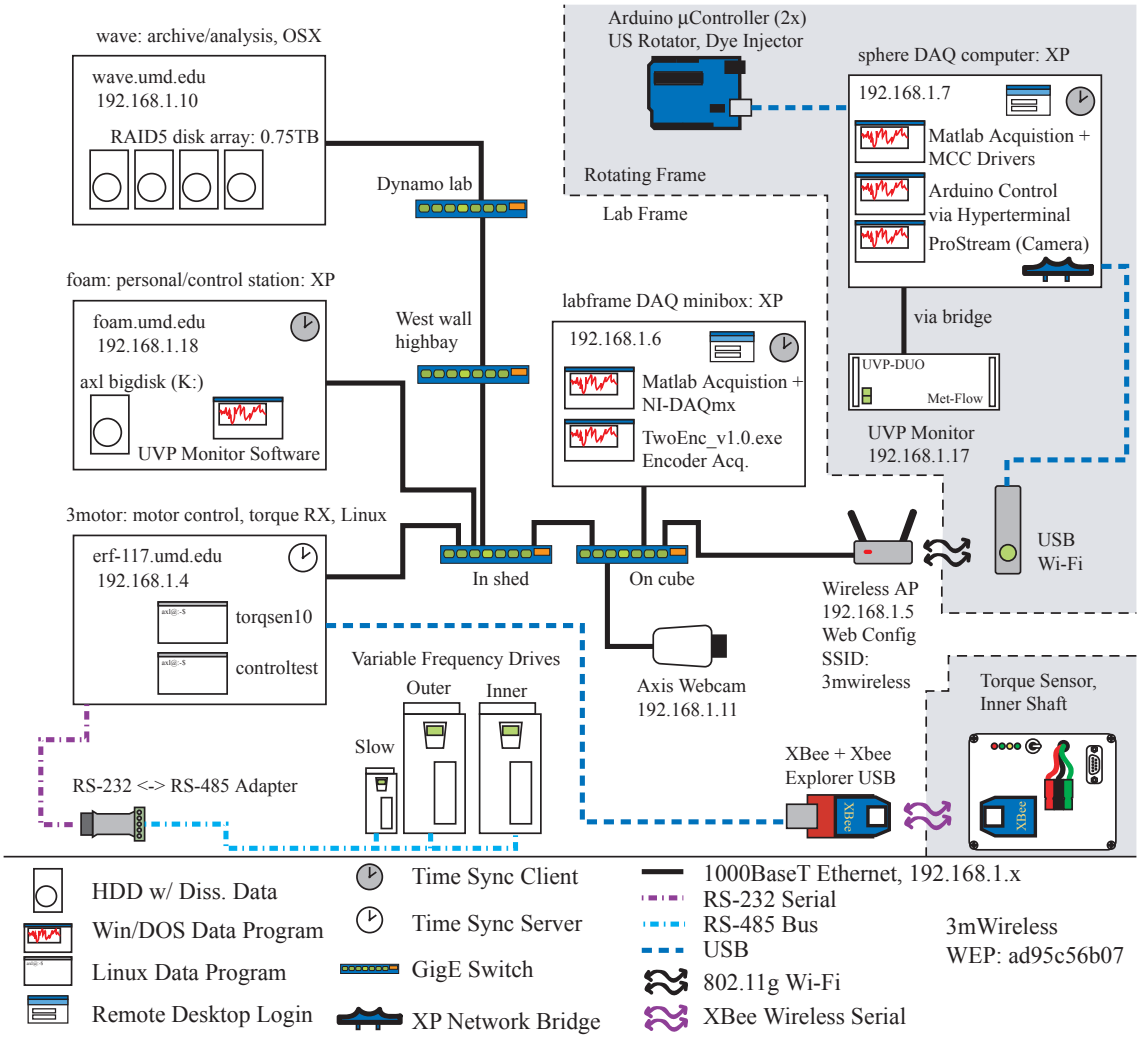

Fig. 3.16: Block diagram of the instrumentation system with legend.

3.5.1 Data and Control Overview

The data and control infrastructure for the three meter experiment is fairly complex. A number of coordinated devices perform control, communication, and data acquisition tasks. Fig. 3.16 is a block diagram of the installed data and communication infrastructure. The basic communications backbone for the system is a private, local TCP/IP network running mostly over wired ethernet. Communica-

tion between the outer sphere rotating frame and the lab frame is handled by an 802.11g wireless access point. This access point is configured to be a largely transparent bridge to the rotating frame. Sustained data rates of about 20MBps are generally possible over this link, sufficient for most tasks to date. A dual quad-core Mac Pro, Wave in Fig. 3.16, houses a large capacity RAID disk array and is used for many data analysis tasks. This machine is used a central repository for data access by all researchers in the lab. It also hosts a simple near-real-time status monitoring web page, **http://wave.umd.edu/3m.php**, which parses data out of the several data log files in the current day's data directory and displays it on an automatically updating web page.

A Debian Linux machine, 3motor, is used for control of the variable frequency drives, using a program written by S.A. Triana. It is used for speed control, can be used to perform automated speed ramps, and reads drive status data, logging it into a file (logfile.dat) in the day's data directory. This computer also acquires torque data from a wireless sensor on the inner shaft, using another program. Finally, 3motor provides a local time server for network synchronization of the acquisition computers, some of which are isolated from the internet[14]. The labframe DAQ computer at present acquires rotation speed data from a pair of optical encoders. The outer sphere has an absolute position encoder accurate to better than 0.02°. The inner sphere has a high resolution speed encoder. Both encoders' outputs are

[14] We have found that the constant updating of the operating systems required for internet-connected computers can sometimes break our data acquisition computers in difficult to debug ways.

streamed to wave. The lab frame computer also acquires accelerometer data on frame vibration, and will eventually acquire magnetic field data in the laboratory frame.

In the rotating frame, the sphere DAQ computer runs a simple MATLAB continuous data acquisition routine, streaming data from sphere frame sensors to wave using an 802.11g USB adapter. The sphere frame computer runs Windows XP Professional, and is operated from the lab frame using Remote Desktop Protocol. There are two ethernet adapters on this computer. A gigabit adapter can connect to a camera in the rotating frame. The camera system is a separate network, running in the 10.0.0.x IP address block. A Win XP network bridge shares the USB WiFi connection over a 100BaseT ethernet port on the motherboard to allow the Met-Flow UVP Monitor to connect to the lab frame network. Software to control the UVP monitor runs on a lab frame machine. The UVP software is Windows-based, and the software seems to require a reasonably fast computer. Depicted in Fig. 3.16 is foam, which is the author's computer, but the experimental physical control location need not be localized to any particular set of computers. Network connections to 3motor are best done from another Linux computer. We have notice a bug with terminal programs running on Windows that can result in a crash[15].

The final piece of equipment to be mentioned in Fig. 3.16 is an Axis 2100 TCP/IP webcam, which can be viewed on a web browser on a computer connected to the internal network. This camera is mounted on the rear strut of the inner motor

[15] Crashing this machine is inconvenient but not dangerous. The motor drives will continue to run at the last setting until 3motor is rebooted, or the drives can be manually shut down.

frame, aimed at the top of the experiment so that it can see the lid of the outer sphere and some of the inner shaft. This allows us to monitor for problems such as leaks or loose wires.

3.5.2 Rotating Instrumentation

A detailed block diagram of the instrumentation in the sphere rotating frame for the water experiments is depicted in Fig. 3.17. The heart of the rotating frame acquisition is the sphere DAQ computer, whose internal layout is shown in Fig. 3.18. This computer is housed in a custom aluminum case, designed and built by the author[16], which bolts solidly to the sphere lid. Acquisition is performed by a Measurement Computing PCI-DAS6402/16 acquisition card. This PCI card provides 64 channels of 16 bit single-ended acquisition. Breakout terminal blocks allow easy wiring. A number of channels are run to front panel BNC connectors on the aluminum computer case. All instrumentation is designed to be single-ended, with one output terminal grounded to the large metal sphere lid and coaxial cables. The computer has a solid state disk to avoid problems with centrifugal and Coriolis forces on a rapidly spinning mechanical hard drive. It has a power supply designed for wide range 9-15 V input and runs directly from four 12 V, 35 Ah batteries that power all of the rotating instrumentation.

Batteries were chosen instead of slip ring power delivery for cost and noise reasons. Battery power and a large ground plane in the form of the lid help to ensure minimal pickup of noise from the variable frequency drives running the experiment's

[16] And possibly the only computer on the planet with *functional* hoodscoops for ventilation.

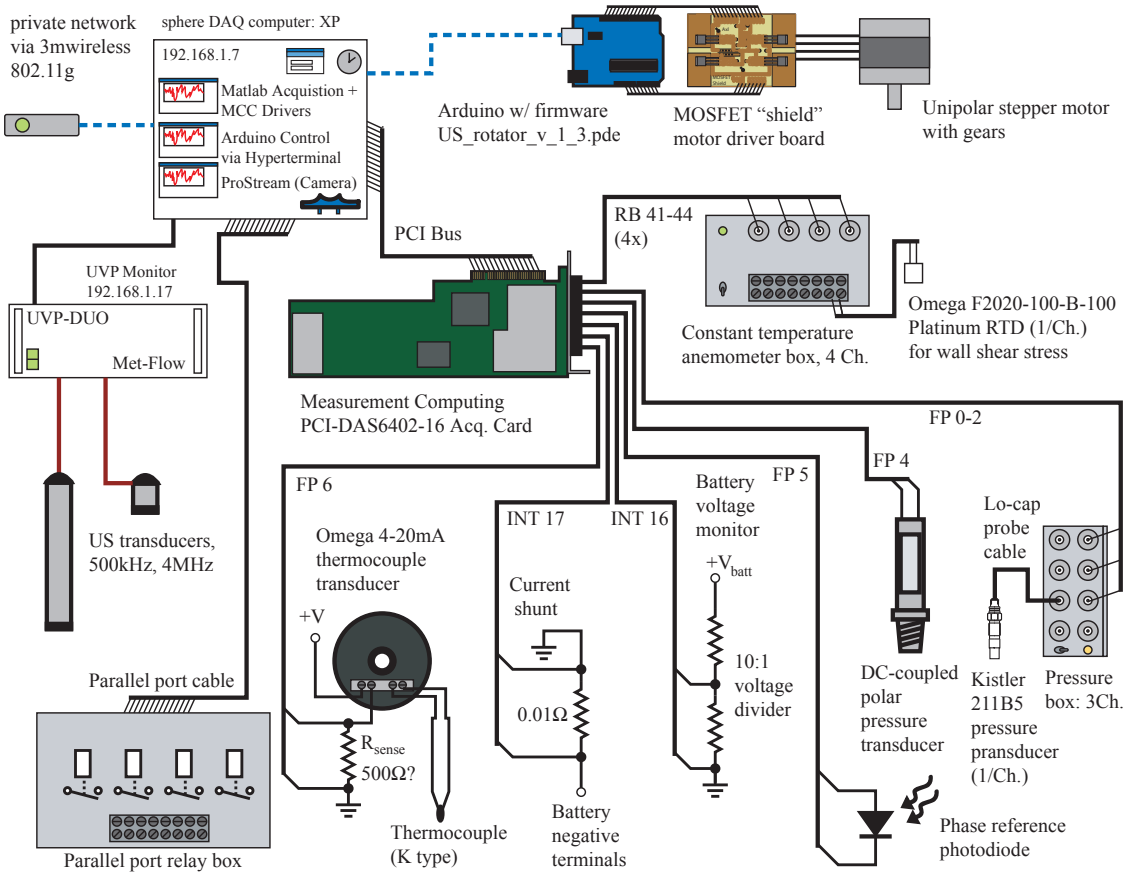

Fig. 3.17: Block diagram of the rotating frame instrumentation.

motors. These drives are the only practical choice for high power mechanical drive, but they emit significant radio frequency energy and great care must be taken to avoid unintentional reception of this noise. Isolating the electrical circuits in the lab frame from those in the rotating frame is useful to minimize noise pickup. Instrumentation requiring voltages other than 12 V is powered from well-filtered DC to DC converters also housed in the computer case. There is a terminal strip inside the case, and another bolted to the sphere lid to distribute power to the instruments. The computer section is isolated from the data acquisition equipment by a shielding wall, to minimize digital noise ingress into the analog system[17].

Two channels of acquisition, labeled INT16 and INT17 in Fig. 3.17 are connected internally to the computer to measure battery voltage and system current draw. Three channels on the front panel, FP0-FP2, acquire pressure signals from a trio of Kistler 211B5 AC-coupled pressure transducers, which are powered and amplified by a homemade conditioning box, designed by S.A. Triana and built by the author. The pressure conditioning box provides a constant current source of 5 mA to power each transducer, and has an overall gain of 70 on each channel. A low pass filter on the output with a -3 dB cutoff of about 160 Hz rolls off the response to help prevent aliasing, especially important as the high frequency machine noise can be substantial in the microphonic pressure sensors. For all of the experiments herein, a sampling rate of 512 Hz was used, and each pressure channel was attenuated approximately 10dB at the Nyquist frequency of 256 Hz. The overall sensitivity of

[17] The MCC DAQ card is, of course, connected to the motherboard, but these devices are designed to isolate the sensitive analog circuitry from the PCI connection.

each pressure channel at the amplifier output is about 0.58kPa/V. These sensors can resolve fluctuations faster than about 0.05 Hz at full sensitivity, with a rolloff at lower frequencies.

Channel FP4 acquires a DC-coupled pressure transducer installed in a bore that reaches to near the north pole on the outer sphere. This transducer allows us to monitor the net static pressure relative to atmospheric inside the sphere. This is important for safety reasons and for preservation of the machine, as overpressure will lead to leaks through the lip seals. This pressure transducer is not primarily intended to be a scientifically interesting measurement, though it has a reasonable frequency response and can be used as a scientific diagnostic. The DC response, provided that the sphere is sealed, can be used as a surrogate measure for the intensity of the global fluid circulation the experiment, which sometimes proves useful. Channel FP5 in Fig. 3.17 acquires the output of a photodiode, which is illuminated by a LED in the lab frame once per rotation. This gives an absolute position reference to the outer sphere which is useful in some circumstances, as well as providing a second measurement of the sphere speed that is synchronized with the data acquisition. Channel FP6 acquires the output of an Omega thermocouple transducer. The thermocouple is immersed a short distance into the fluid. Temperature is an important safety diagnostic in sodium, and is used to provide some temperature compensation of the calibration of the wall shear stress sensors. It is also used to correct the relative viscosity in determining the final Reynolds number at which experiments are run. A note about the thermocouple; it picks up some high frequency noise which does not affect the mean over a few seconds needed for its primary pur-

pose in temperature control, but if a time series of temperature is used to condition any data (like the wall shear stress), it should be numerically low pass filtered first.

Four channels, RB41-44 acquire signals from constant-temperature flush-mount wall shear stress sensors of the author's design, to be discussed separately later. Also depicted in Fig. 3.17 are a parallel port relay box that allows remote switching of four devices. This was used in the water experiments for LED lighting, camera power, and a pressure relief valve. The Met-Flow UVP-DUO ultrasound velocimetry device in the rotating frame has, like the main computer, had its hard drive replaced by a solid state disk to ruggedize it for rapid rotation. It is powered by a commercial 120 V inverter (not shown). The inverter feeds a power strip that could be used for ordinary mains-powered instruments of other types. The UVP Monitor is typically connected to two or three ultrasound transducers mounted in instrumentation ports in various configurations. Software allows selection of these transducers remotely using built-in switching. One 500kHz transducer is mounted intrusively into the flow on a rotatable mount driven by a remotely-controlled stepper motor and worm gear drive. The mount holds the transducer 45 degrees from the vertical, pointing down into the sphere, and the mount can be rotated about a vertical axis. The mount allows 290 degrees of rotation. This allows some degree of flow mapping, and allows tuning of the transducer direction to better pick up fluid oscillations or to turn the transducer out of a mean flow that is too strong. Generally, the trandsucer is rotated so that it is facing upstream, to minimize measurements in its own wake.

The ultrasound rotator is controlled by an Arduino microcontroller board with

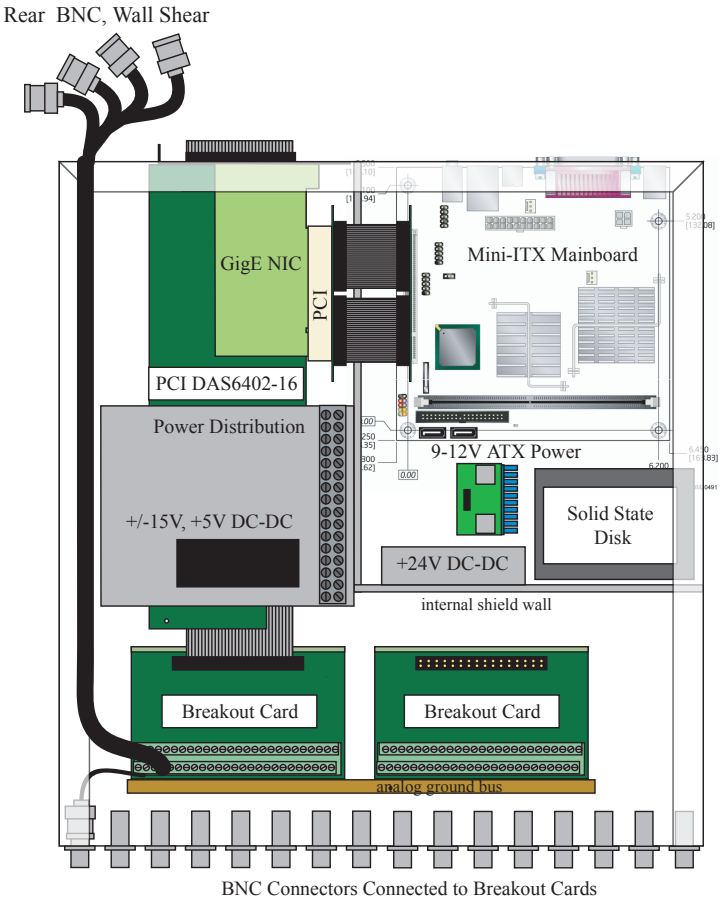

Fig. 3.18: Internal layout of the sphere frame computer. Custom case, complete with air cooling hoodscoops, was designed and constructed by the author to accommodate the large acquisition card and power conditioning circuitry. The main board is an Intel D201GLY2 low power consumption Mini-ITX form factor board. The computer is powered by a boost converter that will run down to 9 V. A solid state disk is used, as Coriolis and centrifugal forces can damage a mechanical hard disk. The main data acquisition is done by a Measurement Computing PCI-DAS6402/16 64 channel, 16 bit PCI card.

switching MOSFET motor drivers, and accepts direction commands using Hyperterminal and a USB serial connection.

Not described here but included in Appendix E is a device that may be of considerable interest to researchers with smaller devices. Before the UVP monitor was installed in the rotating frame, an older prototype unit with no network connection was used in the lab frame, with a resonant RF transformer coupling the 4 MHz signal into the rotating frame. This transformer is a simple pair of copper loops with adjustable capacitors, and works well on small devices. This method on the three meter device was made obsolete by the purchase of the networked UVP-DUO, but those without sufficient space on a rotating table may find the non-contact resonant coupling method useful.

A few final remarks on the ultrasound measurements should be made. While ultrasound Doppler velocimetry can be used to measure the velocity far from the ultrasound transducer, there are practical limitations on the maximum achievable depth due to the high velocities typical in the experiments herein. The 4 MHz measurements may extend 10 cm into the flow, and the 500 kHz perhaps 40 cm when measuring a significant component of the mean flow. When the 500kHz transducer is rotated to be nearly orthogonal to the mean flow and the experiment is operated at the lower end of the speed range, the depth may be occasionally extended to 1 m or more. In addition to the depth limitations, the large particles required to scatter 500 kHz ultrasound are subject to some unusual transport dynamics in some of the flow states described here. We have noticed that some observed turbulent flow states are poor mixers for the fairly large inertial particles we must use, and it

is therefore not always possible to acquire good velocity data.

3.5.3 Speed Encoders

Accurate speed measurement is provided by a pair of pulse encoders attached to the inner and outer sphere motors. These encoders are capable of quadrature operation and output 2500 pulses per shaft revolution. At motor speeds which may rise as high as 33 Hz for the outer motor at maximum speed, the resulting pulse rate is high (83.3 kHz). Simpler encoding schemes in the past have used analog input to measure pulse rates, and high rates can be divided down with extra circuitry. However, the National Instruments USB-6210 on the lab frame computer provides a set of high speed digital inputs that can be used to perform frequency counting tasks. These inputs are used to acquire encoder data. A connection diagram is shown in Fig. 3.19. The outer encoder is set up as an absolute position encoder. The two quadrature channels are used, and the counter may then count up or down depending on the direction of rotation. The "Z" input of the quadrature counter provides a once-per-revolution reset of the outer sphere position. The encoder has such an output, but since it is mounted on the motor side of the reduction drive, it could not be used. Instead, a photointerrupter is provided that pulses once per revolution, interrupted by a small metal flag approximately 0.07° wide.

A lack of inputs restricts acquisition of the inner encoder to a frequency count of a single pulse channel. This has proved adequate for our needs, though it is less accurate if the motor may vibrate torsionally more than 1/2500 of a revolution, as this

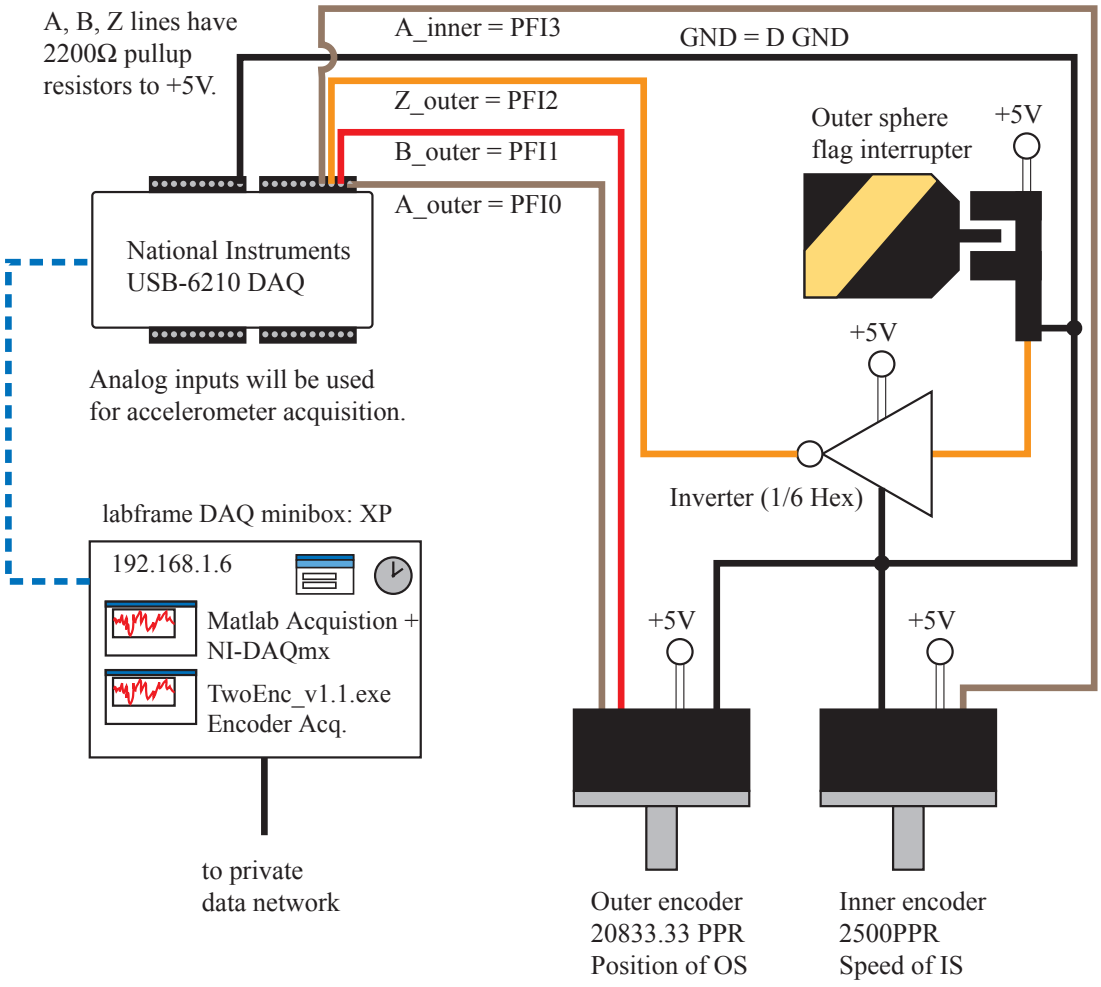

Fig. 3.19: Encoder acquisition block diagram in the lab frame. Both pulse encoders rotate at the motor speeds. The outer motor encoder runs at $400/48 \times 2500$ pulses per revolution because of the speed reduction drive. The inner encoder is directly driven at the motor speed and outputs 2500 pulses per revolution of the inner. These high pulse rates are counted by timer/counter circuitry in the NI USB-6210 card. The outer sphere encoder is an absolute position encoder, with a single photo-interrupter to reset the outer counter once per revolution of the outer sphere. A DOS executable writes outer sphere position and inner sphere pulse count to a file on wave.

causes extra counts. A DOS program written by the author, **TwoEnc_v1.1.exe**[18] A samples the counter synchronously with an analog input running in MATLAB on the lab frame computer and writes those samples to a file on wave. Source code for this program is available in Appendix E. The outer sphere position is written in degrees, and the inner sphere count is recorded as an integer from 0-2500, with the output resetting once per revolution. An analog input dummy routine (no input or output) running at 500 Hz is currently used to provide a sample clock to the counter acquisition program. When the sodium experiments go on line, magnetic field sensors in the lab frame will be acquired along with accelerometers for safety interlocking. For both scientific and vibration analysis purposes, a sample-synchronous, high resolution measurement of the outer sphere position is a useful auxiliary measurement. It will also allow for post-processing phase synchronization of magnetic data in the rotating frame with that taken in the lab frame, by aligning the phase reference photodiode signal with the outer sphere position measurement. We may, however, devise a wireless trigger for synchronizing these measurements using hardware triggers. Then measurements can be made phase synchronous with the outer sphere position acquisition.

3.5.4 Wall Shear Stress Array

Wall shear stress measurements provide a more reliable and more broadband measurement of mean flow fluctuations than the ultrasound velocimetry. In some

[18] Data taken prior to this dissertation used **TwoEnc_v1.0.exe**, which mistakenly reports the outer sphere speed 0.5% too high.

turbulent flow regimes, the mixing of the particles needed to scatter 500 kHz ultrasound is poor. Furthermore, the sampling rate for ultrasound velocimetry is limited by the round trip time to the furthest measurement location. Wall shear stress can be sampled faster and does not suffer from any issues of inertial particle transport, so it is an attractive flow diagnostic. For some of the experiments presented in this dissertation, a Dantec model 55R46 wall shear stress sensor powered by a TSI model 1750 constant temperature anemometer (CTA) circuit was used to make single-point measurements. This sensor failed partway through the experimental campaign. It was desirable to replace it with multiple sensors to allow cross-correlations, but commercially available units rated for use in water cost along with the CTA circuitry needed cost approximately $5,000 per channel in a form factor that can be rotated with the outer sphere. The commercial sensors are small and can therefore resolve short length scales in turbulence. They are also faster than the current probes. However, neither of these characteristics was mandatory for these experiments.

The failed wall shear stress sensor and constant temperature anemometer were replaced instead by a system designed and built by the author. A flush-mount wall shear stress sensor is typically a thin platinum or nickel film deposited on a ceramic substrate, covered with a thin coating of thermally conductive electrical insulator. This film forms a very stable temperature dependent resistor, usually with a value of $5-15\Omega$. The high engineering cost and low sales volume of these devices undoubtedly contributes to their high price. The constant temperature anemometer circuit is, in principle, a simple device that applies a variable amount of electrical power to heat the sensor. It uses a fast feedback loop that keeps the electrical resistance, and

therefore the temperature of the sensor, constant. The power required by the sensor to maintain constant resistance is a function of the fluid flow past it (and therefore the heat flux away from it). This variable power constitutes the output signal of a constant temperature anemometer. Inspection of commercially available constant temperature anemometry circuits shows them to be fairly complex devices, possibly to aid circuit reproducibility, to increase circuit bandwidth, or improve other circuit properties. However, a simpler circuit suffices for lower-accuracy measurement of relatively slow turbulent fluctuations.

The system described here uses very low cost platinum resistive temperature detectors as flush mount wall shear stress sensors. Four sensors were inlaid into a machined plastic substrate in a square array 10.2 cm on a diagonal, depicted in Fig. 3.20 (b). At the location of the ports, the two probes on a line of latitude are separated by approximately 9.7° in azimuth. Those on a line of longitude are separated by about 3.9° in latitude. The RTD device used is an Omega F-2020[19], which measures approximately 2 mm square. Like a hot film flush mount sensor, it consists of a platinum film covered with an insulating coating. The resistance of these sensors is well controlled and the temperature coefficient thereof is reasonably large and extremely stable, consistent with their intended function as temperature-variable resistors. They have some disadvantages. The lowest resistance available for off-the-shelf RTDs is 100Ω. This requires the use of a higher voltage CTA circuit, possibly ruling out the use of commercial circuits. Furthermore, as shown

[19] Available from **www.omega.com** at the time of this writing for $1 per sensor in a quantity of 100, Omega part number F-2020-100-B-100.

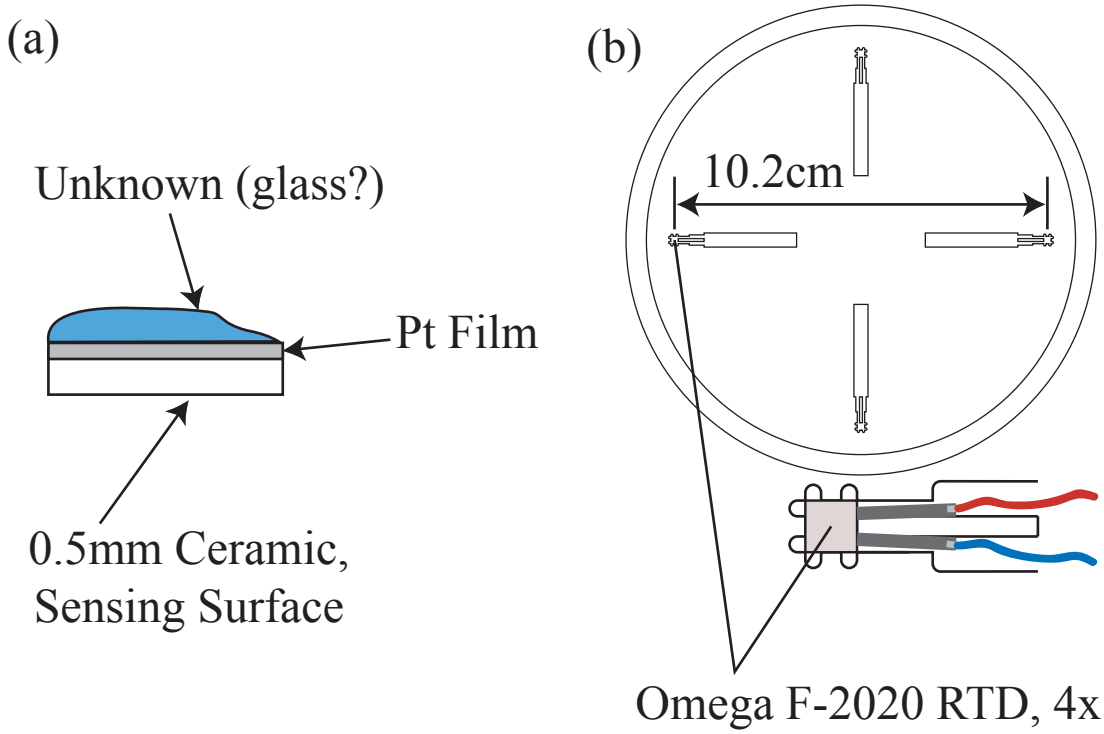

Fig. 3.20: A schematic of an Omega F-2020 sensor layered structure, (a). The flat white thermally conductive ceramic surface is used as the sensing surface, while the unknown blue side faces away from the fluid. Four such sensors are arranged in a square array (b), with a 10.2 cm diagonal. The sensors and their connecting wires are sealed into shallow trenches in the array substrate plastic surface using silicone sealant. This holds them in place and provides electrical insulation from the water, which is critical.

in Fig. 3.20 (a), the platinum film is deposited on a 0.5 mm thick ceramic substrate that is used in this application as the sensing surface, as it is flat and likely made of highly thermally conducting ceramic. The blue coating, likely some sort of glass, is thinner but it is not flat and cannot be flush mounted with a surface. Measurement through a thick ceramic layer will cause undesirable thermal lag and probably lead to phase shifts between the sensor variations and fluid fluctuations when they are fast. This was not assessed in detail, as the sensors performed adequately for the task at hand. Resistive temperature sensors are available in many physical configurations, some of which may be more suited for use in CTA service. The reader is encouraged to investigate other options, as some could be significantly superior while retaining very low cost and drop-in compatibility with the circuit described here.

As mentioned before, the high resistance of the lowest resistance resistive temperature detectors on the market requires the use of high excitation voltage to get significant self-heating. Not all commercial CTA bridges will work properly with a sensor of this resistance. Furthermore, the four channels required for the four sensors of Fig. 3.20 (b) are by themselves cost prohibitive for casual needs. A nearly minimal CTA circuit was designed, the schematic for which is shown in Fig. 3.21. Resistors R1, R2, R_{oh}[20], and the F-2020 sensor form a Wheatstone bridge. The resistors in the left half of the bridge, R2 and R_{oh}, nominally have a value ten times their counterparts in the left half of the bridge. In the final circuit, R1 is nominally 27Ω and R2 is 270Ω. The overheat resistor is nominally adjusted to a value ten times the resistance of the RTD sensor at the desired overheat, which can be

[20] This is a fixed resistor in series with a variable one for finer adjustment.

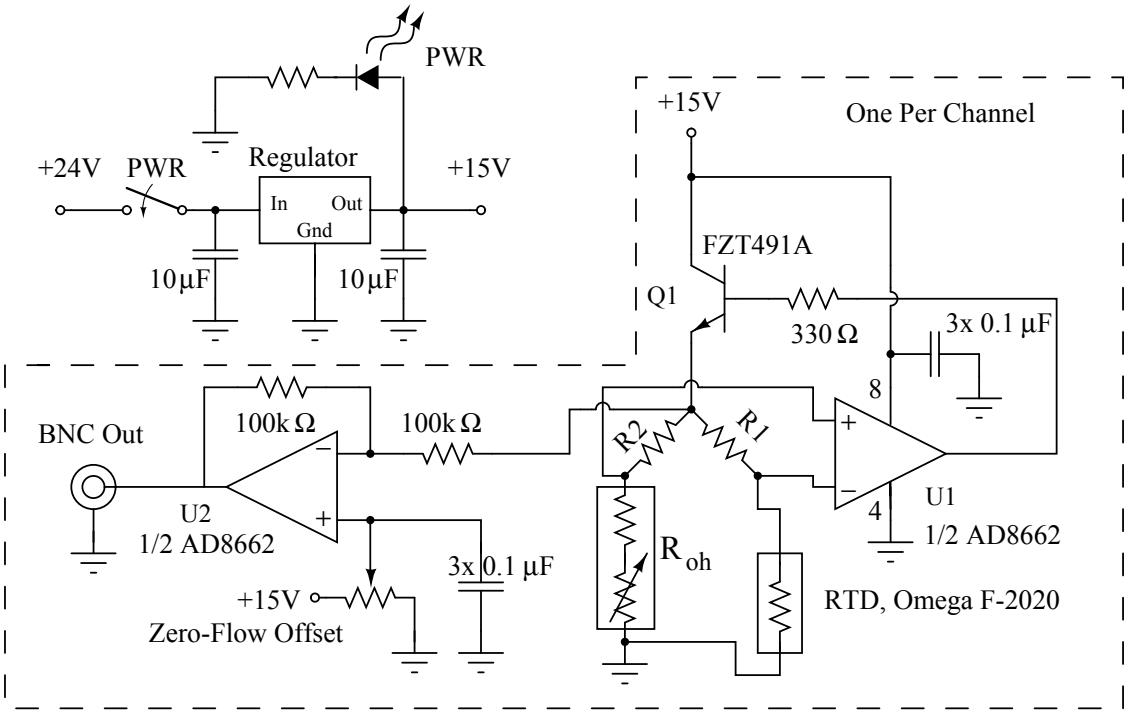

Fig. 3.21: Schematic of simple constant temperature anemometer circuit. The sensor is an inexpensive resistive temperature detector. R1, R2, R_{oh} and the sensor form a Wheatstone bridge that is balanced when the sensor is at a particular temperature, adjustable by the overheat adjustment, R_{oh}, which is a fixed resistor in series with a potentiometer for better resolution. As fluid flows past the sensor, the AD8662 op amp and transistor vary the power to the bridge to keep the sensor temperature constant. Because this voltage may typically exceed the input range of the acquisition card, it is inverted and a zero-flow offset is applied to put the zero-flow voltage at the top of the allowable acquisition input range. As the flow increases, this voltage decreases. In this way, the voltage always remains within the -10 V to 10 V range of the data acquisition card. The output voltage for the experiments here is $11.75 - V_{\text{bridge}}$. The zero-flow bridge voltage is around 3 volts.

calculated using the temperature coefficient of resistance. This is standardized at 0.00385 Ω/Ω°C for most RTD devices. When the RTD sensor is cooler than the overheat setpoint, the bridge is unbalanced, and the output of U1 op amp rises. This increases the current through bipolar transistor Q1 until it is sufficient to keep the sensor at the setpoint. If the sensor is hotter, less power is delivered and it cools toward the setpoint.

The speed of this feedback loop is extremely high, essentially keeping the sensor at constant temperature at all times. In such a circuit it is possible for the loop gain to be too high, and then the circuit may oscillate. It is typical in a CTA circuit to intentionally roll off high frequencies by including a capacitive feedback from the output to the negative input of op amp U1. This was tried initially but the circuit remains stable without any rolloff, so capacitance was omitted here. It is also typical to provide an small inductor in series with the sensor connections to tune out cable capacitance from a long coaxial cable. In this application, the CTA circuits are a short distance from the sensors themselves, connected with twisted pair cable. No inductive compensation was needed, but may be desired if long coaxial cables are necessary.

The output of many CTA circuits is simply taken from the top of the bridge, at the junction of R1 and R2. To help ensure that the output was always within the range of the 10V maximum of the acquisition card, this voltage is fed to a unity gain inverting amplifier with offset based around U2, the other half of the AD8662 dual op amp. A well-bypassed potentiometer allows adjustment of the zero flow voltage to put it near the *top* of the data acquisition range, maximizing the range

in which it can vary. Increasing wall shear stress leads to a decreasing voltage. An updated version of this circuit will use a non-inverting stage instead, but the design is presented here as implemented.

Because of the extremely high gain of the open loop op amp, board layout needs to be neat with short leads. Furthermore, it is critical that the sensor leads be completely insulated from contact with water. The high gain feedback circuit misbehaves spectacularly when water leaks into contact with the leads. A printed circuit board template for this circuit and parts placement diagram is reproduced in Appendix E for the reader interested in reproducing this circuit directly, though a re-worked layout could result in more channels on the same board space.

The wall shear stress system was not exhaustively tested in a known flow to independently assess it for frequency and phase response. Little can be said about the suitability for turbulent flow applications in general, especially those focused on flow spectra. Calibration was done in situ against the torque on the inner sphere. Fluctuations out to the Nyquist frequency of 256 Hz were easily observed with sufficiently high mean flows, and fluctuations out to several tens of Hz at least were resolvable in a zero-flow situation. Response to the mean flow and fluctuations was more than adequate for our purposes. It is likely that smaller surface-mount type RTD sensors used with this circuit would be considerably faster. Characterization and improvement of this circuit for more sophisticated measurements is a matter for future work.

As with all simple hot-element sensor circuits, the temperature of the fluid bears directly on the power delivered to the sensor if a fixed "hot" resistance is used.

An updated circuit could include simple temperature compensation in the form of a temperature-sensitive overheat setpoint resistor, R_{oh}. Excellent absolute temperature control can eliminate the difficulties caused by the fixed overheat resistor in the circuit of Fig. 3.21. However, it is expected that the sorts of experiments in which extremely low cost, modest performance wall shear stress arrays may be most useful will be in small, simple apparatus. In these devices, precise temperature control is not usually practical, with the apparatus being run at whatever room temperature is on a given day. Simple temperature compensation could extend the utility of this sensor to make absolute measurements, and residual temperature dependence could be calibrated out.

3.5.5 Torque Sensor

The torque on the boundaries of a turbulent shear flow is an integrative measurement of the turbulent azimuthal wall shear stress. It quantifies the global energy input and the flux of the axial component of angular momentum from boundary to boundary. Therefore, torque is a quantity of fundamental interest in turbulent shear flow experiments like this one. Some examples of prior work with torque as a primary diagnostic are discussed in Sec. 5.2. The variable frequency drives on the inner and outer motors calculate an estimate of the torque based on the electrical power supplied to the motors and the speed. At low motor speeds, though, this power dissipation is dominated by motor winding losses and the accuracy of the reported torque suffers. Since it has no speed reduction, the inner sphere is more seriously affected by this, and we decided to add a more sensitive torque measurement system

to the inner sphere. Fig. 3.22 is an annotated photograph of the inner sphere torque sensor arrangement.

Torque from the motor is transmitted by a modified Lovejoy CS-285 flexible shaft coupling, Fig. 3.22 (a) to a Futek TFF-600 reaction flange torque sensor. The sensor, Fig. 3.22 (b), is a strain-gauge based device with a maximum measurement rating[21] of 1130 N m, sufficient for the maximum torque output of the motor. The sensor bolts between the lower half of the flexible coupling and an anodized 6061 aluminum adapter, Fig. 3.22 (c), designed and machined by the author, which transmits the torque to the inner sphere shaft, Fig. 3.22 (d). Both the bottom surface of the modified coupler and the top surface of the adapter housing have a circular radial location pin and keyslots with square keys that mate with the sensor flanges. The adapter housing has a pair of diametrically opposing flat surfaces with ten 3/8"-16 tapped holes for solid mounting of electronic equipment to the sides of the housing.

The torque sensor signal is acquired by a high resolution wireless acquisition system, Fig. 3.22 (e), which is powered by a 10 Ah lithium-ion battery pack and power supply, Fig. 3.22 (f). The battery box contains a CUI PK-25-D5-D12 DC to DC converter, which accepts the variable 6-8.3V voltage from the battery pack and supplies steady ±12 V outputs at 850 mA. Battery power is sufficient for approximately 12 hours of continuous acquisition. A schematic of the battery box, including low voltage cutoff circutry to protect the battery from excessive discharge, is available in Appendix E. The battery box and wireless torque sensor are mounted diametrically opposite to help preserve shaft balance. The internal layout of these

[21] The sensor will withstand 150% of this safely.

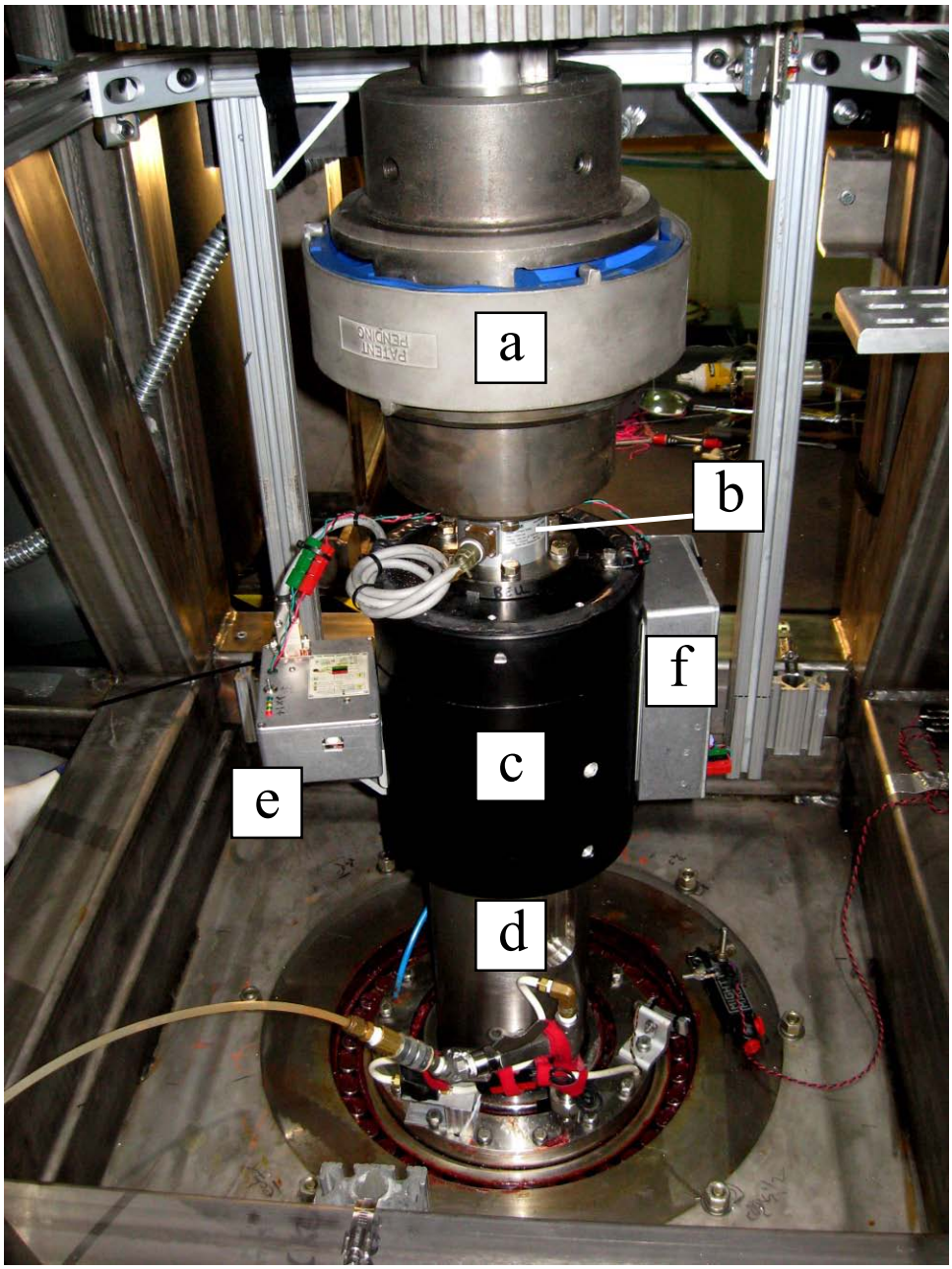

Fig. 3.22: Photo of the torque sensor arrangement. (a) Flexible shaft coupler. (b) Futek TFF-600 torque sensor. (c) Adapter coupling. (d) Inner sphere shaft. (e) Wireless torque sensor, Fig. 3.23. (f) Inner shaft battery box.

devices was carefully considered with regard to large centrifugal accelerations. The devices have been tested to approximately 100 g with the inner sphere rotating at 10 Hz. It is likely that mounting of the battery will need to be improved to reach much higher speeds, although as discussed in Sec. 3.4.4, the maximum operating speed of the inner sphere and shaft is likely to be torque limited.

A block diagram[22] of the custom wireless strain gauge transmitter, designed, built, and programmed by the author, is depicted in Fig. 3.23. The Futek TFF-600 is excited with a DC voltage, and the millivolt output of the bridge is amplified by a low noise instrumentation amplifier with a gain of approximately 100. The output of this amplifier is sampled by a high resolution 22 bit analog to digital converter running at a sampling rate of approximately 30 Hz. A large dynamic range is desirable to measure small fluctuations around the large range of mean torques the sensor is subjected to. The 22 bit converter is not strictly necessary in light of the mechanical confounding errors of seal and bearing drag, mechanical noise, and hysteresis/repeatability limits on the sensor itself; a 16 bit converter would likely suffice.

However, the circuit as built has very low inherent noise and an improved mechanical torque measurement system with less confounding drag and an enhanced dynamic range sensor could fruitfully take advantage of this bit depth. In fact, rather minute fluctuations can be resolved simply by lowering the confounding drag. While a strain gauge type sensor may suffer from repeatability and hysteresis issues that limit its absolute accuracy, it may still be useful to measure tiny relative changes

[22] Full schematic is provided in Appendix E

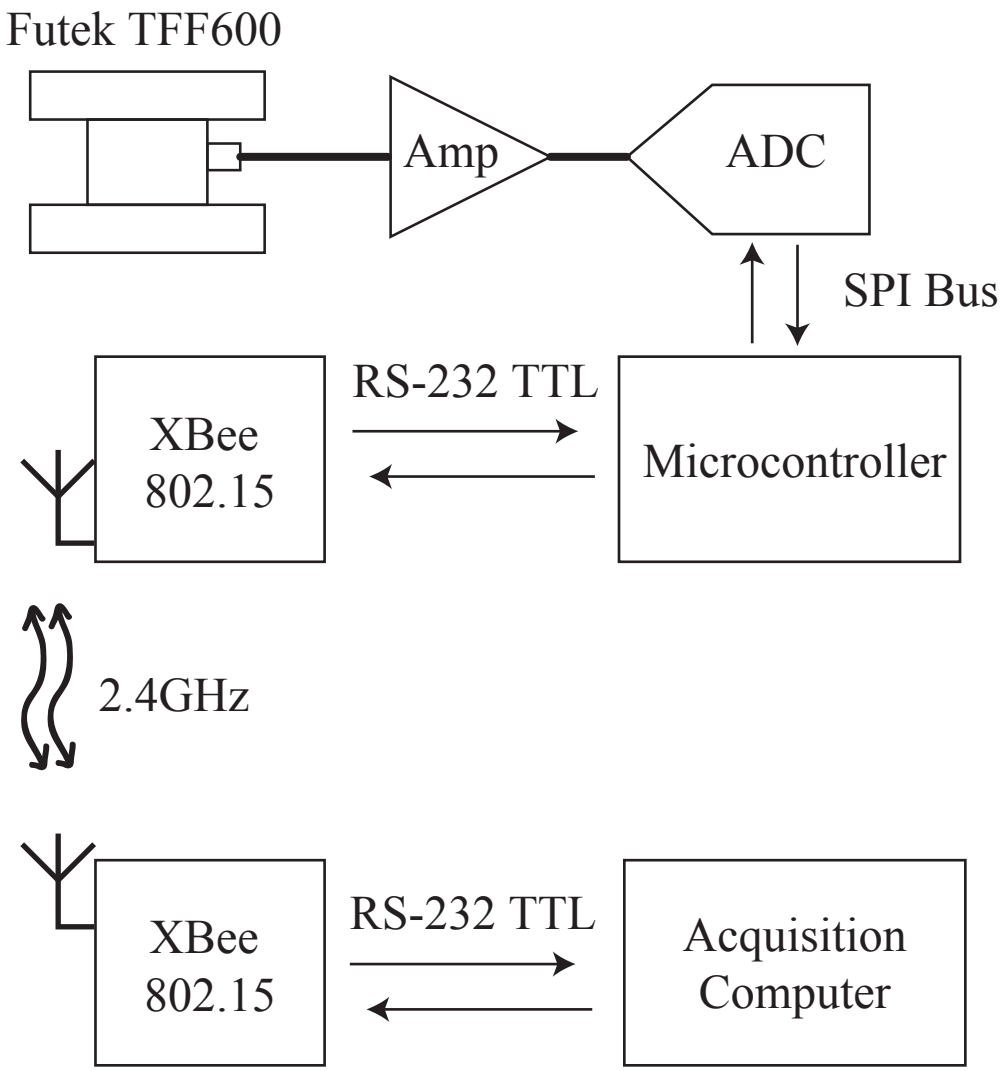

Fig. 3.23: Block diagram of the wireless torque sensor on the inner sphere shaft. Torque from the motor is transmitted through a Futek model TFF-600 reaction flange strain gauge torque sensor. The output of this sensor is amplified, sampled at about 30 Hz using a 22 bit analog to digital converter. This converter is controlled by an Arduino microcontroller board which transmits the data through a 2.4 GHz wireless serial link to a computer, 3motor, in the lab frame. A program called **torqsen7** on this computer writes incoming data to a file.

provided that medium-term drift can be quantified or controlled. The sensor and acquisition as built can detect faint finger pressure on the rim of the sensor. It is estimated that the system as built approximately 18 bits of useful dynamic range in terms of the ratio of minimum resolvable relative fluctuations to the maximum measurable torque. Machinery improvements may allow more of this range to be used.

Conversions are clocked and controlled by an Arduino microcontroller board. This is an inexpensive microcontroller system based around an AVR ATMEGA168 microcontroller. It is supplied with a pre-programmed bootloader that allows it to be programmed through a USB to serial converter included on the board itself. No external programmer is needed. A free and open source development environment with access to many intuitive function libraries speeds the code development process. The microcontroller communicates with the analog to digital converter over SPI, a synchronous serial protocol. The binary 2's complement output of the ADC is converted to a an ASCII encoded signed integer. The output integer ± 1801990 corresponds to ± 1130 N m based on calibration of the amplifier and ADC against a known millivolt source and the factory calibration of the Futek sensor, 1.68 mV/V full scale[23].

Data is transmitted to the lab frame using Digi XBee wireless serial devices. The Arduino communicates using a TTL RS-232 type serial connection with one XBee housed in a radome on the torque transducer box. The XBee in the lab frame

[23] Bridge output per volt of bridge excitation.

is connected to 3motor using a USB to TTL serial converter[24], and the **torqsen7** program receives data and writes it to an ASCII file. The incoming data is timestamped by 3motor as it is received. This timestamp is roughly synchronized to the rotating acquisition with network time synchronization. The XBee serial link is occasionally interfered with, probably by other 2.4 GHz wireless networking. This results in occasional dropped samples, and occasionally a few seconds of interruption. However, since the torque dynamics to be measured are slow, this is not a serious problem. This issue may be addressed if magnetic sensors and good synchronization are desired in the future.

3.6 Sixty Centimeter Apparatus

A smaller predecessor of the three meter device has yielded interesting scientific results [12–15] in rapidly rotating spherical Couette flow of sodium, as discussed in Sections 1.4.4 and 2.3.5, with some results depicted in Fig. 1.6. During the design and construction phase of the three meter system, the author assisted from time to time with instrumentation development and scientific investigations with this device. Some data from the 60 cm apparatus will be presented herein to illuminate some of the turbulent flow states discovered in the three meter device. As discussed in Sec. 2.3.5, the 60 cm device partially overlaps the parameter regime of the three meter device. However, the primary diagnostic in the 60 cm sodium device is the induced magnetic field outside the outer sphere. With an applied field sufficiently

[24] An XBee Explorer board from **www.sparkfun.com**

weak to be dynamically insignificant, the induced magnetic field can be used to infer global information about the fluid flow, consistent with Eq. 2.1. This global flow information is a good complement to the local direct flow measurements and global torque measurements we have available in the three meter device. In those states where data is available from both experiments, we will include some 60 cm data, and so we describe the salient aspects the 60 cm briefly. This device is more fully described in the dissertation [117] of D.H. Kelley.

The experiment is depicted schematically in Fig. 3.24. In most respects, it is simply a 1/5 scale version of the three meter device. The two cylindrical shafts labeled in Fig. 3.24 (a) are the hydrodynamically relevant[25] exception. These cylindrical shafts are approximately half the diameter of the inner sphere and rotate with the outer sphere. The inner sphere's drive shaft is mounted on a pair of bearings near the tips of the large shafts. This is in contrast with the three meter apparatus, where the inner sphere shaft extends all the way to the poles of the outer sphere and is only 16% of the inner sphere diameter. This difference in the geometry has a slight noticeable effect on the observed flow states, in particular, the bounding values of Ro for particular states seem to be shifted.

Some of the induced magnetic field data from the 60 cm apparatus presented in this dissertation is recently collected data intended to more fully explore states discovered in the three meter apparatus. Other data has been pulled from relevant portions of the 60 cm data archives. The older magnetic field data was collected

[25] There is an additional hydromagnetic difference: the inner sphere of the 60 cm apparatus is solid copper, not hollow stainless steel.

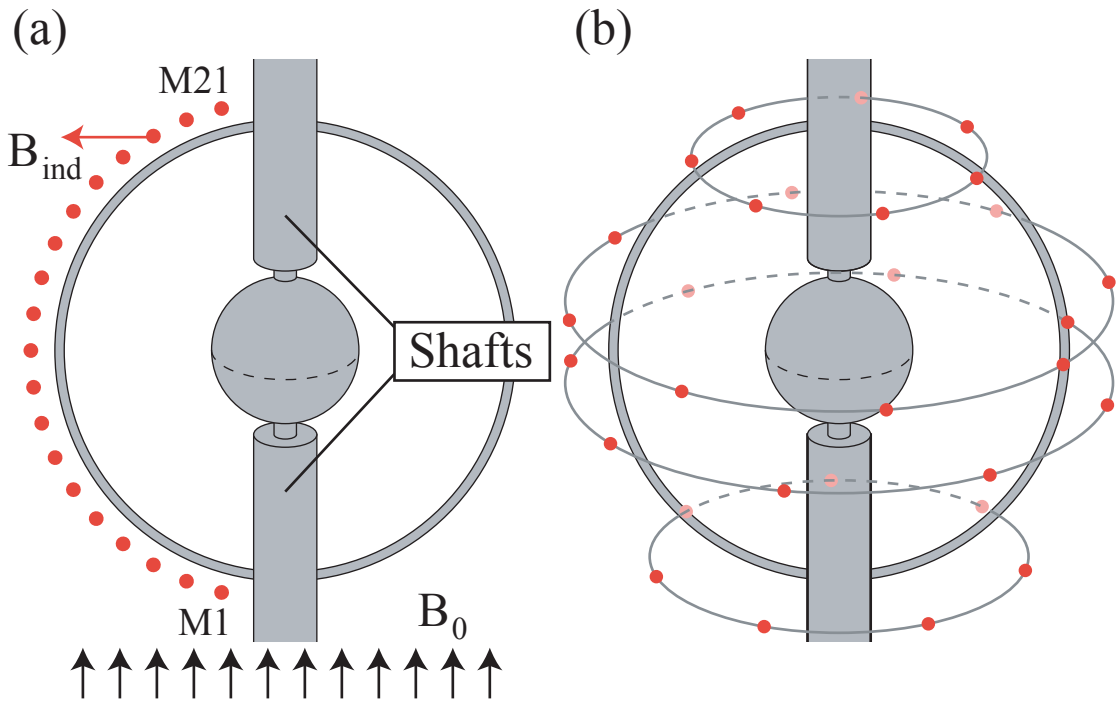

Fig. 3.24: Schematics of the 60 cm sodium spherical Couette apparatus, adapted from the dissertation of D.H. Kelley [117]. This experiment is proportional to the three meter apparatus, and five times smaller, with the exception of the large shafts labeled in (a). These shafts rotate with the outer sphere, and slightly modify the geometry of the experiment with respect to the three meter device. Small red circles denote the location of Hall effect sensors for two different arrays. At (a), an array constructed by the author, has 21 probes spaced equally on a meridian. At (b), a more sophisticated array built later by D.H. Kelley allows decomposition of the induced field into spherical harmonics up to $l = 4, m = 4$. In both cases, a weak, approximately uniform and axial field, B_0, is applied as in (a). The Hall sensors are aligned such that they are perpendicular to the applied field and respond to the cylindrical radial component of induced magnetic field, B_{ind}.

with an array of 21 Honeywell SS94A1F Hall effect sensors that was constructed by the author. This array, depicted in Fig. 3.24 (a), is fixed in the lab frame and lies on a single meridian spaced a short distance from the outer sphere surface. Probe M11 is at the equator. The newer data is collected with a three-dimensional array constructed by D.H. Kelley [117] of substantially similar design to that used by D.R. Sisan in experiments in highly magnetized spherical Couette flow [112, 118]. This array, depicted in Fig. 3.24 (b), can be used to decompose the cylindrical radial component of the induced field, B_{ind}, into spherical harmonic components of degree l and order m, up to $l = 4, m = 4$. It is also fixed in the lab frame. It will be made clear which array was used when magnetic field data is presented in the coming chapters.

4. RESULTS I: TURBULENT FLOW STATES

4.1 Introduction

Now that we have laid the groundwork to help us understand rotating, turbulent shear flow, motivated our experiment from a geophysical standpoint, and described the experiment and its measurement capabilities, we are ready to discuss experimental results. First we will situate ourselves again in parameter space with a brief reminder of the definition of the relevant dimensionless parameters in terms of the dimensional experimental parameters. The experimentally adjustable parameters are the outer and inner boundary rotation rates, Ω_o and Ω_i. The fixed experimental parameters are the viscosity of water, taken to be $\nu = 1 \times 10^{-6}$ m^2/s, the radius ratio $\eta = r_i/r_o = 0.35$, and a length scale close[1] to the gap width $\ell = 1$ m.

One adjustable dimensionless control parameter is the Ekman number, defined using the gap width $\ell = r_i - r_o$ and the outer sphere rotation rate Ω_o as

$$E = \frac{\nu}{\Omega_o \ell^2}. \tag{4.1}$$

The Ekman number, in the context of the experimental results, characterizes the importance of the outer sphere rotation. Generally speaking, we consider this a

[1] The gap is 0.95 m. However, 1 m is convenient and we probably have more than 5% error in our knowledge of the viscosity.

proxy for the overall rotation, but specifically it is the relative importance of viscous forces to Coriolis forces for fluid rotating at Ω_o. As we will see throughout the following chapters, the outer boundary rotation is important even at exceptionally high differential rotation.

The other adjustable dimensionless parameter is the Rossby number, a dimensionless differential angular speed,

$$Ro = \frac{\Omega_i - \Omega_o}{\Omega_o} \tag{4.2}$$

For convenience of comparison with the outer sphere rotating and without, we will always define the Reynolds number this way:

$$Re = \frac{Ro}{E} = \frac{(\Omega_i - \Omega_o)\ell^2}{\nu} \tag{4.3}$$

Although Re is not an additional independent dimensionless parameter to Ro and E, and is not needed when both spheres rotate, we will find that it can be useful to use Ro and Re in interpreting the dependence of the data on the experimental parameters. It is not the usual convention to use the definition of Eq. 4.3 when only the inner sphere revolves, but rather to use a velocity scale equal to the tangential velocity of the inner sphere; however, to define Re in terms of Ro and E without any extra factors of two, we choose the definition in Eq. 4.3. Approximate boundaries of the range of Re, Ro, and E explored in the experiments to be described are given in Table 4.1.

In this chapter, we will give a broad overview of the observed turbulent flow states, dividing the results into three categories based on the Rossby number and observed behavior. First, we will present results with the outer sphere stationary,

Tab. 4.1: The approximate bounds on the dimensionless parameters considered in the experimental results presented here. The values of Ro and E are exclusive of the outer sphere stationary cases, which have $Ro = \infty$ and $E = \infty$. Constraints on time prevented investigation of high negative values of Ro.

Parameter	Minimum	Maximum
E	9×10^{-8}	5×10^{-6}
Ro	-5	100
Re	2.5×10^{5}	6×10^{7}

$Ro = \infty$ and $E = \infty$, with Re ranging approximately over the values in Table 4.1. There is a single turbulent flow state when the outer sphere is stationary, with a scaling for the torque on the inner sphere that is similar to that of the turbulent drag observed and predicted for other shear flows, like pipe flow and flow over a flat plate. However, also observe a system-wide coherence, consisting of a slowly rotating wave motion consistent with an $m = 1$ azimuthal wavenumber. We also observe this wave in the 60 cm apparatus, and magnetic field data is included to further characterize the state.

We then turn our attention to $Ro < 0$, where Kelley *et al.* [12, 14, 15] observe inertial modes in the spherical Couette geometry. Indeed, we observe these modes as well, holding E constant and varying Ro in the range $-5 < Ro < 0$, and we compare to the prior published results. We note some new behaviors, including that one observed mode is apparently part of a resonant triad. We also look at the torque on the inner sphere as a function of Ro and E. Several flow transitions exist in the $Ro < 0$ regime corresponding to different inertial modes, but these can just barely be detected in the torque.

Finally, we will conclude this chapter with results for $0 < Ro < 100$. A number of turbulent flow transitions are observed here as well, but unlike those for $Ro < 0$, the torque required to drive the inner sphere has a more complicated dependence on Ro. There are several distinct transitions as Ro is varied with fixed E, with bistable ranges of Ro where spontaneous transitions involving the two adjacent states are noted. Each different flow state is characterized by its frequency content, much like the inertial mode states for $Ro < 0$. However, the $Ro > 0$ states may also be characterized by different dynamical fluctuations of the torque. When $Ro > 0$, it is often the case that the fluctuations in the fluid drag on the inner sphere lie at low enough frequencies and are sufficiently correlated over the surface of the sphere that we may detect them.

4.2 $Ro = \infty$, Outer Sphere Stationary

4.2.1 Flow Properties

There is not much information available on the fluid flow in turbulent spherical Couette systems, and even less is known when both spheres revolve. When only the inner sphere rotates, as is considered in this section, there are some good measurements of time series and flow spectra for weakly turbulent states at different radius ratios. The turbulent regime reported by Wulf *et al.* [101] for both $\eta = 0.752$ ($\beta = 0.33$) and $\eta = 0.667$ ($\beta = 0.5$) is characterized by chaos in the amplitude of successive velocity extrema. A common feature of both radius ratios investigated, however, is the persistence of "aperiodic coherent structures" as well as a frequency

spectrum that exhibits significant peaks. The weakly turbulent regime for $\eta = 0.667$ exhibits a broad spectral peak at about 0.25 Ω_i and a comb of incommensurate frequencies that lie higher. This lowest frequency is about a quarter of the frequency observed at the laminar onset of traveling waves. For $\eta = 0.75$, the lowest peak in the turbulent spectrum is about half that observed in the first laminar rotating wave state.

To our knowledge, no one has ever published a thorough characterization of the turbulent dynamics of $Ro = \infty$ spherical Couette flow for $\eta = 0.35$ or nearby radius ratios. The only previously reported very low frequency drifting state reported in strongly turbulent, purely hydrodynamic spherical Couette flow seems to be that in the dissertation of D.R. Sisan [118]. Sisan noted a weak, low frequency wave state below onset of hydromagnetic instabilities. In this case the "precession below onset" reported by Sisan was not always observed, and it was ascribed to experimental imperfections, but the data presented here suggests that this may not be the case, at least at our Reynolds numbers.

Based on the work of Wulf *et al.*[101], we may expect a slowly drifting wave in the weakly supercritical turbulent state, and we might expect it to have a lower azimuthal wavenumber and significantly lower frequency than that of the first laminar nonaxisymmetric state. Hollerbach *et al.* [100] predict that the saturated state arising from the first nonaxisymmetric laminar transition for geometries near our radius ratio involves either a $m = 2$ or $m = 3$ drifting wave. The laminar oscillation frequency for our radius ratio, which is in between those given by Hollerbach *et*

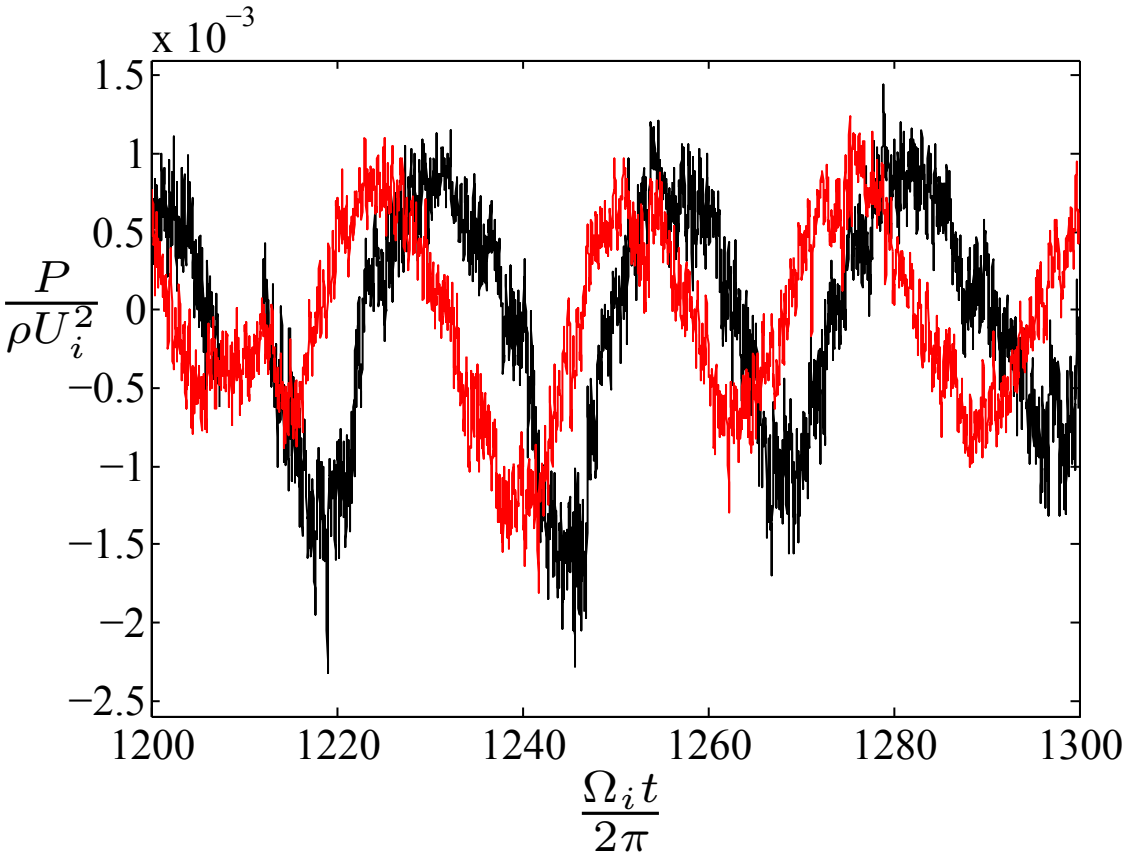

Fig. 4.1: Time series of two pressure sensors installed in adjacent instrumentation ports (Fig. 3.2 (K)), 90 degrees apart. $Ro = \infty$, $Re = 4.4 \times 10^7$. A large-scale pressure oscillation consistent with an $m = 1$ azimuthal pattern is observed. The red curve leads the black, consistent with a pattern propagating in the prograde direction with respect to the inner sphere rotation. Other turbulent fluctuations are present, but the strong wave dominates.

al. [100] may be estimated[2]to be 0.128 Ω_i if the first laminar wave is $m = 2$ and 0.192 Ω_i if it is $m = 3$. If the same trend seen in Wulf *et al.* [101] holds at this radius ratio, we might expect a frequency considerably lower than these laminar frequencies, at least just above the onset of chaos. Our Reynolds number is many orders of magnitude above the likely critical value[3], but we do observe a slowly drifting turbulent wave motion. Figure 4.1 shows a time series of the wall pressure[4] at 23.5° colatitude for two sensors spaced 90° in azimuth. The Reynolds number (Eq. 4.3) is 4.4×10^7. The observed correlation in the pressure sensors is consistent with a prograde drifting pattern with $m = 1$, and it has frequency near 0.04 Ω_i. This is possibly in qualitative agreement with the prior studies discussed above, though it is perhaps initially surprising that wave motion survives to such high Re.

Figure 4.2 depicts a power spectrum of wall shear stress from the three meter experiment at $Re = 4.4 \times 10^7$ and power spectra of cylindrical radial induced magnetic field from the 60 cm experiment[5] at $Re = 3.5 \times 10^6$. The sensor, M10, closer to the equator of the 60 cm experiment responds to the weaker, higher frequency peak seen in the three meter data at 0.066 Ω_i. A midlatitude magnetic sensor, M8, reproduces the three meter peak at $\omega/\Omega_i = 0.040$. The spectra have been normalized so that the 0.04 Ω_i peaks are equal in strength. Despite an order of magnitude difference in Re, the agreement for the large-scale wave motions is excellent. It should be noted that the "wave" frequency peak is rather broad. In this case, the

[2] From quadratic interpolation of the four nonlinear drift speed results of Hollerbach *et al.* [100].

[3] Re_c where turbulence sets in is not known for this η, but it is probably at most a few thousand.

[4] We have checked these oscillations to rule out free-surface dynamics.

[5] Using the array of Fig. 3.24 (a).

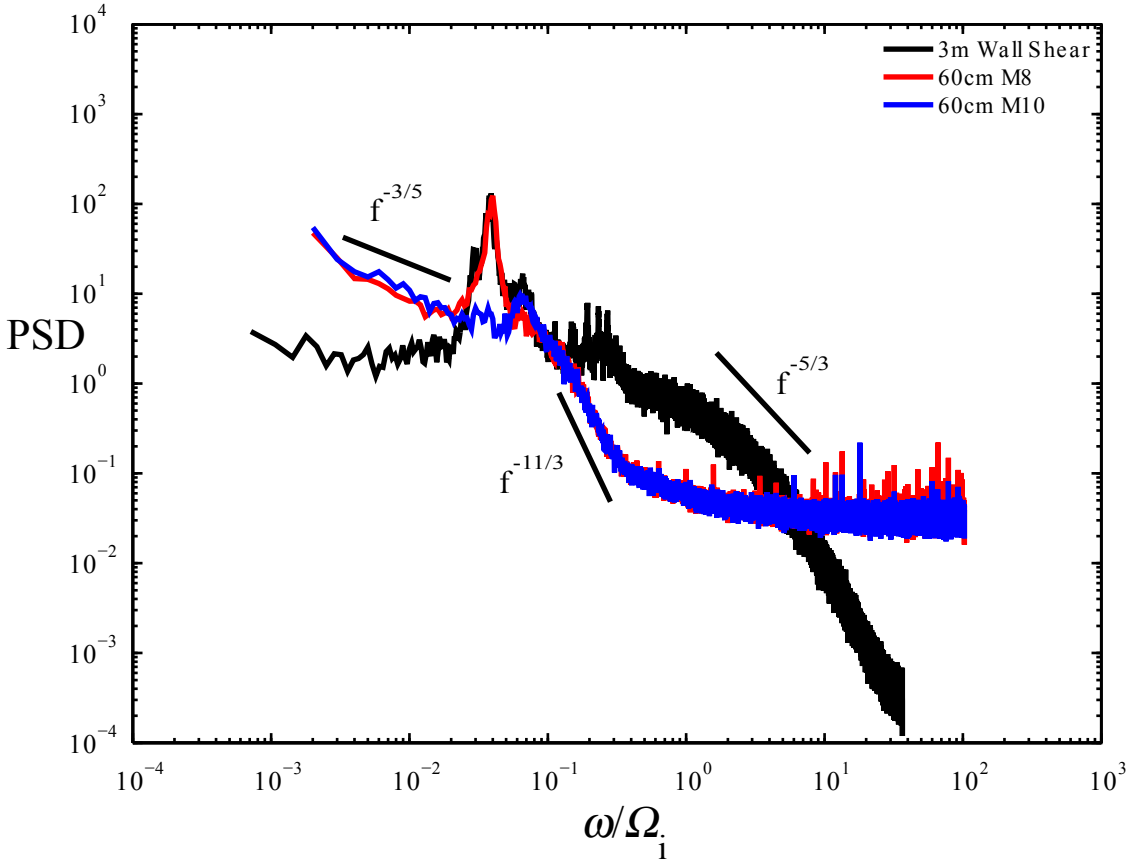

Fig. 4.2: Power spectrum of wall shear stress (black) from the three meter experiment and of the induced magnetic field from the 60 cm experiment for two different sensors from the array of Fig. 3.24 (a), one closer to the equator (M10) and one at midlatitude (M8). Frequency is made dimensionless by the inner sphere rotation rate. For the 60 cm spectra (red, blue), $Re = 3.5 \times 10^6$. For the three meter spectrum (black), $Re = 4.4 \times 10^7$. The strongest peak has $\omega/\Omega_\mathrm{i} = 0.04$. The magnetic field spectrum shows an overall decrease in power with frequency not seen in the shear data. This is discussed in the text, and appears to be a characteristic of the induced magnetic field, not of the turbulence in the 60 cm system. In the low frequency region, where the wall shear stress spectrum is nearly flat, the slope of the magnetic data depends on frequency roughly like $f^{-3/5}$.

half-power fractional bandwidth is around 15%. The wave motion, though it has a well defined center frequency, is deeply modulated with low frequency fluctuations. This is similar to the data of Wulf *et al.* for the weakly turbulent state. They find no significant correlation between the amplitudes of successive maxima of a filtered time series, but temporal correlations are clear in the frequency spectra. The observed waves in the three meter and 60 cm experiments also seem to be consistent with the frequency of the "precession below onset" reported by Sisan. Sisan does not state the frequency, but the weak-field end of the "O1"[6] spectrogram, Fig. 4.13 (a) of the dissertation [118], suggests a weak peak near the right frequency.

Aside from the strong modulated waves, the overall shape of the fluctuation spectrum for wall shear and magnetic field data is different, likely due to magnetic filtering of the fluctuations. The filtering effect likely has two causes. The induced field in a multipole expansion representation depends on polar wavenumber l like $r^{-(l+1)}$. Furthermore, the linear magnetic induction, Eq. 2.1 will be influenced by stronger diffusion and weakened advection of fields at shorter spatial scales. These small scales map to higher frequencies as they are swept past the array by the mean flow. It is also the case that very high frequencies will be filtered by the finite conductivity of the titanium alloy outer sphere. However, the shell of 60 cm is about one skin depth thick at 28 Ω_i. Since the magnetic field fluctuations are already deep below the noise floor by this frequency, the filtering due to electromagnetic skin effect plays no role.

A few reference slopes are provided in Fig. 4.2. The $f^{-11/3}$ scaling is a

[6] Odd equatorial symmetry, $m = 1$.

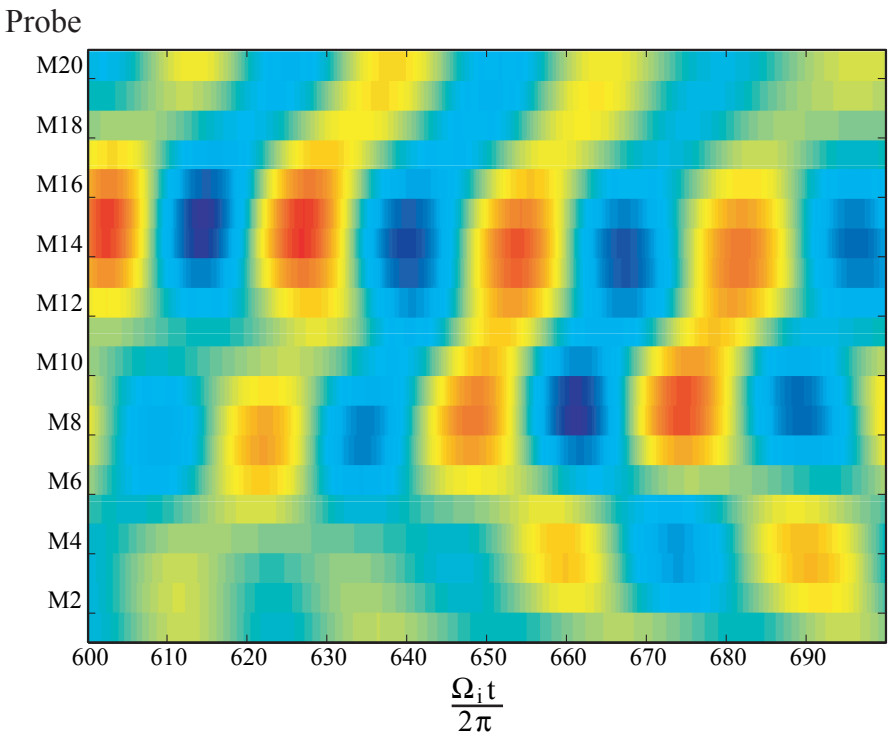

Fig. 4.3: Spacetime diagram of the radial induced field on the array of Fig. 3.24 (a), for $Ro = \infty$, $Re = 3.5 \times 10^6$. The vertical axis maps to latitude, with sensor M11 at the equator. Time is measured in units of inner sphere revolutions. This data is temporally bandpass filtered with passband between the -3dB points satisfying $0.02 < \omega/\Omega_i < 0.12$ to highlight the large-scale wave. As can be seen from Fig. 4.2, the overall induced magnetic field spectrum is broadband.

weak-field prediction by Peffley *et al.* [119] for diffusively dominated magnetic field fluctuations generated by $E(k) \sim k^{-5/3}$ turbulence. Peffley *et al.* make a prediction for mixing-dominated induction that should apply at longer wavelengths, $E_B(k) \sim k\ E(k)/\omega$. The dispersion relation relating k and ω is taken to be Taylor's frozen turbulence hypothesis, $\omega = U\ k$, there predicting $E_B(k) \sim k^{-5/3}$ for the external field fluctuations. However, no $k^{-5/3}$ spectra are noted[7] even in direct flow fluctuations. If there is a $k^{-5/3}$ spatial spectrum of velocity fluctuations, it seems that Taylor's hypothesis fails. Given that some of the most energetic motions in the flow are large-scale and oscillatory, we might expect this. Weak turbulence advected rapidly past the sensor by a uniform free stream flow is probably not the right picture in this case.

The large-scale structure of the observed slow turbulent wave motion is made clearer by the global magnetic field measurements from the 60 cm apparatus. Figure 4.3 is a space-time diagram of the twenty-one sensors pictured in Fig. 3.24 (a). These sensors are spaced out along one meridian fixed in the lab frame. The signal from each sensor was filtered with a phase-preserving filter with passband extending from 0.02 Ω_i to 0.12 Ω_i, to help distinguish the "wave" region of the frequency spectrum from the rest of the turbulent fluctuations. Approximately 3.5 periods at 0.04 Ω_i are shown in Fig. 4.3 as the wave sweeps by the Hall sensor array. The symmetry across the equator is similar to the "shift-and-reflect" symmetry of laminar wide gap wave states reported by Hollerbach *et al.* [100]. The motion in the lagging hemisphere in Fig. 4.3 lags most of the time. As with all other quantities associated

[7] Perhaps the nearly $k^{-11/3}$ region in the magnetic spectrum is simply a coincidence.

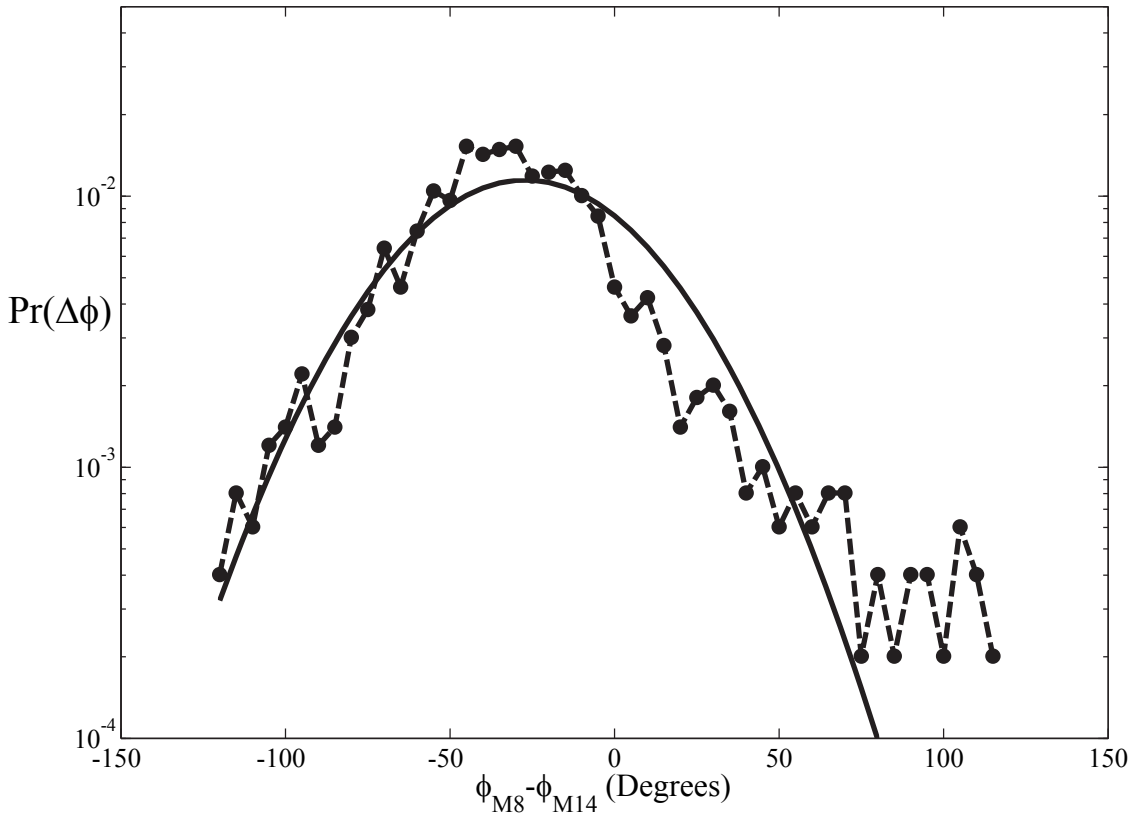

Fig. 4.4: The probability distribution of the lag angle between the Northern and Southern hemisphere wave maxima of Fig. 4.3. A running cross-correlation of the filtered data of Fig. 4.3 is taken with a four period window (with $T = 2\pi/0.04\ \Omega_i$) and histogram taken of the resulting lag angles for a long data set. The most probable lags are between 30° and 45°.

with this state, the lag angle between hemispheres is a statistical property of the turbulent flow state and therefore is strongly fluctuating. A probability distribution of the lag angle is depicted in Fig. 4.4. Typically, one hemisphere lags the other by 30° to 45°. There is substantial short-term variation in the phases of the two hemispheres, possibly due to other strong fluctuations in this frequency band, but the picture of Fig. 4.3 may be considered typical, as it has a lag close to the mean value in Fig. 4.4.

The wall shear power spectrum[8] is indicative of strong turbulent fluctuations over a wide range of length and time scales, even if it is not consistent with appearance of an inertial range of K41 turbulence. The wall shear spectrum shows measurable broadband fluctuations out to the Nyquist frequency of 37 Ω_i and a nearly flat spectrum below about 0.4 Ω_i with the exception of the strong waves. Even the "coherent" waves have large temporal and spatial variation. We may expose this further by looking at the probability distributions of measured fluctuations compared to previously studied turbulent flows. As an example, Fig. 4.5 depicts a probability distribution of wall shear stress at $Re = 4.4 \times 10^7$, normalized by the mean shear stress. The distribution is nearly log-normal, with high shear stress events much more likely than low. The same was observed in high Re turbulent Taylor-Couette flow by Lathrop *et al.* [120] and Lewis and Swinney [121]. Interestingly, there is little about Fig. 4.5 to suggest a strong wave. It may be inappropriate to think of the wave as separate from the turbulence.

We hypothesize that the large-scale wave motion for $Ro = \infty$ spherical Couette flow is a slow modulation of the inner sphere's turbulent equatorial jet, such that the jet is not (statistically) axisymmetric, flat, and of uniform strength. The resulting recirculation pattern may be complex in this case. The jet itself should be a robust feature over a wide range of Re, because it relies only on a centrifugal pumping effect from the gradient of the pressure in the fluid being out of balance with the centrifugal force near the inner sphere. This will be the case whenever the inner sphere is rotating faster than the bulk fluid in its vicinity. This jet should persist even

[8] And any other quantity we can measure.

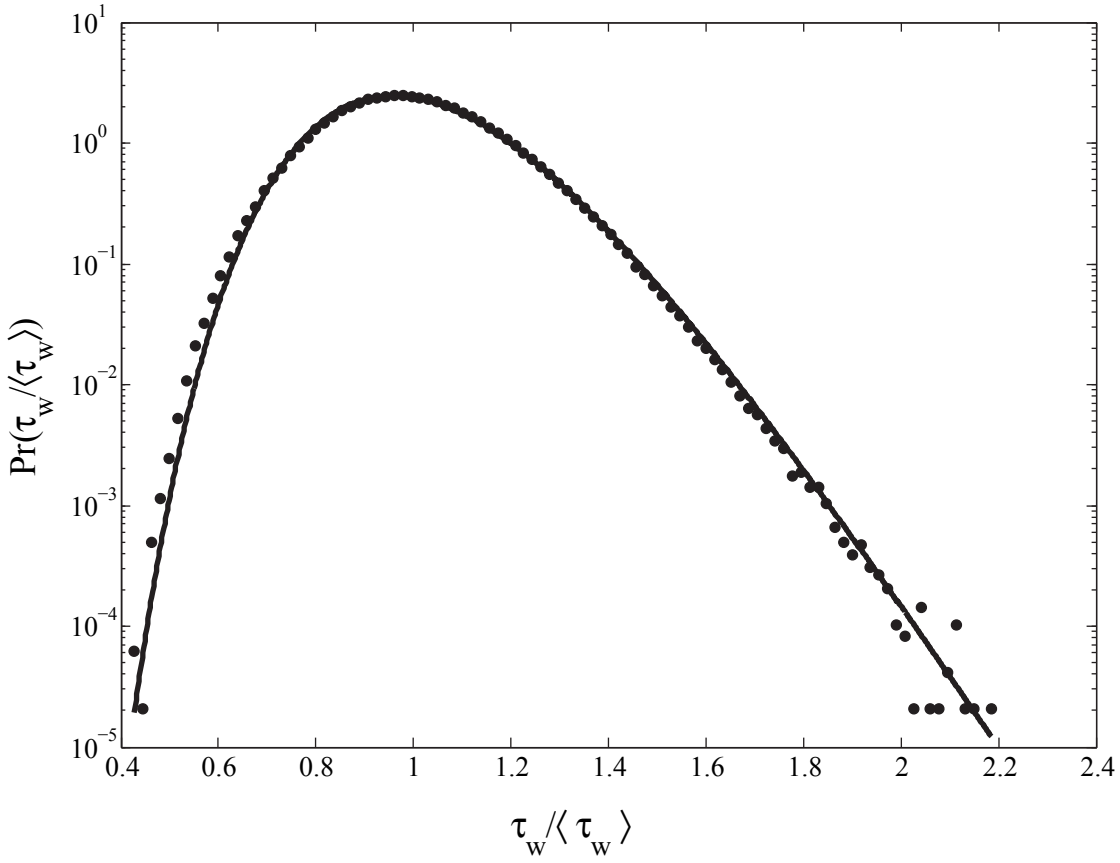

Fig. 4.5: The probability distribution of wall shear stress at $Re = 4.4 \times 10^7$ is approximately log-normal, similar to the findings of Lathrop *et al.* [120] and Lewis and Swinney [121] in Taylor-Couette flow. Here the wall shear stress has been normalized by its mean.

with a fully turbulent Ekman layer near the inner sphere, as turbulent momentum transfer spins up fluid near the sphere surface.

The boundary layer near the inner sphere in the three meter experiments is probably completely turbulent. It is possible that this is not always so in the 60 cm experiments. Kohama and Kobayashi [107] study the transition to a turbulent boundary layer on a rotating sphere in air up to Reynolds numbers

$$Re_i = \Omega_i r_i^2 / \nu \tag{4.4}$$

of approximately 5×10^5. We use Re_i to distinguish this inner-radius based Reynolds number, which is approximately one quarter of Re as we have defined it in Eq. 2.6. At the highest Re in their study, the turbulent boundary layer extends up to 40° latitude. Above that latitude laminar spiral vortices and a steady laminar layer are observed. A rough extrapolation of their results might require a fully turbulent boundary layer to have Re_i of a few million to make the turbulent transition latitude reach the pole.

As Re_i for the three meter data exceeds 10 million, we expect a fully turbulent Ekman layer on the inner sphere. However, Re_i for the 60 cm data shown in Fig. 4.2 is just under 900,000. If the boundary layer still exhibits a laminar portion anywhere in the Reynolds number range $9 \times 10^5 < Re_i < 1 \times 10^7$, it must not have much effect, given the good agreement of the observed wave states between the two experiments. It should be noted that the experiments of Kohama and Kobayashi entrain quiescent fluid by Ekman layer suction. The spherical Couette case will be influenced by the turbulent fluctuations already present in the entrained fluid. We cannot so simply

predict the behavior of the flow in spherical Couette flow at $\eta = 0.35$ from data as $\eta \to 0$.

Indeed, the results of Kohama and Kobayashi [107] and Bowden and Lord [105] note no wavy modulation of the equatorial jet position or strength as fluid is entrained from and pumped into quiescent surroundings in either the laminar or the turbulent case. It is clear that wavy behavior requires something more. Confinement of the resultant jet the azimuthal and meridional recirculation of fluid in the gap is probably a necessary ingredient. Hollerbach *et al.* [100] come to this conclusion regarding the laminar states in comparison to the results for an isolated rotating sphere, and note that it takes a long time to establish the steady state circulation in wide gaps.

This is consistent with our observations in the three meter experiment. The jet from the inner sphere begins immediately; a vigorous equatorial outflow can be observed visually as polystyrene particles settled on the inner sphere surface scatter when it is started. The slow wave state, however, takes several thousand inner sphere rotations to set in. In fact it takes several hundred rotations of the inner sphere before the wall shear stress array on the outer sphere registers a shear signal. Even with turbulent momentum mixing, it takes a long time to build up angular momentum in the gap. At early times no slow wave is observed, even if turbulence is already established.

We may propose a simple mechanism for outflow jet deflection and modulation of strength in high Reynolds number spherical Couette flow that satisfies the constraints of the observations. The mechanism should perhaps not depend too

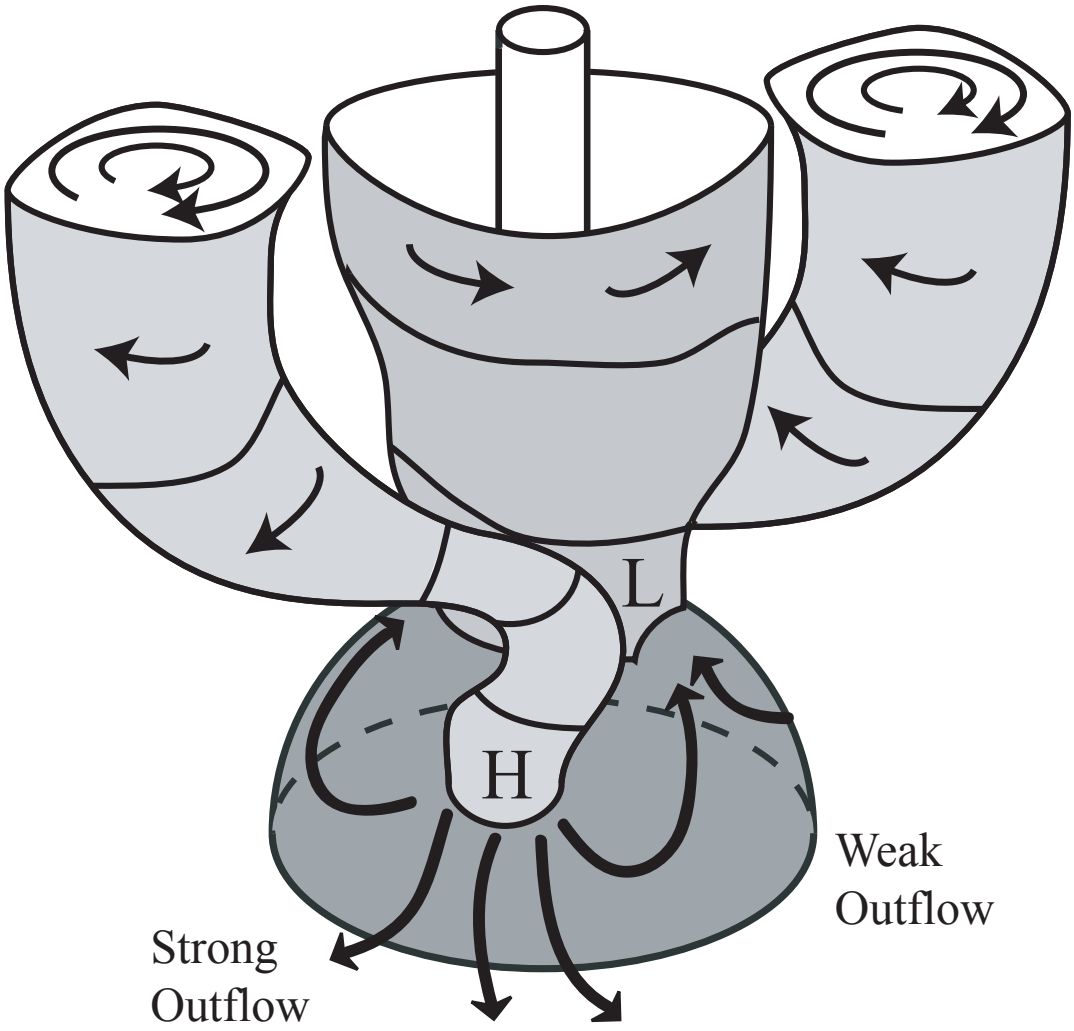

Fig. 4.6: Schematic of large vortex feedback on the boundary layer on the inner sphere. The pattern as drawn would appear as an $m = 2$ pattern on the probes, not $m = 1$ as we observe. However, as discussed in Sec. 4.4, we observe several significantly different turbulent flow states when the outer sphere revolves, and different bulk flows may be selected in that case.

much on the exact details of the inner sphere boundary layer, applying equally to a turbulent or partially laminar boundary layer. Since the outflow jet is driven by centrifugal forces that are not balanced by the pressure gradient in the fluid, the pressure distribution over the surface of the inner sphere will affect this outflow. In a large-scale-axisymmetric turbulent basic state, the pressure distribution would be axisymmetric, on average. However, we propose that regions of high and low pressure near the inner sphere associated with large-scale circulations could modulate the strength of the turbulent outflow jet into a large-scale pattern. The modulated outflow and resultant recirculation may then have the right spatial dependence to sustain the large-scale vortex patterns, closing the feedback loop. A schematic of this process is shown in Fig. 4.6. Deflection of the jet from the midplane could proceed similarly, provided that the large-scale motions on the lower hemisphere were not completely symmetrical with those on the upper. Then, the impinging boundary layer flows at the equator would be unequal in strength, the extra vertical momentum of the stronger flow would deflect the jet away from the high pressure side.

It is worth mentioning that large-scale, low-frequency fluctuations similar to those observed here are an area of interest in large industrial mixers. So-called "macro-instabilities" in these devices involve large-scale, precessing, turbulent vortices. These flows can contain a substantial fraction[9] of the total fluid kinetic energy [122–125]. Roy *et al.* [123] report slow variations in the large-scale circulation patterns in a dished-bottom, impeller driven mixer. The "macro-instablity" in this

[9] Values of 10%-30% are found in the literature, depending on mixer geometry.

case is identified with the influence of the large-scale circulation on the trailing edge vortices and axial outflow from the impeller. The large departures from axisymmetric flow pattern have important consequences for turbulent transport and the structural soundness of large mixing tanks. The three meter device is a particularly simple geometry for a turbulent mixer, and some mixers have a free surface, but there are no other significant differences[10], when the outer sphere is stationary.

Much of the work surveyed on the topic of these low frequency mixer dynamics makes the point that these flows cannot be characterized without long observation times. Among other things, this makes simulations exceedingly difficult. Lavezzo *et al.* [125] expended significant effort in a modern computation to increase their simulated time from three impeller revolutions to twenty-one. The time series of wall shear stress used to make Fig. 4.2 was nearly sixty *thousand* inner sphere rotations long. Welch's method of power spectral density estimation was used, using a sliding window of 4000 inner sphere revolutions. Motions varying on long timescales comprise a great deal of the fluctuation energy. The successful prediction of turbulent flow and turbulent transport requires that we understand when and why such energetic but slowly evolving dynamics may occur. Several thousand rotations' worth of simulated time would be needed just to see the beginning of the dynamics presented here if the initial condition were not well chosen.

[10] Up to and including the manufacturer of the outer vessel.

4.2.2 Torque

The torque demanded by the flow at constant boundary speeds has been well characterized in high Reynolds number Taylor-Couette flow with stationary outer cylinder [120, 121], and some data exists with rotating outer cylinder [126, 127]. The torque required to drive the flow between two spheres has received fairly little attention. In the turbulent case, Sisan [118] reported the hydrodynamic torque as part of an investigation on the effects of strong magnetic fields in this geometry. The scaling of the torque required to drive the inner sphere where the outer sphere is stationary is similar to the case with the outer cylinder stationary in the Taylor-Couette system. Following Lathrop *et al.* 1992 [128], we define the dimensionless torque G on the inner sphere in terms of the fluid density ρ, viscosity ν and inner sphere radius r_i as

$$G = \frac{T}{\rho \nu^2 r_\mathrm{i}}. \tag{4.5}$$

The argument can be made on dimensional grounds, as in Lathrop *et al.*, that the dimensionless torque G should vary as $G \propto Re^2$ in the asymptotic range of Reynolds number. The measurements of Lathrop *et al.* , further refined by Lewis and Swinney[121], demonstrate that the torque in Taylor-Couette flow has no single scaling exponent even at high Re. Whether we should expect this in the spherical geometry is not obvious, but our confounding errors and limited range of Re mean that it is not worthwhile to investigate this. We use a simpler model and fit a power law for the torque with the outer sphere stationary. The power law fit is shown in Fig. 4.7 for a range of Re accessible in this experiment, exhibiting a $Re^{1.89}$

dependence.

At lower rotation rates, the measurement is significantly confounded by the bearing and seal torque. A constant drag torque, $G_d = 3.3 \times 10^{10}$, is subtracted from the data before the fit is carried out. This drag is based on measurements with the sphere emptied of fluid[11], and is fairly constant with rotation rate. The error bars on Fig. 4.7 are constant error bounds of approximately 1.1×10^{10} based on the maximum observed range of seal fluctuation in several repeated trials with the spheres empty. Typically, the medium-term fluctuations over a day's run, especially for a single continuous ramp, are significantly smaller than this, but systematic day-to-day offsets of this magnitude are, unfortunately, common. Curiously, the typical change from day to day is fairly well described by a *discrete* change by this amount, possibly due to varying engagement by one of the two lip seals. Therefore, we choose between 3.3×10^{10} and. 2.2×10^{10} as the constant drag removed. To be concrete, we model the effect of the confounding drag on the dimensionless torque as

$$G = G_{meas} - \begin{cases} 2.2 \times 10^{10} \\ \\ 3.3 \times 10^{10} \end{cases} \tag{4.6}$$

with the choice made for better collapse. There are other minor fluctuations which cause a good deal of scatter in the data at low speeds, but cannot fit a constant to deduce the drag, as we do not know the scaling exponent independently. However, we choose to correct for the major component of the drag, and use the restricted model of Eq. 4.6 based on repeated observations that the mean drag is close to one of the values listed, fluctuating only slightly about one or the other.

[11] The air torque is assumed to be negligible.

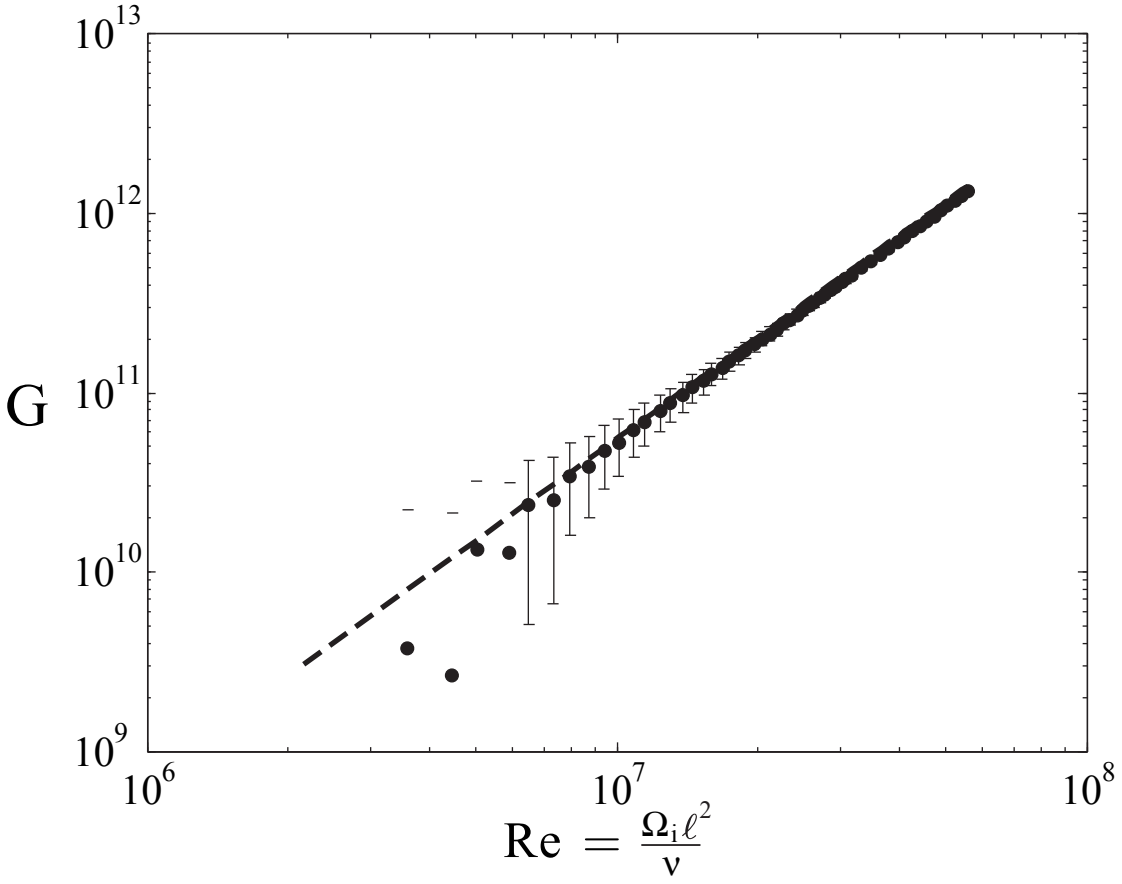

Fig. 4.7: Dimensionless torque, G vs. Reynolds number Re. Based on measurements with the sphere empty, a constant drag torque of $G_d = 3.3 \times 10^{10}$ has been subtracted from the data. Error bars are $\pm 1.1 \times 10^{10}$ based on the worst case variation implied by Eq. 4.6. The model fit is $G = 0.003 Re^{1.89}$. We will use this model to express the Re-dependence of the torque in the rotating states, and so we define $G_\infty(Re) = 0.003 Re^{1.89}$. This is the predicted torque as a function of Reynolds number when $\Omega_o = 0$, in other words, when $Ro = \infty$.

The torque fit in Fig. 4.7 will be used later to normalize the torque measured with both spheres rotating. In some subsequent discussion when both spheres revolve, the Reynolds number is calculated with Eq. 4.3 and the predicted torque,

$$G_\infty = 0.003 Re^{1.89}, \tag{4.7}$$

is used to normalize the measured torque. The quantity G/G_∞[12] seems to be dominated by the Ro-dependence of the torque, and provides a useful summary of the torque results. This will be discussed in detail in Chapter 6.

4.2.3 Summary

The torque as a function of Re of Fig. 4.7 is ultimately similar to other turbulent shear flow experiments. In terms of the torque and the wall shear stress fluctuations of Fig. 4.5, turbulent spherical Couette flow when only the inner sphere revolves is not much different, to our measurement capabilities, than turbulent Taylor-Couette flow reported by Lathrop *et al.* [120] and Lewis *et al.* [121]. However, the turbulence contains large-scale, unusually slow but energetic wave motions. These are reasonably coherent in the sense that they exhibit peaks in temporal autocorrelation (frequency spectra) and spatial cross correlation, but nevertheless are significantly fluctuating and should be considered part of the overall inhomogeneous turbulence.

[12] For experiments that do not use multiple fluids to extend the range of Re, this is the ratio of the dimensional torques.

4.3 $Ro < 0$, Outer Sphere Rotating

4.3.1 Flow Properties

This section will be somewhat brief compared to Section 4.2, as the inertial mode states presented here are more well understood, reported earlier by Kelley and collaborators [12, 14, 15]. However, the broader conclusions of Chapter 6 will discuss this, so it is worth mentioning some properties of the turbulent flow that we observe when $Ro < 0$.

A broad view of the observations for $-4.2 < Ro < 0$ is provided in the wall pressure spectrogram of Fig. 4.8. Each vertical line is a power spectrum, with frequency normalized by the outer sphere rotation speed. The logarithmic color scale represents the magnitude of the power spectral density. Significant strong peaks are noted over ranges of Ro and many can be identified as inertial modes. The identification in Fig. 4.8 of the annotated peaks (b), (c), (d), (e) and (f) with particular inertial modes similar to those in the full sphere is based partially on observation of modes with these frequencies in Kelley *et al.*, 2007 [14]. The nature and role of the low, broad energy peak around the frequency of (a) for large ranges of Ro are not known. We will not provide a thorough comparison of these observations with the observations and predictions of Kelley *et al.*. More solid identification of the observed modes by azimuthal wavenumber should be possible using the wall shear array of Sec. 3.5.4. However, detail regarding the mechanism of excitation of these modes and the verification that they are identical to those seen before is outside the focus of this dissertation. More information on inertial modes, including

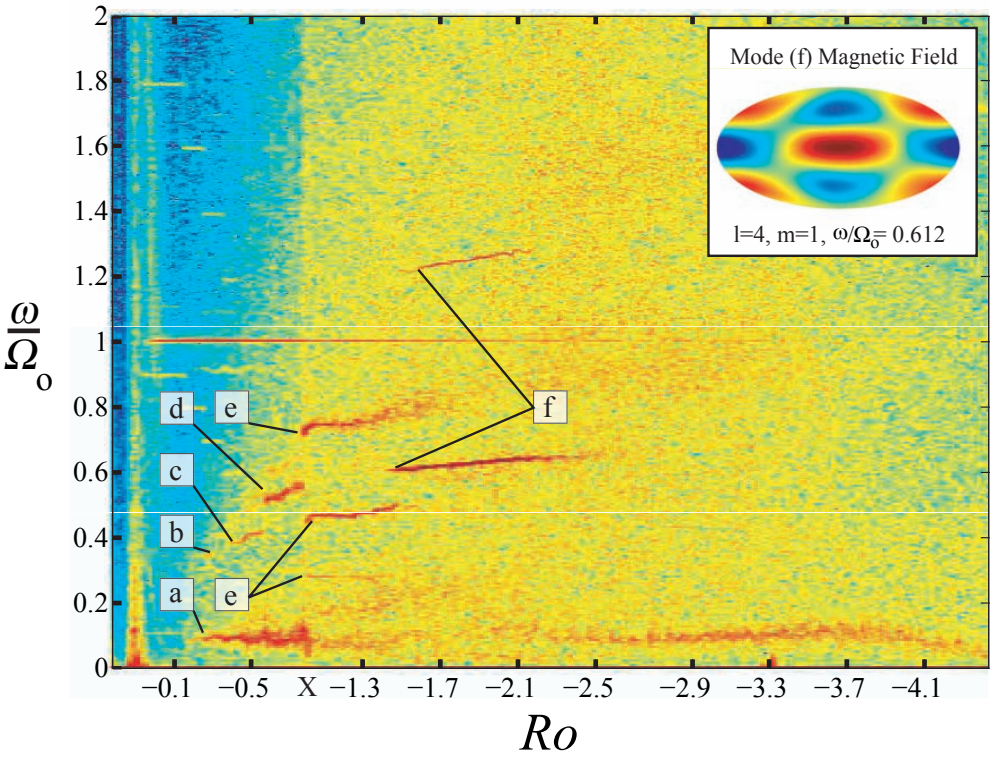

Fig. 4.8: Spectrogram from a wall pressure sensor at 23.5° colatitude as a function of Ro for $Ro < 0$, $E = 1.6 \times 10^{-7}$, showing inertial mode states with annotations. A series of inertial mode states are excited. The frequencies are as follows. The broad, persistent peak, (a), is at 0.083 Ω_o. At (b), a small region of 0.333 Ω_o is probably (6, 5, 0.333). At (c), initial frequency of 0.38 Ω_o is likely (6, 3, 0.378). Peak (d), starting at 0.51 Ω_o is probably (4, 3, 0.500). Peaks (e) are an interesting case. The middle-frequency peak is probably (6, 1, 0.44). However, the peaks at 0.27 Ω_o and 0.75 Ω_o are previously unreported, and the three frequencies form an approximately resonant triad. Peaks (f), at 0.61 Ω_o and 1.22 Ω_o are probably (4, 1, 0.612) and its second harmonic, which could excite the mode (4, 2, 1.23). The discontinuity in the spectrum, especially evident at higher frequencies and marked with an "X," is due to a gap of inaccessible Ro. This covers approximately $-1.2 < Ro < -0.7$ where the inner sphere motor cannot revolve slowly enough. The inset shows a Mollweide projection of the induced magnetic field from the 60 cm experiment for the (4, 1, 0.612) mode, (f), showing how much the simple spatial pattern dominates the induced field.

mode identification, can be found in the dissertation of S.A. Triana.

Here we are concerned more with the properties of the turbulence associated with these states with strong inertial modes. As can be seen from Fig. 4.8, significant broadband fluctuations are observed. The equivalent spectrogram of the magnetic induction presented by Kelley *et al.* [14] shows a banded structure of the broadband fluctuations, coexisting with the strong inertial mode. However, the broadband part of the fluctuation spectra here is simple (see also Fig. 4.9). It may be that the banding observed by Kelley *et al.* is not a property of the turbulence itself. Instead, it may be a characteristic of the magnetic induction by this particular velocity field. Two-dimensional motions do not cause any induced field with a uniform, axial applied field, so low-frequency inertial modes and other nearly two-dimensional motions will exhibit weak induction. The existence of broad bands higher than 2 Ω_o in the spectra of Kelley *et al.* are due to frequency shifts, $\omega_{lab} = \omega + m\ \Omega_o$ of the azimuthal wavenumber spectrum because the magnetic sensors are in the lab frame. It seems likely that much of the structured appearance of the broadband magnetic field fluctuations reported previously is because of particulars of the induction and the measurement frame of reference. Nevertheless, here we present point measurements of what is undoubtedly extremely inhomogeneous turbulence. It may be that banded spectra are associated with the smaller scales of turbulent flow nearer the equator, for example, far from our sensors' location.

We can see the broadband turbulent power spectrum more clearly in Fig. 4.9, a power spectrum of the wall shear stress for $Ro = -1.8$. The strong peaks include the mode (4, 1, 0.612) and its second harmonic, as in Fig. 4.8 (f). It also appears

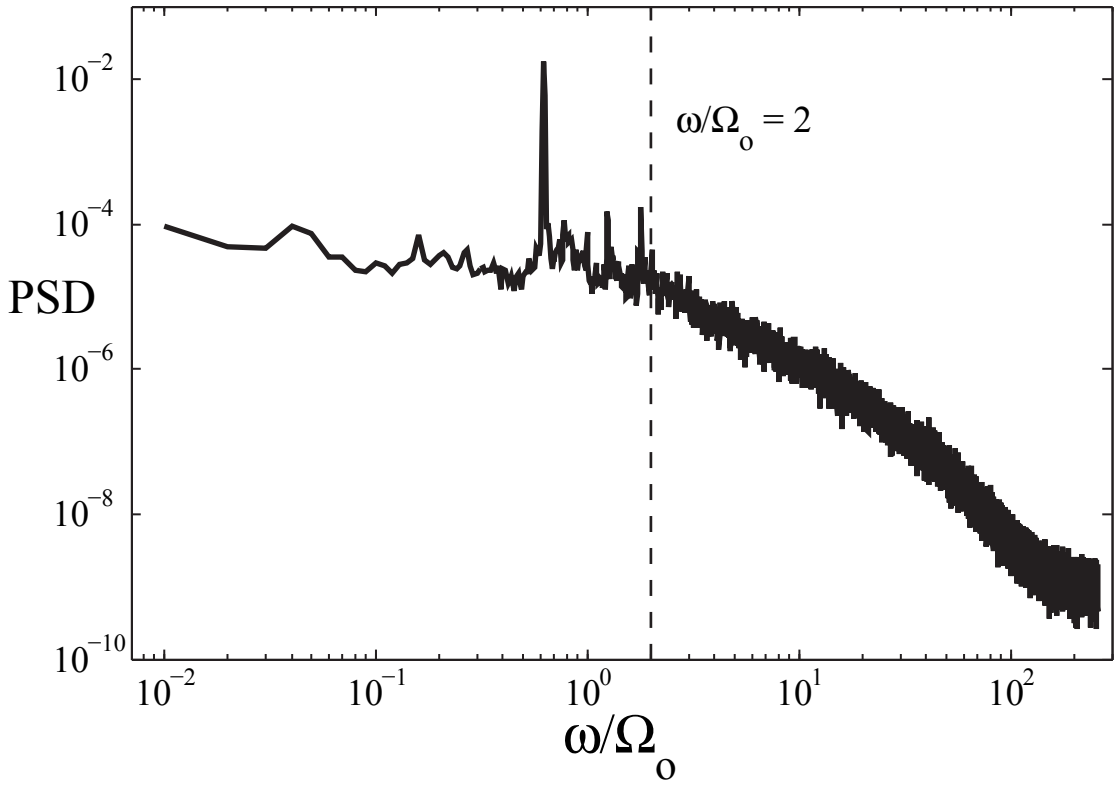

Fig. 4.9: Wall shear stress power spectrum for $Ro = -1.8$, $E = 1.6 \times 10^{-7}$, with strong inertial mode $l = 4$,$m = 1$,$\omega/\Omega_o = 0.612$. The measured frequency is slightly higher, $0.618\Omega_o$, as is typical as Ro increases above onset. Unlike the turbulent wave of Fig. 4.2, the fractional bandwidth of the inertial mode peak is extremely narrow. The inertial mode power is approximately 400 times higher than the turbulent background. It is strong, but significantly less so than the relative power of the modes in the magnetic observations of Kelley and collaborators [12, 14, 15]. It is not thought that this is a deficiency in the power of the wave, but rather that the filtering of the turbulent fluctuations by the magnetic field emphasizes the large-scale inertial mode in the magnetic measurements. For reference, we include the maximum possible inertial mode frequency , 2 Ω_o, as a vertical dashed line. The spectrum is nearly flat below this frequency aside from the few strong peaks.

that the third harmonic is present in the wall shear stress data. The inertial mode peak is strong, approximately four hundred times the background turbulence level. This is not as strong as the relative strength reported by Kelley *et al.* who put the (4, 1, 0.612) mode nearly six thousand times stronger than the noise. However, this is likely due to the reduced strength of higher frequency magnetic fluctuations similar to Fig. 4.2. We therefore interpret this discrepancy not as a deficiency in the strength of the inertial mode, but rather that our wall shear stress sensor is significantly more sensitive to the turbulence than the induced field measurements are.

The turbulent fluctuations at the measurement location have considerable total power with respect to the mode. While the mode itself stands out significantly, it is narrow-band, and the range of energetic fluctuations is wide. The spectrum is almost flat below the inertial mode upper limit of 2 Ω_o. Figure 4.10 shows the probability distribution of wall shear stress fluctuations normalized by the mean wall shear. The low shear and high shear tails are similar to those of Fig. 4.5, but the weak bimodality is the signature of the wave.

A time series of the wall shear stress for $Ro = -1.8$ is shown in Fig. 4.11. These results, Fig. 4.8 through Fig. 4.11, establish that the inertial modes coexist with even stronger turbulence than could be deduced from the measurements of Kelley *et al.*. Furthermore, we note signs of inertial mode nonlinearity, for example, in the second harmonic of Fig. 4.8 (f) and the resonant triad of Fig. 4.8 (e). The turbulence is probably extremely inhomogeneous, and without measurements throughout the bulk fluid, we cannot quantify the total energy in the turbulence vs. that in the

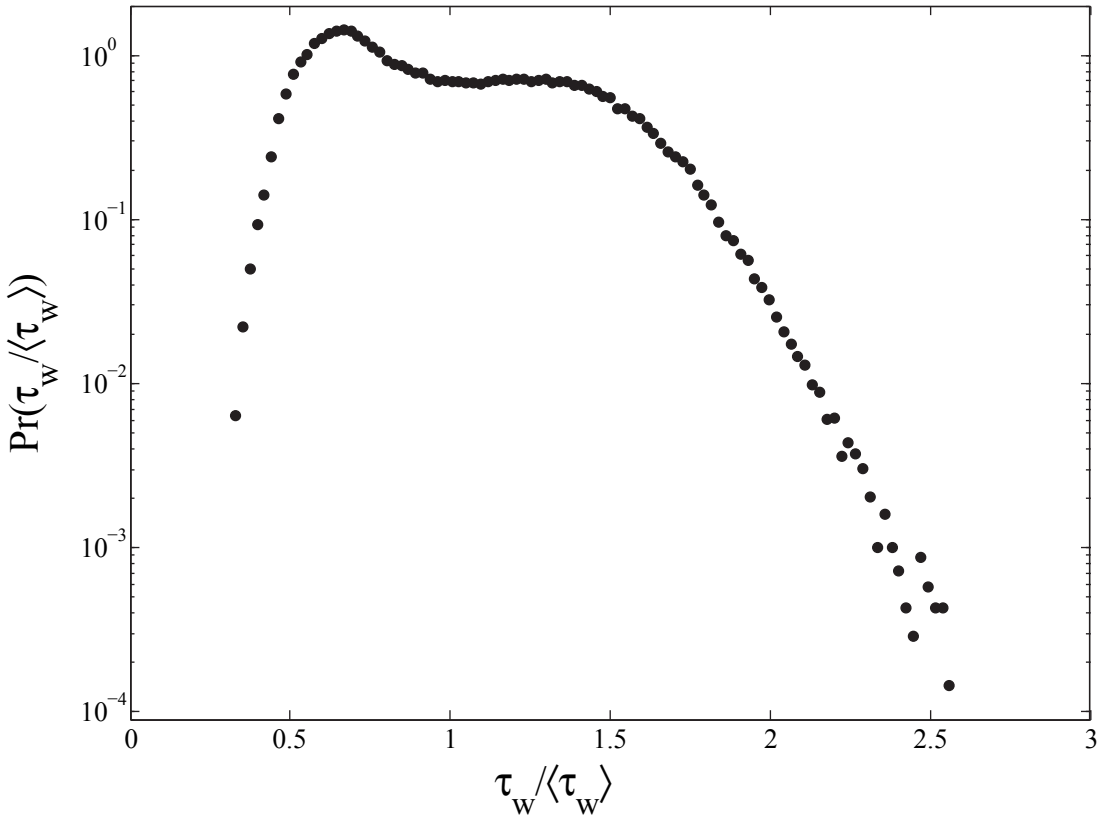

Fig. 4.10: Wall shear stress probability distribution for $Ro = -1.8$, $E = 1.6 \times 10^{-7}$ normalized by its mean value. Compare with Fig. 4.5. In this case, the strong, narrow inertial mode leaves its signature with a bimodal distribution of wall shear stress. The upper and lower tails of the distribution seem to have the same log-normal character as that in Fig. 4.5.

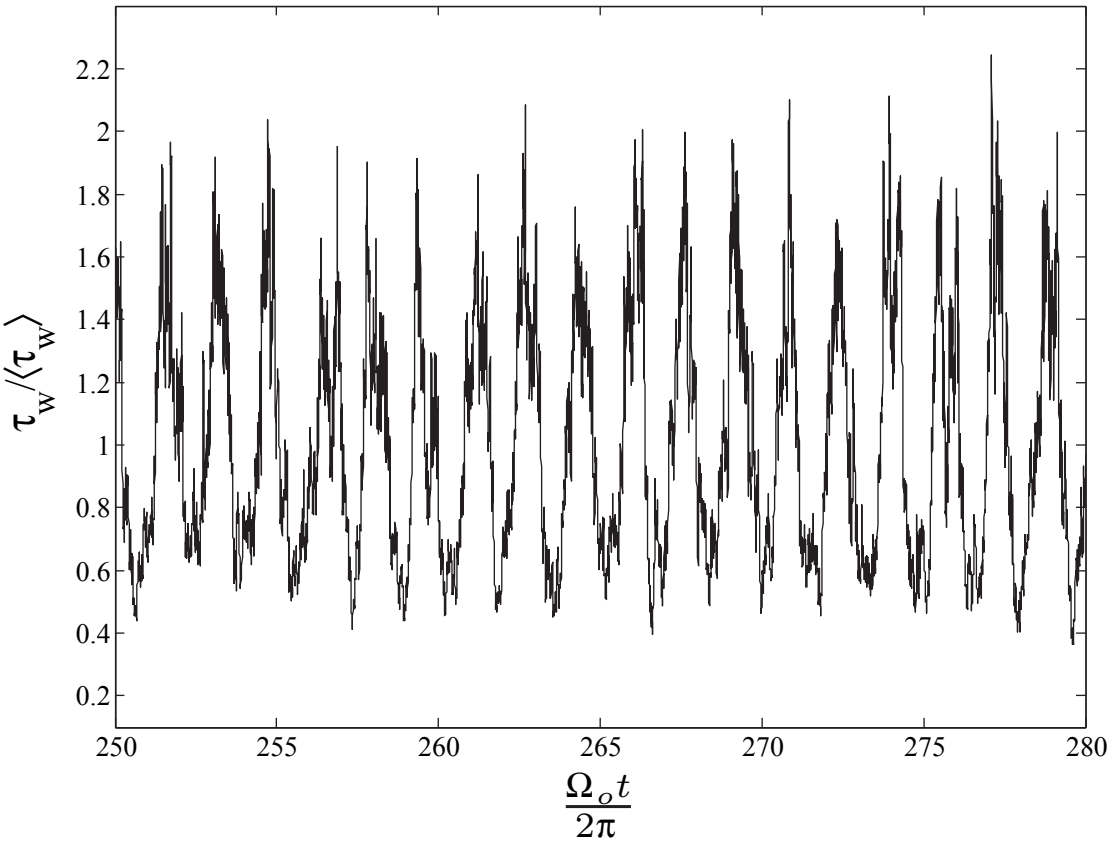

Fig. 4.11: Time series of the wall shear stress at $Ro = -1.8$,$E = 1.6 \times 10^{-7}$, normalized by its mean value. The strong oscillation is an inertial mode, $l = 4$,$m = 1$,$\omega/\Omega_o = 0.612$. Turbulent fluctuations are more evident here than in the magnetic measurements of Kelley *et al.* [14].

inertial mode, nor can we rule out that the wave lives mostly in a quiet region of the flow. Nevertheless, we establish that there is an even more turbulent background than is apparent from the magnetic data of Kelley *et al.*, suggesting that inertial modes are fairly robust to the presence of other turbulence.

4.3.2 Torque

We conclude this section with a brief mention of the torque, which we will revisit as part of the broad Ro dependence in Chapter 6. Figure 4.12 shows the dimensionless torque on the inner sphere as a function of Rossby number. A constant seal drag has been subtracted. In this case the constant drag subtracted is less than that of Fig. 4.7, at $G_d = 2.2 \times 10^{10}$, as discussed in Sec. 4.2. The gap around $Ro = -1$ is due to the fact that the inner sphere motor can not be stably rotated slowly in the range of about $-1.2 < Ro < -0.8$, where $Ro = -1$ corresponds to $\Omega_i = 0$. This gap is not explicitly shown in Fig. 4.8, but it is the reason for the spectral discontinuity marked with an "X" there.

As Ro is changed for fixed E, as in this plot, both Ro and Re vary. The resultant scaling is dominated by the Re dependence, and is similar to that for the outer sphere stationary, close to $Re^2 = (Ro/E)^2$. Residual dependence on Ro is pictured in the inset of Fig. 4.12, where the torque on the inner sphere is divided by the predicted value at the same Re, if the outer sphere were stationary[13]. This compensated torque plot makes it easier to see the small effect of the inertial mode transitions. The transition from the triad Fig. 4.8 (e) to the mode Fig 4.8(f) can

[13] G_∞, see Eq.4.7

be seen at $Ro \sim -1.5$ and the cessation of the mode Fig. 4.8(f) can just barely be detected in G/G_∞ at $Ro \sim -2.4$.

The compensated inset of Fig. 4.12 shows that the Re-dependence of Eq. 4.7 overpredicts the torque at small negative Ro, rising slowly toward agreement as the magnitude of Ro is increased. It is not known if the large change in the apparent value of G/G_∞ across $Ro = -1$ is a fluid effect or an effect of directional seal wear leading to direction-dependent drag. The much quieter broadband spectrum for low negative Ro in Fig. 4.8 does suggest the turbulent fluctuations are much weaker overall, so perhaps the drop is due to a real flow transition. The inertial mode excitation smoothly varies across $Ro = -1$, but it is possible that other properties of the turbulence and angular momentum transport do not.

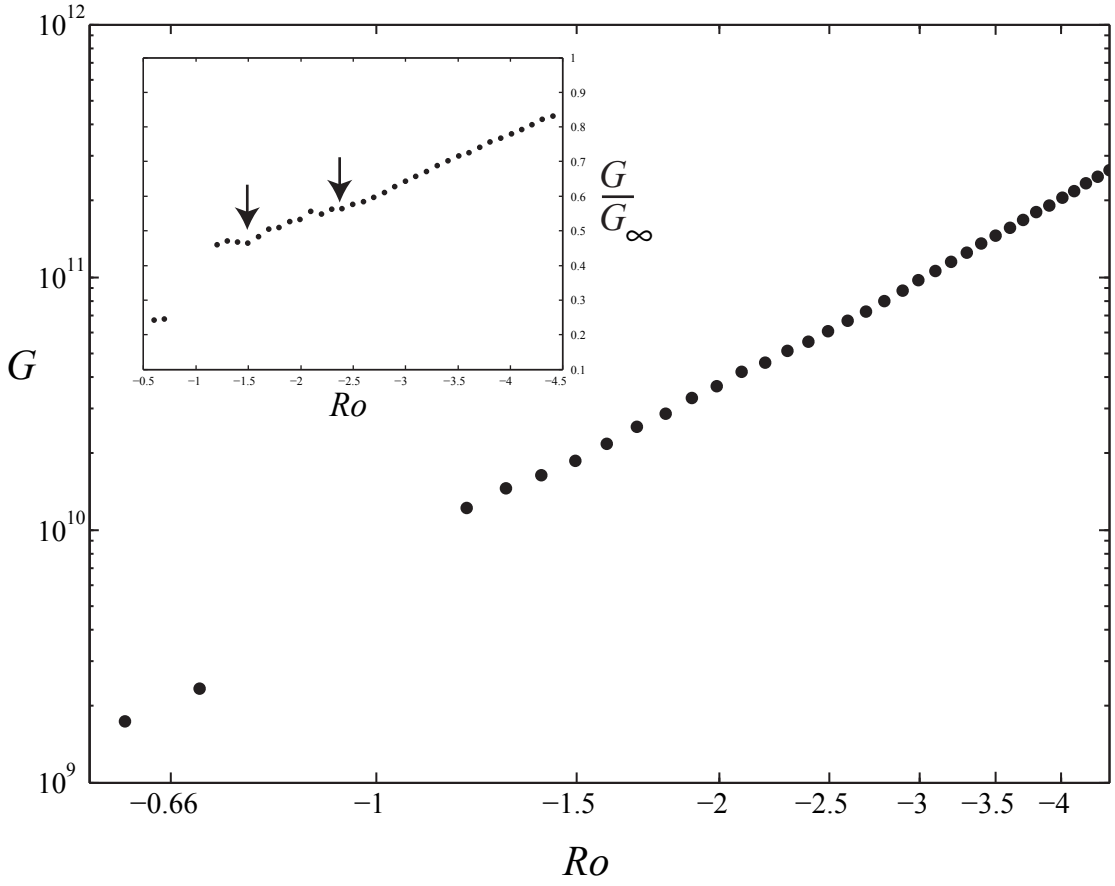

Fig. 4.12: Dimensionless torque vs Rossby number, $E = 1.6 \times 10^{-7}$. Despite the inertial mode flow transitions evident in Fig. 4.8, there is a small effect on the torque, which varies roughly quadratically with Ro. As Ro is changed, $Re = Ro/E$ also changes. The inset shows G divided by the value it would have at the same Reynolds number with the outer sphere stationary. This compensated torque plot exposes the residual dependence of G on Ro more clearly, eliminating the large Re dependence typical of a turbulent shear flow. The arrows denote two inertial mode state changes. It appears that a slight drop in the compensated torque can be seen for two mode transitions.

4.4 $Ro > 0$, Outer Sphere Rotating

4.4.1 Narrow Range, $Ro < 5$

The flows in this section, those when the inner sphere super-rotates, have been the main focus of the experimental campaign in water. Like the case when $Ro < 0$, a number of different flow states may be identified in ranges of Ro, with boundaries that depend weakly on the Reynolds number[14] if at all. These flow states are also marked by strong wave motions. Unlike the negative Rossby states, however, each state transition involves an general re-organization of the turbulent flow, and some of the wave motions are much more like that of Sec. 4.2, deeply modulated by low frequency fluctuations. The spectrogram of Fig. 4.13 provides an overview of the fluctuation spectra for $Ro < 4.5$. Turbulent flow transitions are evident near $Ro = 0.5$, $Ro = 1$, $Ro = 1.8$ and $Ro = 3.3$. In some regions of Ro, like the region discussed in detail in Chapter 5, the flow exhibits bistable behavior, transitioning between each of the turbulent states observed adjacent to the bistable range and spending a long time in each.

The mean torque and the size and character of temporal torque fluctuations are very different in each identified flow state, unlike the case when $Ro < 0$. Large, low frequency temporal fluctuations in the torque are common for the states identified for positive Rossby number. In the bi-stable ranges the torque demanded by one turbulent state is considerably higher than the torque demanded by the other. Fig. 4.14 shows the dependence of the torque on Rossby number for fixed Ekman

[14] Or, equivalently, the Ekman number E.

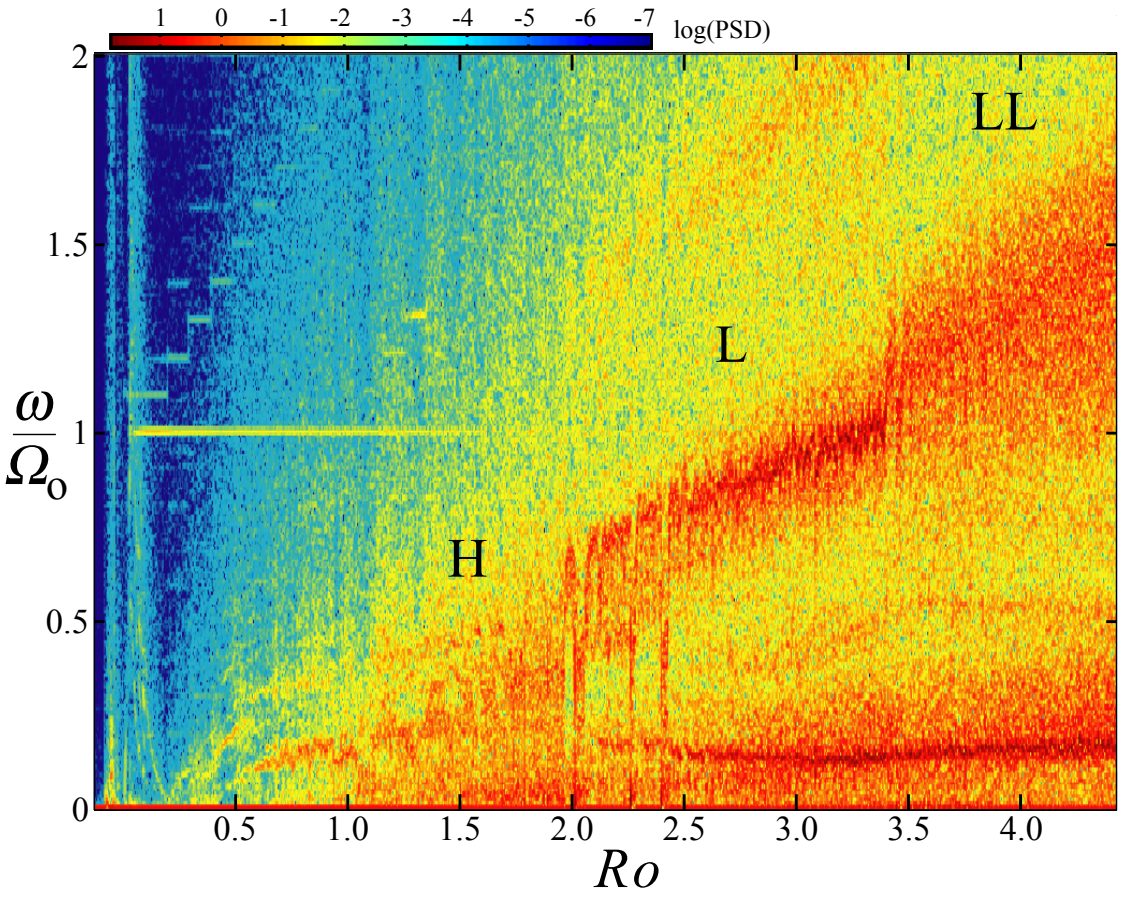

Fig. 4.13: Pressure spectrogram, $E = 1.6\times10^{-7}$. Several turbulent transitions are noted. It is clear that the turbulence changes character at each transition, and that the wave states here are mostly broadband compared to those of Fig. 4.8. This spectrogram will be discussed in more detail in Chapter 5.

number. Like Fig. 4.12, the inset shows the compensated torque, G/G_∞. The ranges of Ro where this relation is not single-valued are those where the flow is bistable. Long enough observation times here expose flow transitions between the states that appear on either side of the overlapping range. The torque in these regions exhibits a bimodal probability distribution[15], and when this is the case, the torque is reported as the two modes of the distribution instead of the mean. Because of the transitions, neither the torque nor the mean power dissipation[16] are a monotonically increasing function as Ro is increased.

Throughout the rest of the dissertation, we adopt labels for the states on either side of the most pronounced torque transitions. The high torque state, H, exists alone from $Ro = 1$ to $Ro = 1.8$. The low torque state, L, becomes possible around $Ro = 1.8$ and exists alone until approximately $Ro = 3$, where a subsequently lower torque state becomes possible, the LL state. Unlike the $Ro < 0$ inertial mode state transitions, the factor G/G_∞ varies a great deal between the two adjacent states. The H state torque for a given Re is 1.4-1.7 times that of the L state torque in the transition region. The boundaries of onset are suggested by Figs. 4.13 and 4.14, but precise determination of boundaries requires acquisition of more data than time allowed[17]. A manual division of the torque into state based on qualitative identification of the states results in a somewhat different set of state boundaries. Figure 5.2 in the next chapter is perhaps more suggestive of the points of bifurcation where

[15] Skip ahead to the next chapter, Fig. 5.4, for an example.

[16] The torque on the inner sphere and the speeds of the spheres are sufficient to know the power input.

[17] A much faster experiment at the same dimensionless parameters would make this possible.

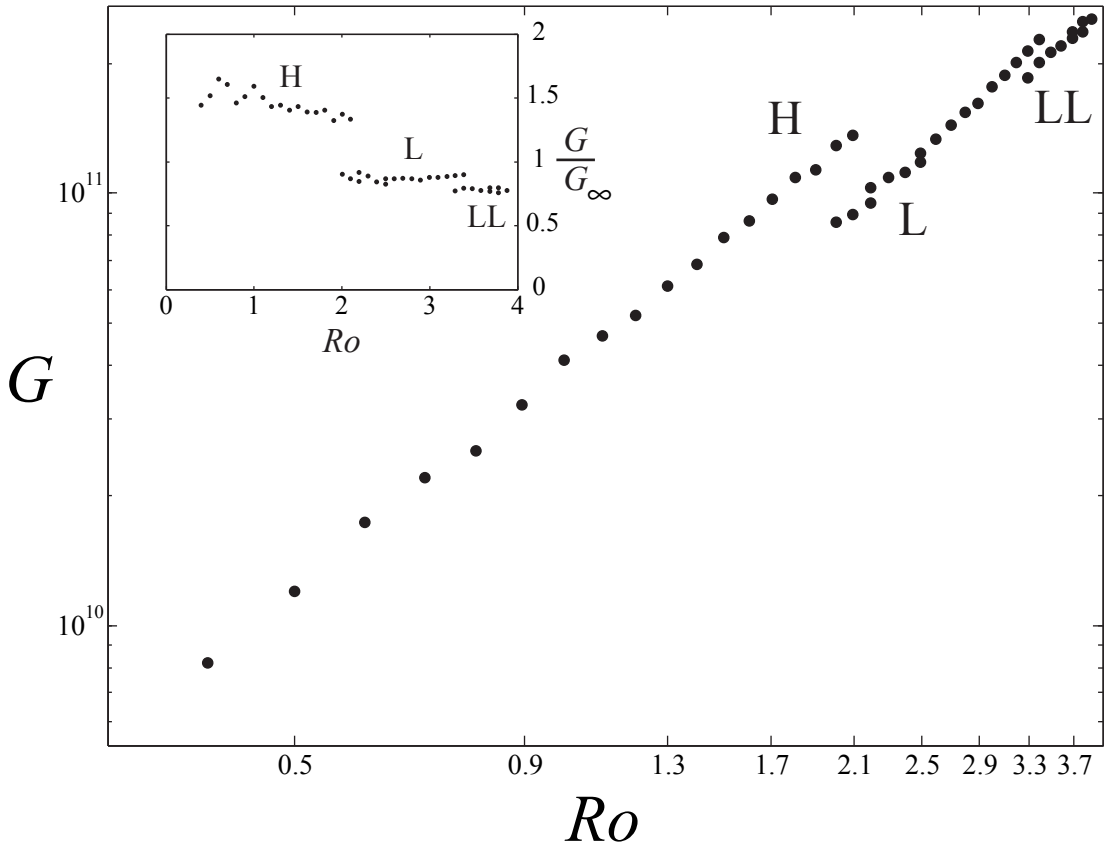

Fig. 4.14: Torque as a function of Rossby, $E = 1.6 \times 10^{-7}$, with compensated torque inset. Where bimodal torque distributions are noted, the torque is split into two branches corresponding to the two modes. Overlapping regions are associated with intermittent transitions between the two turbulent flow states adjacent to the switching region.

new states come in, though it is not as objective.

More thorough characterization of the H and L states are the topic of Chapter 5, but we will state an additional conclusion here to frame the broader picture of $Ro > 0$ state transitions. Fig. 4.15 shows time series of the dimensionless torque in the H/L transition regime, at $Ro = 2.13$, as well as the measured zonal[18] ve-

[18] Azimuthal motions that are invariant in the vertical coordinate, which is a strong assumption. Often used in the literature on rotating flows.

locity, normalized by the outer sphere tangential velocity[19] and low pass filtered with a cutoff frequency comparable to that used to filter mechanical noise out of the torque. The bistablity and slow fluctuations in the zonal velocity are clearly anti-correlated with the torque on the inner sphere. As we will see later in this section, this is typical of all of the turbulent states for $Ro > 0$ that correlate with the flow fluctuations at all. This anti-correlation seems to involve zonal-flow induced transport barriers to angular momentum. Because of this, the velocities (and wall shear stress) at the measurement location increase in the higher shear, lower torque state, even as the torque[20] decreases. In Chapter 5 we discuss and interpret these zonal flow observations more fully.

4.4.2 Wide View, $0 < Ro < 62$

We have performed some experiments to explore the turbulent flow states out to high positive Rossby number. In doing so, we have identified three more states on the basis of flow spectra and torque fluctuations. The distinctions drawn here are more qualitative. Some transitions are extremely subtle, and the transitions Ro higher than approximately[21] $Ro = 5$ do not show long residence times in identifiable adjacent states. It is only the H/L and L/LL transitions that seem to be clearly qualitatively bistable, and the transitions for higher Ro are more smeared out and gradual. However, up to $Ro = 15$, the system still exhibits torque that fluctuates in

[19] Meaning that it can be interpreted as the local Rossby number of the mean zonal flow, as mentioned in Table 2.1.

[20] And probably the total power dissipation.

[21] The end of the LL state range.

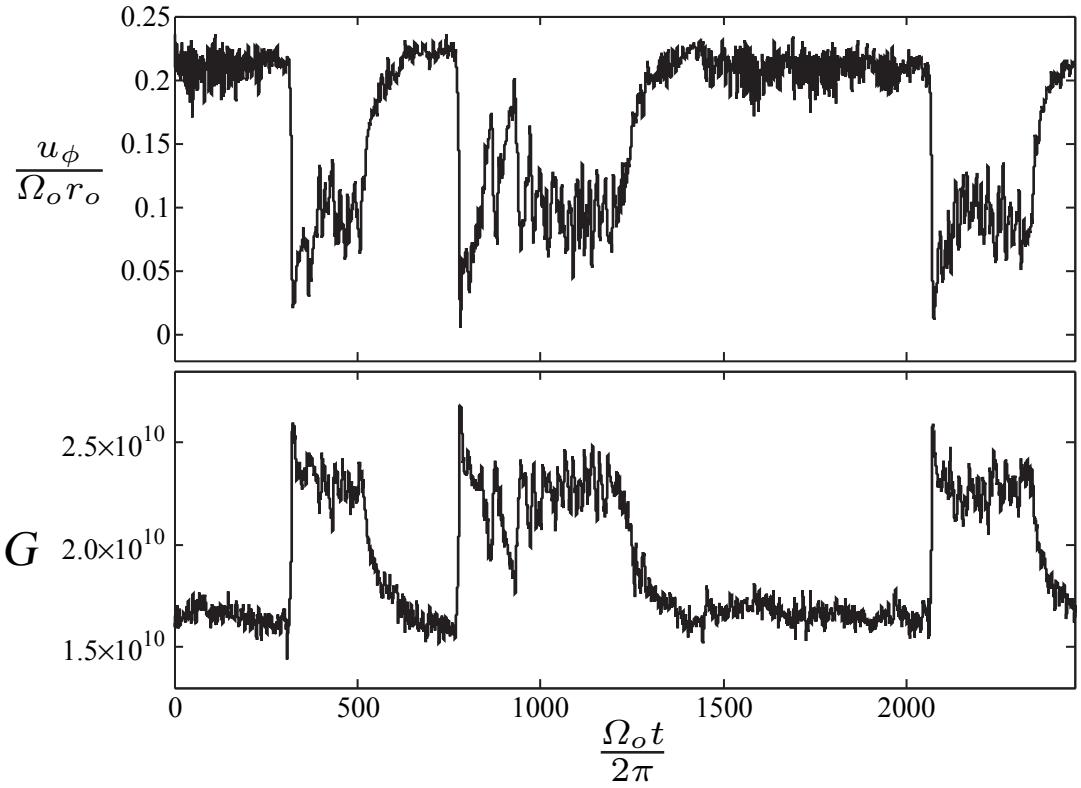

Fig. 4.15: Torque and low pass filtered velocity time series, $Ro = 2.13$, $E = 5.3 \times 10^{-7}$, 10 cm from the wall at 60 cm cylindrical radius. The onset of the high torque state involves a rapid crash of the mean zonal velocity with a corresponding abrupt rise of the torque. The return to the low torque involves an exponential decay of the inner sphere torque associated with spin-up of the mean zonal velocity. The torque fluctuations are anti-correlated with the slow velocity fluctuations.

time in a way that is correlated strongly with the flow measurements. Wall shear stress frequency spectra over the range $1.8 < Ro < 62$ are depicted in Fig. 4.16, with six states labeled. In addition to the H, L, and LL states, we identify three more, B, Q, and E, and we will briefly discuss their characteristics below.

The L to LL state transition is fairly subtle in the spectra, with the upper large frequency peak increasing in frequency and broadening. It is easier to see in Fig. 4.13. This transition exhibits torque bistability like the H to L transition does, with the LL state exhibiting about 10% lower torque than the high. Fig. 4.17 (a) shows the correlated torque and slow wall shear stress dynamics over 4500 outer sphere rotations. Like the H to L transition, the lower torque state is associated with higher mean wall shear stress at the measurement location, and the slow fluctuations of the wall shear stress and the torque are clearly anti-correlated. As in the H/L transition, the new state has lower torque, but higher wall shear stress at the measurement location[22].

The LL to B ("bursty" state) transition is fairly indistinct, and may probably be considered a modulation on the LL state. In Fig. 4.16, the spectrum for $Ro = 5.3$ shows the growth of a broad peak at a frequency of 0.34 Ω_o, in addition to the peaks at 0.18 Ω_o and 1.5 Ω_o shared[23] with the LL state spectrum at $Ro = 4.6$. The torque in of the B state exhibits positive-going torque bursts, shown for $Ro = 6.3$

[22] As a reminder, this is 60 cm cylindrical radius and even for the velocities, never more than 15 cm from the wall.

[23] The 0.18 Ω_o peak is a feature of most of the states for $Ro > 0$. It is likely to be a prograde inertial mode, (3, 1, -0.1766).

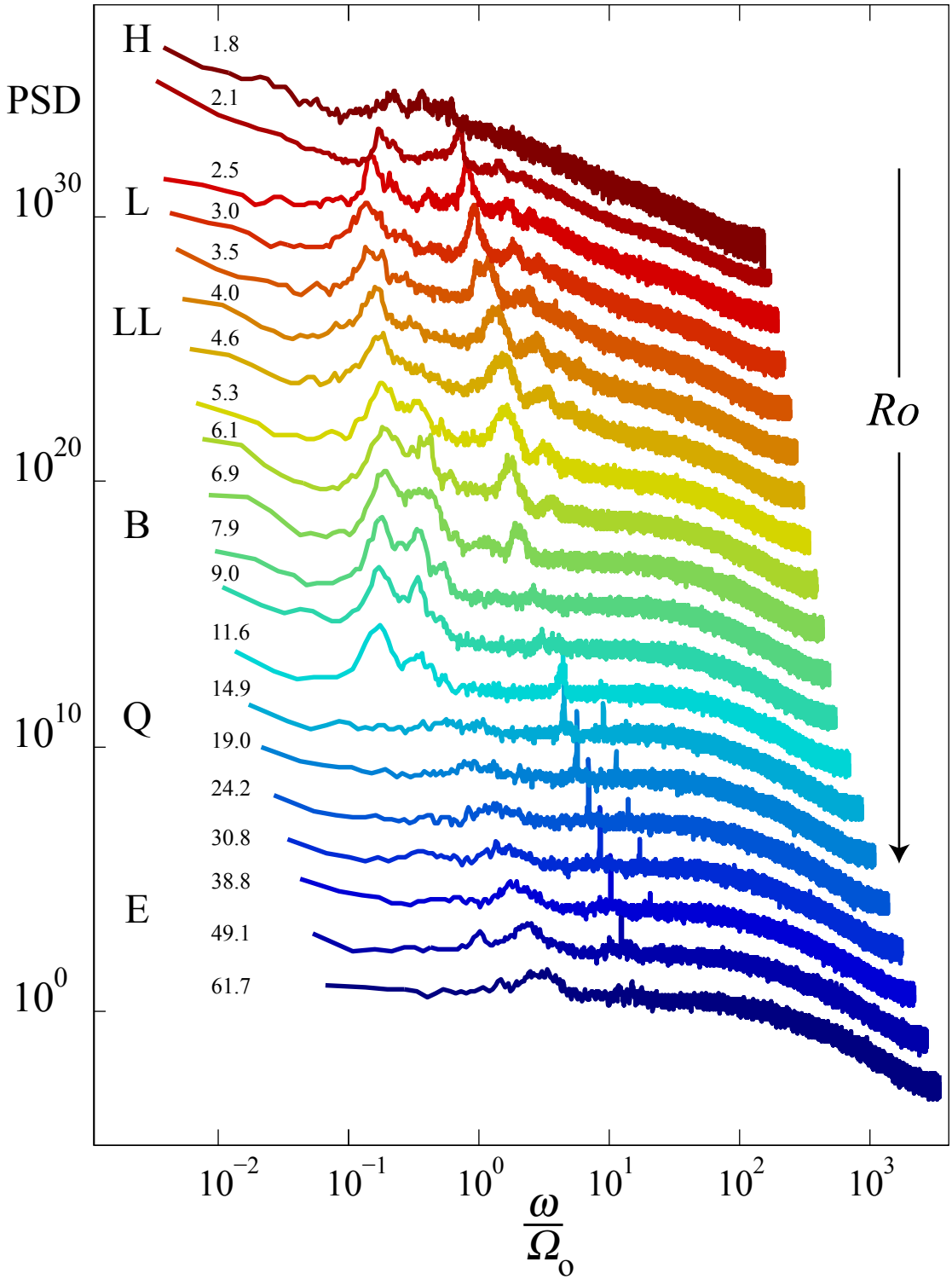

Fig. 4.16: Wall shear stress spectra vs. *Ro*, wide positive Rossby ramp. For clarity, spectra have been shifted vertically by successive multiplication by 50.

in Fig. 4.17 (b). At this Ro, the bursts come fairly rapidly, with a burst every 125 rotations of the outer sphere. The bursts are associated with peak torques 5%-10% higher than the lowest values. As with the lower states, low frequency wall shear stress fluctuations are anti-correlated with the torque. Higher torque implies lower wall shear stress at the measurement location[24]. The faster oscillations on the wall shear stress are the wave at 0.18 Ω_o, which at this outer sphere speed falls inside the low pass filter. The B state exists over a large range of Rossby number, approximately $5 < Ro < 15$.

The Q state starting[25] around $Ro = 14.9$ is associated with a disappearance of the waves in the spectra of Fig. 4.16. The Q ("quiet") state spectra are rather featureless, with the exception of a narrow peak that appears at $Ro = 14.9$ with a frequency of 4.5 Ω_o and moves up in frequency as Ro increases. In addition to the nearly featureless, broadband wall shear stress spectra, the temporal fluctuations in torque greatly diminish[26] and are not seen to correlate with fluid motion anymore.

By $Ro = 25$, a weak buildup of energy is seen in the $2 - 3$ Ω_o frequency range, at $Ro = 61.2$ it is centered around 3 Ω_o, which is consistent with the $Ro = \infty$ wave doppler shifted by the outer sphere speed. A reasonable picture of the temporal dynamics of the E state is that the flow fluctuations involve the same wave as that for $Ro = \infty$, but the sensors rotate slowly around that turbulent flow, sampling the dynamics from their slowly moving reference frame. However, though the frequency

[24] The reader is assured that the wall shear stress plots are not upside down.

[25] The data in this region is widely spaced, so this is not a good estimate of where the waves die out.

[26] To the point where the resolvable fluctuations are dominated by the seals, most likely.

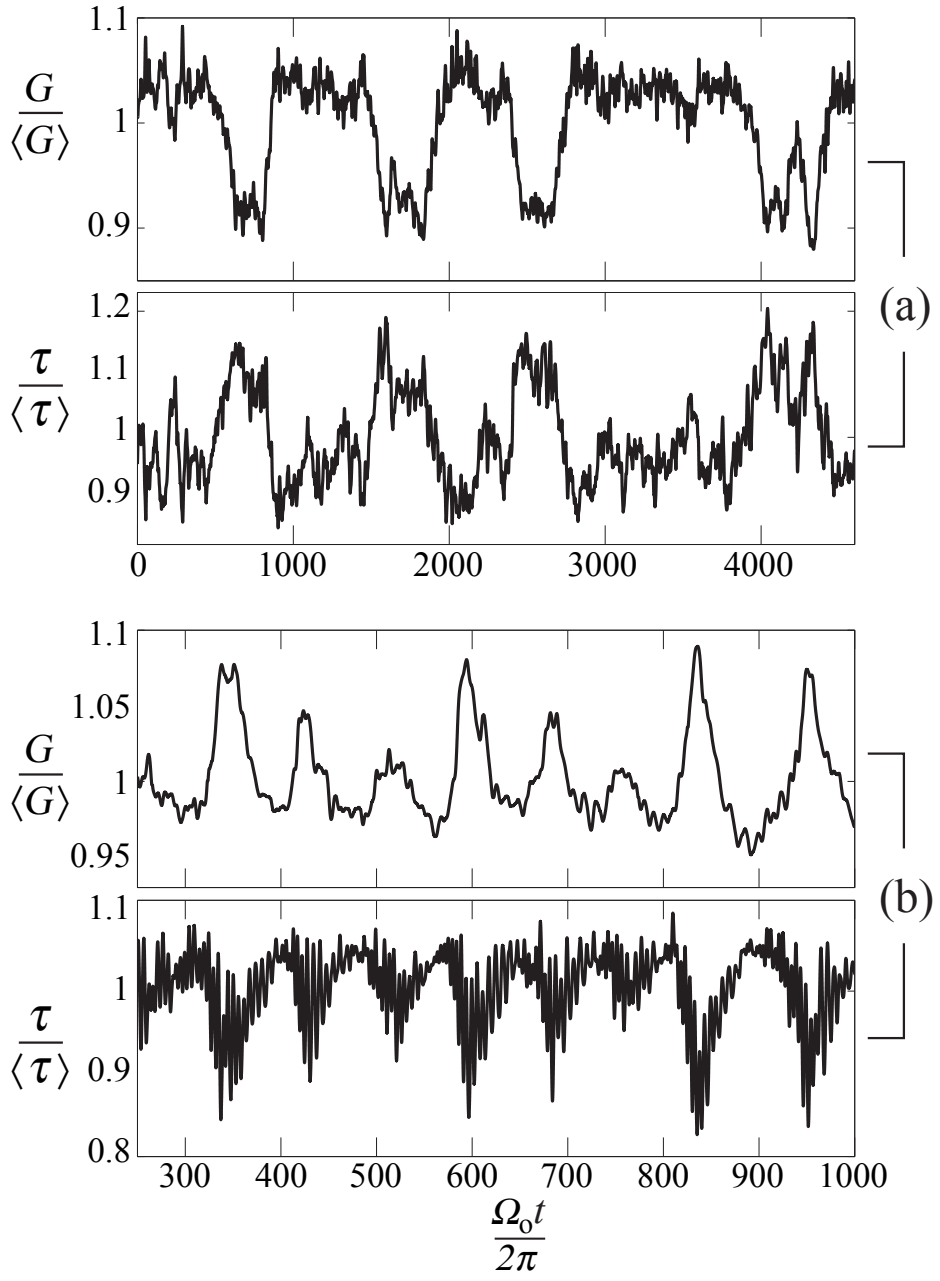

Fig. 4.17: Torque and wall shear time series, corroborating the anti-correlation of these two quantities. Time is measured in outer sphere revolutions. Part (a) is a time series of several L/LL state transitions at $Ro = 3.2$. The torque (top) and wall shear stress (bottom) normalized by their mean value. The same quantities are shown in (b) for the B state at $Ro = 6.3$. The wall shear stress has been low pass filtered the same as the torque.

is right, the wave is extremely weak compared to that in Fig. 4.2. Furthermore, as we will see in the next section, the torque in the E ("Ekman") state is not yet the same as that in the outer sphere stationary state. In other words, G/G_∞ has not yet returned to unity. We will present evidence in Chapter 6 that G/G_∞ may take on two different values, at least as a transient, in the E region. We attribute the weak wave and the lower relative torque in this region to the existence of an Ekman boundary layer on the outer sphere when it revolves that is not present when it is stationary. At the slowest outer sphere rotations we can achieve, approximately one revolution per 30 s, the Ekman number is still extremely low on the outer boundary, $E = 5 \times 10^{-6}$. This is considerably different from the situation with a nonrotating[27] outer boundary. It may be that Ekman suction and pumping on the outer boundary is responsible for the difference in the two states seen in the E region. It is not the case that $Ro \to 100$ can be identified with $Ro \to \infty$.

4.4.3 Wide $Ro > 0$ Torque and Shear

We will conclude this section with the overall view of the torque for large positive Ro. Figure 4.18 shows the compensated torque G/G_∞ for $1.8 < Ro < 62$. The six states discussed in the last section are labeled for reference. The general trend in the torque is that a global minimum in G/G_∞ is found between $Ro = 7$ and $Ro = 8$. The Rayleigh line, where the angular momenta of the fluid on the two

[27] Actually, the outer boundary rotates once per day with the Earth, with an Ekman number of about 10^{-2}, crossed with our axis according to our latitude. If this mattered, however, the 60 cm data, with an Ekman number an order of magnitude higher, would probably be different.

boundaries at the equator[28] are equal,

$$Ro_R = \frac{1}{\eta^2} - 1 = 7.16 \tag{4.8}$$

is shown as a vertical line. The global minimum of G/G_∞ is found near Ro_R. Above the Rayleigh line, inviscid, axisymmetric, axially invariant flows are unstable to axisymmetric overturning motions. It is not known to what extent the Rayleigh line is important in spherical Couette flow, as the fluid angular momentum varies along the boundaries. The relationship between the angular momentum distribution on the outer boundary and inner boundary does not lead to obvious predictions as it does for axisymmetric flows in axially invariant geometry, like the flow between two infinite rotating cylinders. This line is not particularly special in delineating state transitions. The flow on the Rayleigh line shows typical B-state bursting dynamics, which persist much higher and lower in Ro. It is possible that *local* centrifugal instability plays some role in the difference between states at low positive Ro and high positive Ro, but we have scant evidence for this. It may simply be an interesting coincidence that the global minimum of G/G_∞ is near the Rayleigh line.

The behavior below $Ro = 4$ is consistent with Fig. 4.14. As the LL state transitions in to the B state as Ro is further increased beyond $Ro = 4$, the compensated torque G/G_∞ falls until it reaches Ro_R, where there is a shallow, nearly flat minimum that shows B state dynamics. With further increase in Ro, G/G_∞ starts to rise and the Q state, free of waves, sets in. From the B/Q transition on, G/G_∞ rises toward unity.

[28] Or any equal latitude.

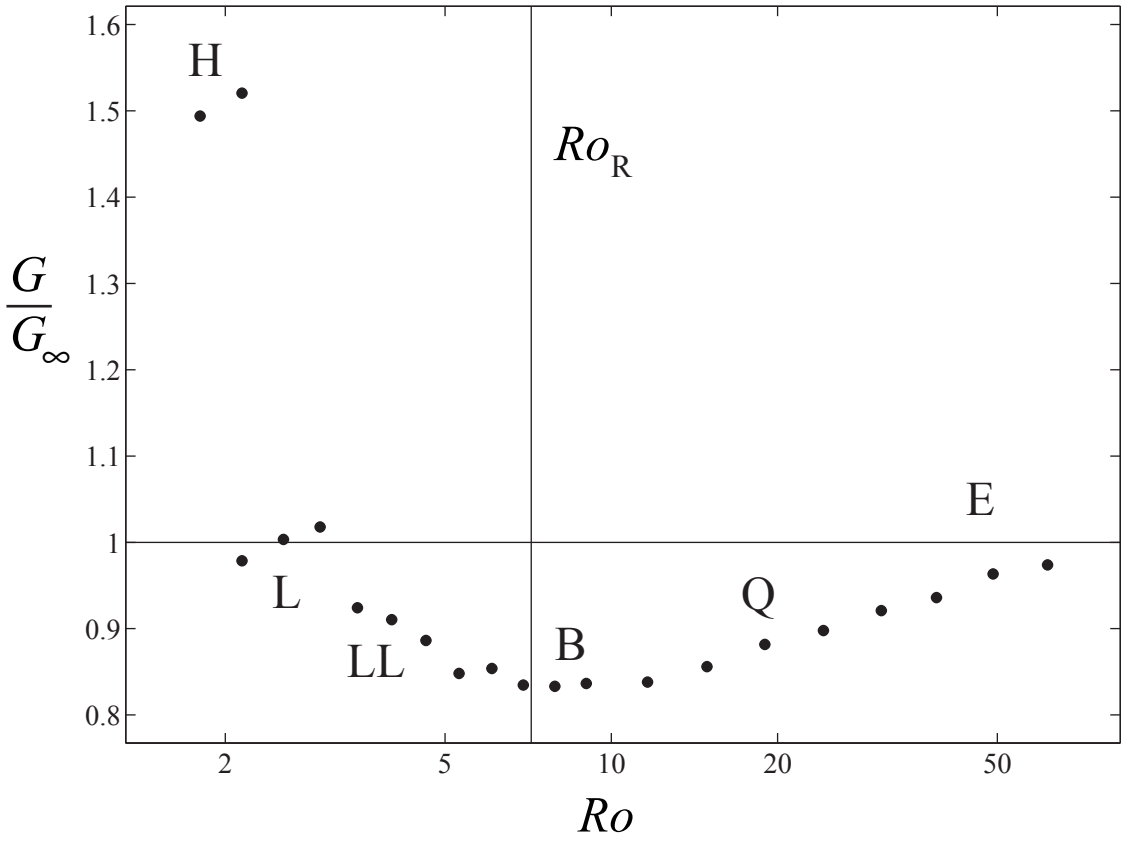

Fig. 4.18: Compensated torque vs. Ro for $1.8 < Ro < 62$ and $9.2 \times 10^{-8} < E < 2 \times 10^{-6}$. The Ro-axis is logarithmic. At $Ro = 61.2$, the outer sphere revolves once every 13 s. Note, however, that G/G_∞ has not yet reached unity. At $Ro = 61.2$ the flow still feels the outer boundary rotation. Ro_R denotes the Rayleigh line, which is where the angular momenta of the fluid at a given latitude on the boundaries are equal, and is close to the global minimum of G/G_∞ for $Ro > 0$. The rough area in which the six states identified in Fig. 4.16 exist are labeled here.

A broad view of the wall shear stress as a function of Ro is consistent with the observations of shear-torque anti-correlation discussed in Sec. 4.4.2. Figure 4.19 shows what we might call the "shear stress concentration factor." The wall shear stress sensors on the outer wall are calibrated in situ against the torque on the inner sphere, under the assumption of a particular[29] constant factor relating the local wall shear stress on the outer sphere to the torque on the inner,

$$\tau_\infty = CT_{inner}. \tag{4.9}$$

The quantity τ/τ_∞ concisely expresses how changing Ro affects the spatial distribution of the wall shear stress on the outer sphere. Ultimately, the torques on the two spheres must balance, and so the integrated torque contributed by the shear stress on the outer sphere must equal the torque on the inner sphere. However, at different Ro, the spatial distribution of the stress that integrates to a given total torque is not the same. Figure 4.19 depicts τ/τ_∞ for the wide range of positive Ro. This quantity peaks near Ro_R, where G/G_∞ has its minimum. Therefore, we see that the anti-correlation between wall shear stress and torque persists over the whole range of positive Ro, both in the temporal dynamics at a fixed Ro and also as Ro is varied. The lowest mean value of G/G_∞ coincides with the *largest* mean τ/τ_∞.

A possible general mechanism for the $Ro > 0$ states we have observed may involve angular momentum throttling by zonal[30]-flow induced transport barriers. The results here are consistent with larger and larger zonal circulations at the core

[29] Equation 5.7, which assumes wall shear stress falls off linearly with cylindrical radius.

[30] Or if not zonal, fast azimuthal circulations with a 3D dependence.

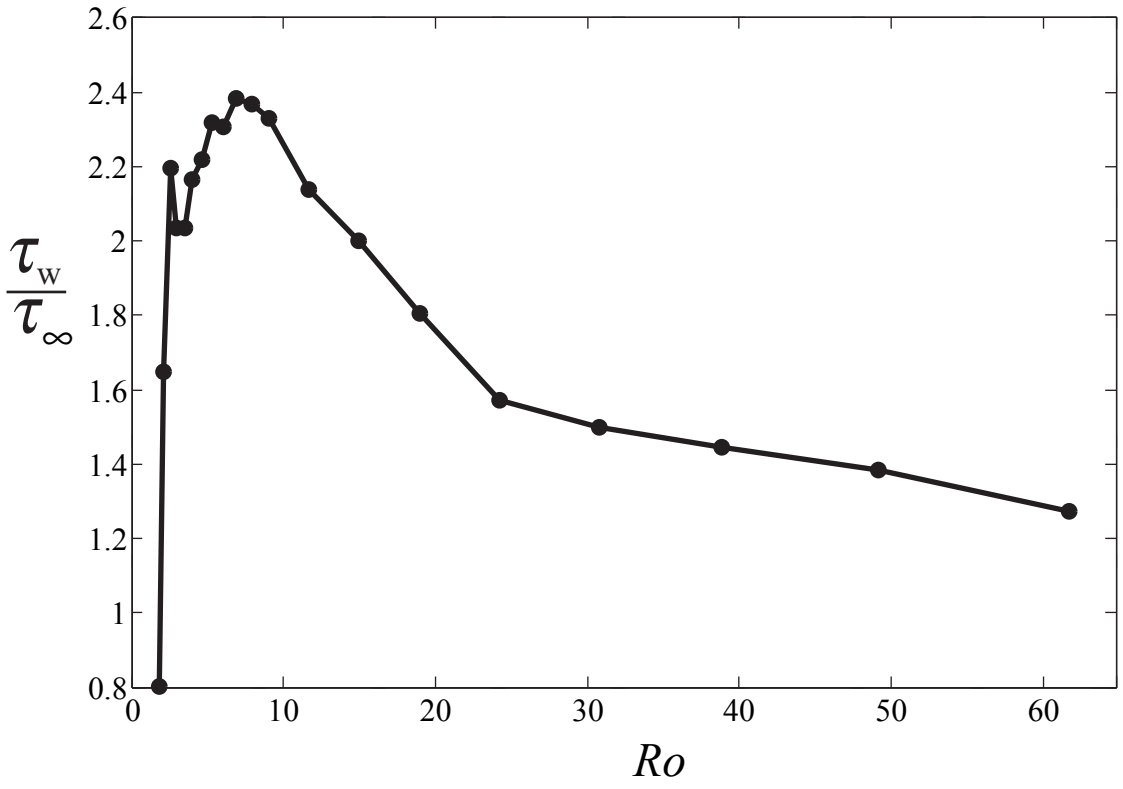

Fig. 4.19: Mean wall shear stress made dimensionless by the value it would have if the outer sphere were stationary, based on calibration against the inner sphere torque described in Sec. 5.3.1.

of the experiment as G/G_∞ approaches its minimum from either side. It may be that each distinct torque state is associated with a different zonal circulation pattern, with the inner-most flow[31] highest at the peak of Fig. 4.19 and the minimum of Fig. 4.18. If there is really stronger zonal flow with reduced angular momentum transport heading toward Ro_R, it is clear that we can not make any kind of maximization argument for energy dissipation or angular momentum transport to explain these flows. The large zonal circulations that arise seem to *reduce* angular momentum transport. They seem to trap that angular momentum which is shed from the inner sphere at small cylindrical radius.

Each state also has associated wave states, which may feed off the shear or modulate the boundary layer like the hypothesized state in Sec. 4.2. As the Ekman pumping on the inner sphere becomes stronger and stronger, we eventually expect a jet like Fig. 2.3 (b), and we may expect more 3D motion to become important. That jet, however, represents a large gradient of vertical velocity, which by Eq. 1.15 gives a source term for vorticity. Eq. 1.15 implies a large variety of wave states, Rossby waves and inertial modes, and the long wavelength versions of these all consist of large-scale vorticity patterns.

We suggested in Section 4.2 that even in the $Ro = \infty$ case, non-trivial large-scale recirculation patterns in the bulk can interact with the boundary layer on the inner sphere in a self-reinforcing way. Perhaps this is the case for all of the states when $Ro > 0$. large-scale, nonlinear waves of vorticity, whether they are Rossby waves or other strong inertial modes, could modulate the boundary layer

[31] That at smallest cylindrical radius

on the inner sphere and the strength of the inevitable outflow from its surface, or they could grow on the (presumably) zonal shears observed. We should work to understand whether the wave patterns are important to the observed zonal flows; it seems unlikely that the changes in the waves would change simultaneously with the observed mean flows if they were not.

5. RESULTS II: H/L BISTABILITY IN DETAIL

5.1 Introduction

The preceding parameter space overview established the existence of multiple turbulent flow states with transitions well defined at different *Ro*. This chapter will focus on one of them, the high/low (H/L) state transition discussed briefly in Section 4.4. The material in Section 5.2 through Section 5.5 is nearly a verbatim excerpt from a paper recently submitted to Physics of Fluids. The author of this dissertation is first author of the paper, and was responsible for all data collection and data analysis, generation of figures, and drafting of the text of this paper. The co-authors of the submitted paper, S.A. Triana and especially D.P. Lathrop made some intellectual and editing contributions to this paper, these being roughly comparable in scope to those in the rest of this dissertation. As is the case with this entire dissertation, the experimental team worked together to improve the experiment. However, this work is predominantly the author's work regarding the analysis of the H/L transition in detail. Section 5.6 is not part of the Physics of Fluids submission. It is new data taken with the help of Matthew Adams, who is currently working with the 60 cm apparatus toward his Ph.D..

5.2 Torque-Derived Measurements

5.2.1 Torque Revisited

We will begin the discussion of the H/L state transition with a reminder of the torque results for $Ro > 0$ and how they differ from what we might consider the base-state case with $Ro = \infty$. Fig. 5.1 is a reproduction of Fig. 4.7, and shows the torque on the inner sphere as a function of Reynolds number when only the inner sphere revolves.

In the context of this chapter, we note mainly from Fig. 5.1 that G is monotonically increasing in Re. At first glance[1], this might be the general expectation for turbulent torque scaling in a shear flow experiment. The higher the differential rotation between the boundaries, the higher the torque. However, we established in Chapter 4 that this is not necessarily the case when we impart global rotation. When we hold the outer sphere speed constant and super-rotate the inner sphere as in Fig. 5.2, we find that the mean torque on the inner sphere is non-monotonic as the dimensionless differential speed, Ro, is increased. In ranges of Ro in Fig. 5.2 where the torque data are presented in overlapping branches, the flow exhibits bistable behavior with associated abrupt changes in inner sphere torque.

A representative time series of the torque in the first bistable regime is shown in Fig. 5.3, with $E = 2.1 \times 10^{-7}$ and $Ro = 2.13$. The onset of the high torque state is abrupt, taking on the order of 10 rotations of the outer sphere. The torque overshoots the high state mean value at high torque onset by 10-15%. The end of

[1] If you hadn't read the preceding chapters...

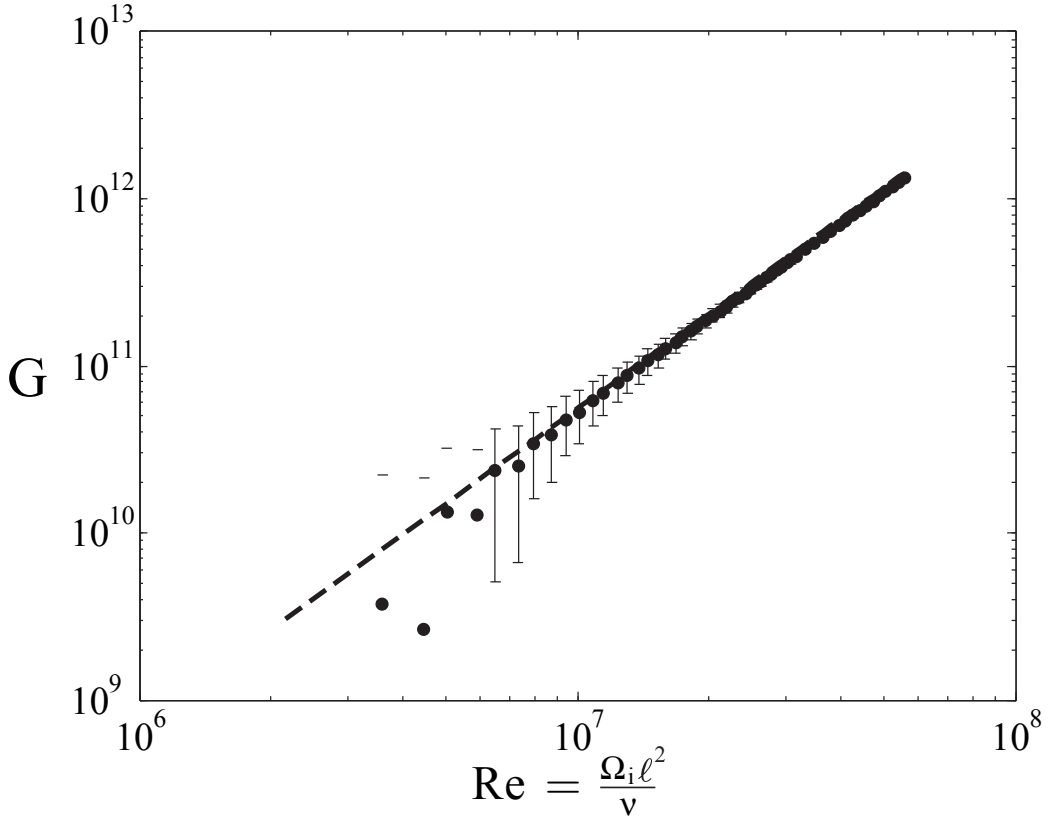

Fig. 5.1: The dimensionless torque G vs. the Reynolds number Re for the case $\Omega_o = 0$, stationary outer sphere. This is the same as Fig. 4.7, reproduced here to keep this figure closer at hand and and to keep the flow of this section as written. We recall that the torque is monotonic with Re and the dashed line is the fit $G = 0.003 Re^{1.89}$.

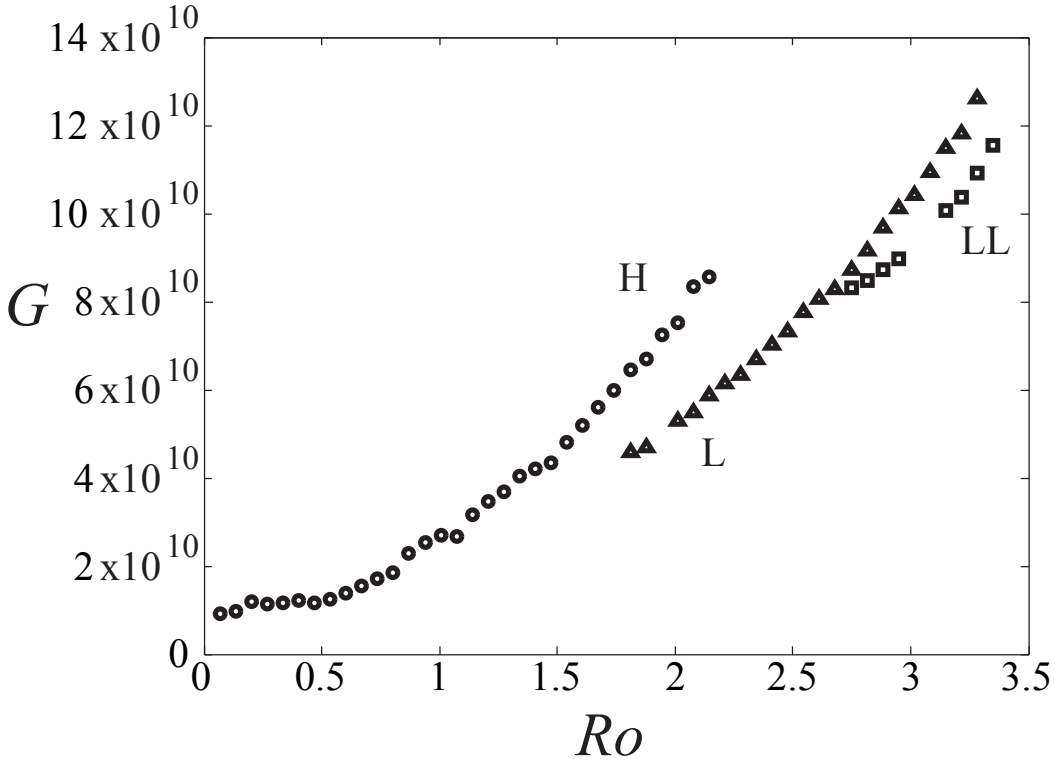

Fig. 5.2: Mean value of the dimensionless torque G vs. Ro at $E = 2.1 \times 10^{-7}$. Ro is varied by increasing the inner sphere speed in steps of $Ro = 0.067$, waiting about 450 rotations per step. Three curves are differentiated by circles, triangles, and squares. In the ranges of Ro where the symbols overlap, flow exhibits bistable behavior. Several other flow transitions exist below $Ro = 1.5$ but do not involve significant measurable torque variation. H and L denote the torque curves of the the "high torque" and "low torque" states discussed from here on. There is a second bistable regime starting around $Ro = 2.75$, the lower torque state of which we label LL.

the high torque state exhibits a slow exponential decay of the torque to the low torque value with a mean characteristic time of 40 rotations. In addition to the full transitions between the two torque levels, there are "excursions" where the torque decays toward the low mean value or rises toward the high mean value without fully reaching the other state.

The qualitative bistability in Fig. 5.3 manifests itself quantitatively in the bimodal probability distribution of the torque shown in Fig. 5.4. The division of data into high torque and low torque states was done manually so as to exclude the transition regions. The resulting individual distributions of G for the high and low states are also shown in Fig. 5.4. There is a small region of overlap in the "high" and "low" state individual distributions due to the difference drawn between "transitions" and "excursions." The same manual division in states is used throughout this chapter to condition other data on state. With the division as shown, the high state mean torque is 1.4 times that in the low state. The torque fluctuations in the high torque state are much higher than in the low; the standard deviation of the high state torque is 1.8 times that in the low state. These low frequency fluctuations are clear in the velocity and wall shear, and this will be further discussed in Sections 5.3.1 and 5.3.2.

In both Fig. 5.3 and Fig. 5.4 the torque data has been numerically low pass filtered. In Fig. 5.4, the filter cutoff frequency was chosen where the apparent fluid torque power spectrum crosses the mechanical vibration noise floor, thereby retaining the hydrodynamically relevant fluctuations.

The interval between transitions is somewhat irregular, and it is difficult to

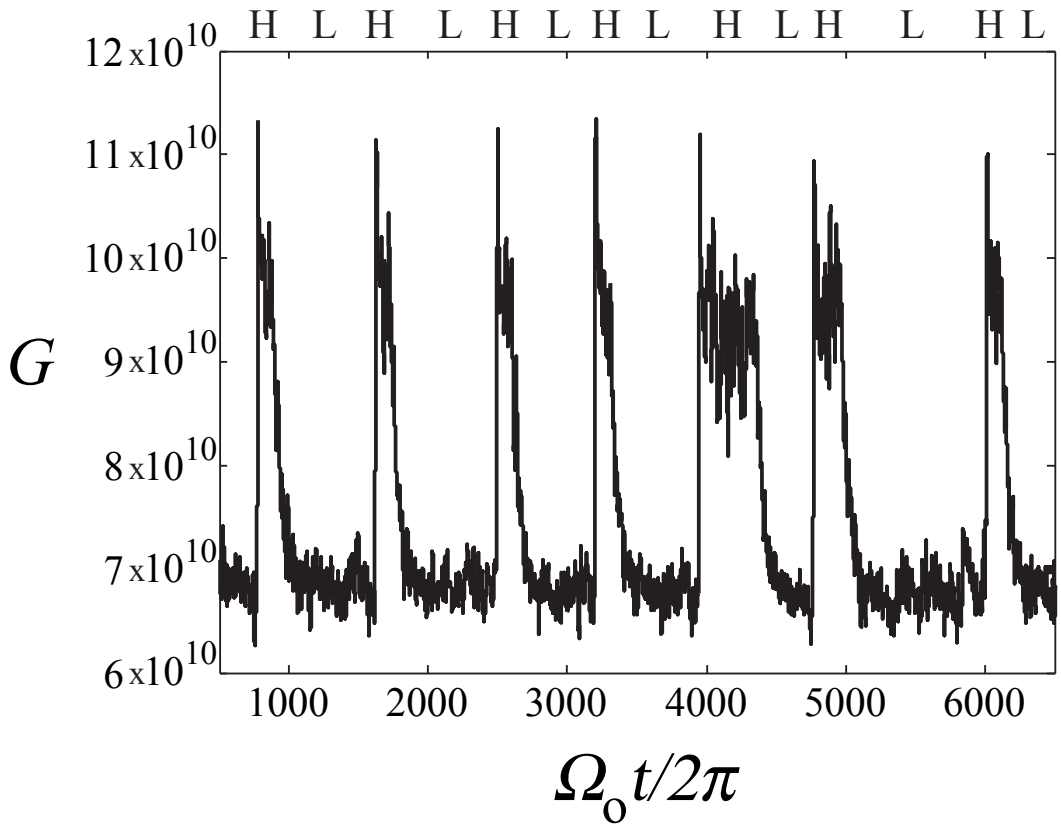

Fig. 5.3: Time series of G at fixed $Ro = 2.13$ and $E = 2.1 \times 10^{-7}$, with time made dimensionless by the outer sphere rotation period. The raw torque signal has been numerically low pass filtered ($f_c = 0.05$ Hz, 15 rotations of the outer sphere.).

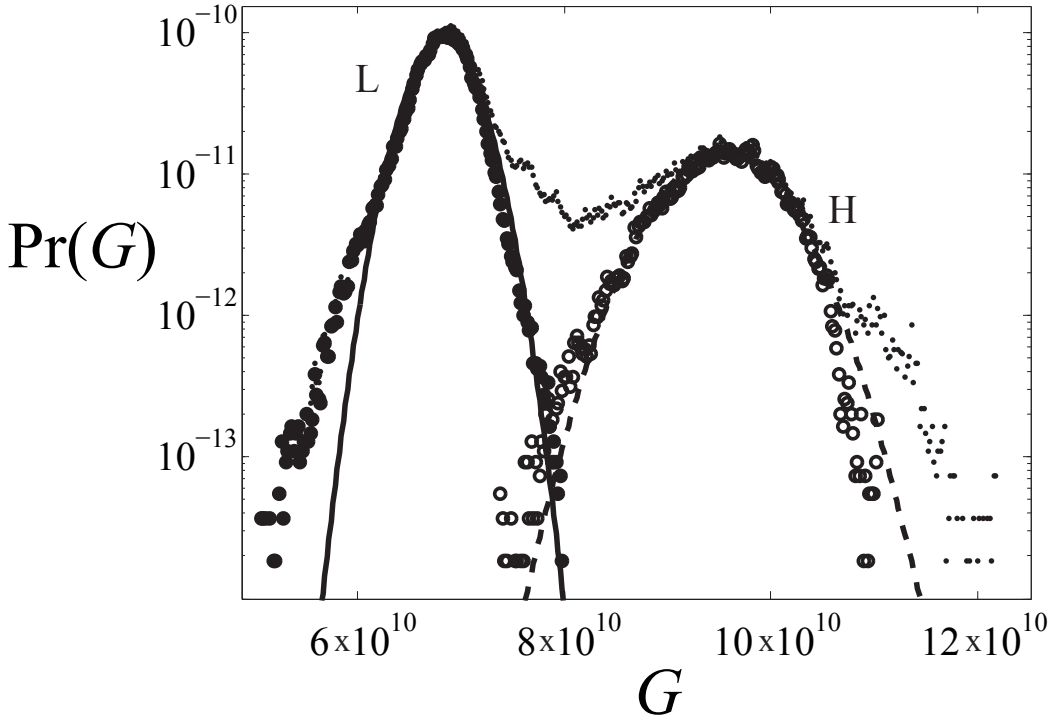

Fig. 5.4: Probability density of the dimensionless torque at $Ro = 2.13, E = 2.1 \times 10^{-7}$. The full distribution is denoted by small points. Solid circles denote conditioning on low torque state, and open circles on the high, with Gaussian solid and dashed curves for the low and the high respectively. The mean and standard deviation of the low torque state data are $\langle G \rangle = 6.82 \times 10^{10}$ and $\sigma_G = 2.74 \times 10^9$. In the high torque state they are $\langle G \rangle = 9.53 \times 10^{10}$ and $\sigma_G = 5.02 \times 10^9$. The data were low pass filtered at $f_c = 0.5$ Hz.

get good statistics on the state switching due to the slow dynamics, which allow observation of only 10-20 transitions per experimental run at a fixed pair of system parameters. However, over 45 transitions at the parameters in Fig. 5.3, we observe the statistics shown in Table 5.1.

Tab. 5.1: Statistics of the interval between high torque onsets. $\Delta t'_{\mathrm{H}}$ is the time interval between two subsequent high torque onsets made dimensionless by $\Omega_{\mathrm{o}}/2\pi$, so the time interval is measured in outer sphere rotations. $Ro = 2.13$, $E = 2.1 \times 10^{-7}$. These are the mean, standard deviation, maximum and minimum of the interval between high-going transitions.

$\langle \Delta t'_{\mathrm{H}} \rangle$	$\sigma_{\Delta t'_{\mathrm{H}}}$	$\mathrm{Max}(\Delta t'_{\mathrm{H}})$	$\mathrm{Min}(\Delta t'_{\mathrm{H}})$
717	313	1917	390

We also observe that the probability the system is in one state or the other is a function of Ro in the bistable range. Above a threshold value of Ro, we begin to observe state transitions to the low state, and as Ro increases, the high torque state becomes less likely. Fig. 5.5 shows the probability, based on measurements over 4000 rotations, that the system is in the high or low torque state over the first range of Ro where state switching is observed. Outside of this range, transitions were not observed for more than 4000 rotations of the outer sphere, and those points have been assigned a probability of one or zero accordingly. The probability that the system was in the low state was fit to

$$\Pr(L) = \begin{cases} 0 & : Ro < Ro_{\mathrm{c}} \\ 1 - exp(-\gamma(\frac{Ro - Ro_{\mathrm{c}}}{Ro_{\mathrm{c}}})) & : Ro > Ro_{\mathrm{c}} \end{cases} \tag{5.1}$$

with $\gamma = 8.25$ and $Ro_{\mathrm{c}} = 1.80$. The high torque probability is given by $\Pr(H)$ = 1-$\Pr(L)$. The physical implication inherent in the exponential form is that there is no

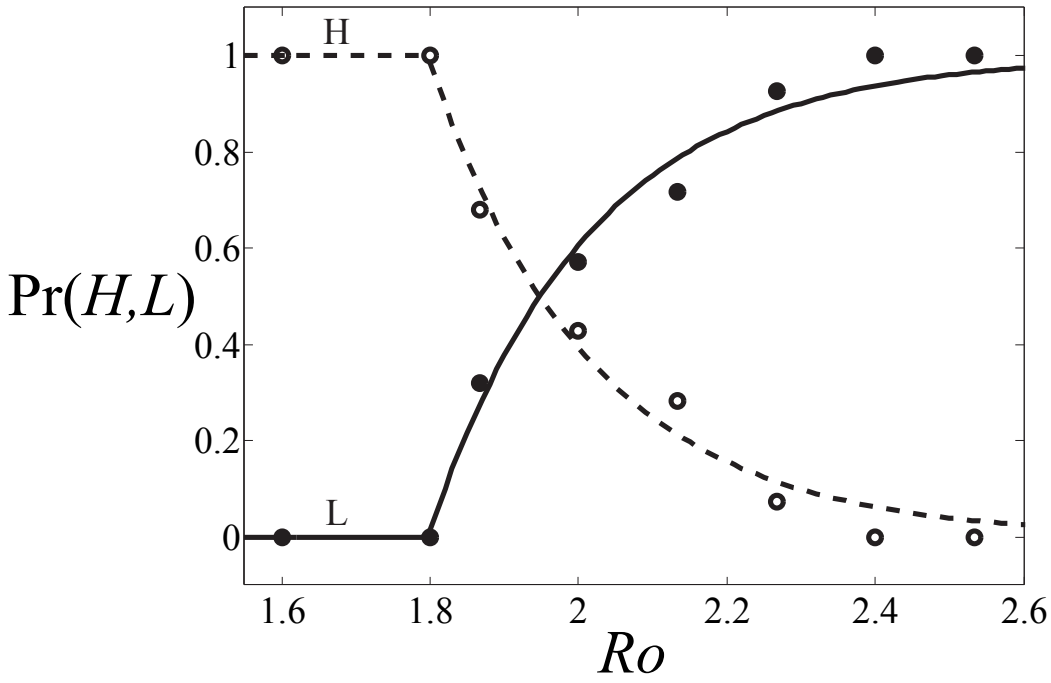

Fig. 5.5: Probability that the flow was in the high torque (open circles) or low torque (closed circles) state as a function of Ro over the first bistable range with fixed $E = 2.1 \times 10^{-7}$. The dashed and solid lines are fits to the exponential form of Eq. (5.1).

upper threshold where the high torque state becomes impossible but only becomes less likely as Ro is increased. However, the lower threshold for state transitions is well defined at Ro_c.

5.2.2 Net Angular Momentum

The torque measurements presented so far have focused only on the inner sphere. To get a complete picture of the angular momentum transport processes in the system, we must examine the torque on both boundaries. To do so, we record the torque reported by the variable frequency drives. Therefore, we are able to detect

the fluctuating fluid torque on the outer sphere, though with less sensitivity than our inner sphere measurements. Perhaps the simplest expectation for the torques would be that the inner sphere torque level would be promptly mirrored by the outer sphere torque. That would indicate that the angular momentum flux across the gap switches between two statistically steady values depending on the internal flow state, and furthermore that the net angular momentum of the fluid should be constant when averaged over the turbulent fluctuation timescales. This must be true with sufficiently long averages. The inner and outer boundaries are rotating at constant speeds of 2.35 Hz and 0.75 Hz. So, on averages over arbitrary long times the fluid can neither be accelerating or decelerating. However, the net torque on the system presented in Fig. 5.6 reveals long periods of angular acceleration and deceleration interspersed with plateaus where the net angular momentum of the fluid remains nearly constant.

The net torque is shown in Fig. 5.6 along with the separate inner and outer torques with the steady outer sphere bearing and aerodynamic drag subtracted. Up to a constant of integration, we can calculate the net angular momentum $L(t)$ about the rotation axis from the net torque,

$$L(t) = \int_0^t T_{\text{net}}(t')dt'. \tag{5.2}$$

Due to measurement limitations, we cannot integrate the torques from the start of the boundary rotation where we know the initial angular momentum is zero. Instead, we set the initial value of L to zero at an arbitrary time and make the resulting quantity dimensionless by dividing it by the angular momentum the fluid

would have if it were in solid body rotation with the outer sphere,

$$L' = \frac{L}{I_{\text{fluid}}\Omega_{\text{o}}}. \tag{5.3}$$

The moment of inertia of the fluid filling the gap is

$$I_{\text{fluid}} = \frac{8\pi\rho}{15}(r_{\text{o}}^5 - r_{\text{i}}^5), \tag{5.4}$$

which has a value of $(1.14 \pm 0.02) \times 10^4$ kg m^2.

At the onset of the high torque state, as at Fig. 5.6(a), there is a prompt response of the outer sphere torque, indicating a certain amount of increased angular momentum transport. However, the increase in the torque on the outer sphere is insufficient to fully oppose the increased inner sphere torque. At this point, the net torque becomes steadily positive, and the fluid accelerates. As this happens, the fluid torque G_{o} on the outer sphere tends to slowly decrease in magnitude, though with large fluctuations. Eventually the inner sphere torque G starts the slower transition to the low torque state. At a point during the high to low transition, as at Fig. 5.6(b), the net torque becomes negative and the the net angular momentum starts to decrease. The torque on the outer sphere continues a slow decay toward a value opposite and equal to that on the inner sphere, sometimes reaching a net torque fluctuating about zero as in times after Fig. 5.6(c).

Overall, the torque measurements in the rotating system show a behavior that contrasts sharply with the case with the stationary outer sphere. When both spheres rotate the angular momentum flux in the range of Ro considered here may be partially a slow "store and release" process where long lasting imbalances in the torques on the inner and outer spheres can lead to fluid spin up and spin down. It

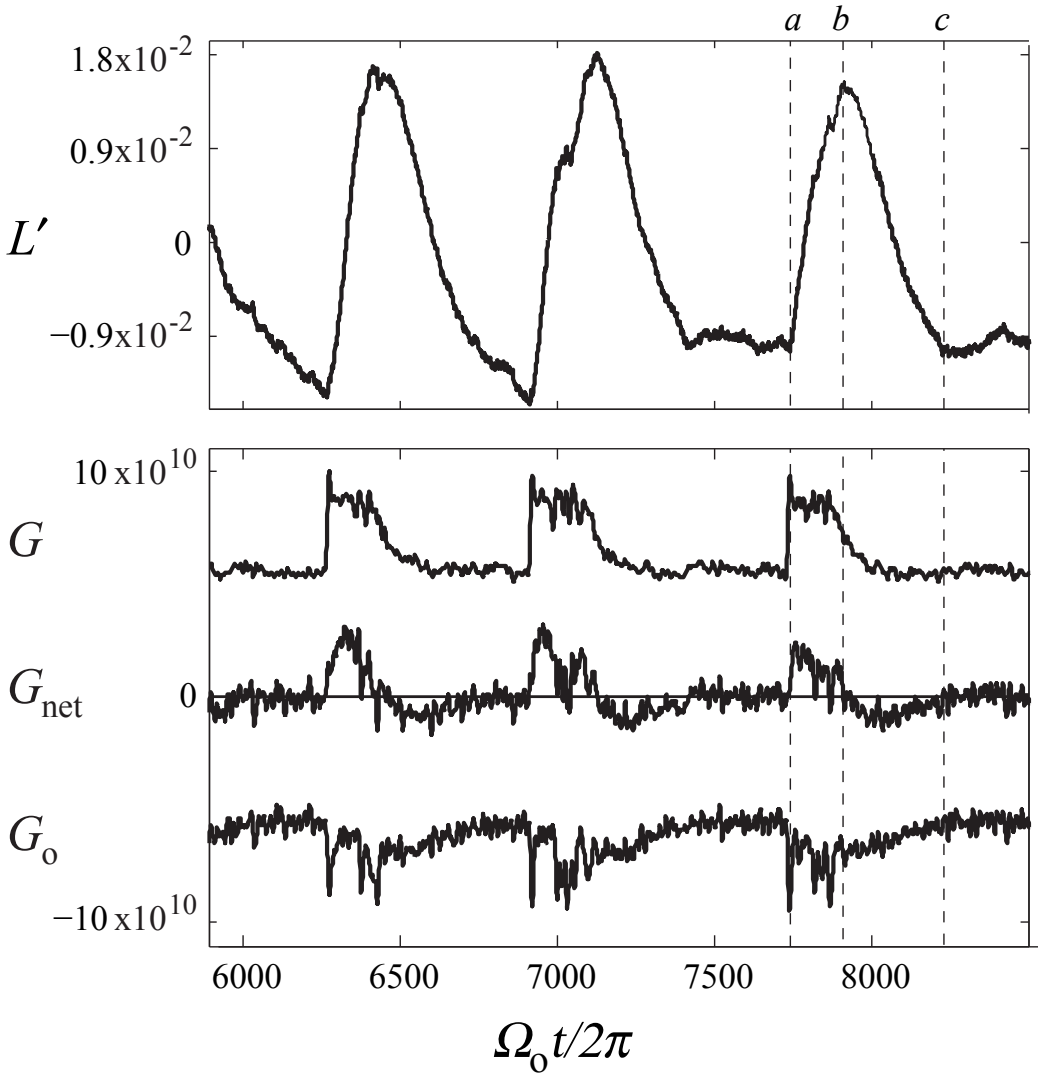

Fig. 5.6: The angular momentum, inner torque, outer torque, and net torque. $Ro = 2.13$, $E = 2.1 \times 10^{-7}$. The upper plot shows the dimensionless angular momentum L' as defined in Eq. (5.3). The lower plot shows the inner torque G, the outer torque $G_{\rm o}$, and their sum $G_{\rm net}$. The bearing and aerodynamic drag on the outer sphere have been subtracted off, and the torques have been low pass filtered as in Fig. 5.3.

is worth noting that the average magnitude of torque is similar between the outer stationary and the outer rotating cases for similar differential rotation across the range of Fig. 5.2. In both cases the mean torque on the inner sphere is between $G = 10^{10}$ and $G = 10^{11}$. Although the dynamics of the angular momentum transport seem quite different, the magnitude of the transport has not changed drastically.

5.3 Direct Flow Measurements

5.3.1 Mean Flow Measurements

All measured flow quantities undergo transition in a qualitatively bistable way with the inner torque. The time averaged wall shear and measured velocity near an instrumentation port decrease sharply the onset of the high torque state, as shown in Fig. 5.7.

The velocity is measured in a shallow range near the outer sphere surface at 23.5° colatitude, 60 cm cylindrical radius from the axis of rotation. This location is about 9 cm outside the cylinder tangent to the inner sphere equator. We calculate the time averaged azimuthal velocity at this location,

$$\langle u_\phi \rangle_t = \frac{\langle u_{\text{meas}} \rangle_t}{\sin(23.5°)}, \tag{5.5}$$

and make that dimensionless by the outer sphere equatorial tangential velocity,

$$\langle u' \rangle_t = \frac{\langle u_\phi \rangle_t}{\Omega_o r_o}. \tag{5.6}$$

Ultrasound doppler velocimetry only measures the component of the velocity parallel to the beam axis. In this experiment, the beam from the transducer near the outer

sphere is inclined 23.5° from pointing straight down, and lies in the plane normal to cylindrical radius at the transducer location. This orientation of the transducer axis makes it sensitive to the cylindrical radial, azimuthal, and vertical velocity components, u_s, u_ϕ, and u_z. Near the transducer, u_s has very little projection onto the beam direction. We expect little time averaged response to u_z since z-independence and the experiment's rotational symmetry make persistent vertical velocities at the probe location unlikely. So we believe that Eq. 5.5 is justified. The distance along the beam y' has been made dimensionless by the gap width ℓ.

The wall shear stress sensor has been calibrated against the torque measurements from the data in Fig. 5.1 with the outer sphere stationary. The mean wall shear τ_w on the outer sphere at the probe cylindrical radial location s_o was assumed to be

$$\tau_w = \frac{T}{4\pi r_o^2 s_\mathrm{o}}. \tag{5.7}$$

This assumes that the wall shear falls off linearly with cylindrical radius. This is motivated by the nearly constant angular momentum profile seen in turbulent Taylor-Couette [121]. Under these assumptions, we fit the constant temperature bridge voltage V and mean wall shear calculated from the measured torque by Eq. (5.7) to

$$V^2 = A\tau_\mathrm{w}^{2/3} + B\tau_\mathrm{w}^{1/3} + C \tag{5.8}$$

as in [128]. We then use the calibration coefficients A,B and C to calculate the wall shear from the measured bridge voltage for subsequent runs with the outer sphere rotating.

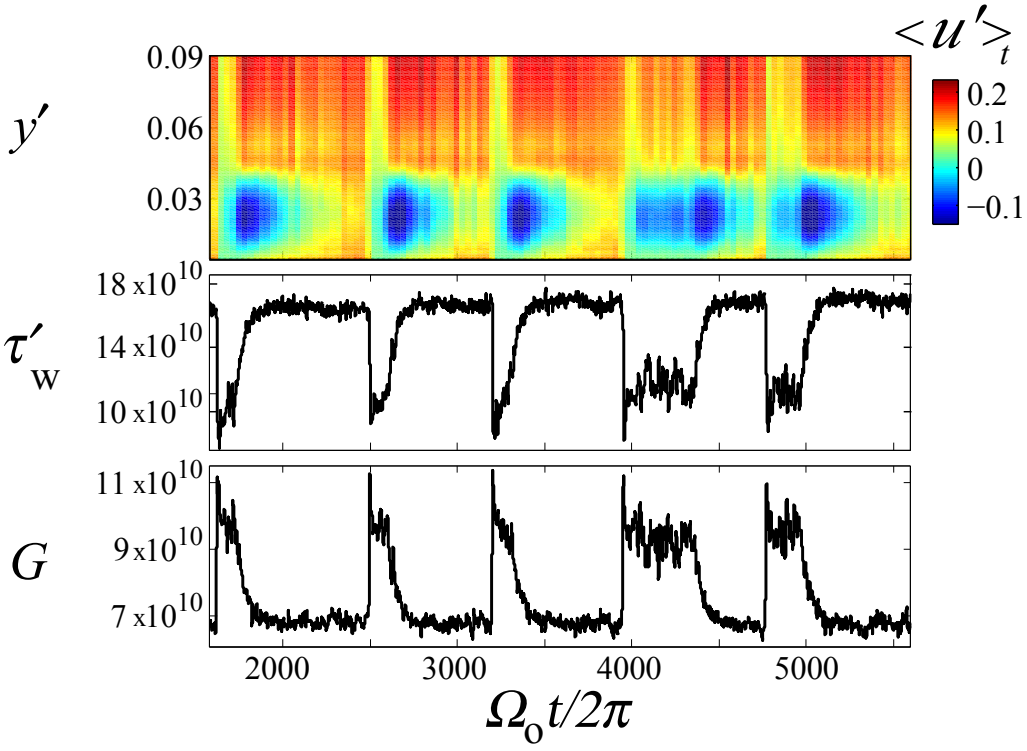

Fig. 5.7: Velocity, wall shear stress, and torque. The top plot is the measured velocity u', defined in Eq. 5.6 as a function of distance from the transducer and time. It is time averaged over 30 rotations of the outer sphere. This measurement should be dominated by the azimuthal velocity u_ϕ. The velocity u' is made dimensionless by the outer sphere tangential velocity, and so can be interpreted as a locally measured Rossby number. The middle plot is dimensionless wall shear stress $\tau'_w = 4\pi r_o^3 \tau_w / (\rho \nu^2 r_i)$, and the lower plot is the dimensionless torque G. The wall shear stress and torque have been low pass filtered with $f_c = 0.05Hz$ as before, which is comparable to the time averaging of the velocimetry.

In contrast with observed behavior with outer sphere stationary, the wall shear at the measurement location on the outer sphere does not always increase with the inner sphere torque. At fixed parameters in the torque switching regimes, the time averaged wall shear behavior is anti-correlated with the inner sphere torque. The non-monotonic behavior of the wall shear measured at the sensor location cannot be representative of the integrated shear stress over the whole outer sphere. Fig. 5.6 shows that the torque the fluid exerts on the whole outer sphere is indeed greater in the high torque state. However, the mean shear stress at the measurement location in the high torque state is only 65% of that in the low torque state (see Fig. 5.9). This indicates a different latitudinal pattern of shear stress on the outer sphere. This observation is consistent with the mean velocity measured near the probe location.

In the high torque state, the measured velocity $\langle u' \rangle_t$ for $y' > 0.05$ averaged over 30 rotations drops to 41% of its low torque state value. Using dye injections and a camera mounted in the rotating frame, we have also observed visually that the azimuthal zonal circulation essentially stops during the short duration torque overshoot. Despite the increase in angular momentum input into the system from the inner sphere, and the increase in angular momentum flux from boundary to boundary, the time averaged fluid velocity and transfer of momentum to the wall at the sensor locations show a sharp decrease at the onset of the high torque state. It is clear from the shear and velocity measurements that the low torque state is associated with something like a fast central zonal flow. This central circulation drops suddenly at the high torque onset, leading to greatly increased torque on the fast moving inner sphere. When the fluid around, above, and below the inner sphere

is circulating faster, there is less torque on the inner sphere. The unusual aspect of this is that it takes less torque, and therefore less power input, to maintain the faster circulation. This suggests formation of a transport barrier to energy and angular momentum in the low torque state. This change in transport is also important for the observation that the total angular momentum is decreasing (See Fig. 5.6, line (b)), while the low torque state fast circulation is growing.

5.3.2 Flow Fluctuations

The turbulent fluctuations in the system show a significant change through the transition. The measured velocity fluctuations in the high torque state are larger than those in the low torque state, although with a lower mean. Fig. 5.8 shows the probability density of the dimensionless velocity conditioned on the low and high torque states, with Gaussian curves for comparison. The mean velocity measured in the low torque state is 2.45 times that seen in the high torque state. However, the fluctuations in the high torque state are 1.5 times the low torque state fluctuations. Based on this measurement, the high torque state has a turbulence intensity $\sigma_{u'}/\langle u' \rangle$, of 57% while that for the low torque state is 16%. Some of the difference in fluctuation intensity could potentially be attributed to different velocity anisotropy between the two states. The assumption of insensitivity to vertical velocities discussed in Sec. 5.3.1 is only reasonable for time averages, not for fluctuating velocities.

The wall shear fluctuations are similar in magnitude between the two states. Wall shear distributions are shown in Fig. 5.9. The low torque state mean wall shear

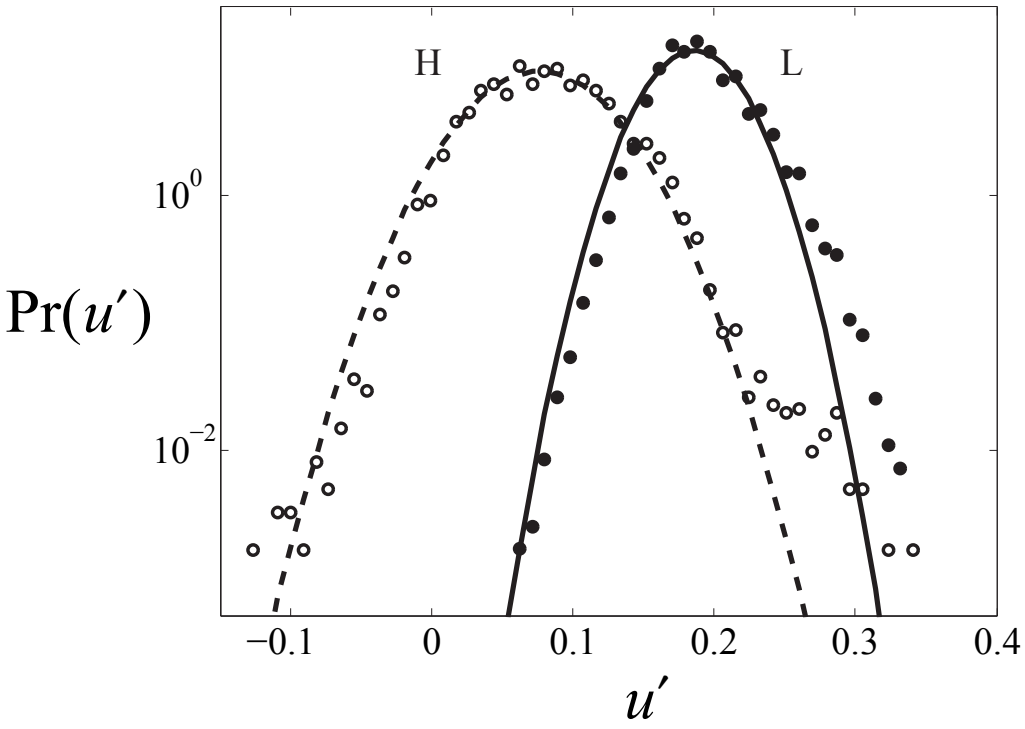

Fig. 5.8: The probability density of the dimensionless velocity conditioned on the torque state, with solid circles denoting the low torque state and open circles denoting the high. The dashed and solid lines are Gaussian curves with the same mean and standard deviation as the data set. The standard deviation in the high torque state is $\sigma_{u'} = 0.043$, and in the low, $\sigma_{u'} = 0.029$. The high state mean $\langle u' \rangle = 0.076$ and the low state mean $\langle u' \rangle = 0.186$. These data are for a distance from the transducer $y' = 0.03$, with the transducer beam 45° from the vertical in the same plane as in Fig. 5.7. The velocity is divided by $\sin(45°)$ under the assumption of azimuthal dominance discussed above. Velocity sampling rate was 100 Hz

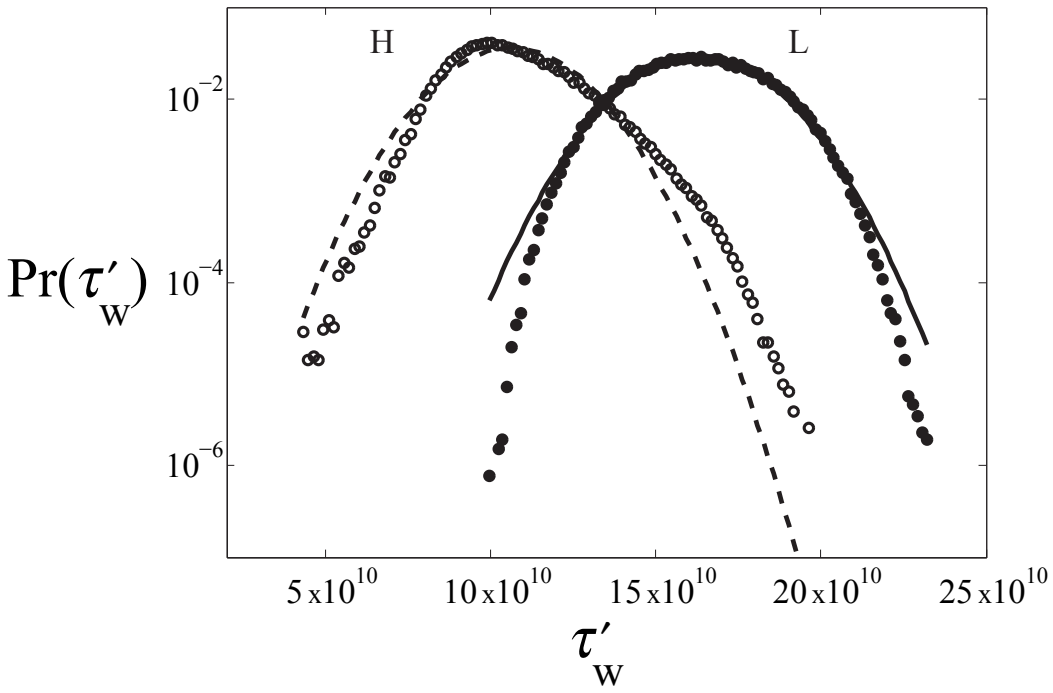

Fig. 5.9: The probability density of the dimensionless wall shear conditioned on torque. Solid circles again denote the low torque state, and open circles the high, with Gaussian solid and dashed curves. The mean and standard deviation in the low torque state are $\langle \tau'_w \rangle = 1.63 \times 10^{11}$ and $\sigma_{\tau'_w} = 1.81 \times 10^{10}$. In the high torque state they are $\langle \tau'_w \rangle = 1.06 \times 10^{11}$ and $\sigma_{\tau'_w} = 1.71 \times 10^{10}$.

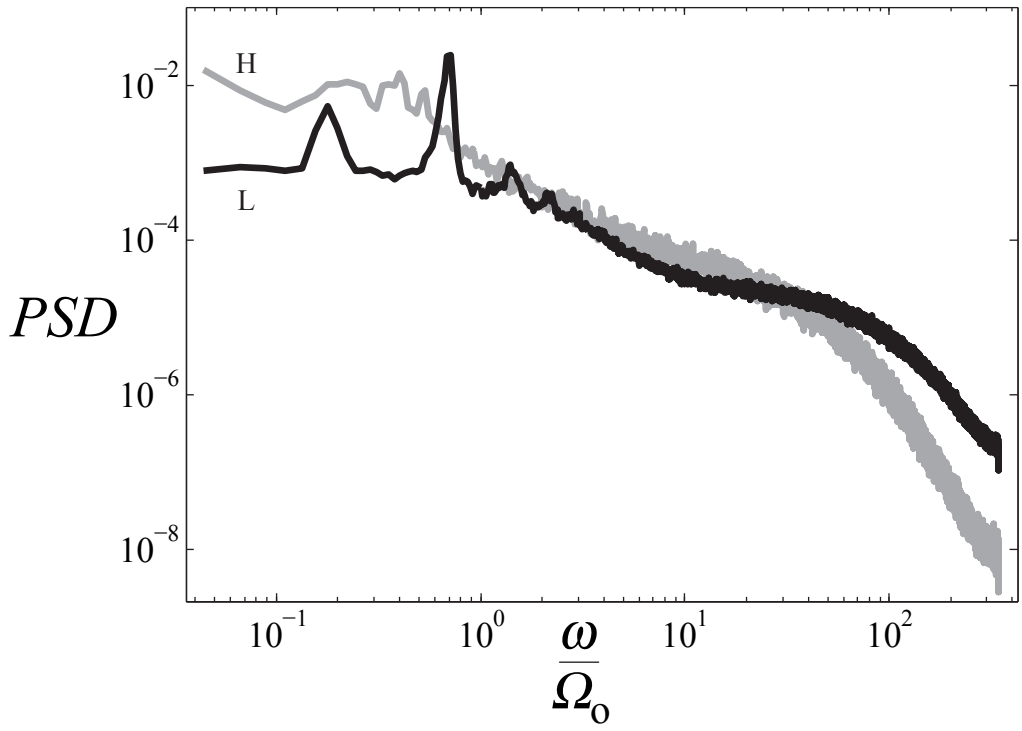

Fig. 5.10: Power spectra of wall shear stress at $Ro = 2.13$ and $E = 2.1 \times 10^{-7}$. Frequency has been made dimensionless by the outer sphere rotation rate. The black curve is the spectrum from the low torque state, and the gray curve is that in high torque state. The low torque spectrum has prominent peaks at $\omega/\Omega_o = 0.18$ and at $\omega/\Omega_o = 0.71$ and its harmonics. In the high torque state there are slight peaks at $\omega/\Omega_o = 0.40$ and 0.53 and a broader buildup around $\omega/\Omega_o = 0.22$

is about 1.5 times that in the high torque state, and the standard deviation between the two states is within 5%. In the low torque state, $\sigma_{\tau'_w}/\langle\tau'_w\rangle$ is 11% compared to 16% for the high torque state. The high torque state wall shear distribution is significantly skewed, with a skewness of about 0.6. Gaussian curves with the same mean and standard deviation as the measured distributions are included for comparison. High wall shear fluctuations are significantly more likely in the high torque state.

The flow fluctuations are broadband overall. Kelley *et al.* [14] made the case for strong inertial waves on a somewhat turbulent background flow with comparable absolute magnitude of *Ro*. However, without flow measurements little could be said about the nature or strength of the turbulence in the flow. The turbulence is clear here from the direct measurements of Fig. 5.8-5.10. However, power spectra of the flow quantities, shown for the wall shear in Fig. 5.10, reveal prominent narrow frequency peaks. These may be inertial or Rossby waves or coherent superpositions thereof. The high torque state is characterized by stronger broadband low frequency fluctuations. The slow fluctuations in wall shear and velocity in the high torque state are very similar to the torque fluctuations in that state.

The weak peak around 0.40 Ω_o in the high torque state spectrum appears to be associated with the same wave as that responsible for the 0.71 Ω_o peak in the low torque spectrum. This wave increases in frequency and strength through the high to low torque transition until the frequency remains steady at 0.71 Ω_o. Again, the high to low transition involves a steadily increasing azimuthal circulation at the measurement location. The increasing frequency of this wave suggests that it is being advected by the azimuthal flow. That the frequency of this wave increases with increasing *Ro* is more evidence of this advection. This can be seen in the spectrogram in Fig. 5.11. If the 0.40 Ω_o peak in the high torque state and the 0.71 Ω_o peak in the low torque state are the same wave, we have some extra information about the relationship among the wave frequencies observed in the system. The frequency of this wave observed in the frame rotating with the outer sphere, ω_{obs}, can be written in terms of a natural oscillation frequency ω_w and azimuthal wavenumber m in a

frame rotating faster than the outer sphere by an amount Ω',

$$\omega_{\text{obs}} = \omega_{\text{w}} + m\Omega'. \tag{5.9}$$

Assuming that the ratio of wave advection angular speeds $\Omega'_{\text{L}}/\Omega'_{\text{H}}$ is that of the means of the velocity distribution in Fig. 5.8 and noting the measured frequencies at the wave onset and in the steady low torque state, we can write a system of equations for wave's frequency ω_{w} in the faster rotating frame:

$$0.71\ \Omega_{\text{o}} = \omega_{\text{w}} + m\Omega'_{\text{L}} \tag{5.10a}$$

$$0.40\ \Omega_{\text{o}} = \omega_{\text{w}} + m\Omega'_{\text{H}} \tag{5.10b}$$

$$\Omega'_{\text{L}} = 2.45\ \Omega'_{\text{H}}. \tag{5.10c}$$

For any m, the solution for the wave frequency in the frame rotating with angular speed Ω' is $\omega_{\text{w}} = 0.186\ \Omega_{\text{o}}$, near that of the other, steady frequency observed wave. There is a sign ambiguity due to the fact that we do not know if the waves are prograde or retrograde. So not only is the $0.71\ \Omega_{\text{o}}$ wave in the low torque state advected by the fast inner circulation, but it seems to be the result of nonlinear interaction between the other observed steady frequency wave and the azimuthal circulation.

Fluctuation spectra as a function of Ro over a broader range allow us to delineate the observed flow states more clearly. Fig. 5.11 shows a spectrogram of the wall pressure at one sensor location as a function of Ro for fixed $E = 1.3 \times 10^{-7}$. The logarithmic color scale denotes the power in each frequency bin, and the vertical axis is frequency made dimensionless by the outer sphere rotation speed. Below

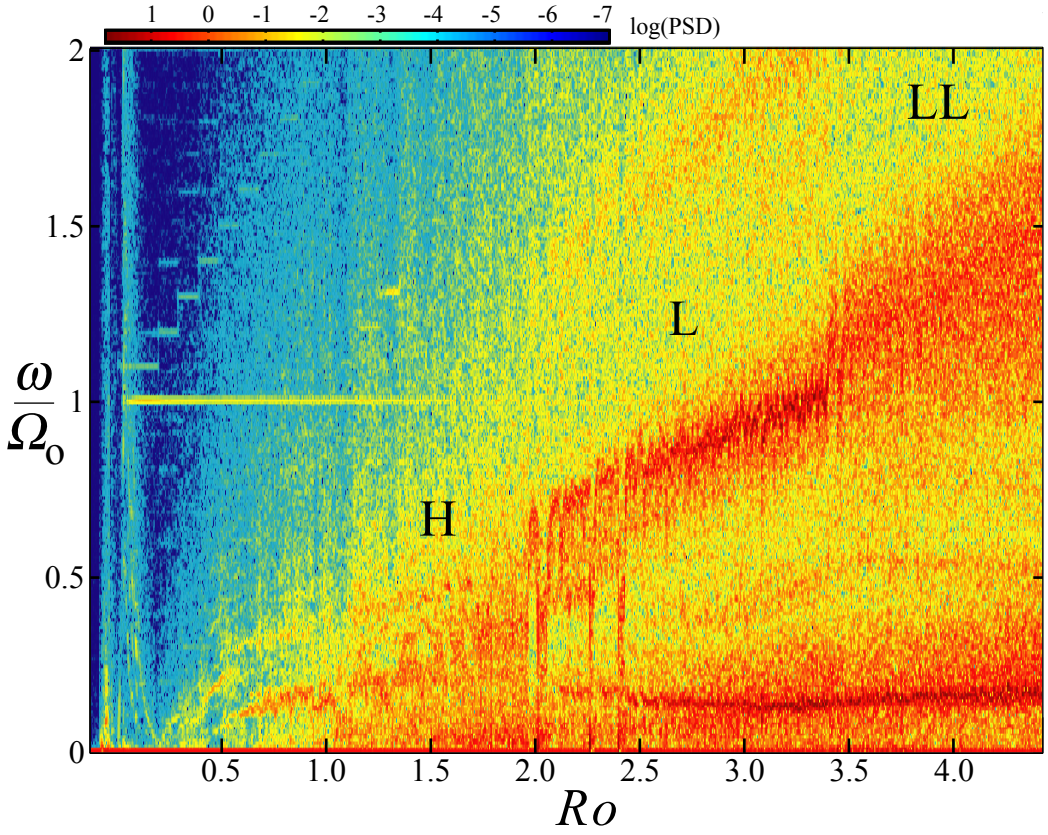

Fig. 5.11: A spectrogram of wall pressure at 23.5° colatitude shows evidence of several flow transitions as Ro is varied. $E = 1.3 \times 10^{-7}$ and $0.1 \leq \mathrm{Ro} \leq 4.4$, waiting 430 rotations per step with steps of $Ro = 0.1$. Instead of averaging the power spectra over an entire step of Ro, there are 30 spectra per step in Ro, so some temporal evolution is visible at a given Ro. This figure is identical to Fig. 4.13, reproduced here for the sake of the detailed discussion.

$Ro = 1$ there are a number of different wave states, some of which are visible here. It is possible that at extremely low Ro there are transitions similar to those seen in simulations by Hollerbach *et al.* [109], however at these low Ekman numbers, the Stewartson layer instability onset is probably much lower Ro than the slightest differential rotation we can achieve [35]. At similar E with Ro somewhat lower than the lowest here, Schaeffer and Cardin [33] report Rossby wave turbulence in numerical models. It may be that we have observed such turbulence, and investigation of those model predictions may be fruitful in the future. As Ro is increased, we would not expect agreement; the quasigeostrophic model used to achieve this low E at modest Ro uses depth averaged equations and therefore cannot exhibit three dimensional effects. The waves visible at lowest Ro in Fig. 5.11, are probably over-reflected inertial modes [14]. These are already three dimensional, and we might guess that the higher Ro behavior involves further 3D motion. We do not focus on lower Ro here, but we note that a variety of different turbulent flows are likely present in a small region of parameter space.

Between $Ro = 0.5$ and about $Ro = 1.0$ there are a pair of waves with frequency increasing with Ro. A transition to the high torque state flow occurs around $Ro = 1$. This flow is more turbulent but still shows some evidence of the waves in the prior state. It is unclear whether this transition can be reliably detected in the inner sphere torque, although there seems to be some effect. The high torque state flow starting near $Ro = 1.0$ is observed alone until the Rossby number exceeds $Ro_c = 1.8$. Between $Ro = 1.8$ and $Ro = 2.4$ in Fig. 5.11 several transitions between the high and low torque states are noted. Above the first observed torque switching regime,

the waves dominating the low torque spectrum in Fig. 5.10 remain.

The frequency of the wave at 0.18 Ω_o varies only a small amount with Ro over the measured range, while the higher wave frequency increases with Ro. Again, this is consistent with advection of the higher frequency wave by increasing azimuthal velocities. The nature of this higher frequency wave is still unknown. One possibility is a Rossby wave of one particular wavenumber; Rossby waves are advected by the mean flow. The multipole vortices studied by Van Heijst, Kloosterziel, and Williams [52, 129] are another possible candidate. These consist of a central cyclonic vortex with weaker anticyclonic satellites. The whole multiple vortex structure slowly rotates about the central cyclone axis. Our observations would be consistent with what Van Heijst *et al.* call a tripole, two satellites on a central vortex. This structure appears to be nonlinearly stable even at similar E to our experiment and $Ro > 1$ based on the relative velocity of the stirred vortex.

The lower frequency wave may be an inertial mode of the sphere. The inertial modes observed in spherical Couette flow at lower Ro oscillate at a frequency near the natural frequency of the corresponding full sphere mode over wide ranges of Ro [14]. An inertial mode of the full sphere exists near the observed frequency. That mode has N=1, m=1, $\omega = -0.1766$ in the notation of Zhang *et al.* [10], or (3,1,-0.1766) in the (l, m, ω)notation of Greenspan [6] and Kelley *et al.* [14].

The spectrum of the flow associated with the "LL" curve in Fig. 5.2 is clearly present in this spectrogram beyond $Ro = 3.3$. With longer residence times at each step of Ro, intermittent transitions between the "L" and "LL" states can be observed at lower Ro consistent with Fig. 5.2. This transition from the 'L" state to the "LL"

seems to involve an increase in the wave speed and intermittency of the higher frequency "L" state wave, resulting in a more turbulent, broadened frequency peak. The lower frequency wave remains relatively unaffected. As in the "H" to "L" transition on which we've focused, the "L" to "LL" transition is also accompanied by an increased mean azimuthal circulation and an increase in the local wall shear at the measurement location.

The flow spectra and other fluctuation measurements provide a clear distinction among the various turbulent flow states present in rapidly rotating, strongly sheared spherical Couette flow. We expect that further measurements will help illuminate the precise nature of the observed waves and allow us to understand whether they have a prominent, primary role in the overall dynamics observed here or are present as a peculiar secondary feature of the turbulent flow.

5.4 Discussion

We hypothesize that the state transitions discussed here involve formation and destruction of a fast zonal circulation at small cylindrical radius. The fast mean circulation and strong local shear in the low torque state, along with the falling total angular momentum of Fig. 5.6 mean that there must be a change in the shape of the angular mean angular velocity profile $\Omega(s)$ from that of the high torque state. The flow must change to favor, on average, fast fluid at the center of the experiment and slower fluid at larger radius. A simple possibility would be a central zonal circulation bounded by a sharp shear layer with waves, shown schematically in

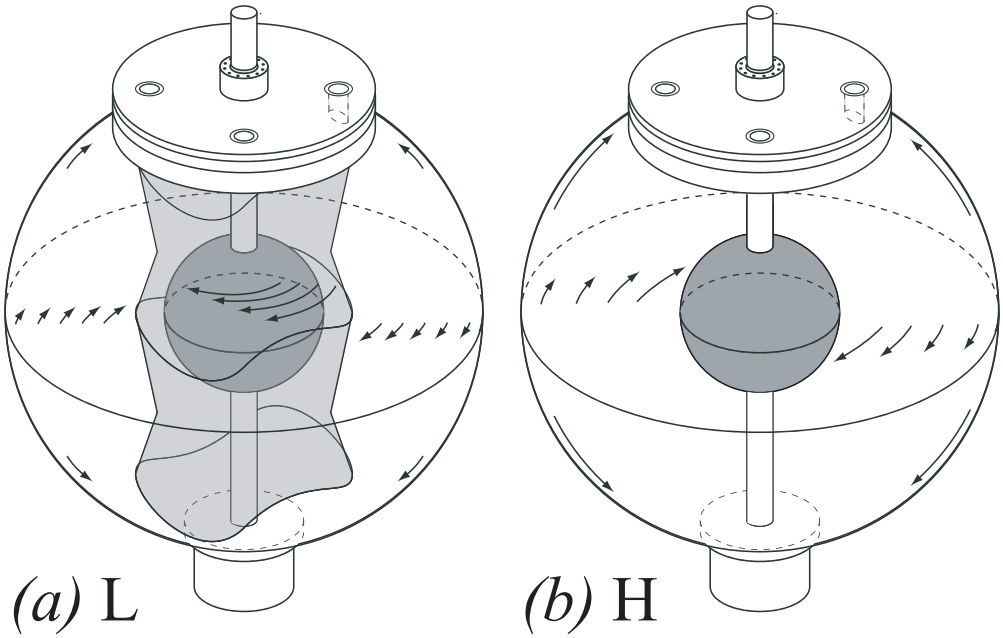

Fig. 5.12: A sketch of the possible mean flow states. The low torque state is labeled L and the high labeled H. The low torque state at (a) is characterized by fast zonal circulation near the core of the experiment and attendant waves. The waves may exist throughout the sphere. In the high torque state, the velocity profile must be flatter. The zonal circulation has been destroyed by angular momentum mixing, so the fluid near the inner sphere is slower and the torque higher.

Fig. 5.12(a). The abrupt transition to the high torque state may involve a collapse of this fast central zonal flow. The very short timescale of the azimuthal flow crash, 10 rotations of the outer sphere, suggests that rapid mixing is responsible for the crash; it would be difficult for other processes to act quickly enough. So, we might expect a fast relaxation to a less steeply varying angular velocity profile, as in Fig. 5.12(b).

The bistable regime we have focused on here is in a part of parameter space that is far from the known basic states discussed in Section 2.3 for spherical Couette

with and without overall rotation. We are also far from previously studied turbulent regimes. So, it is not obvious what flows to expect when Ro is moderate and E is very low. The basic state spherical Couette flow for low E and infinitesimal Ro shows a free shear layer on the cylinder tangent to the inner sphere equator, the Stewartson layer [102]. Outside the Stewartson layer the fluid is locked in solid body rotation with the outer sphere [103, 130, 131]. No angular momentum is transported across the Stewartson layer. Instead, high angular momentum fluid from the Ekman boundary layer on the inner sphere is pumped vertically to the outer sphere inside the Stewartson layer. This layer also resolves the angular velocity jump across the tangent cylinder. In quasigeostrophic simulations by Schaeffer and Cardin, at E comparable to that in our experiment, the Stewartson layer becomes unstable at very low Ro, $Ro \sim 10^{-3}$, [35, 108]. These simulations find Rossby wave turbulence lower than any Ro lower than any presented here [33]. The angular velocity profile $\Omega(s)$ in the Rossby turbulence regime predicted by Schaeffer and Cardin still shows evidence of a concentrated shear like the Stewartson layer. The inertial wave overreflection presented by Kelley *et al.* [14] demonstrates that three dimensional fluid motions become important at low E and moderate Ro. However, the flow with strong inertial waves is still very different from that with the outer sphere at rest.

When the outer sphere is stationary, an equatorial jet erupts radially outward from the inner sphere equator, carrying angular momentum toward the outer sphere [101, 104, 132, 133]. The boundary layer on the outer sphere pumps fluid poleward. This forms a large scale poloidal circulation throughout the volume even at low Re. At higher Re, a series of nonaxisymmetric instabilities and transition

to turbulence are observed in wide gap flow [101]. The equatorial jet persists in the turbulent flow [105]. The mean angular velocity profile in highly turbulent flow with outer sphere stationary is near $\Omega(s) \sim s^{-3/2}$ [112, 118]. We hypothesize that we could approach this state, plus an overall constant, at high enough Ro that the differential rotation completely dominates the dynamics.

The shape of the mean angular velocity profile, not just its overall magnitude, is very different between the previously studied turbulent states. We might expect that each turbulent flow transition could involve a significant change in the the mean angular velocity profile. Complex patterns of zonal flow (along with waves and localized vortices) are a prominent feature of rapidly rotating turbulent flows. The schematic flows of Fig. 5.12 are presented as two of the infinite number of possibilities consistent with the observations we present.

In the low torque state schematic, Fig. 5.12(a), the azimuthal flow outside the central zonal circulation is slow, but not locked to the outer sphere. The torque measurements of Fig. 5.6 suggest it spends a long time slowing. The Ekman suction on the outer boundary drains angular momentum from this exterior fluid region faster than the flux across the zonal flow boundary can replenish it until an equilibrium is reached. The boundary of the zonal flow supports wave motion; again, these waves could be Rossby waves or other vortex structures. The waves could extend throughout the fluid volume or be fairly localized. The abrupt onset of the high torque state is associated with a destructive instability of the zonal flow. The ensuing angular momentum mixing provides a mechanism for the sudden reduction in the observed azimuthal circulation. When this happens, the inner sphere, now

surrounded by much slower mixed fluid, demands more torque from the motor. The angular momentum flux from the inner sphere now exceeds the flux out of the system from Ekman pumping on the outer sphere. Overall, the net angular momentum begins to increase. However, since the fast zonal circulation near the experiment core is gone, the measured velocities at small radius remain slow. The increased angular momentum flux from inner sphere to the bulk fluid persists throughout the high torque state, and the fluid angular momentum rises.

At the transition from the high torque to low torque state, the slow exponential decay of the inner torque and rise of the observed fluid velocity and wall shear means that the angular momentum transport barrier bounding the central zonal flow has re-formed, but the inner sphere must still provide angular momentum and energy to spin up the fast central flow. At this point, since the exterior fluid is now weakly coupled to the fast inner sphere, it starts to spin down.

There is one direct piece of supporting evidence for Ekman circulation related to spin down of fluid outside a central zonal flow in the existing velocimetry. Beyond $y' = 0.05$ in Fig. 5.7, the observed velocity is high and positive, consistent with a fast prograde circulation. However, the the negative going jet for $y' < 0.05$ in Fig. 5.7 is correlated with the angular momentum, and is probably a manifestation of the Ekman circulation on the outer sphere.

The data in Fig. 5.13 and that in Fig. 5.7 is affected by unusual probe mounting geometry. In this data, the port insert with a flush mounted ultrasound probe is turned 90 degrees from the orientation that makes the plug insert flush with the inner sphere surface. This forms a wedge shaped cavity. So this measurement is

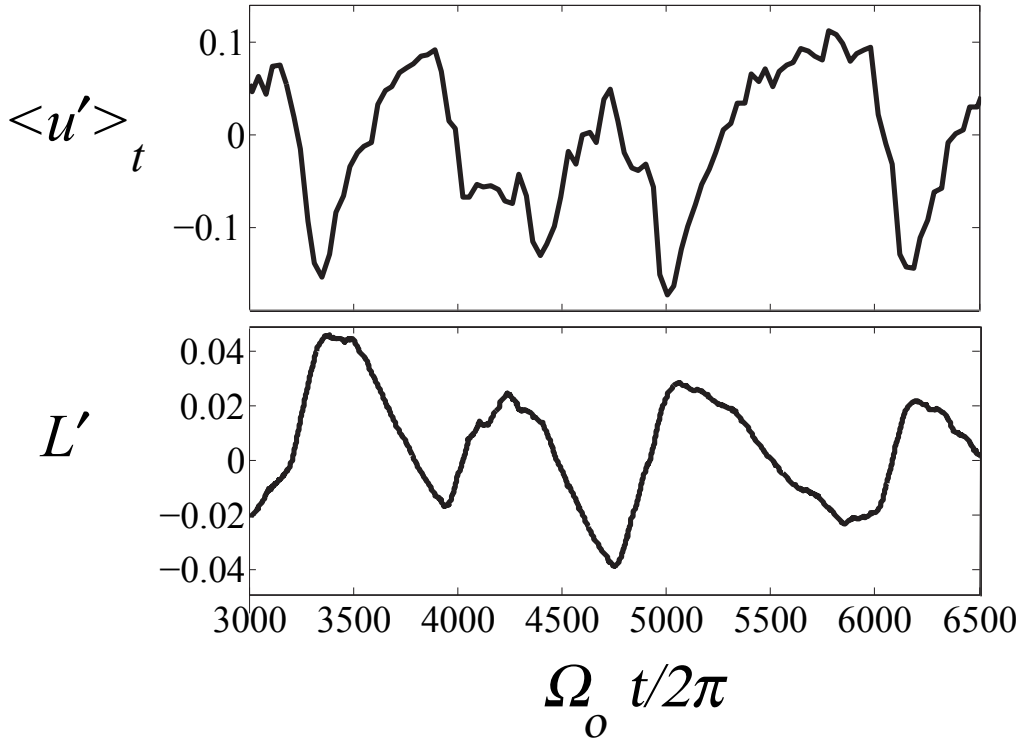

Fig. 5.13: Jet velocity, time averaged and depth averaged from $y' = 0.02$ to $y' = 0.025$ and angular momentum, $Ro = 2.13$, $E = 2.1 \times 10^{-7}$. The velocity in the observed jet in Fig. 5.7 peaks at the same time the angular momentum starts to decrease. It is likely that this jet is related to the Ekman circulation on the outer sphere, though it is not likely to be a direct observation of flow in the Ekman layer, but rather its interaction with a wall cavity formed by the particular transducer mounting used for this run.

not necessarily a direct measurement of the Ekman layer on the outer sphere. If the Ekman layer is stable, it would be much too thin to see with our instrumentation. However, the correlation between the near-wall jet seen in Fig. 5.7 and this measurement is clear, and perhaps it is caused by the Ekman layer flow over and into the cavity. In subsequent experiments with less intrusive transducer mounting, we do not observe this near wall jet clearly.

5.5 Dynamical Behavior

Geophysical and astrophysical systems exhibit bistability. The dynamo generated magnetic fields of the Earth and Sun reverse polarity. Ocean currents, namely the Kuroshio current in the North Pacific near Japan and the Gulf Stream both exhibit bistability in meander patterns [134]. Multi-stability and spontaneous transitions among turbulent flow states have been noted in a number of turbulent laboratory flows as well. The mean circulation in highly turbulent thermal convection cells is observed to switch direction abruptly [135]. Hysteresis in the large scale flow states is seen in surface waves excited by highly turbulent swirling flows in a Taylor Couette geometry with a free surface [136]. Von Karman flow in a cylinder between two independently rotating impellers has been shown to exhibit multi-stability and hysteresis of the mean flow despite very high fluctuation levels at high Reynolds number [137, 138]. Magnetohydrodynamic experiments in the Von Karman geometry have succeeded in producing dynamos that show reversals of the generated magnetic field [76, 77] from a very turbulent flow.

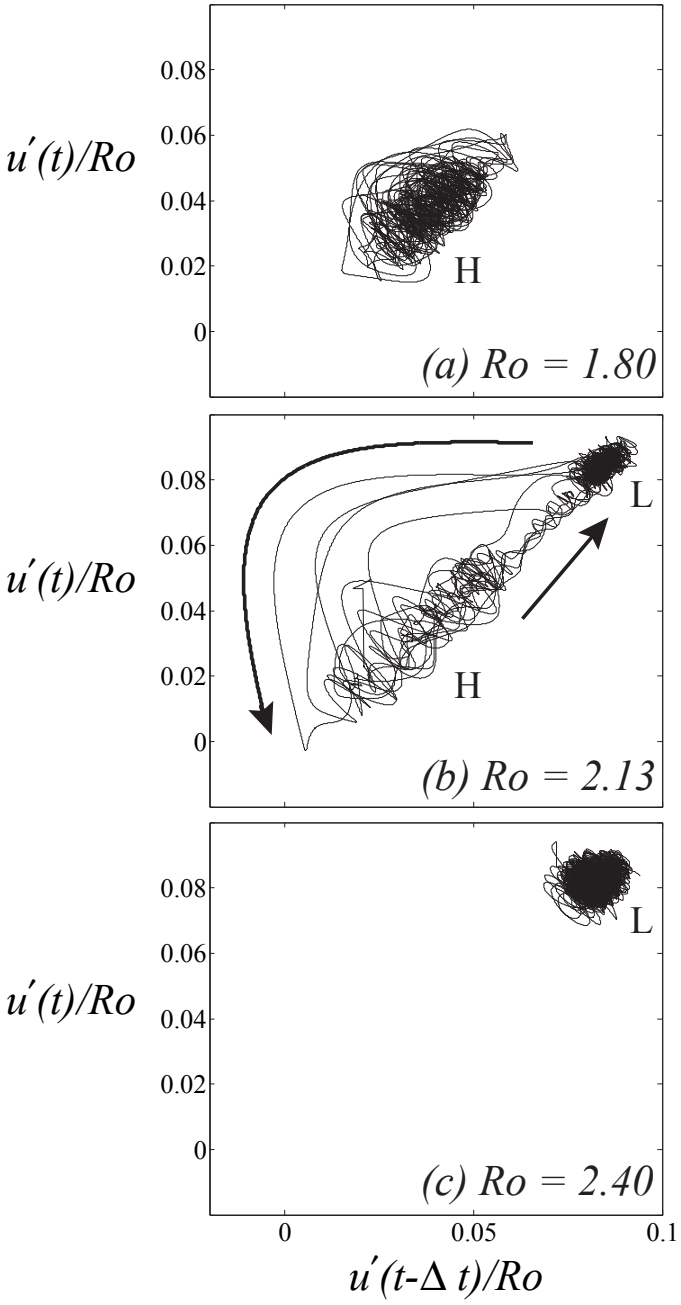

Fig. 5.14: Time delay embeddings of the slow velocity fluctuations at $y' = 0.02$ for three values of Ro below, in, and above the bistable range. Arrows in (b) show the direction taken by the transitions. The time delay Δt is 4.5 rotations of the outer sphere in all three cases. The dimensionless velocity as defined previously has been scaled by Ro, roughly collapsing the mean velocity and fluctuation levels of each state. These data have been low pass filtered with $f_c = 0.1$ Hz, or a period of 7.5 rotations of the outer sphere.

That we can see bistable behavior requires a special sort of separation of spatial structures or time scales. We must be able to recognize the bistable behavior beyond the turbulent fluctuations and their high dimensional dynamics. If a few flow states well separated in phase space play a major role in defining the dynamics, filtering and projection may provide some insight. In many flows, however, we rely on observation of changes in mean flow or low frequency dynamics to provide information on what sort of filtering and projection to use. *A priori* knowledge of relevant states analogous to those relevant in pipe flow and plane Couette flow [139–142] near turbulent transition may allow suitable projection of the full dynamics onto a lower dimensional subspace of possible fluid motions. There are many fluid degrees of freedom that we recognize as irrelevant in the definition of the observed multiple "flow states." The actual flow in each is associated with a trajectory through a very high dimensional phase space, and the division of that space into a small number of regions that correspond to different "states" can be non-obvious. In this sense, the novelty of bistability in experiments may be that we notice it at all.

We investigate phase space trajectories using low dimensional time delay embedding of low pass filtered data. Figure 5.14 is a 2D embedding of a low pass filtered velocity time series. The filter is a 4th order Butterworth with a cutoff frequency $f_c = 0.1$ Hz. This corresponds to a period of 7.5 rotations of the outer sphere. This velocity signal was plotted against the same signal 4.5 rotations prior. Data are shown for three different values of Ro at $E = 2.1 \times 10^{-7}$. At (a), $Ro = 1.8$, which at the low threshold of the first bistable range, in (b), $Ro = 2.13$, the same as in Fig. 5.3, where the bistable switching is evident, and in (c), $Ro = 2.4$, above

the range where spontaneous transitions are observed.

The velocity is rescaled here by the outer sphere tangential speed to make it dimensionless. It is also scaled by Ro, the expected dimensionless velocity scale relative to the outer sphere. We expect that within each state, the mean measured velocity increases with Ro. Scaling by Ro seems to equalize the mean velocity observed in the pure high torque state in Fig. 5.14(a) and that observed in the pure low torque state in Fig. 5.14(c) with the mean velocities of the corresponding states in Fig. 5.14(b). Figure 5.14(b) seems to represent a heteroclinic connection between two turbulent attractors, with connections between the high torque flow state in (a) and the low torque flow state in (c). The arrows in Fig 5.14(b) show the direction of flow in phase space as the system undergoes several transitions. Below the critical Rossby number in Eq. 5.1, we expect all connections to be broken between the two different attractors. Above the bistable range, we recall the probability of state as a function of Ro of Eq. 5.1 and Fig. 5.5 and expect that connections between attractors do not break. Rather, they become extremely unlikely.

5.6 Magnetic Field Measurements

We have performed some experiments in the 60 cm experiment in an attempt to reproduce the H/L transition switching state, and we have evidence that it is reproducible there. These magnetic field measurements are not included in the Physics of Fluids submission but are added to this chapter because they fit best with the detailed discussion of the H/L state transitions herein. We do not know

to what extent magnetic field measurements of the bistable torque regime will be performed in the future[2], and we wish to include these observations here even if a few discrepancies could bear more investigation. We will propose resolutions of these discrepancies, but these should be tested.

Figure 5.15 shows the torque normalized by its low state value and one coefficient[3] of the spherical harmonic expansion of the cylindrical radial induced field outside of the 60 cm experiment. This data was taken using the three dimensional array of Figure 3.24 (b). The Gauss coefficient plotted in Fig. 5.15 is that for the spherical harmonic with $l = 3$ and $m = 1$. This coefficient is not a signature of the (3,1,-0.1766) inertial mode, but rather of the higher frequency wave that, in the rest of this discussion, lies at $0.71\Omega_o$ when $Ro = 2.13$.

The g31 Gauss coefficient is clearly correlated with the torque transitions. The torque behavior is roughly consistent with the H/L transition in magnitude and dynamics.

The g31 coefficient is not identified with the $l = 3$, $m = 1$ dominated velocity field of the inertial mode since the induced magnetic field arising from the linear induction of an $l = 3$ velocity field acting on the axial, axisymmetric applied magnetic field will be comprised only of even polar wavenumbers. This is established by the velocity and magnetic field selection rules laid out for the induction equation by Bullard and Gellman [71]. The induced field should be dominated by polar

[2] We will try in the three meter sodium experiments, but it may be impossible to reproduce the same hydrodynamic states exactly if we find dynamo action!

[3] Known as a Gauss coefficient.

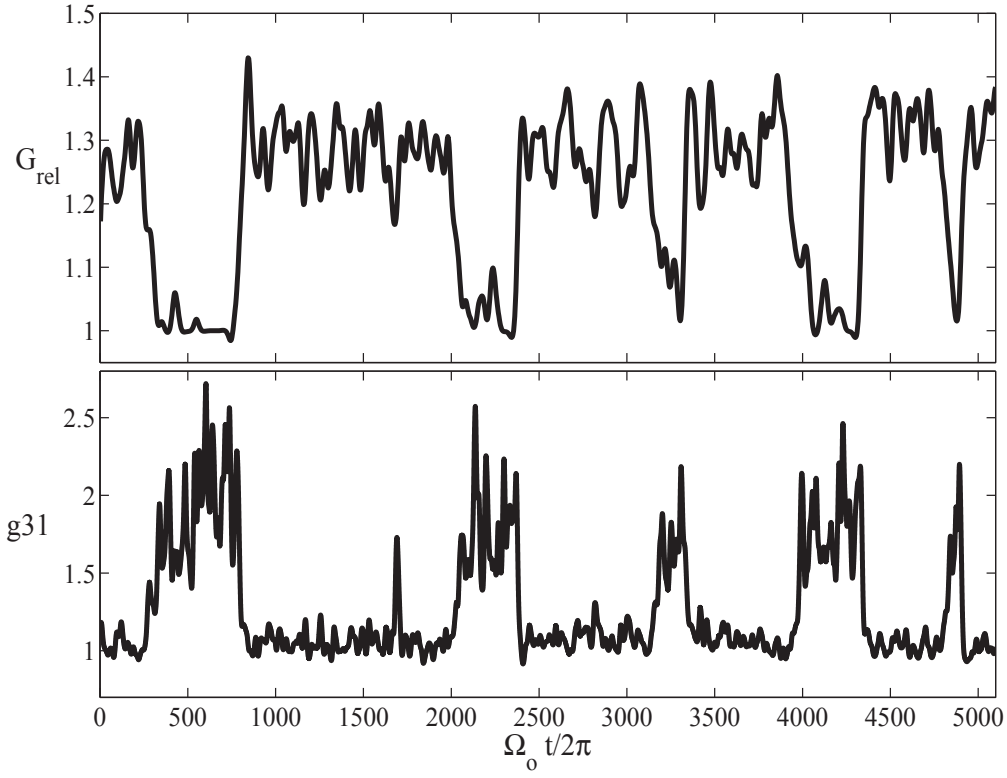

Fig. 5.15: Dimensionless torque (top) and magnitude of the $l = 3$, $m = 1$ coefficient in a spherical harmonic decomposition of the induced cylindrical radial magnetic field outside the 60 cm experiment. This coefficient of the spherical harmonic expansion of the magnetic field is also known as a Gauss coefficient. The torque data is consistent with the observations in the H/L transitions, with the H state about 1.3 times higher than the L state. The torque is poorly temporally resolved because of the low sampling rate of the motor drives on the 60 cm experiment, but the first L to H transition appears to show overshoot, and the H state decays seem slower than the onsets. The g31 Gauss coefficient is unmistakably present only in the low torque state, and one brief excursion around 1750 outer sphere rotations is noted. The source of the g31 coefficient is discussed in the text. For this data, $Ro = 2.7$, $E = 3.2 \times 10^{-7}$, which is higher Ro than what we would predict based on the three meter data. This is discussed in the text.

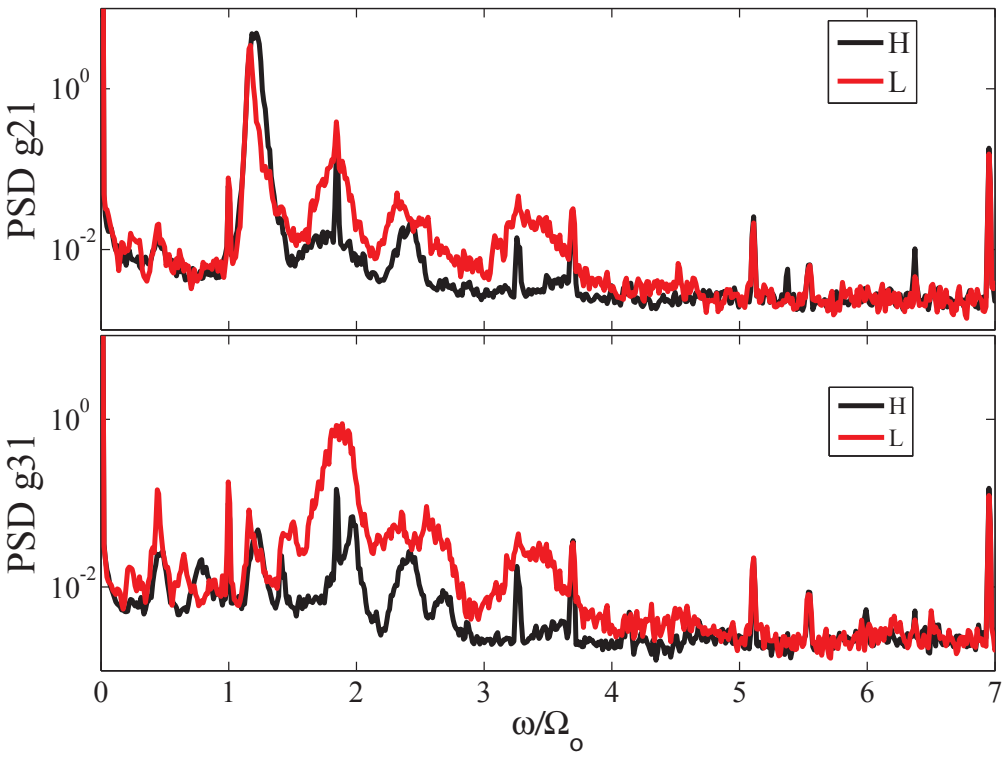

Fig. 5.16: Induced magnetic field spectra from the 60 cm experiment at $Ro = 2.7$, $E = 3.2 \times 10^{-7}$. The largest peak in the g21 spectrum is at a frequency near 1.18 Ω_o, which is what should be seen for the (3, 1, 0.1766) wave doppler shifted into the lab frame. Interestingly, the main effect of the state transition is that the peak is sharper in the L state. The g31 coefficient is clearly the one that turns on and off with the state transitions. Its frequency is 1.87 Ω_i, consistent with the higher frequency L wave peak at this Rossby number.

wavenumber $l = 2$, arising from the interaction of the $l = 3$ velocity field with the $l = 1$ dipole component of the applied field, and the magnetic field induced the axisymmetric ($m = 0$) applied field will preserve the azimuthal wavenumber of the underlying velocity field. Therefore, if the inertial mode (3, 1, -0.1766) is present, its magnetic signature will be in the g21 Gauss coefficients, which have $l = 2$, $m = 1$.

Figure 5.16 shows power spectra for the g21 and g31 Gauss coefficients condi-

tioned on the torque state. The g21 coefficient shows a frequency consistent with the (3, 1, -0.1766) inertial mode. The negative frequency inertial modes are prograde[4], and a $m = 1$ prograde wave will be doppler shifted[5] upward by Ω_o, leading to the observed frequency near 1.18 Ω_o. There is not much change in the observed wave in the torque state conditioning, but we note from Fig. 5.10 that the direct flow measurements show fluctuations that may obscure the influence of the weaker 0.18 Ω_o wave at their location. We recall from Fig. 4.16 that the peak near 0.18 Ω_o persisted over much of the range of positive *Ro*. The fairly steady g21 peak in Fig. 5.16 might imply that this wave is present during the high torque state, but that local turbulent fluctuations in the three meter data obscure it at the measurement location at 23.5° colatitude.

Identification of the g31 coefficient with the higher frequency wave is not so straightforward and requires some discussion. First of all, this is the coefficent that changes most strongly with the torque, consistent with the three-meter observations. The dominant frequency in the g31 L state spectrum is consistent with what we would expect from the L state wave. The magnetic induction arising from this motion is $m = 1$, and assuming it is also prograde, the frequency 1.87 Ω_o in the lab frame corresponds to 0.87 Ω_o in the rotating frame. We can see from Fig. 5.11 that this is close to what we would expect for the higher frequency L state wave at this Rossby number.

There are two difficulties with the identification of the g31 coefficient with the

[4] Due to the choice of $e^{i\omega t}$ instead of $e^{-i\omega t}$ in the inertial mode ansatz.

[5] $\omega_{meas} = \omega + m\Omega_o$.

higher L state peak. The pressure measurements in the sphere frame imply an *even* azimuthal wavenumber pattern for the upper peak in the L state. Furthermore, the g31 coefficient is substantially weaker than the g21 coefficient, even though the upper L state wave is significantly stronger. These discrepancies would be explained if the higher frequency L state peak is associated with a Rossby type wave near the core of the experiment. Two dimensional motions acting on an axial, uniform field cause no induction. The actual applied field is not perfectly uniform and axial, nor are any motions precisely two-dimensional. However, the field is probably close to a uniform and axial idealization near the axis of the magnet coils, and Rossby type waves will be very close to two dimensional.

Therefore the induction by a 2D wave near the experiment core would be nominally invisible provided that the only applied field were that which is intentionally applied. However, Earth also applies a transverse field to the experiment. The transverse component of this field is dominated by azimuthal wavenumber $m = 1$, and by the selection rules of Bullard and Gellman, a $m = 2$ velocity field acting on a $m = 1$ applied field may give $m = 1$ magnetic induction. The transverse field applied by Earth, while weak, may interact with the very strong two-dimensional motion. This would explain the lacking strength and the azimuthal wavenumber discrepancy. We would expect weak induction with l odd (broadband in l) and $m = 1$ from the action of an $m = 2$ Rossby type wave interacting with Earth's magnetic field.

The discrepancy in the onset Rossby number, $Ro \sim 2.5$ instead of $Ro = 1.8$, for this state must be addressed as well. We identify this bistable regime with the

H/L transition, first because it is the first flow transition that has a significant effect on the torque. Second, the relative change in the torque is about 30%, and as we noted in Chapter 4, the H/L transition has the biggest difference in the mean torque between the two states, with the other torque dynamics not exceeding about 10%. Third, the frequencies seen in the magnetic induction are consistent with those of the L state at $Ro = 2.7$ when doppler shifted according to the observed magnetic azimuthal wavenumber. In contrast, the upper peak of the LL wave state measured in the rotating frame is always higher than 1.0 Ω_o. The 0.87 Ω_o peak observed here is therefore more consistent with the L state.

The Rossby number discrepancy has a plausible explanation. We recall from Fig. 3.24 that the geometry in the 60 cm experiment is slightly different from that in the three meter experiment, with the inclusion of large shafts that rotate with the outer sphere. It may be that the delayed onset in Rossby is simply due to the need to spin the inner sphere a bit faster to achieve maintenance of the fast zonal flow and its associated transport barrier, given that it must interact with a large, slower shaft.

Enough of the state characteristics match to make a strong case that this is the same physical process with the same waves, but with a shift in Ro related in a intuitively simple way to the geometrical difference. If this flow transition is essentially identical to that observed in the three meter experiment, the apparently small effect of the perturbed geometry is interesting. We observe a measurable difference in the dynamics, but we also show some robustness of the physical processes to changes in geometry. The evidence presented here also corroborates the hypothesis

that the (3, 1, -0.1766) inertial mode is an important feature of the states where torque switching is observed, and it suggests that the other, higher frequency wave is more nearly two dimensional, like a Rossby wave. Indeed, a Rossby type wave propagating on the zonal flow responsible for the angular momentum transport barrier is consistent with the discussion in Sec. 5.3.2 and Sec. 5.4, and would explain the increasing wave speed as the zonal flow speed increases with increasing Ro.

6. TURBULENT SCALING

6.1 Torque Scaling

6.1.1 Torque Collapses

In Chapters 4 and 5 we have established that a number of different turbulent flows exist in certain regions in the (Ro, Re), or equivalently, (Ro, E) parameter plane for high Reynolds number, rapidly rotating spherical Couette flow. Much of the prior discussion focused on the dynamics of angular momentum, with large changes in the driving torque required to maintain states at a given point in the parameter plane. We propose that at high enough Re, the dimensionless torque G can perhaps be expressed as

$$G = f(Ro)\, g(Re). \tag{6.1}$$

We predict that the relation of Eq. 6.1 should hold approximately for all turbulent swirling flows when overall rotation is added. In general, $G = h(Ro, Re)$, but we propose that at least as $Re \to \infty$, this relation will factorize into Eq. 6.1, and we will present evidence that this is nearly the case in the three meter data.

The function $g(Re)$ in Eq. 6.1 should be similar to that for turbulent drag in all geometries. While we suggest that $g(Re)$ may share similarities with other

experiments, we may not go so far as to suggest that it should be universal. Even for well studied flows, this part of the relation 6.1 remains incompletely understood, and will depend on the geometry and the finiteness of the Reynolds number, as well as the details of the boundary layers. The variation of G with Re can be complicated for finite Re, as seen in Taylor-Couette flow by Lathrop *et al.* [120], where a turbulent flow transition is noted as Re is increased.

However, in a generic geometry, we expect that the function $g(Re)$ expressing the Reynolds number dependence of the turbulent drag will be a monotonic function bounded from above by Re^2 power law scaling, as is the case in other turbulent shear flows like Taylor and plane Couette flow, pipe flow, and others. Also, while we suggest a single function $g(Re)$ is appropriate to capture the dependence on the overall velocity scale, with $Re = UL/\nu$, our data suggests that this might not be true in spherical Couette flow until $g(Re)$ has reached Re^2, as might be the case in rough-wall shear flows.

We propose that the relation $f(Ro)$ of Eq. 6.1 completely expresses the influence of the different turbulent flow states discussed in previous chapters on the torque. It is a non-universal, geometry-dependent relationship. We have established that a wide variety of flow states may arise when Ro is varied, even in $Re \sim 10^7$ turbulent flow. We observe drops in torque as Ro is increased and multi-stability, meaning that $f(Ro)$ is not necessarily monotonic or single-valued[1]. We see that

[1] Although we condition our data on flow state, the long term averages *are* single-valued. We do not, however, rule out parameter space path-dependence and hysteresis in turbulent swirling flows *a priori*. See, for example, Ravelet *et al.* [137] and Mujica and Lathrop [136].

the effects of rotation extend to rather high Ro. The observed dynamics, even at $Ro = 100$, are never exactly consistent with those at $Ro = \infty$, so that the need to know $f(Ro)$ to predict G is not at all limited to weak differential rotation. It does seem, however, that $f(Ro)$ is simpler at high Rossby number.

The form of Eq. 6.1 implies that $f(Ro)$ plays a similar role as the flow geometry in other turbulent drag laws. The relation $f(Ro)$ encapsulates both the geometry dependence and the particular transport properties of the distinct flow states. In other turbulent flows, the drag force is often represented as $c_f(Re)\,Re^2$, with the friction coefficient $c_f(Re)$ expressing the effects of the flow geometry, including (implicitly) the behavior of the large scales and the effects of wall roughness, while showing a residual Re-dependence based on viscous effects in the boundary layers. At high enough Re, it is anticipated that $c_f(Re)$ asymptotes to a constant for a given geometry. However, when both boundaries of a turbulent swirling flow revolve, many extremely different flows are evidently possible in the *same* geometry. Indeed, we notice more or less intense zonal circulation and different drifting large-scale wave motions in different ranges of Ro, which will remain the same if Ro is held constant and only Re is varied. So identifying the effect of changing Rossby number as a Ro-dependent geometry of the *flow* may be a reasonable physical picture.

We have used the quantity G/G_∞ in Chapter 4 to compensate for the Reynolds number dependence of the torque as Ro is changed, and we propose that it can be identified as the Ro-dependent prefactor,

$$f(Ro) = \frac{G}{G_\infty}, \tag{6.2}$$

at least as $Re \to \infty$, though G/G_∞ will be shown to not be completely Re-independent for finite but large Re.

The compensated torque G/G_∞ for rotating data over the small range of Re that we can access here shows an approximate collapse, as depicted in Fig. 6.1 for the narrower range of the $Ro > 0$ data and in Fig. 6.2 for the wide-range positive Rossby data. We remind the reader that these data all have a constant drag removed, consistent with

$$G = G_{meas} - \begin{cases} 2.2 \times 10^{10} \\ \\ 3.3 \times 10^{10} \end{cases}, \tag{6.3}$$

with the choice made for better collapse. Without this drag removal, there is a great deal of splaying of the low Ro tails, as Re will drop many orders of magnitude between $Ro = 1$ and $Ro = 0$ while the drag torque stays constant. Beyond the subtracted drag, residual failure of the collapse seems to have two components. One is a random long-term and medium-term variation in the confounding torque of the seals. It is clear from Fig. 6.1 that this dominates the failure of collapse of G/G_∞ for low Rossby number, again, small dimensional seal drag here is significant. As Ro is increased, this random drag variation is a decreasing percentage of the total dimensional torque, and the scatter is improved. There may also be a systematic variation, which we leave for a moment.

Fig. 6.1 and Fig. 6.2 suggest the common Ro-dependence of all the observed states, just what would be needed for the relation $f(Ro)$. The compensated torque

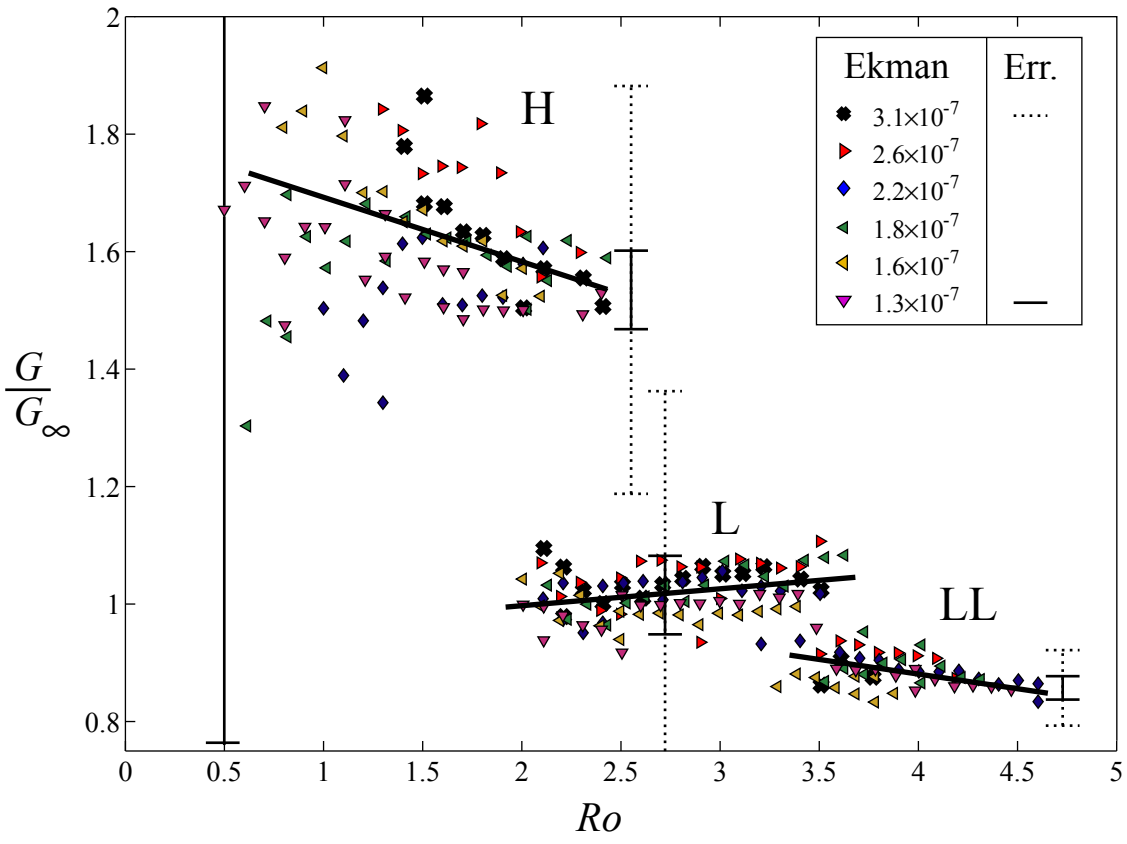

Fig. 6.1: G/G_∞ for the narrow positive Rossby range, showing the H, L, and LL approximate collapse. Collapse is better as Ro and Re are increased, due to reduced seal torque as a percentage of total torque. Some selected error bars are plotted based on the maximum observed systematic difference in the seal torque, $\Delta G_{drag} = 1.1 \times 10^{10}$, and error bars are given for the highest Ekman number (slowest overall rotation) and the lowest Ekman number (fastest). These error bars are both off-scale at the lowest Ro, but a systematic shift of this level is not ever observed within any given run, and the drag model of Eq. 6.3 seems justified. This effect is thought to be the result of varying seal engagement of one of the seals from day to day. In any given constant-E run, the drag torque is reasonably described by choice of the better of $G_{drag} = 3.3 \times 10^{10}$ or $G_{drag} = 2.2 \times 10^{10}$, and for whatever reason, the drag does not switch values mid-run. We can see that the difference between these values is not a good estimate of the random errors within a given run. Furthermore, we can see that the lower E, higher Re, faster rotation runs have unambiguous separation between states even in terms of the maximum seal error. The equations for the solid line fits are given in Eq. 6.4.

G/G_∞ for the H, L and LL states can be modeled by:

$$\frac{G}{G_\infty} = \begin{cases} -0.10Ro + 1.8 & \text{for} \quad 0.5 < Ro < 2.4 \quad : \text{H} \\ 0.03Ro + 0.9 & \text{for} \quad 1.8 < Ro < 3.5 \quad : \text{L} \\ -0.05Ro + 1.1 & \text{for} \quad 3.3 < Ro < 4.6 \quad : \text{LL} \end{cases} , \tag{6.4}$$

with some possibility that the borders in Ro will extend beyond the stated range if one waits long enough at a fixed Ro.

We establish the Ro-boundaries fairly well with the aggregate data here, although there is still some uncertainty stemming from the fact that state transitions become extremely rare in the border regions[2]. In fact, we imply in Sec. 5.2 that the H state does not ever become impossible. In practice, we do not always observe a transition at a given Ro as we step through parameter space, so the overlap ranges of Ro will exceed the overlap implied in Eq. 6.4. We prefer to do continuous ramps to limit the seal variation *within* each Ekman number presented, and as it stands, each Ekman number in Fig. 6.1 represents a ten to twelve hour continuous run, about the limit of the batteries on the rotating frame and torque sensor. Lengthening the time at each torque step would have split each Ekman number over two days, which is undesirable from a practical point of view.

The two wide Ro ramps of Fig. 6.2 provide some evidence that the approximate collapse exists over the full range of Ro, but we note the discrepancy at the high Rossby number end, where the two constant Ω_i wide range ramps depart significantly. When the outer sphere is turned on, G/G_∞ rises significantly. After a

[2] See Fig. 5.5

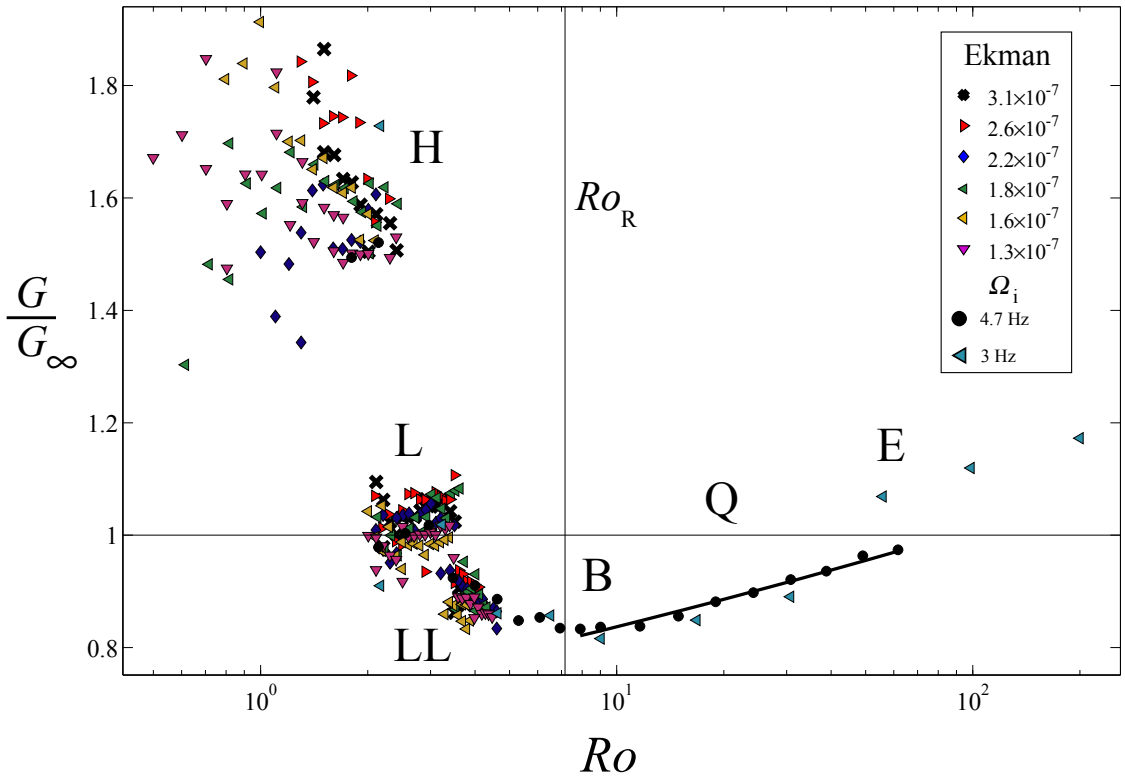

Fig. 6.2: G/G_∞ for the wide positive Rossby range, showing the entire studied range of $Ro > 0$ with state labels corresponding to Fig. 4.16. Symbols are the same as Fig. 6.1 with black circles and cyan triangles representing two wide-range ramps with $\Omega_i/2\pi = 4.725$ Hz and $\Omega_i/2\pi = 3$ Hz respectively. The three data points at large Ro with $G/G_infty > 1$ in the state range labeled E appear to be a real physical phenomena. In the wide-range 4.725 Hz data, the torque on the inner sphere persisted a short time and then dropped to a value consistent with the lower branch curve. However, in the 3 Hz data, this drop occurred on the third ramp step. We hypothesize that this drop has something to do with the formation of an Ekman layer on the outer sphere, and it is possible that the spin-up required to get the torque drop at 3 Hz took longer than the first couple of ramp steps. The large difference between the outer sphere stationary and the outer sphere rotating at 0.030 Hz seems strange at first. However, the Ekman number in the outer boundary layer drops from $E = \infty$ to 5.3×10^{-6} when this happens. Caution is advised, then, in identifying seemingly high Ro with asymptotically high Rossby number. The solid line fit is $G/G_\infty = 0.17 \log_{10} Ro + 0.67$, which is not a reasonable fit form for an asymptotic approach to unity as $Ro \to \infty$, but it does not seem that we should expect that anyway.

few ramp steps[3], this higher branch dropped to the lower in the middle of a step. It is not know if this might be a bistable or hysteretic state, or if it was just a long-time transient. There were other flow changes associated with the torque change, with increased mean velocities. In this case, the transducer was oriented to pick up nearly meridional circulations, which increased near the transition. Furthermore, the north polar pressure was observed to drop along with the torque increase.

When the vessel is sealed, the polar pressure givesn another corroboration of the conclusions regarding fast zonal flow. The polar pressure registers lower when the zonal flow is fast, and higher when it is not. So the conclusion regarding the three points of the 3 Hz data in Fig. 6.2 is the same as is reached in the rest of the states: lower torque is concurrent with faster zonal circulation. It may be that exceptionally long waiting times may permit observation of a bistable state in this region. Furthermore, this state may be hysteretic[4]. However, the extremely long times it may remain in either state make investigation of this phenomenon in the three meter experiment impossible.

Once low enough Ro is reached, the 3 Hz wide-range Ro data seems to agree well with that at 4.725 Hz. We fit G/G_∞ vs. $\log_{10} Ro$ for $Ro > Ro_R$ ($Ro > 7.16$) and obtain

$$G/G_\infty = 0.17 \log_{10} Ro + 0.67. \tag{6.5}$$

This is not a reasonable model if we expect an asymptotic approach to unity. How-

[3] 1.5 hours!

[4] Though no other state transitions seem to be so, excessively fast slewing of parameters can make transitions *appear* hysteretic.

ever, the observed multiple states at high Ro and the difference between the high Ro wave state and that with the outer sphere stationary may imply that there is not really a physical reason to expect an asymptotic approach from $Ro = 100$ to $Ro = \infty$ without further transtions. The state is simply different.

Though we do not have multiple data sets to collapse, we include fits to our measurement of G/G_∞ when $-4.5 < Ro < -1$ for the sake of completeness. These fits quantify the small contribution of the inertial modes. Figure 6.3 shows fits to G/G_∞ for the three ranges. The compensated torque for $Ro < 0$ can be modeled as

$$\frac{G}{G_\infty} = \begin{cases} -0.135Ro + 0.30 & \text{for} \quad Ro > -1.3 & : \text{(a)} \\ -0.135Ro + 0.27 & \text{for} \quad -2 < Ro < -1.5 & : \text{(b)} \\ -0.135Ro + 0.24 & \text{for} \quad -4.5 < Ro < -2.4 & : \text{(c)} \end{cases} . \tag{6.6}$$

The strong inertial modes simply seem to add a small amount to G/G_∞. The percentage change is about 6% for the (4, 1, 0.612) inertial mode that is active in range Fig. 6.3 (b). In Eq. 6.6, we forced the slope for the two points in Fig. 6.3(a) to be the same as the others.

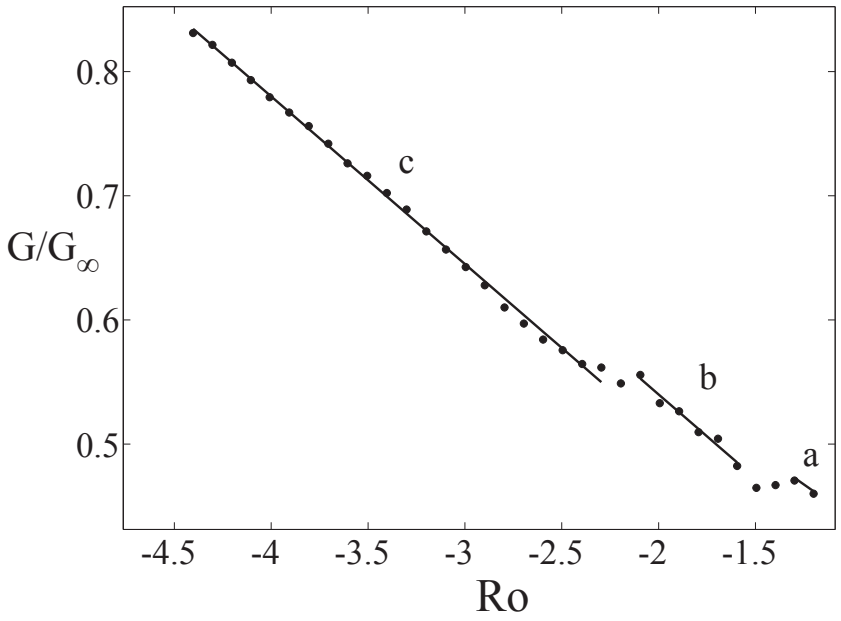

Fig. 6.3: G/G_∞ for the negative Rossby range. The influence of the inertial modes active in (b) and (a) seems to be additive to the background contribution. Fits are given in the text.

6.1.2 Constant Rossby Number

We mentioned before the possibility of residual Re-dependence in the quantity G/G_∞. The data of Fig. 6.4, G/G_∞ for a few ramps at constant Ro supports this idea. Figure. 6.4 includes data for $Ro = -2.15$, where the inertial mode $(4, 1, 0.612)$ is excited, and see that it fits into the overall picture, but with a significantly lower torque for a given Reynolds number than the other states. The rotating states scale a little more steeply with Re than the data with the outer sphere stationary, even when G/G_∞ is rather low, as with the $Ro = -2.15$ inertial mode state.

In Fig. 6.5, we divide the dimensionless torque by an alternative factor, CRe^2, with C chosen to make G/G_∞ the low torque state torque be close to unity, and note that the rotating states seem to be closer to the asymptotic scaling. We believe that the higher velocities and velocity fluctuations that are present in the rotating states cause this. Even when the torque is relatively smaller than that demanded at the same Re by the outer, the fast velocities and more vigorous velocity fluctuations caused by spatial concentration of the momentum transport mean that the boundary layers may be thinner. The stresses at the walls are then dominated by the pressure drops across the small roughness elements of the boundary surfaces, and viscous effects are negligible. This could happen even though the integrated stress is lower, because the local Re in the boundary layer is higher.

The normalizing factor we chose, G_∞, does not yet scale this steeply. So, we cannot yet identify G/G_∞ with a completely Re-independent Rossby dependence, and we cannot factorize the torque into a Rossby dependent friction factor and a

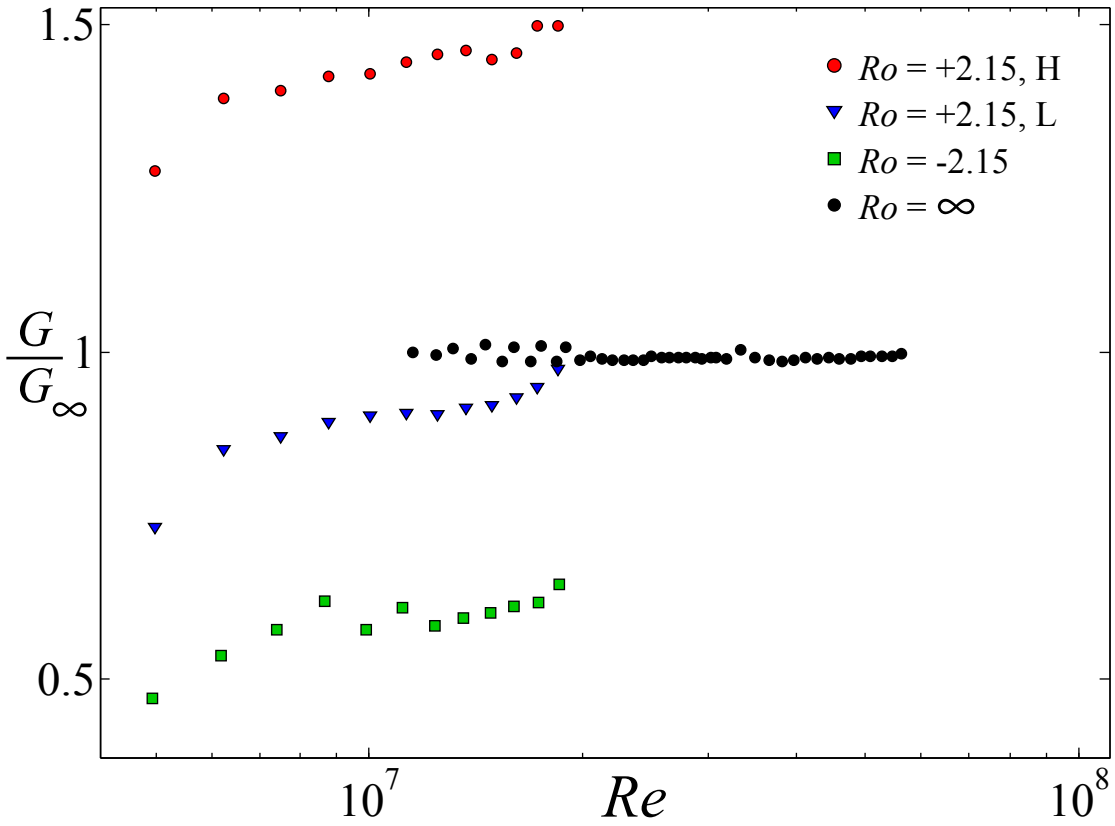

Fig. 6.4: G/G_∞ for selected data at constant Ro. The rotating states apparently scale a little more steeply than the nonrotating. Each value of Ro is done in a single continuous ramp, starting at high Ro and going downward, in the hopes of "breaking in" the seals for the day and stabilizing the medium-term drift.

single scaling with Reynolds. However, if we were able to reach the asymptotic $G \sim Re^2$ scaling in the outer sphere stationary state, G/G_∞ should become completely independent of Re. In other systems, it is possible that G/G_∞ does not have a systematic Re dependence because of the particulars of the system. We cannot rule out that $G/G_\infty = f(Ro)$ for other geometries at large but finite Re, because other systems may have the same residual effects of viscosity in all flow states.

The prediction of Eq. 6.1 is one of the significant testable predictions of this dissertation, and can be tested approximately by investigating G/G_∞ or G/Re^2. The complex Rossby dependence in spherical Couette flow, especially at low Ro, will be different in other geometries, as it appears to involve inertial modes of the sphere here. The slight changes in the switching boundaries seen at the end of Chapter 5 in the perturbed geometry of the 60 cm experiment make it clear that even small changes in geometry have an effect. A slightly perturbed geometry results in a $f(Ro)$ with minor shifts in state switch boundaries. However, a different geometry, like Taylor-Couette flow, will exhibit a much different $f(Ro)$. Furthermore, it is anticipated that geometrical details that significantly change the engagement with one rotating boundary or another would result in significant changes in $f(Ro)$. Examples of apparatus changes expected to greatly influence $f(Ro)$ might be roughening of the inner sphere in spherical Couette or changing of the end-cap speeds in a Taylor-Couette apparatus. The latter is of interest in Taylor-Couette experiments aimed at tuning the bulk velocity profile to study the magnetorotational instability[143]. Usually, the ends of a Taylor-Couette apparatus revolve with the outer cylinder, which is a closed tank. Split end rings or end rings coupled to the inner should

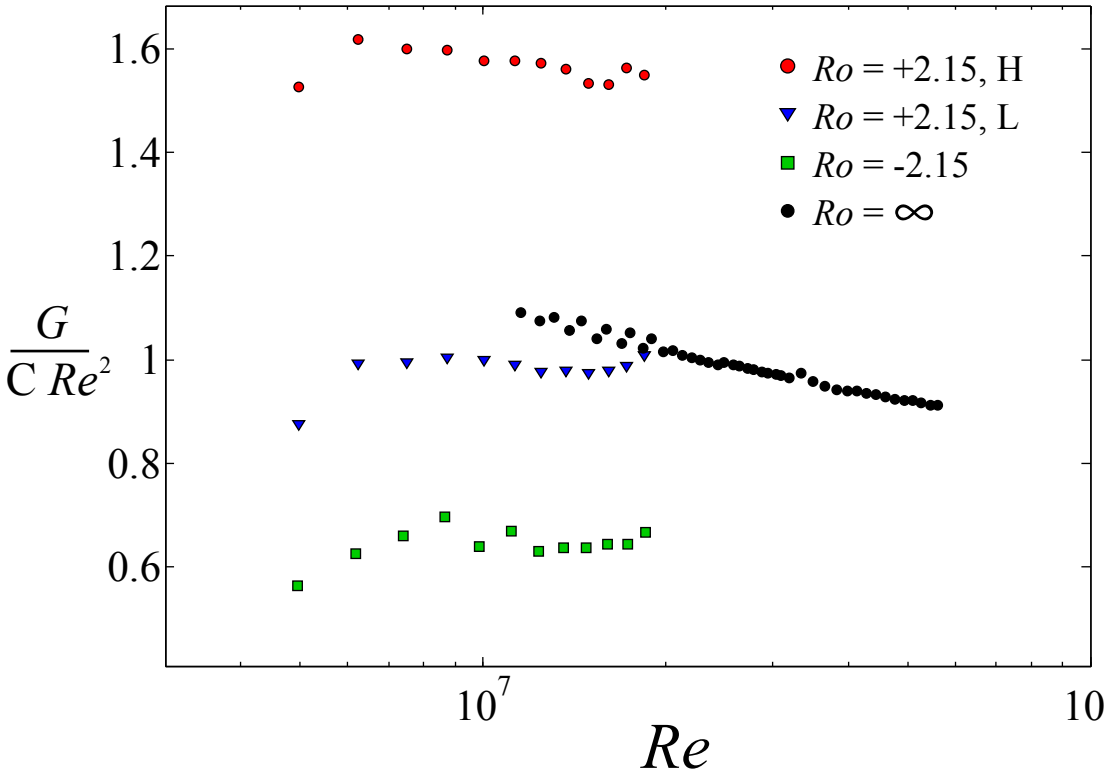

Fig. 6.5: G normalized by an alternative scaling $G\ Re^2$ with a normalization with respect to the low torque state. The scaling in the rotating states, even when the relative torque is low with respect to outer stationary, seems to be somewhat closer to Re^2. It is possible that this is due to the shear concentration of Fig. 4.19, resulting in higher velocities and closer-to-asymptotic turbulent boundary layers even when the total angular momentum transport is throttled by zonal flow transport barriers.

significantly modify $f(Ro)$.

We note a recent result by Ravelet *et al.* [127], where turbulent flow in a wide gap Taylor-Couette apparatus shows a bifurcation to a secondary flow state as a quantity similar to the Rossby number[5] is varied. The torque on the inner cylinder seems to give results consistent with ours at high enough Re. The rotation number of Ravelet *et al.* selects different turbulent flow patterns and the torque for different flows approaches the same scaling when Re exceeds 10^4. The highest Re reached is about 2×10^5. Data soon to be submitted for publication by Paoletti *et al.* on high precision torque measurements in independently rotating Taylor-Couette flow reaches the same conclusion as well. The compensated torque G/G_∞ is a function primarily of Ro [144]. It is, however, nothing like the dependence noted in spherical Couette flow, consistent with the prediction that geometry plays a critical role.

6.2 Fluctuation Scaling

We conclude this chapter with some analysis of the scaling of the turbulent fluctuations and waves in the system. We investigate the collapse of wall shear stress spectra with Re for two different constant values of Ro. The frequencies of all of the motion at a given value of Ro should scale with the overall system timescale. Whenever the outer sphere revolves, we have normalized the frequencies by the outer sphere rotation frequency. We have not explicitly discussed this as an expected scaling, but we will see below that it it appropriately collapses the

[5] They use a different parameter, which they call the rotation number $(1-\eta)(Re_i+Re_o)/(Re_i-Re_o)$, and they also use the abbreviation Ro.

frequency content of the turbulent motions in the system. We define

$$\omega' = \frac{\omega}{\Omega_o}, \tag{6.7}$$

the dimensionless frequency of the turbulent motions.

We will investigate power spectra of the wall shear stress. The wall shear stress is linearized using the procedure described in Sec. 5.3.1, and has units of Pa. We recall the expected stress scale from the equations of motion Eq. 1.8, $\rho\Omega LU$. We chose this as the dimensionless pressure scale, and we adopt it here as a dimensionless wall shear stress scale as well. With $L = \ell = r_i - r_o$, $U = Ro\,\Omega_o L$, and $\Omega = \Omega_o$, we may construct a quantity, $\rho^2\Omega_o^3 Ro^2\ell^4$ that has the units of the power spectral density, $\mathrm{Pa}^2/\mathrm{Hz}$. We use that quantity to make the power spectra dimensionless as

$$S'(\omega/\Omega_o) = \frac{S(\omega/\Omega_o)}{\rho^2\Omega_o^3 Ro^2\ell^4}. \tag{6.8}$$

We will see that this collapses the broadband portions of the spectra fairly well for the low torque state at $Ro = +2.15$. However, when $Ro = -2.15$, it is the power in the strong inertial mode (4, 1, 0.612) that collapses best. The broadband background collapses upon further multiplication by $Re^{2/3}$. The power in the frequency band identified with the inertial mode in both states scales differently than the broadband background.

6.2.1 $Ro = +2.15$, Bistable L State

We choose to look at fluctuation scaling using the frequency spectra[6] due to the wide variety of wave motions we observe. Figure 6.6 depicts the dimensionless

[6] Rather than, say, the standard deviation of fluctuating quantities.

power spectra $S'(\omega')$ as defined in Eq. 6.8. The low-frequency fluctuations in the frequency range labeled LF, and the turbulent 0.71 Ω_o wave in the frequency range labeled TW both show good collapse in their dimensionless power spectra. However, we notice that the inertial mode (3, 1, -0.1766) in the frequency range marked W is stronger in some of the spectra. This wave grows in relative strength as Re is increased. Furthermore, the high frequency end of the spectrum does not show a good collapse here, with the power in the high frequency fluctuations falling with Re.

We can investigate this more quantitatively by calculating an approximation of the total dimensionless power in each of the marked frequency bands,

$$P_{\omega'} = \sum_{\omega'} S'(\omega')\Delta\omega'. \tag{6.9}$$

In Fig. 6.7, we plot the Reynolds number dependence of $P_{\omega'}$ for four of the bands marked in Fig. 6.6.

The fit for the LF region has a slight Reynolds number dependence but is close to flat. The inertial mode peak, Fig. 6.6 W, grows one power of Re faster than the broadband low-frequency turbulence. This seems to be at the expense of the high frequency fluctuations, as there is a steep decrease in the bands around 25 Ω_o and 90 Ω_o, scaling like $Re^{-2.1}$ and $Re^{-2.6}$ respectively.

Because $Re = Ro/E$, and Ro is held constant, we see that the inertial mode power in the band W is growing in importance as rotation is increased. The fractional power in the inertial mode rises from 6% of the total spectral power at the lowest rotation rate to 25% of the total spectral power at the fastest rotation rate.

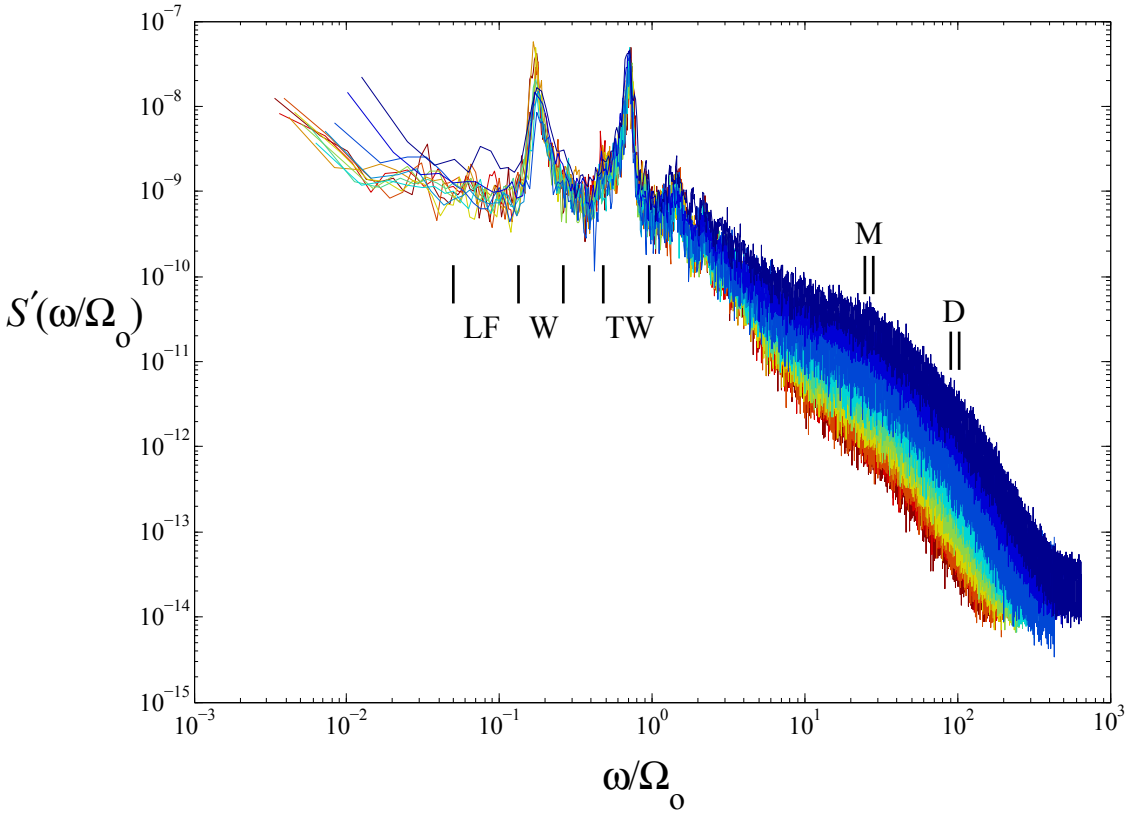

Fig. 6.6: Wall shear stress dimensionless power spectra $S'(\omega')$ conditioned on the low torque state $Ro = +2.15$, $5 \times 10^6 < Re < 5 \times 10^7$. Dark blue is the lowest Re and deep red is the highest. The expected scaling for the power spectral density based on the expected scaling of fluid stresses collapses the low-frequency broadband region well. The the turbulent L state wave in the region TW collapses as well. However, we see that the region marked W, which we identify as the inertial mode (3, 1, 0.1766), scales a little more steeply than the rest of the turbulence, and the high frequency region of the spectrum scales less steeply. We label the M and D frequency ranges for reference in Fig. 6.7.

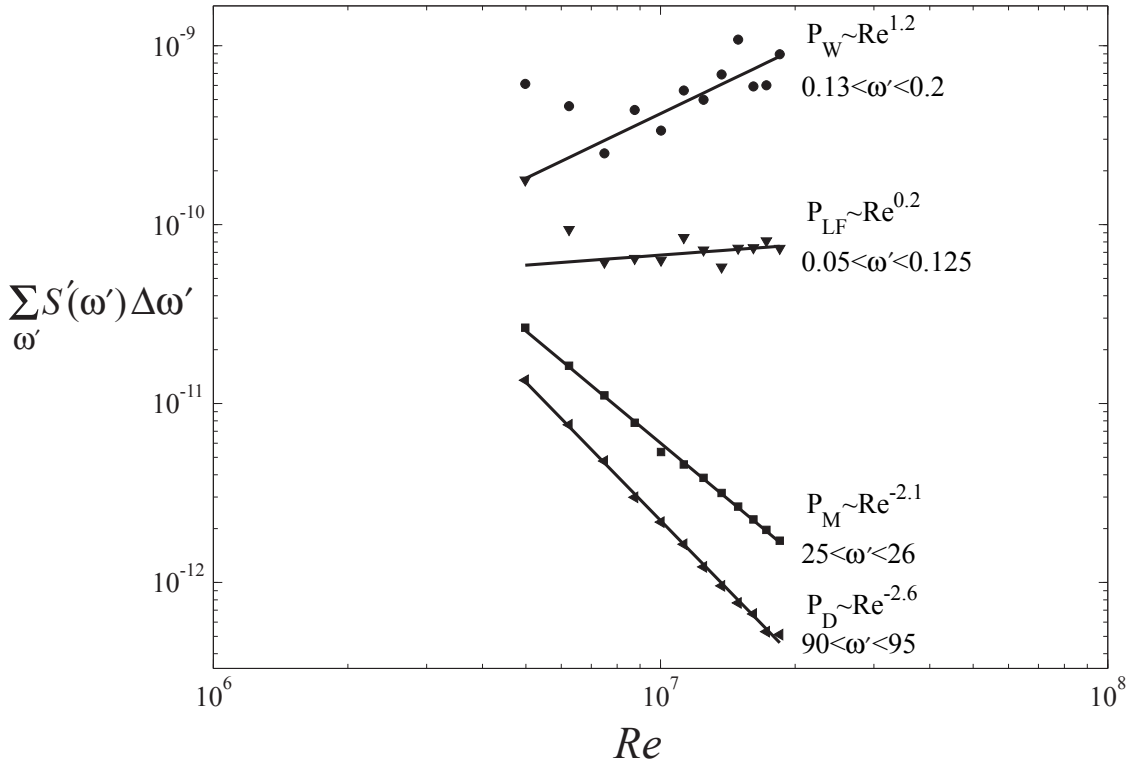

Fig. 6.7: Scaling of the power spectral density $P_{\omega'}$ for the low torque state at $Ro = +2.15$. The power averaged over the frequency band listed, S_{LF}, is nearly flat, showing that the expected stress scale captures the scaling well. The power spectral density in the inertial mode W band scales more steeply than the turbulence, while the power spectral density in the M and D high frequency bands decrease with increasing Re. The inertial mode appears to be growing at the expense of the higher frequency fluctuations, which are probably associated with small spatial scales. Because $Re = Ro/E$, it seems that lowering E by increasing the rotation results in more importance of the inertial mode in the total fluctuations.

The strengthening of the inertial mode at the expense of the high frequency fluctuations suggests that the mode may somehow be suppressing small scale turbulent fluctuations.

6.2.2 $Ro = -2.15$, *Inertial Mode Dominated*

We repeat the same analysis above for the strong excitation of the (4, 1, -0.612) inertial mode for $Ro = -2.15$. The dimensionless power spectra divided by $Re^{-2/3}$ are plotted in Fig. 6.8. We choose to include the factor of $Re^{2/3}$ to collapse the spectra of the broadband energy containing fluctuations at low frequencies, based on the empirical scaling shown in Fig. 6.9.

We see from Figure 6.9 that the inertial mode peak itself scales with the predicted power spectral density scale of Eq. 6.8. The inertial mode frequency band has constant spectral power as Re is increased, or equivalently, as E is decreased. The other fluctuations, including the broad band of LF fluctuations, are all decreasing as the rotation increases. The total dimensionless spectral power is nearly constant, but the inertial mode contains much of that power.

We should mention, finally, that we conclude that the turbulent fluctuations are weakening with respect to the inertial mode using wall shear stress sensors. A critique may be posed, as we have not corrected for spatial averaging by the 2 mm square sensors. Our sensors are approximately 40 Kolmogorov lengths ($L_{\text{Kolm}} = (\nu^3/\epsilon)^{1/4} \sim 50$ μm) square at the highest Re presented here. It is well known that the spatial averaging of fluctuations results in decreasing spectral power with increasing Re [145, 146]. The inertial mode power, with its global scale, would

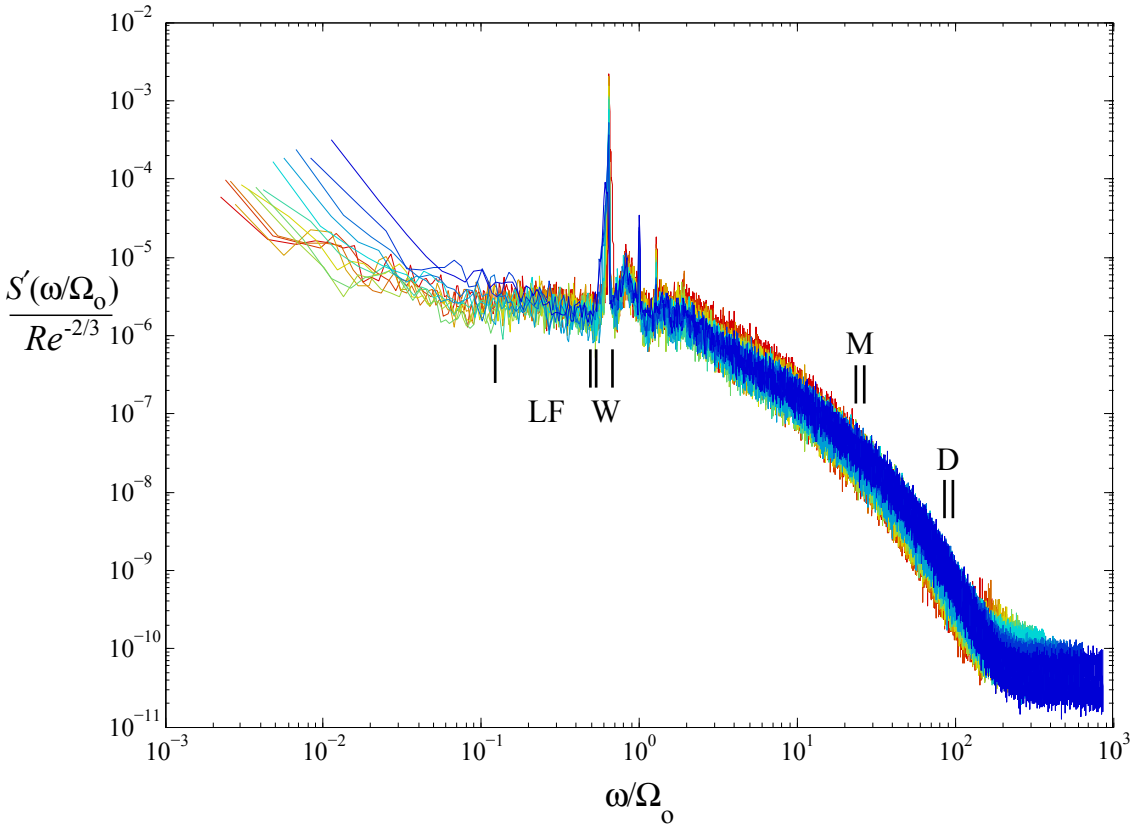

Fig. 6.8: Dimensionless wall shear power spectral collapse , $Ro = -2.15$, $5 \times 10^6 < Re < 5 \times 10^7$. The strong inertial wave peak of the (4, 1, -0.612) inertial mode (actually at 0.64 Ω_o at this Ro), has constant dimensionless spectral power, with the rest of the fluctuations falling with Re (or alternatively, falling with decreasing E, highlighting the importance of rotation.)

not be influenced by spatial averaging. Corrections for these effects are beyond the scope of this dissertation, but we do not think that they are a major issue to our interpretation.

The low-frequency and turbulent wave region of Fig. 6.6 show good collapse in the same spectral region where the inertial mode is growing when collapsed by the expected power spectral scale. The low-frequency regions are associated with large spatial scales which will not be averaged over by our 2 mm square sensor, and the inertial mode peak Fig. 6.6 W is growing with respect to these fluctuations. Some of the rolloff of the high frequency fluctuations may be due to spatial averaging, but the basic conclusion would appear to be sound. In both Fig. 6.6 and Fig. 6.8, the inertial mode peak is strengthening in relative power compared to the energy containing low-frequency turbulence. The energy containing large scales will be responsible for the majority of the transport in the bulk. The observed high frequency rolloff may be partially or wholly due spatial averaging by the wall shear stress sensors used, but the strengthening of the inertial mode with respect to the low-frequency, typically large-scale fluctuations is enough to make our case.

6.3 Inertial Modes' Role

In both of the cases considered here, the spectral power associated with an inertial mode becomes increasingly important to the overall turbulent flow as the rotation rate is increased. We should not necessarily take that observation to mean that the turbulence is weakening in favor of a simple, sinusoidal motion of fluid

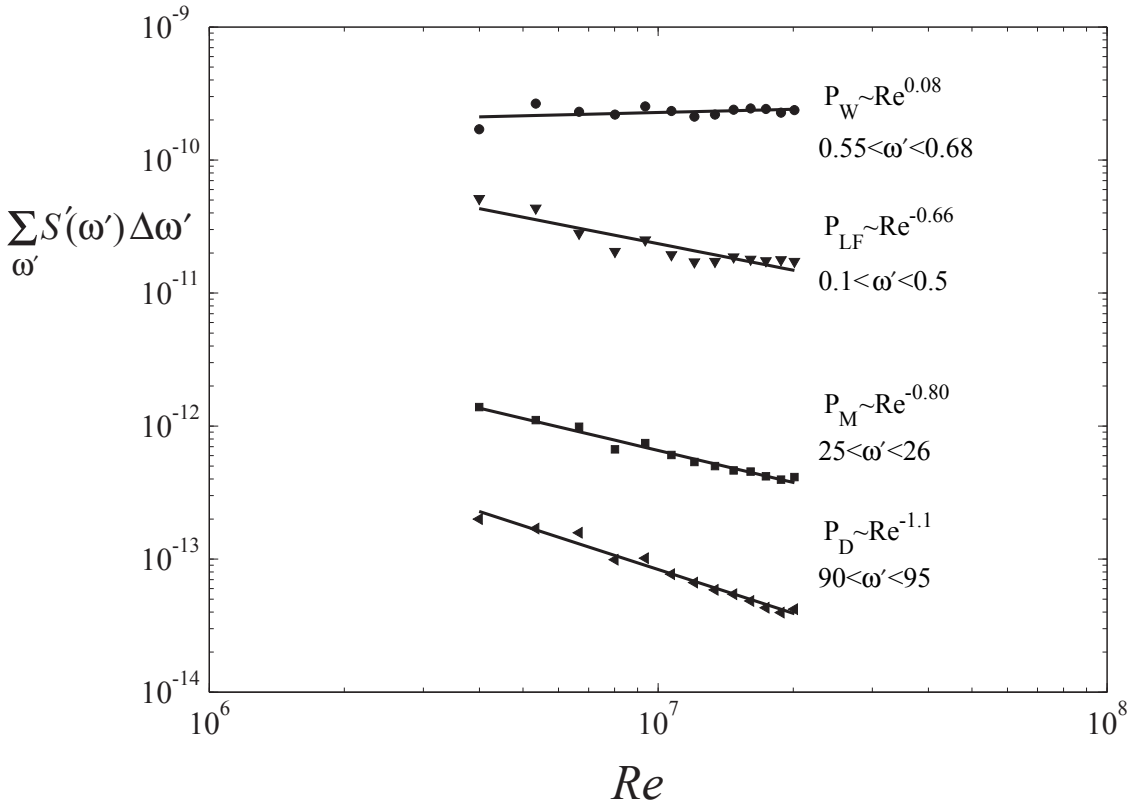

Fig. 6.9: Scaling of the power spectral density $P_{\omega'}$ in the bands indicated in Fig. 6.8. The inertial wave is scaling more steeply with Re than the rest of the turbulence. The deficient scaling at high frequency may be a property of the flow, but it may also be due to the changing bandwidth of a CTA circuit with mean flow speed.

particles. The motion associated with the narrow inertial mode peak in Fig. 6.8 is complicated. Fig. 6.10 shows a band-pass filtered velocity time series. The velocity measurement is taken approximately 20 cm from the outer sphere wall at a cylindrical radius of about 68 cm and the transducer beam is 45° down from the vertical and turned 45° out of the $s - z$ plane, so that it is sensitive to all three velocity components.

The velocity signal is filtered using a phase-preserving fourth-order Butterworth bandpass filter with 20% fractional bandwidth[7]. This is comparable in width to the band used to calculate the wave power in Fig. 6.9, and little motion outside that which is responsible for the large peak of Fig. 6.8 is admitted by the filter. Fig. 6.10 suggests that the inertial mode itself is deeply modulated by low-frequency fluctuations. The lower plot is a zoom showing the inertial mode "carrier" wave and its modulation envelope. Both velocities are normalized by the outer sphere tangential velocity, so they can be considered the local Rossby number of this motion.

The modulation envelope velocity u_e is calculated as

$$u_\mathrm{e} = \sqrt{2\mathcal{F}\left\{u_\mathrm{w}^2(t)\right\}}. \tag{6.10}$$

where the filter operator $\mathcal{F}$ is a fourth order Butterworth filter with a cutoff 90% of the inertial mode frequency. Equation. 6.10 is a type of running RMS calculation[8]. Figure 6.11 shows a probability distribution of the inertial mode's envelope. The probability distribution is gaussian, with a mean $u_\mathrm{w}/(\Omega_\mathrm{o} r_\mathrm{o}) = 0.014$ and a standard

[7] Cutoff frequencies ±10% of the center frequency

[8] Done with a rectangular window, this applies a "boxcar" filter to the data. The Butterworth has a flatter amplitude response with frequency in the passband, so the author prefers it.

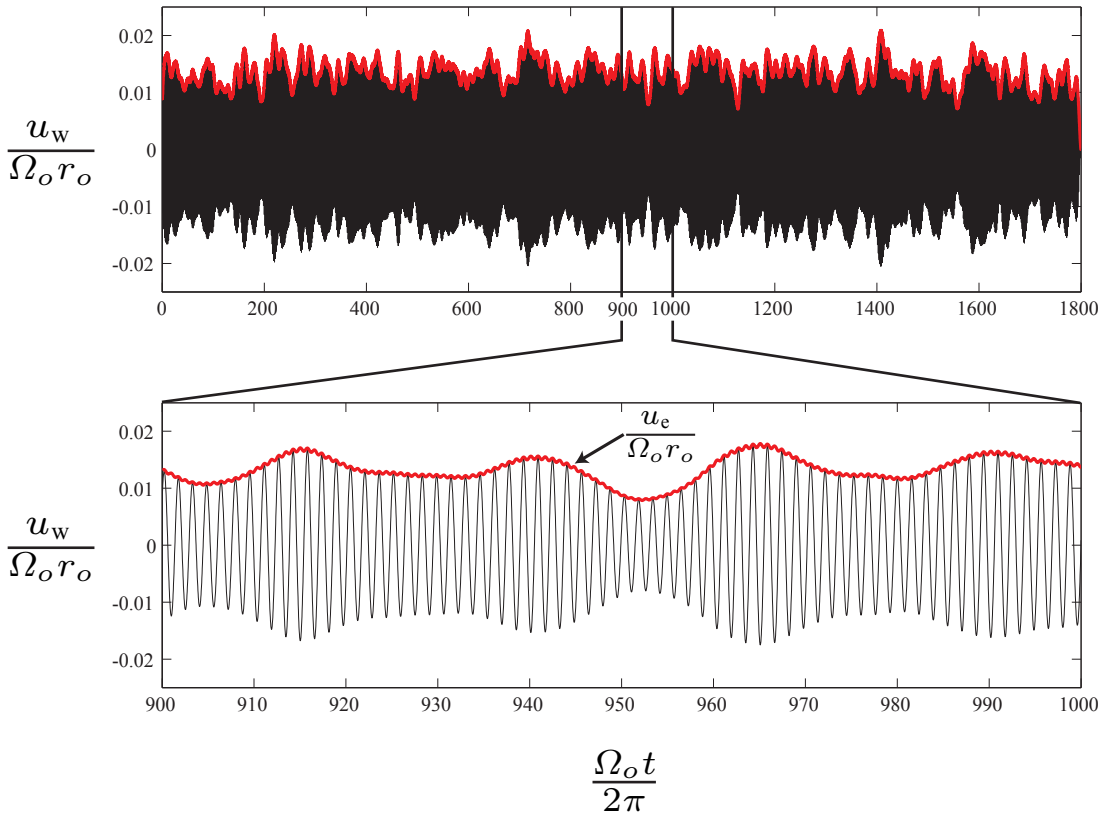

Fig. 6.10: Band-pass filtered velocity time series of an inertial mode and calculated modulation envelope , normalized by the outer sphere tangential velocity, $Ro = -2.15$, $E = 1.1 \times 10^{-7}$. The band pass filter has a fractional bandwidth of 20%, comparable to the band over which the "wave" power was calculated in Fig. 6.9. The lower plot is a zoom in clearly showing the modulated inertial mode oscillations. The red curve is the modulation envelope, defined in Eq. 6.10. The inertial mode appears to be deeply amplitude modulated, possibly due to significant non-linear interactions.

deviation 17% of the mean. It seems that the inertial mode is strongly fluctuating, and although it is not at high amplitude, there is reason to believe it could be important to the transport.

A single linear inertial mode cannot, by itself, transport angular momentum. However, Tilgner [21] has shown that the internal shear layers associated with an inertial mode are capable of driving zonal flows, and the ratio of the zonal flow energy compared to the oscillatory energy can rise to large levels at small E. This has been investigated in an experiment by Morize *et al.* down to $E = 3 \times 10^{-5}$ in a full sphere [147]. For $E \sim 10^{-7}$, the zonal flows in Tilgner's numerical study equilibrated at $10^2 - 10^6$ times the energy of the mode that was driving them. An upper estimate of the zonal flow Rossby number is given by Tilgner, which reduces to

$$\frac{u_\mathrm{Z}}{\Omega_\mathrm{o} r_\mathrm{o}} = \frac{2\pi}{3} \left(\frac{E}{10^{-3}} \right)^{-3/4} \left(\frac{u_\mathrm{w}}{\Omega_\mathrm{o} r_\mathrm{o}} \right)^2 . \tag{6.11}$$

With a mean wave amplitude $u_\mathrm{w}/(\Omega_\mathrm{o} r_\mathrm{o}) = 0.014$, and $E = 10^{-7}$, this gives a prediction of an average zonal flow of $u_\mathrm{Z}/(\Omega_\mathrm{o} r_\mathrm{o}) = 0.4$.

Generation of a zonal velocity of this magnitude would be more than sufficient for the mode to participate significantly in the angular momentum transport. If the wave could force retrograde zonal velocities at large radius and prograde zonal flows, this would cause additional drag on the inner sphere, transporting angular momentum from the more rapidly rotating fluid at large radius and transferring it to the inner boundary. Increasing efficiency of this process may short-circuit other types of nonlinear angular momentum transport and subsequently reduce those

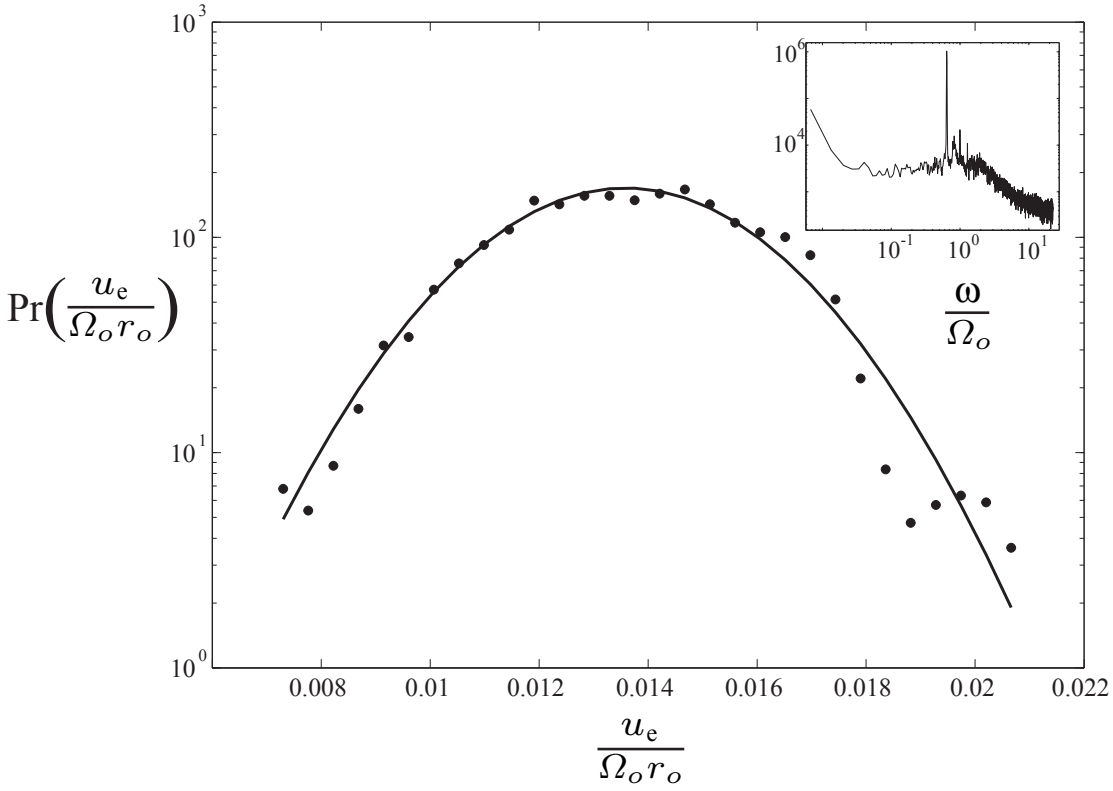

Fig. 6.11: Probability distribution of the modulation envelope velocity u_e defined in Eq. 6.10 and shown in Fig. 6.10, normalized by the outer sphere tangential velocity. The envelope fluctuations are nearly gaussian, with a standard deviation 17% of the mean. The inset shows a velocity power spectrum of the unfiltered data, to reinforce the point that the modulations are at very low frequencies, so that a narrow inertial mode peak may still come from a strongly fluctuating wave.

turbulent fluctuations not associated with the mode.

The deep low-frequency modulations of the inertial mode might imply that a growing zonal flow pattern interferes with the energy source for the inertial mode. The over-reflection mechanism proposed by Kelley and collaborators [12, 14, 15] implies that modes in spherical Couette flow are excited by fluid shear in a a self-consistent feedback process. This is unlike the body force drive invoked by Tilgner for tidally driven inertial modes, which cannot be modified by the flow. A wave-generated zonal circulation might interfere with the over-reflection process once it became strong enough. This sort of feedback, coupled with the likely long time lag for zonal flow spin-up could lead to slow modulations on an over-reflectionally excited inertial mode.

This is only one of many possible mechanisms for angular momentum transport in inhomogenous rotating turbulence, but it is a simple one that does not rely on large amplitude waves. That does not mean that high amplitude waves are not important[9]. Wave breaking processes of large amplitude Rossby waves are important to momentum transfer into the jet streams [88, 89]. Wave breaking can be the primary mode of cross-flow transport when strong zonal transport barriers are present. This is important in stratospheric mixing. There is little transport across the boundaries of the stratospheric polar vortices on Earth except when Rossby waves can grow and break on the zonal flow [63–65]. Something like Rossby wave breaking could play an important role in our experiment.

[9] And we do not have a good idea of what "high amplitude" is in terms of the wave Rossby number where significant nonlinearity is noted.

We may also consider the possibility that inertial modes may grow large and break, or that they may undergo some kind of shear or centrifugal instability. A phenomenon called resonant collapse is noted in experiments on inertial modes forced resonantly by precession in cylinders [148] and spheres [149, 150]. Inertial mode breaking by instability of strong modes could explain a fluctuating mode. However, it might be expected that the energy in a mode in that case would grow somewhat slowly and then crash quickly as instability set in.

We focused the discussion of this section particularly on the mode (4, 1, 0.612). There were several reasons to discuss it in the context of inertial modes in turbulence. It has been documented before [12, 14, 15], with an over-reflection mechanism proposed for its excitation. It also exists alone as the strongest wave motion, unlike the waves observed in the $Ro > 0$ low torque state, the higher frequency of which cannot yet be identified with an inertial mode. However, the lower frequency wave in many of the $Ro > 0$ states appears to be the inertial mode (3, 1, -0.1766), which persists through several flow transitions to extremely high Ro. It is deeply modulated like the mode discussed above, in fact, it is more so. The wide range over which it exists makes it somewhat difficult understand the role it plays.

The same can be said for the low-frequency, as of yet unidentified[10] wave for $Ro < 0$ visible in Fig. 4.8 at $0.083\Omega_o$, which is only completely absent when the (4, 1, 0.612) mode is strong. What we do know about both of these low-frequency waves is they are relatively unaffected by the Rossby number. The (3, 1, -0.1766) inertial mode has much of its kinetic energy located at large cylindrical radius, near

[10] The lowest wavenumber possibility for a retrograde mode near this frequency is (23, 20, 0.0896).

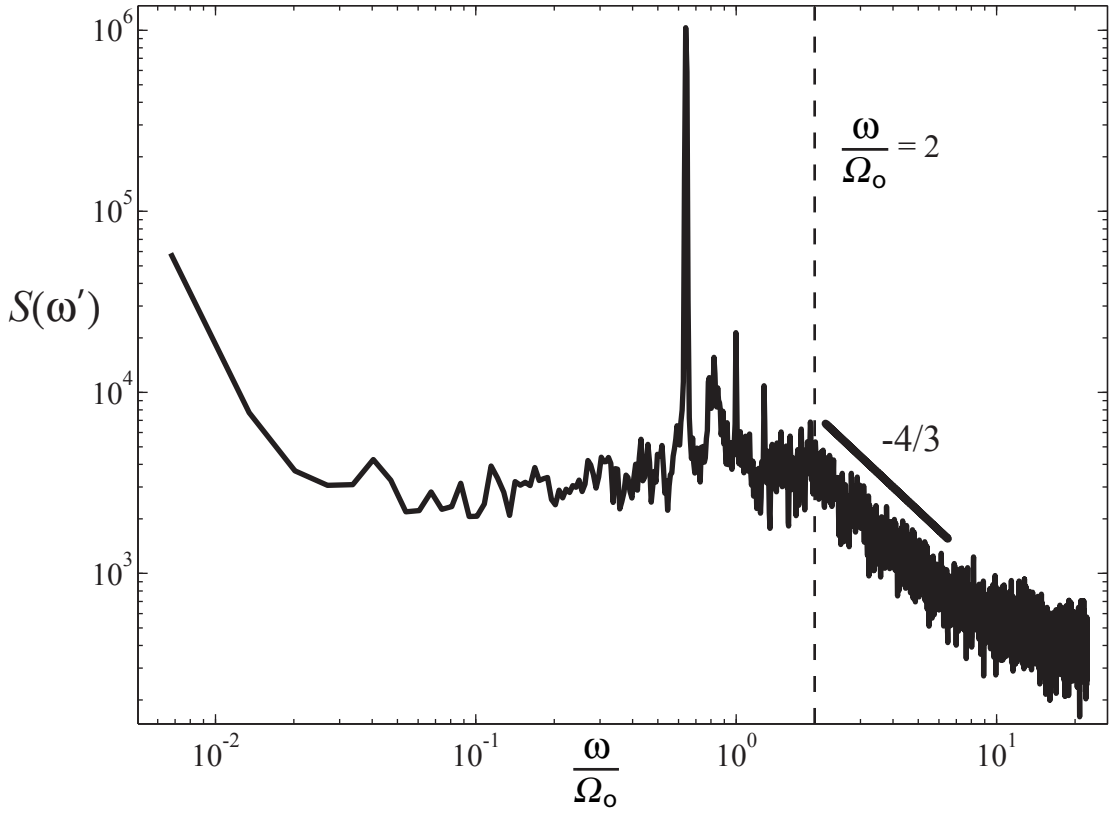

Fig. 6.12: Velocity power spectrum, $Ro = -2.15$, $E = 1.1 \times 10^{-7}$, the same as inset of Fig. 6.11, showing a knee at 2 Ω_o. This suggests that inertial waves or modes are important to the low-frequency, probably large to medium scale portion of the broadband turbulence.

the equator of the outer sphere, perhaps making it understandable that it would be less modified by the flow nearer the inner sphere. But what is it doing there? Perhaps it plays a very general role in angular momentum transport in much the same way that a few simple inertial modes may arise to transport heat in rapidly rotating spherical convection [22]. It may be that the (3, 1, -0.1766) mode plus one or two other Rossby-type modes associated with the other peaks in Fig. 4.16 are associated with the bulk of the angular momentum transport for $0 < Ro < 15$.

We should mention again a point that we touched on briefly in Sec. 4.3. Gen-

erally speaking, in addition to the strong single inertial modes excited as part of the flow when both spheres revolve, the broadband portion of the spectra of rotating states tends to be rather flat at frequencies less than twice the outer sphere rotation rate. This is true for Fig. 4.9, Fig. 6.6, Fig. 6.8, and the velocity power spectrum inset of Fig. 6.11 which we reproduce here in Fig. 6.12, as it is a nice example. Below twice the outer rotation rate, the spectrum is somewhat flat, and a knee is present around 2 Ω_o with higher frequencies falling off like $\omega^{-4/3}$. The persistence of a knee near 2 Ω_o in many states when the outer sphere revolves suggests that inertial waves and modes play a role in the broadband turbulent background, as they cannot exist above this frequency. The flat spectrum by itself is not much evidence, but the fact that rolloff occurs in the vicinity of 2 Ω_o is suggestive of turbulence consisting of a sea of inertial modes.

7. SUMMARY, SPECULATION, AND FUTURE WORK

7.1 Summary

We have described a series of hydrodynamic experiments in turbulent, rapidly rotating shear flow of water between concentric rotating spheres. The world-unique experiment is the result of a long design and construction process in which the author played a key role. In most of these experiments, we have reached unprecedented dimensionless parameters for this geometry. We drive strong turbulence with Reynolds number up to 56 million and study the effects of rapid rotation, lowering the Ekman number down to 10^{-7}. In most regions of parameter space that we have studied, the flow is characterized not only by intense turbulent fluctuations, but by large-scale energetic wave or vortex motions.

For $Ro = \infty$ with the outer sphere stationary, we observe low-frequency oscillations consistent with slowly precessing large-scale vortical motions in the system with $m = 1$ and broken equatorial reflectional symmetry. We hypothesize that they result from a pressure-driven modulation of the equatorial outflow from the turbulent Ekman boundary layer near the rapidly rotating inner sphere. These motions are confirmed over at least an order of magnitude in Re by comparison of data from the sixty centimeter experiment with that from the three-meter experi-

ment. These low-frequency oscillations contain a great deal of energy and imply that some energetic non-universal large scales in high Re turbulence may go unnoticed if experimental observations or simulation runs are not conducted over long enough times.

When $Ro < 0$, we confirm the excitation of inertial modes similar to those of the full sphere[1], as reported previously in this geometry at similar parameters [12–15]. We establish that these inertial mode motions appear to be robust to turbulence in the system, and show signs of nonlinear evolution. Furthermore, as Re is increased (or E decreased, equivalently), the inertial modes appear to further dominate the turbulence. We hypothesize that non-linear processes involving inertial modes may play a role in non-local angular momentum transport by zonal flow generation, reducing that which must be transported by the turbulent fluctuations.

When $Ro > 0$, we observe that transitions between the turbulent flow states are associated with more dramatic changes, including the torque on the inner sphere, measured mean velocities and fluctuations. The temporal fluctuations of torque on the inner sphere are stronger for turbulent states in the range $0 < Ro < 15$. The mean torque at a given Reynolds number is significantly different for each of the observed turbulent flow states for all Ro, but the mean difference in G/G_∞ between adjacent states is dramatic when $0 < Ro < 5$. We find that the wall shear stress and mean azimuthal velocity at our measurement location at 23.5° co-latitude is anti-correlated with changes in the relative torque. We analyze one turbulent flow transition in detail and conclude that different angular momentum transport barriers

[1] Modes indistinguishable from the full sphere modes by our measurements, at least.

due to different zonal flows are responsible for the turbulent flow transitions. The wall shear stress and azimuthal velocities at our measurement location are higher in the lower relative torque states because of the stronger zonal flows, despite a lower total angular momentum flux away from the inner sphere.

The regions of parameter space where particular turbulent flow states exist appear to be bounded simply by constant Rossby number, with the overall strength of the motion, turbulent fluctuations, and angular momentum transport scaling with Re in a similar way to other turbulent flows. We hypothesize that the torque in a turbulent swirling shear flow with overall rotation should take the form $G = f(Ro)\, g(Re)$ at least as $Re \to \infty$ with $g(Re) \to Re^2$. We find that the quantity G/G_∞, the dimensionless torque divided by the fit to torque measured at the same Re when $Ro = \infty$, is a nearly Re-independent quantity. The compensated torque G/G_∞ summarizes the effect of the very different turbulent flows occurring at different Rossby number on the torque. When Re is high enough, we hypothesize that G/G_∞ should become a relation that only depends on Ro. At the Reynolds numbers we investigate $G/G_\infty = h(Ro, Re)$ may be interpreted as a friction factor that expresses, in part, the effect of the self-organizing *flow* geometry on the turbulent drag forces on the walls. The quantity G/G_∞ should be a useful quantity to express the effects of the different possible turbulent flows on the angular momentum transport in any turbulent rotating shear flow.

The experiments presented here show the rich behavior possible in inhomogeneous, anisotropic turbulent flow with and without outer boundary rotation. We make a few concrete predictions that should extend to other turbulent shear flows.

We find that inertial modes appear to be important as part of the large-scale energetic flow in all rotating states. Furthermore, we note a knee in power spectra at $2\Omega_o$ when both spheres revolve suggesting that the turbulence for fluctuation frequencies $0 < \omega < 2\Omega_o$ may reasonably described as a sea of interacting inertial modes or inertial waves. However, the inhomogeneity and waves in high Reynolds number shear flow between concentric spheres do not require outer boundary rotation, as we see from the large-scale wave when $Ro = \infty$. In all cases, the turbulence is inhomogeneous, anisotropic, wavy, and influenced by the boundary layers to form non-trivial large-scale flows that contain much of the energy. These energetic non-universal, large-scale flows are not annoyances to be eliminated from a turbulence experiment, but important parts of a realistic high Reynolds number flow that must be understood fully in order to make good predictions about the turbulent transport properties in real systems.

7.2 On Extreme Inhomogeneity

We might offer some further speculation on the interesting dynamics of the large scales presented here with regard to what to expect in inhomogeneous systems. When we have presented long-time dynamics throughout this dissertation we have made heavy use of numerical low pass filtering and band-pass filtering to reveal some of the fluid behavior. We might reflect a bit on why this was necessary. The underlying issue is that fast turbulent fluctuations are so large that they generally obscure the mean shifts and slow fluctuations. The slow fluctuations in low pass

filtered data are clearly and unambiguously correlated with other dynamics, as in the torque and azimuthal velocity time series of Fig. 4.15. The torque fluctuations are low-pass filtered naturally[2] by mechanical damping and integration of stress fluctuations over a large area. The velocity fluctuations are not.

The velocity fluctuations in the H and L states, for example, overlap significantly in the tails of the distributions. This is clear from Fig. 5.8. Typically, we have large levels of velocity fluctuations, with RMS velocities 16% of the mean in the low torque state and approaching 60% in the high torque state. The large high frequency fluctuations can obscure the low-frequency fluctuations which are well correlated with other measurements like the torque.

Evidently, there are a wide range of length, time and velocity scales for the velocity fluctuations that do not present sufficient perturbation via advective nonlinearity to promptly change the large-scale flows. Undoubtedly, these fluctuations matter to the overall transport when the Reynolds stresses from long lasting velocity correlations act over long times, but in the instantaneous measurements, they appear as noise. We might think of a simpler system that shows the same behavior. Figure 7.1 depicts two turbulent mixers connected by pipes such that they will generally pump fluid into the other. Let's imagine that the typical flow rates in the pipes when one mixer blade is stationary may correspond to one-tenth of the azimuthal velocities typical in each mixer.

Each mixer has its own turbulent dynamics. If the experiment is large enough and powerful enough, the flow in the apparatus could be turbulent throughout for

[2] Though mechanical noise is still be filtered out with a low pass filter.

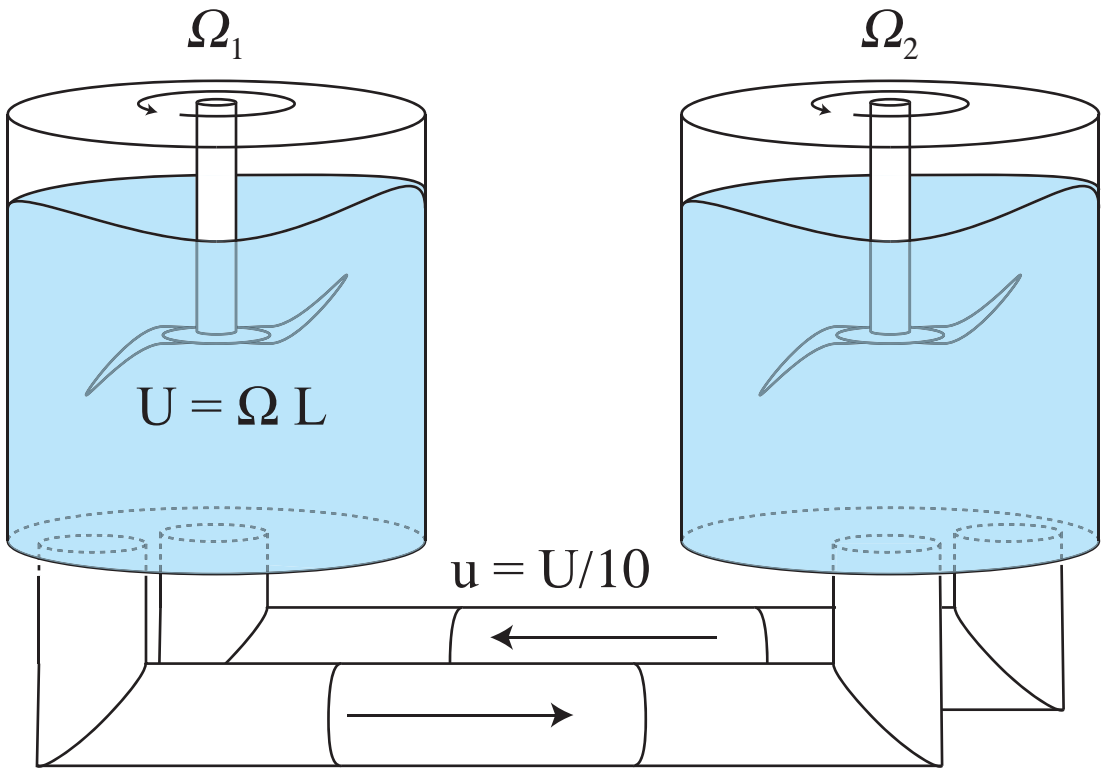

Fig. 7.1: Two identical turbulent mixers are cross connected by pipes, allowing them to pump fluid into each other with weak flow in the pipes. We may expect a wide variety of collective dynamics as the ratio Ω_1/Ω_2 is adjusted.

any speed ratio, including when one blade is stationary. But the turbulence would be extremely inhomogeneous, with relatively weak flow and small fluctuations in the the inoperational tank. It is likely that the collective turbulent motion when both impellers revolve would be much different than when only one mixer was operational. With both impellers rotating in the same direction, the mass flux and fluctuation levels in the pipes would typically be much higher than with only one rotating. And we might expect that the collective dynamics would be a sensitive function of Ω_1/Ω_2. In this thought experiment[3], it is not irrelevant that each system is turbulent. The large-scale turbulent pressure and velocity fluctuation profile and infrequent, intense fluctuations at the inlet and outlet ports will greatly affect the mass flow and the level of the fluctuations advected through the pipes.

But at the same time, the relative influence of the two systems on each other will be fairly weak on short timescales. Large vortices shed from the second impeller cannot directly advect the flow from the first. The collective dynamics would probably be, in general, slow, with some time needed for the mass flux to change, and for swirling fluid in the pipes to spin up and down. The influence of the other system on the dynamics of the first would be undeniable, but it would take time to act. The fast velocity fluctuations in an active mixer of the coupled system might not show much clear difference from a single running mixer until a large change occurred in the flow between mixers. Many of the measured fluctuations would be irrelevant to the behavior of the other system except in their average effects on the long-time collective dynamics. The physically imposed inhomogeneity makes it hard

[3] Which may easily be turned into a real experiment.

to imagine a situation where the flow in system as a whole could approach a turbulent state that had any properties that only depended on the total power input. It would seem very unusual if the large-scale flow state, especially the circulation through the pipes, was found to decouple from the ratio of the impeller speeds in this hypothetical system. However, if point measurements were made in tank number one, it might be difficult to appreciate the difference between the situation when impeller two was rotating and when it was not, unless time series were long and the fast, smaller scale fluctuations in the measurements were filtered out.

We might imagine that a similar process is responsible for the states we observe in the three-meter apparatus. Instead of two mixers weakly coupled with pipes, we might imagine that regions of the experiment act as lightly coupled turbulent systems. Zonal flow transport barriers and regions of relatively quiet fluid with weak turbulence could partially isolate parts of the fluid from each other. Motions near the outer sphere may always be expected to locked more to the outer sphere by the effects of the rotation, while those inside the tangent cylinder and near the inner sphere will always feel more influence of the inner sphere. These regions of the fluid are not uncoupled, and it is not irrelevant that each sub-region of the fluid is fully turbulent. But they may communicate mostly via wave-driven momentum fluxes and slowly acting Reynolds stresses due to persistent correlations of faster fluctuations. The internal dynamics of each fluid sub-region could be somewhat robust, and the communication between the regions potentially somewhat weak.

Increasing the overall strength of the velocity fluctuations does not imply that the nonlinear advection between systems will destroy the dynamics of the inde-

pendent systems. At a given speed ratio in either case, the individual systems' "internal" dynamics increase in strength in proportion to the cross coupling. There will always be a need for the second dimensionless parameter, $Ro = \Omega_{\mathrm{i}}/\Omega_{\mathrm{o}} - 1$ in spherical Couette and, similarly, the speed ratio Ω_1/Ω_2 in the case of the mixing tanks. The same may be said for any other dual-driven system. Taylor-Couette flow with independently rotating cylinders should always have Ro as an important parameter, and von Kármán flow with independently rotating impellers will depend sensitively on Ω_1/Ω_2, even as $Re \to \infty$. In such inhomogeneous systems, at any point the strong fluctuations from the "far" impeller cannot be expected to wholly overwhelm the fluctuations from the "near" impeller just because the overall vigor of the flow is increased, and that is really what would be needed to homogenize an inhomogeneous system. Indeed, von Kármán flow is a system known to exhibit multi-stability and even hysteresis in highly turbulent flow [137].

7.3 Potential Impacts

7.3.1 Atmospheric Dynamics

We may make some speculative predictions as to the applicability of this work in other flows that show some of the same characteristics. In Chapter 2 we mentioned that the mean circulation in the three-meter experiment filled with water and the jet streams in the atmosphere of the Earth are reasonably close to the same Rossby number, and the Ekman number in the atmosphere for motions on the scale of the troposphere thickness is only two orders of magnitude lower than that in the

experiment. We might briefly revisit this idea now that we have discussed the wide variety of motions that are possible in the experiment.

We hypothesize that zonal flow transport barriers and/or interactions of large vortical motions with the turbulent boundary layers in the experiment are relevant to the development of the different turbulent flow states, and we establish that the important control parameter selecting different flows is Ro. In the case of the Earth, Ro and Re are slaved together for a given flow pattern. However, if our observation applies two orders of magnitude lower in E, as it might if all the boundary layers are fully turbulent and we have reached an asymptotic regime, there may be some applicability to climate prediction.

The large-scale flows herein may be considered the global general circulation of the experiment. We have observed complex, multi-stable behavior in a similar parameter regime to our atmosphere that seems to rely only on inhomogeneity of the turbulence (not the fluid) and a dimensionless ratio of two advective timescales, Ro. It is probable that the influence of the large-scale flows on the net transfer of momentum and energy out of the boundary layers is of some importance in all of the states observed here. However, each state is present over a fairly wide range of Ro, making it clear that modest changes of energy input and fluctuations do not change the general pattern except at critical values of Ro.

If the turbulence in Earth's atmosphere behaves in a similar way, perhaps it would allow some aspects of possible changes to global circulation patterns to be modeled with simpler models for the energy inputs than those commonly used, provided that the turbulent momentum fluxes were parameterized appropriately. It

may be that the properties of the turbulent momentum transport could dominate over subtle issues of the energy budget. Working to understand the multi-stability in systems free of the additional complications of moisture, stratification, dust transport, and radiative processes could prove fruitful.

7.3.2 Dynamo Prognosis

The three-meter experiment, as we discussed in Chapters 2 and 3, is intended to model the flowing molten iron in the outer core of the Earth. We will soon fill it with liquid sodium metal and perform these experiments, but we may ask what we have learned from the purely hydrodynamic experiments we have completed. One of the critical ingredients in a successful turbulent dynamo is some measure of self-organization.

Other hydromagnetic experiments [76, 151, 152] suggest that large flow fluctuations are important in raising the critical magnetic Reynolds number of turbulent liquid metal dynamos above a value that the experiment was designed to achieve. Some experiments are designed using water models with flow visualization, and the time-averaged velocity field tuned toward a pattern that would act as a kinematic dynamo at an achievable magnetic Reynolds number. These experiments have shown that this condition is insufficient, because the flow is rarely close to an instantaneous snapshot of the mean flow [152]. Large scale fluctuations frequently spoil the suitability of the actual velocity field as a low critical R_m dynamo. Consequently, these apparatus do not self-generate even though their mean flow would if it were steady.

The induction measurements of Volk *et al.* [152] show that the fluctuations of magnetic induction and flow field in turbulent Von Kármán flow at the desired rotation rate ration have largely flat, featureless spectra, indicating that there is no preferential time or spatial scale for fluctuations[4]. However, we find that no state in spherical Couette flow is free from strong waves, some of which are extremely coherent in terms of frequency and spatial correlation. And though we discussed the fluctuating nature of these waves, those in the rotating states, especially for $Ro < 0$ inertial mode excitation, are easily recognizable in time snapshots of the magnetic induction. While they are fluctuating, they remain similar to an instantaneous snapshot of an inertial mode. Furthermore, inertial modes seem to be strengthening with respect to other fluctuations as the rotation rate is increased. We might hope that these self-organizing turbulent flows could be useful for dynamo action, and we may look in particular at inertial modes because they are in a sense the "most coherent" motions in the system.

It is known that one important ingredient in some dynamo scenarios is flow helicity [153]. The helicity is the volume integral of the helicity density $h = \mathbf{u} \cdot (\nabla \times \mathbf{u})$. Helicity is important for the so-called α-effect in dynamo action, wherein fields are twisted and stretched by helical motion, such that the field lines resemble the Greek letter α. The the α-effect may result in a dynamo when combined with the differential rotation. Such a dynamo is referred to as an $\alpha\omega$-dynamo [153]. It seems that an inertial mode may generally provide some α-effect. Figure 7.2 shows a Mollweide

[4] Volk *et al.* *do* find a low-frequency modulation at 1/100 the disks' frequency involving their midplane shear layer, but filter it out.

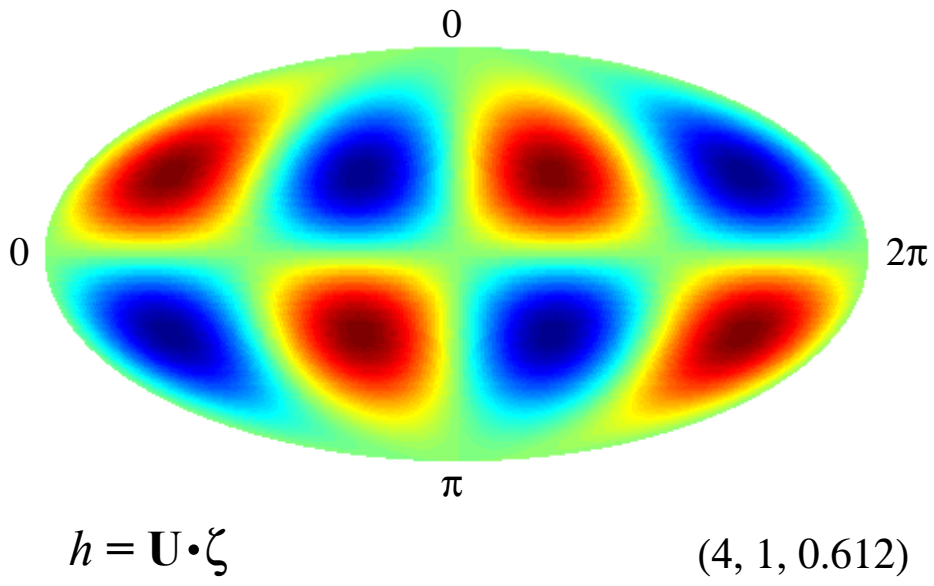

Fig. 7.2: Mollweide projection of the helicity density $h = \mathbf{U} \cdot \nabla \times \mathbf{U}$ for the (4, 1, 0.612) inertial mode of the full sphere. The vorticity $\boldsymbol{\zeta} = \nabla \times \mathbf{U}$ given in Appendix A. While the net helicity of every inertial mode seems to be zero, the modes possess large-scale patches of helicity, which is thought to be a useful ingredient for dynamo action.

projection of the helicity density of the inertial mode (4, 1, 0.612) calculated from the velocities given by Zhang *et al.* [10] and the curl of those expressions, provided in Appendix A. This $m = 1$ inertial mode has an $m = 2$ pattern of large-scale patches of helicity density. The volume integral of the helicity density is zero, which can be anticipated by symmetry arguments. But the large-scale patches of alternating helicity density may be beneficial for a dynamo.

We may estimate the maximum magnetic Reynolds number for this inertial mode motion from our measured velocities. Figure. 6.11 shows that the mean amplitude of the (4, 1, 0.612) inertial mode is $U/(\Omega_o r_o) = 0.014$. Furthermore, this mode would only show velocity fluctuations of about half the global maximum am-

plitude because of the measurement location. So we may expect $U/(\Omega_o r_o) \sim 0.028$ peak velocity for this mode. The magnetic Reynolds number for this motion at this dimensionless velocity scale and the outer sphere rotating at 4 Hz, using a typical length scale[5] of 2 m is

$$R_m = \frac{0.028 \cdot 2\pi \cdot 1.5m \cdot 4Hz \cdot 2m}{0.083m^2/s} = 25. \tag{7.1}$$

The typical velocity of the differential rotation in this state might be $U/(\Omega_o r_o) = 0.2$, giving $R_m = 180$ for the zonal flow. So, at maximum design rotation rate, we may expect a strong self-consistent flow that includes useful ingredients of helicity and differential rotation and has R_m based on actual flow measurements greatly exceeding unity. Furthermore, while we find that the inertial mode is fluctuating, its motion typically rather strong with respect to other turbulent fluctuations. The water measurements seem to support the idea that we could achieve high R_m large-scale-coherent flow organized by rapid rotation, possibly one that is useful as an $\alpha\omega$-type dynamo.

7.4 Future Work

Drawing to a close here, at the culmination of a long and interesting program of study toward a Ph.D., one must wonder what the future holds. In this case, the most immediate future is known. The author has devoted the best part of a decade toward this experimental apparatus, and would prefer to be among the first authors

[5] One quarter of the circumference at 30° latitude, as typical of where the helicity patches are strong.

on the first publications if it is indeed a liquid sodium dynamo. If all goes smoothly in the next year or so, the intention is to fill with sodium and begin hydromagnetic experiments in a brief post-doctoral stint.

The large and difficult task of fielding the experiment means that this apparatus may not have been been wrung dry of results[6] even in terms of what can be learned from the hydrodynamic flows. However, the author did reach a point of diminishing returns at the end of the experimental campaign. In fact, one might say that a point of collapsed returns was reached, where new ideas for measurements that would give more insight yielded zero new results for a couple of weeks, and that spelled the end of the experimental campaign. It is just simply too difficult to make the hydrodynamic measurements necessary to better characterize the flow in this device.

Therefore, a similar device, smaller and faster to reach similar dimensionless parameters, but with optical access could finish the scientific story we have presented here. We have generated a long list of hypotheses regarding the inhomogeneity, the mean zonal flows, and the location and nature of the observed wave states. It would be gratifying to have these hypotheses confirmed and possibly even more interesting to falsify them. The author has used a great deal of imagination in this dissertation work. What we know about the time-averaged zonal flows in this apparatus might be best described as educated imagination. This has been, at times, frustrating, to have a rather small peephole into such an interesting flow. It would be something of a relief to shine a few watts of laser sheet into a seeded flow of a 1 m spherical

[6] Though it will be thoroughly wrung dry of *water* before the sodium fill.

Couette apparatus rotating some 10 Hz or so. Although this is a massive experiment by many standards, it seems like a small task now.

An interesting question in more general terms is the relationship between the flux of some quantity through a turbulent flow and storage of the same quantity by the fluid. We recall the angular momentum fluctuations of Figure 5.6 in Chapter 5. In the author's opinion, this was one of the most surprising findings to come out of this experimental campaign. The z-component of angular momentum enters and leaves via the boundaries, but the question of how much of it is present at any time in the fluid between the boundaries is not something that occurred to the author before these results were found. A turbulent shear flow apparatus with very sensitive strain-gauge torque measurements on both the inner *and* outer boundaries could allow much more information about the angular momentum transport and storage, and would allow absolute integration from fluid start-up. Corroborating these results with direct measurements of the relative angular momentum in the rotating frame using velocimetry could be quite fruitful.

In terms of the medium term goals of the scientific program in the University of Maryland three-meter experiment and suggestions for the author's successors on this project, it is important to develop as many flow diagnostics as is possible. Permanent magnet potential probes may stand in for wall shear stress sensors [154]. Ultrasound velocimetry is useable but some additional design is necessary to improve the transducers used by Sisan *et al.* [118] for deeper measurements in sodium. A magnetic field array like that used by Sisan [118] and Kelley [117] can be fielded quickly, but longer-term plans call for a higher resolution magnetic field array with

three-dimensional sensors. Because of the large size of the experiment, it is possible that instrumenting the inner sphere could be fruitful as well. A more sophisticated version of the wireless acquisition device used for the torque, but with many channels of 16 bit acquisition should now be possible (see Appendix E), and could acquire torque as well as data from an array of field and flow sensors on the inner sphere. Ultrasound transducers could be installed in the inner shaft or on the inner sphere, and this would be considerably safer than installing them at low latitudes on the outer sphere. It is important to have good flow measurements to corroborate magnetic measurements and to participate in the process of understanding appropriate parameterizations for the effects of turbulence or reduced models based on intelligent truncations of the velocity field into inertial modes and geostrophic components. Work of this nature will be critical for prediction of high Reynolds number hydromagnetic flows for many decades to come.

APPENDIX

A. VORTICITY OF INERTIAL MODES IN A SPHERE

The net helicity

$$H = \int \mathbf{U} \cdot \zeta \, dV \tag{A.1}$$

and the helicity density

$$h = \mathbf{U} \cdot \zeta \tag{A.2}$$

for inertial modes in a sphere may be interesting quantities relevant to magneto-hydrodynamics in spherical Couette flow, given the observed strong excitation of such modes in that geometry [12, 14] and the importance of helicity to the dynamo problem. The vorticity

$$\zeta = \nabla \times \mathbf{U}, \tag{A.3}$$

of the inertial modes of a full sphere can be calculated by taking the curl of the velocities given by Zhang *et al.* [10]. The expressions are recorded here for convenience in future work. The analytical form for the net helicity is not immediately applicable to this dissertation so no attempt has been made to calculate the volume integral given in Eq. A.1. A numerical estimate for the net helicity of several modes has been made by calculating the helicity density on a grid of points and summing, and as expected by symmetry considerations, it seems to be zero. However, most inertial modes exhibit large regions of alternating-sign helicity density. A few notable

exceptions will be discussed at the end of this appendix.

The velocity of each inertial mode is given by Zhang *et al.*, 2001 in the form $\mathbf{U} = \langle U_\mathrm{s}, U_\phi, U_\mathrm{z}\rangle\ e^{\mathrm{i}(m\phi+2\sigma t)}$. In cylindrical coordinates, the components of $\zeta = \langle \zeta_\mathrm{s}, \zeta_\phi, \zeta_\mathrm{z}\rangle\ e^{\mathrm{i}(m\phi+2\sigma t)}$ are, for equatorially symmetric modes, (Eqns. 4.1 in Zhang *et al.*)

$$\begin{aligned}
\zeta_\mathrm{s} &= -\sum_{i=0}^{N}\sum_{j=0}^{N-i} C_{ijmN}\ \sigma^{2i-1}\ (1-\sigma^2)^{j-1}\ (2i)(m+m\sigma+2\sigma j)\ s^{2j+m-1}\ z^{2i-1} \\
\zeta_\phi &= -\mathrm{i}\sum_{i=0}^{N}\sum_{j=0}^{N-i} C_{ijmN}\ \sigma^{2i-1}\ (1-\sigma^2)^{j-1}\ (2i)(m+m\sigma+2j)\ s^{2j+m-1}\ z^{2i-1} \\
\zeta_\mathrm{z} &= \sum_{i=0}^{N}\sum_{j=0}^{N-i} C_{ijmN}\ \sigma^{2i}\ (1-\sigma^2)^{j-1}\ (4j)(j+m)\ s^{2j+m-2}\ z^{2i}
\end{aligned} \tag{A.4}$$

Note that the above summations all start at $i = 0$. The first term in the i sum will be zero for the radial and azimuthal vorticities, but it is written in to avoid index confusion.

For the equatorially antisymmetric modes, with velocities given by Eqns. 4.6 of Zhang *et al.*,

$$\begin{aligned}
\zeta_\mathrm{s} &= -\sum_{i=0}^{N}\sum_{j=0}^{N-i} C_{ijmN}\ \sigma^{2i-1}\ (1-\sigma^2)^{j-1}\ (2i+1)(m+m\sigma+2\sigma j)\ s^{2j+m-1}\ z^{2i} \\
\zeta_\phi &= -\mathrm{i}\sum_{i=0}^{N}\sum_{j=0}^{N-i} C_{ijmN}\ \sigma^{2i-1}\ (1-\sigma^2)^{j-1}\ (2i+1)(m+m\sigma+2j)\ s^{2j+m-1}\ z^{2i} \\
\zeta_\mathrm{z} &= \sum_{i=0}^{N}\sum_{j=0}^{N-i} C_{ijmN}\ \sigma^{2i}\ (1-\sigma^2)^{j-1}\ (4j)(j+m)\ s^{2j+m-2}\ z^{2i+1}
\end{aligned} \tag{A.5}$$

The coefficients C_{ijmN} for the equatorially symmetric and antisymmetric modes can be found in Zhang *et al.*.

Some special inertial modes of subclass $N = 0$ with $l - m = 1$ have *identically* zero helicity density $\mathbf{U} \cdot \zeta$. The most obvious example is that of the spinover mode, $(N, l, m, \omega) = (0, 2, 1, 1)$. This mode consists of solid body rotation about an axis orthogonal to the rotation axis. In this case, it is clear that the velocity and vorticity will be everywhere perpendicular. However, it appears that this is the case for every inertial mode with $(N, l, m, \omega) = (0, l, l - 1, \omega)$. These modes are also those with zero spherical radial velocity, and are therefore modes of the spherical shell [17]. These modes are among those observed in spherical Couette flow [14].

It is unknown whether this property of mutually perpendicular velocity and vorticity everywhere is of any interest in real physical systems, but it seemed sufficiently notable for inclusion here.

B. SHORT FORM EXPERIMENTAL OVERVIEW

For those not interested in the detailed description of Chapter 3, a short-form experimental description sufficient to situate the reader for the scientific results of Chapter 4 and forward is reproduced here:

The three meter spherical Couette apparatus allows independent rotation of the nominally 3 m diameter outer shell and 1 m diameter inner sphere. Instrumentation in the rotating frame allows measurements of velocity, wall shear and pressure on the turbulent flow of water, as well as the torques required to maintain the boundary speeds. The apparatus is depicted in Fig. B.1.

The stainless steel outer vessel has a 2.92 ± 0.005 m inner diameter and is 2.54 cm thick. It is mounted on a pair of spherical roller bearings that are constrained by a stainless steel framework. The vessel top lid, which is inserted in a 1.5 m diameter cylindrical flanged opening, has a hemispherical bottom surface that completes the outer sphere. The top lid has four 13 cm diameter instrumentation ports centered on a 60 cm radius. The ports have inserts that hold measurement probes nearly flush with the inner surface of the outer sphere. The 1.02 ± 0.005 m diameter inner sphere is supported on a 16.8 cm diameter shaft held coaxial with the outer shell by bearings at the bottom of the outer sphere and in the top lid. The outer sphere is driven by a 250 kW induction motor mounted to the support

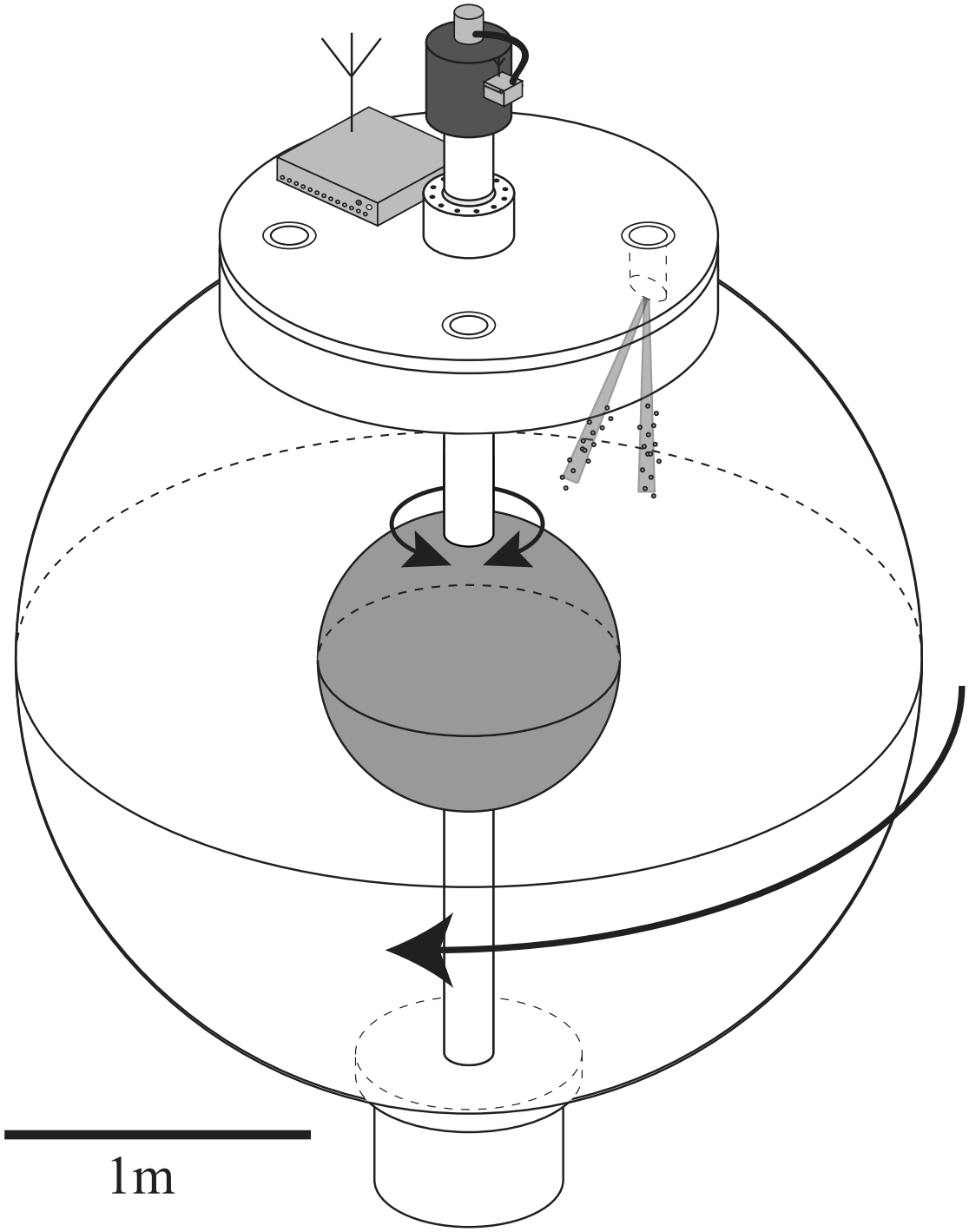

Fig. B.1: A schematic of the apparatus showing the inner and outer sphere and locations of measurement ports in the vessel top lid at 60 cm radius (1.18 r_i). Data from sensors in the ports are acquired by instrumentation, including an acquisition computer, bolted to the rotating lid and wirelessly transferred to the lab frame. Also shown is the wireless torque sensor on the inner shaft.

frame. A timing belt couples the motor to a toothed pulley on the lid rim, reducing the shaft speed by a factor of 8.33. The inner sphere is directly driven from a second induction motor through an elastomeric coupling and a calibrated Futek model TFF600 torsional load cell.

A rotating computer acquires data from sensors that include a Dantec model 55R46 flush mount shear stress sensor driven by a TSI model 1750 constant temperature anemometer and three Kistler model 211B5 pressure transducers. These transducers are AC coupled with a lower -3 dB cutoff frequency of 0.05 Hz, allowing sensitive measurements of pressure fluctuations on top of the high steady centrifugal background pressure encountered in rapid rotation. A thermocouple is used to monitor fluid temperature and a DC-coupled pressure transducer in a port near the pole of the outer sphere allows monitoring of the overall system pressure. The sampling rate for these sensors is 512 Hz. The rotating acquisition computer is networked to the lab frame using wireless ethernet, allowing storage of the data on a lab frame computer and remote control of the acquisition and various auxiliary equipment.

A Met-Flow UVP-DUO pulsed Doppler ultrasound velocimeter is mounted in the rotating frame and paired with Signal Processing transducers. Communications with this instrument are handled over the wireless connection. Some velocity data in this paper was acquired with a Met-Flow UVP-X1-PS in the lab frame using a resonant transformer arrangement to couple the signal to and from the transducer in the rotating frame. The flow is seeded with 150 μm $-$ 250 μm polystyrene particles with nominal density of 1050 kg/m^3. An emission frequency of 4 MHz was used for the measurements presented here. Limitations on the product of maximum

measurable velocity and measurement depth constrain the velocity measurements in this paper to be very close to the wall, typically in the range of 30-100 mm deep. Three transducers are installed in the experiment, and can be configured to measure the velocity along the spherical radial direction, a direction parallel to the rotation axis or in a direction contained in the plane normal to the cylindrical radial direction, inclined at an angle $\pm 45^\circ$ or $\pm 23.5^\circ$ with the vertical.

Power for instruments on the outer sphere rotating frame is supplied by a bank of four parallel 35 Ah 12 V sealed lead acid batteries. DC-DC converters supply needed voltages for instrumentation and an inverter provides 120 VAC for the UVP-DUO. The millivolt signal from the Futek torque sensor mounted on the inner sphere shaft is amplified and digitized, and the data transmitted to the lab frame using a wireless serial connection. The torque is sampled approximately 32 times per second. Power for the inner torque sensor is provided by lithium polymer batteries.

The induction motors' speeds are controlled by variable frequency drives under computer command. Optical sensors monitor the inner and outer sphere speeds which are controlled to better than 0.2%. The drives estimate the motor torque from electrical measurements and the torque measurements agree well with the calibrated torque sensor at motor speeds above 2 Hz. This allows measurement of the torque required to drive the outer sphere over much of the operational range of the experiment. There is a confounding effect of the inner shaft's bearings and seal, and a confounding effect of aerodynamic and bearing drag on the outer sphere. The average outer sphere confounding torque can be subtracted off by measuring

the torque demanded with no differential rotation.

C. MECHANICAL DRAWINGS

This appendix collects some relevant mechanical drawings produced in the course of this dissertation work.

all dimensions in inches

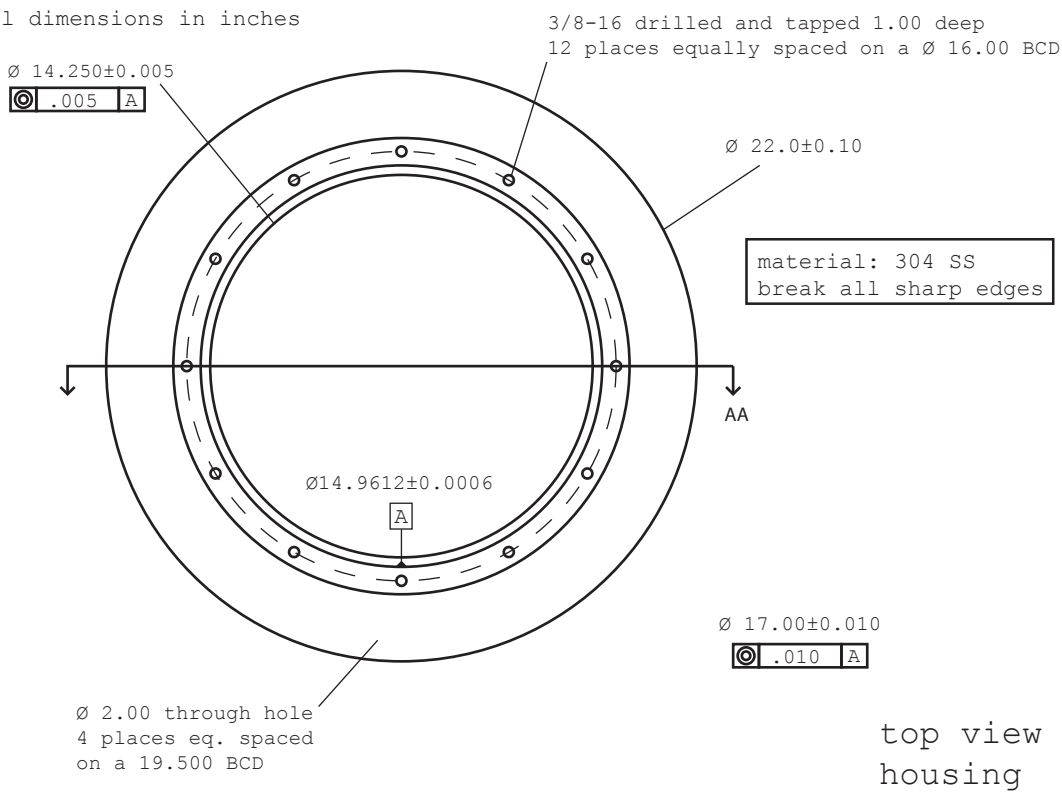

top view
housing

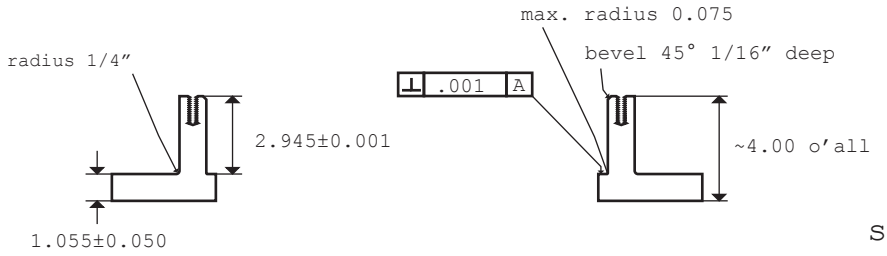

section AA
housing

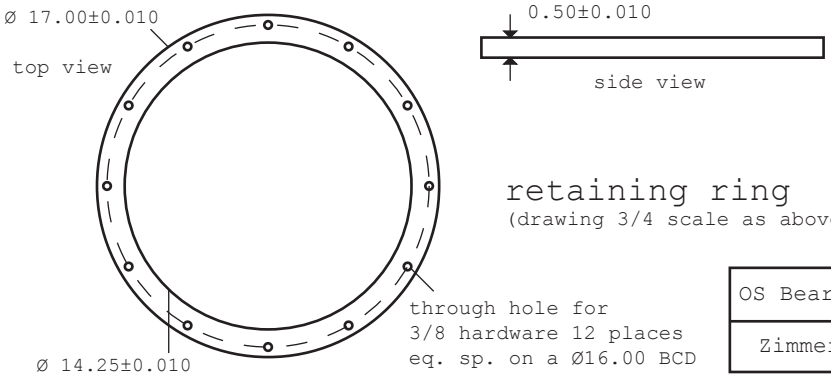

material: 304 SS
break all sharp edges

retaining ring
(drawing 3/4 scale as above!)

OS Bearing Housing / Retainer	
Zimmerman	25 May 2007

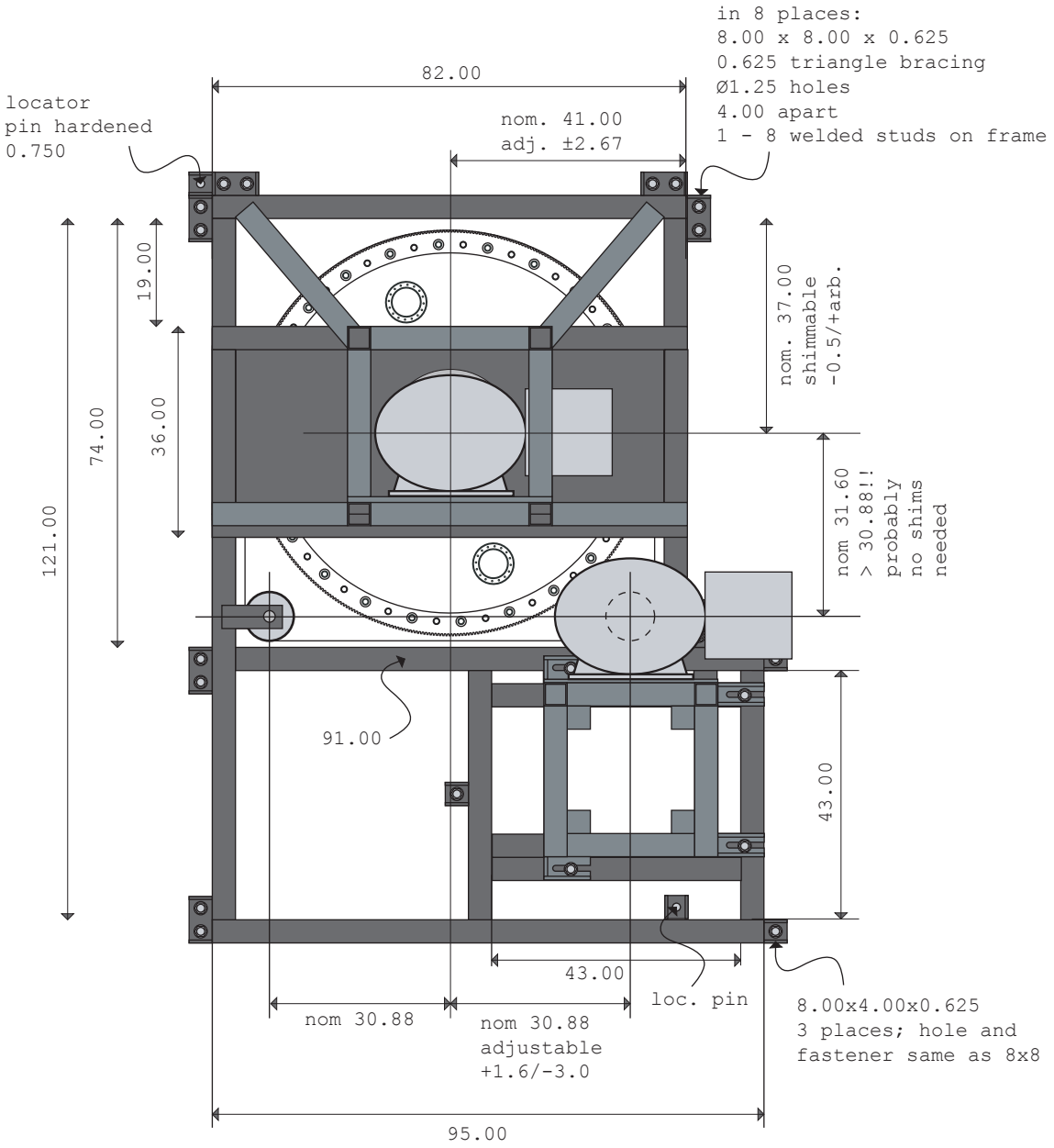

Motor Mount - Top View	
Zimmerman	23 May 2007

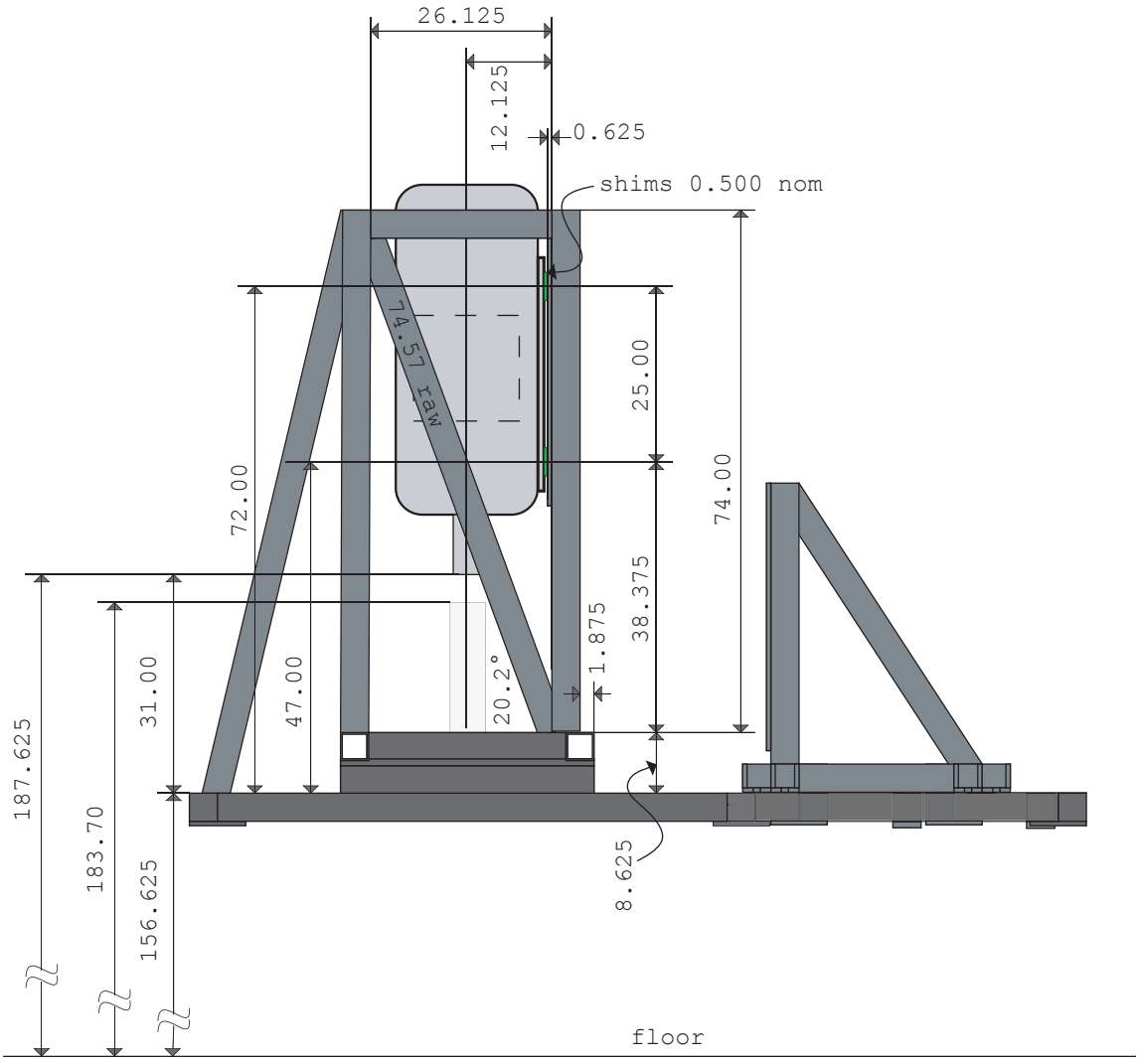

Motor Mount - Side View	
Zimmerman	23 May 2007

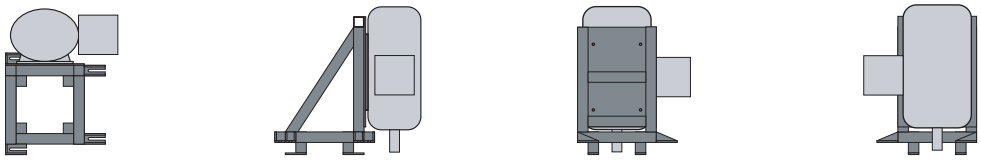

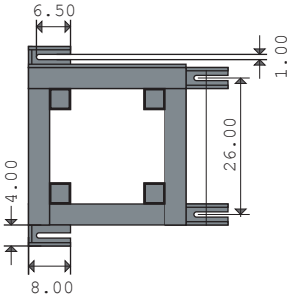

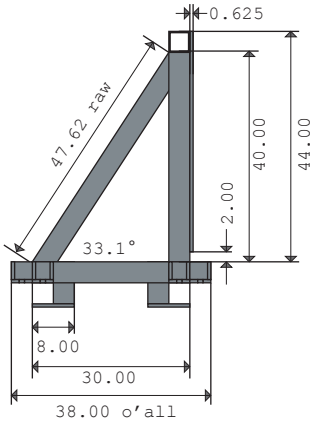

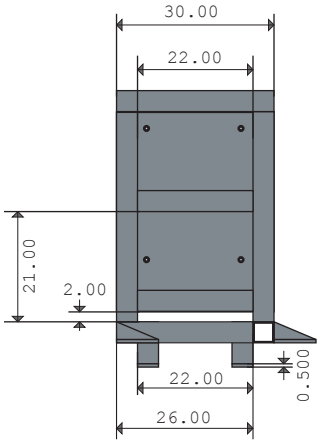

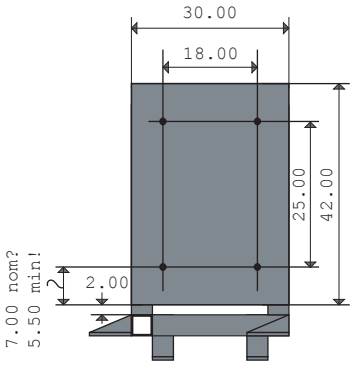

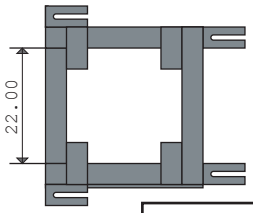

Outer Motor Sliding Mount Detail	
Zimmerman	23 May 2007

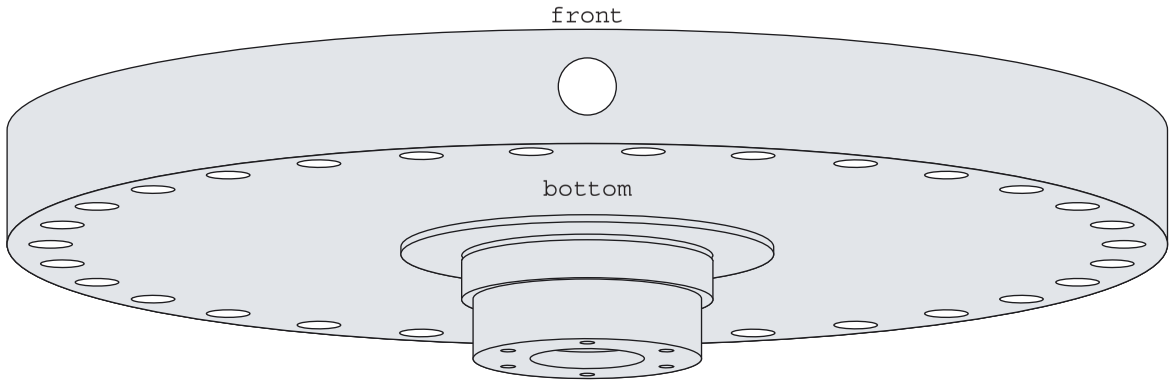

Bottom Head Overview	
Zimmerman	16 July 2003

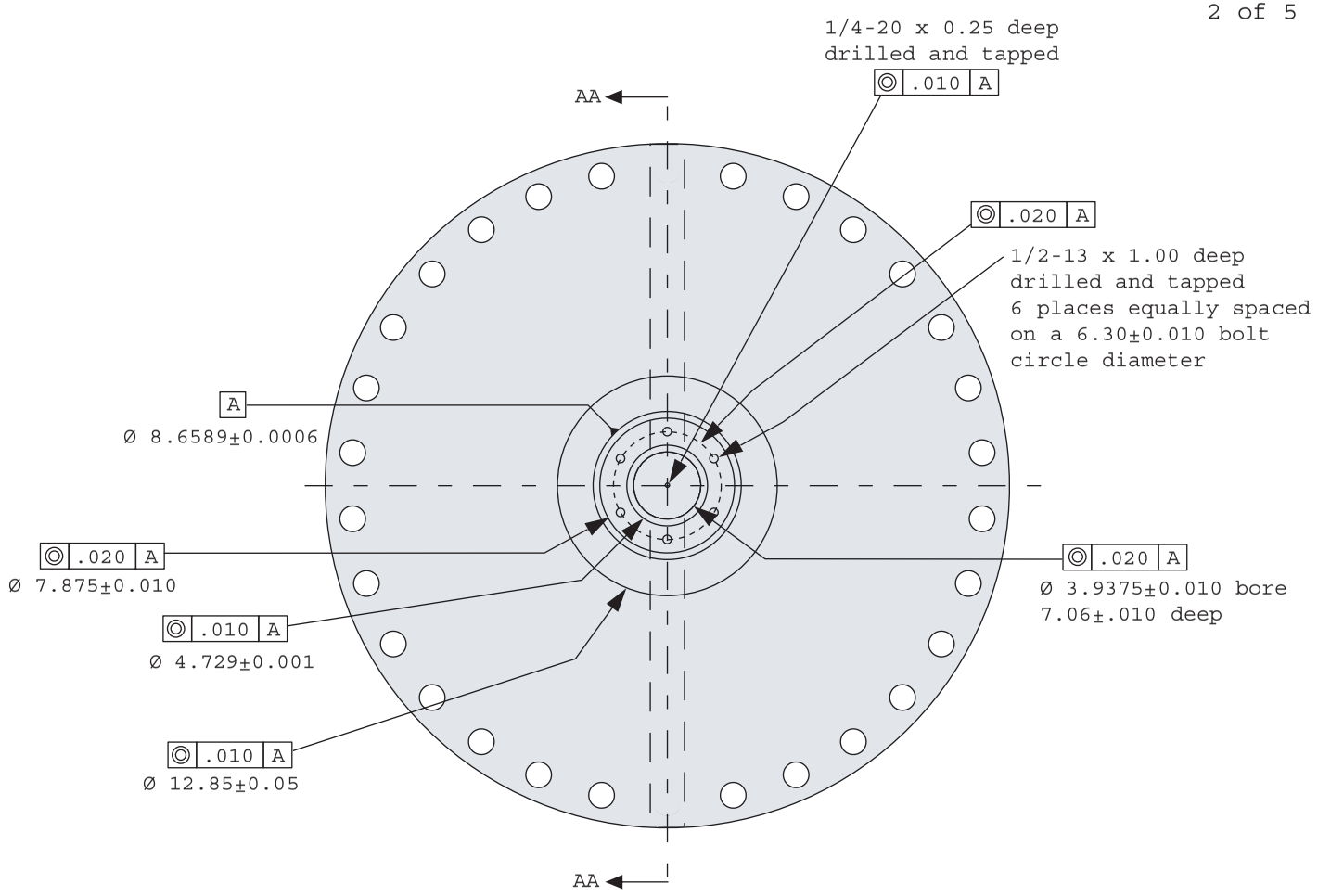

Bottom Head Bottom View	
Zimmerman	15 July 2003

bottom view

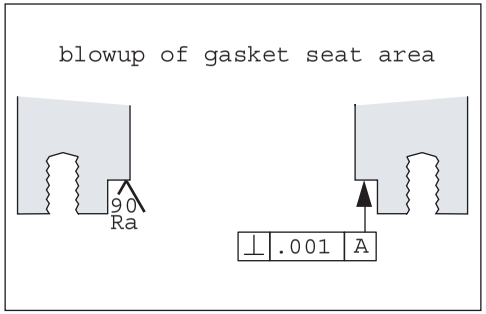

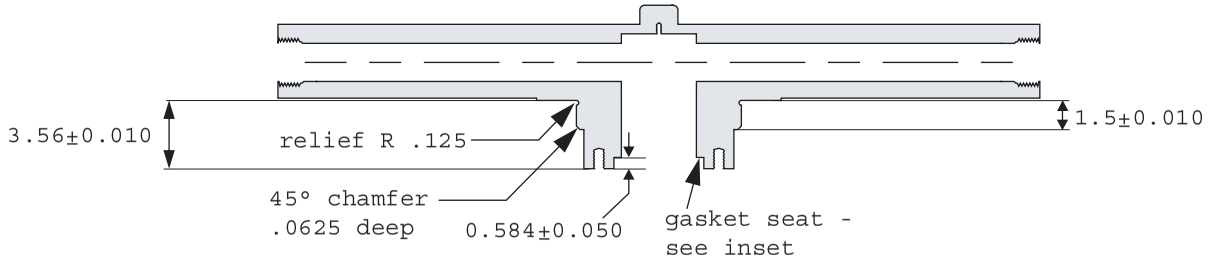

cross section AA

Bottom Head Cross Section	
Zimmerman	15 July 2003

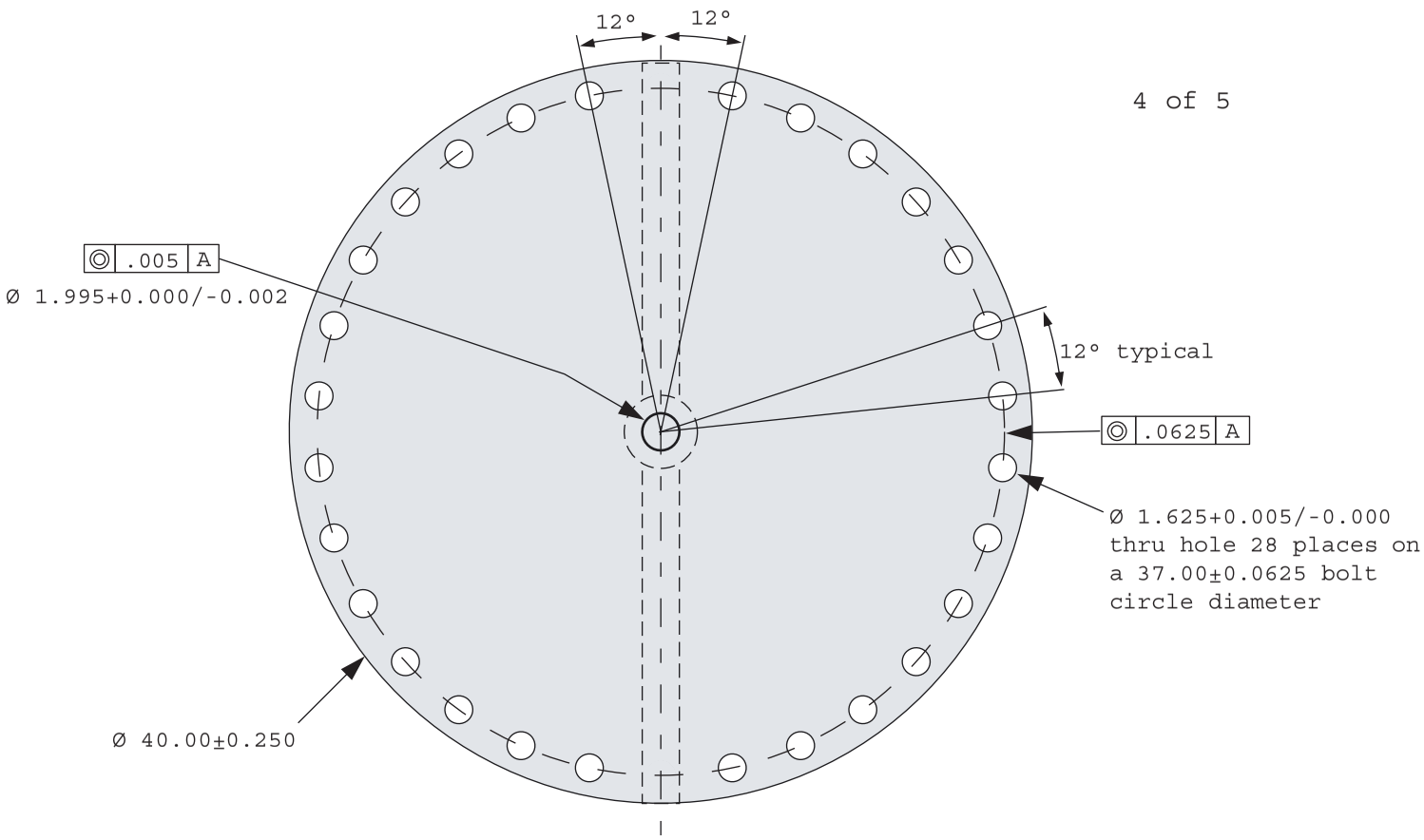

Bottom Head Top View	
Zimmerman	15 July 2003

top view

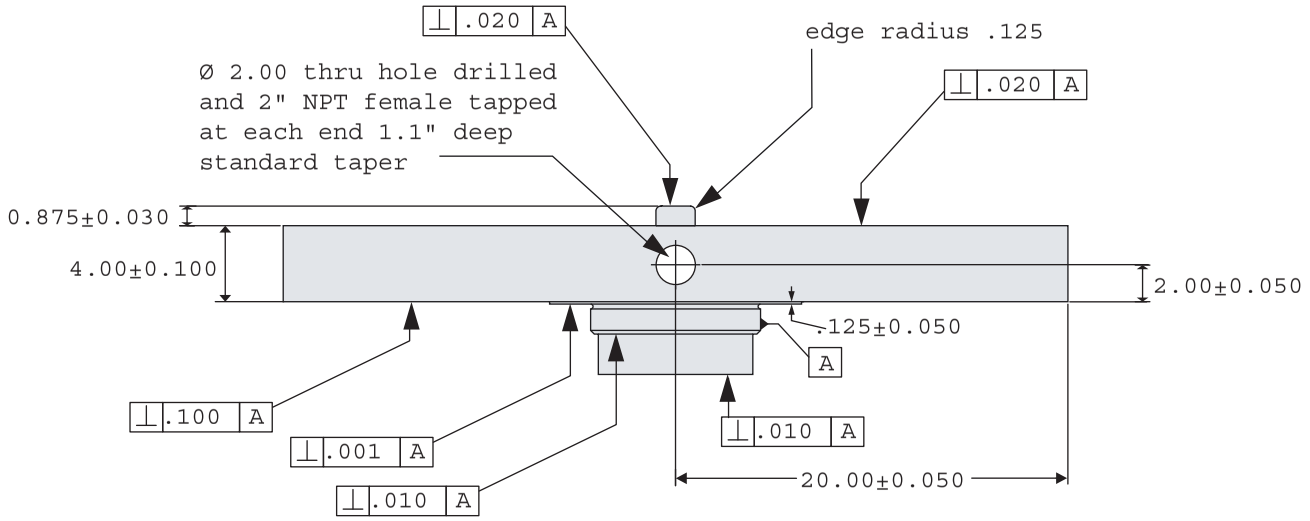

front view

Bottom Head Front View	
Zimmerman	15 July 2003

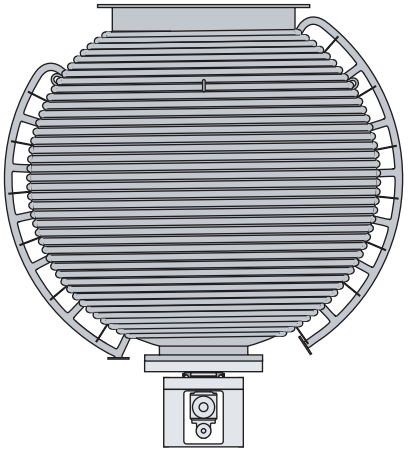

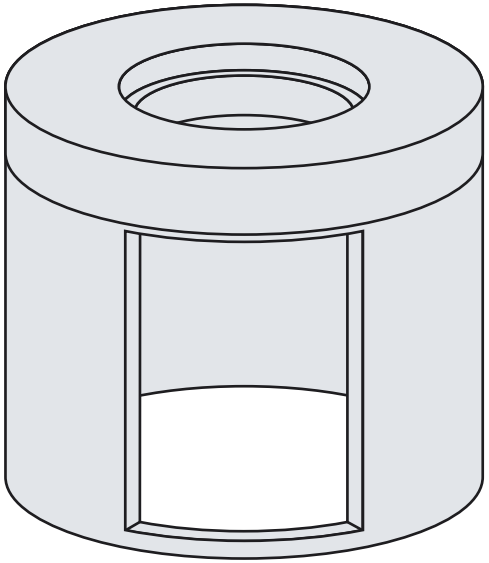

Base Overview	
Zimmerman	11 Aug 2003

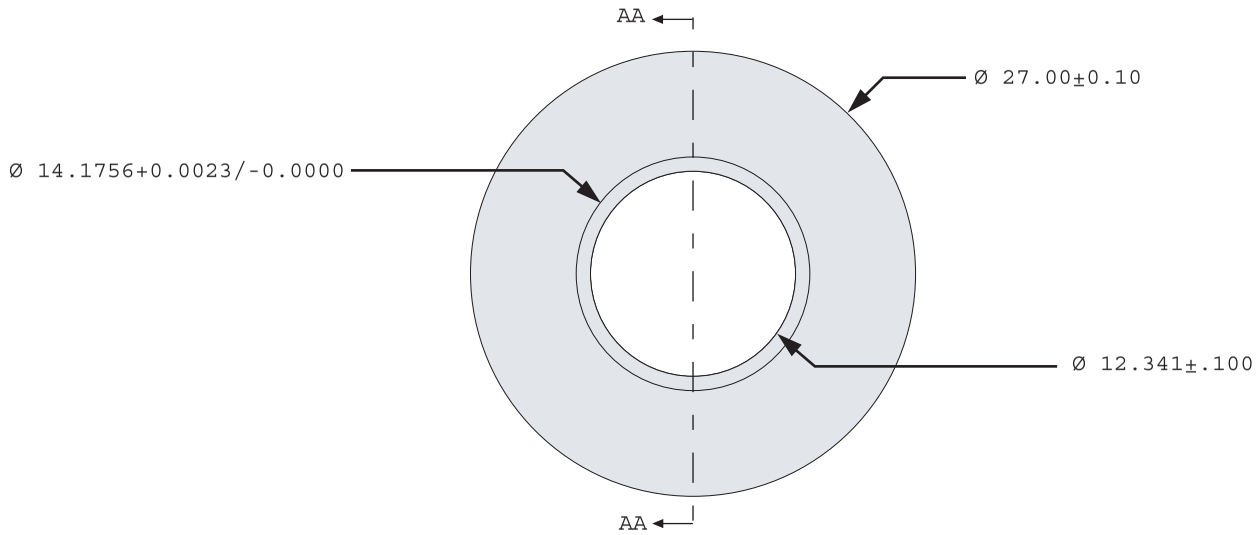

top view

Base Top View	
Zimmerman	11 Aug 2003

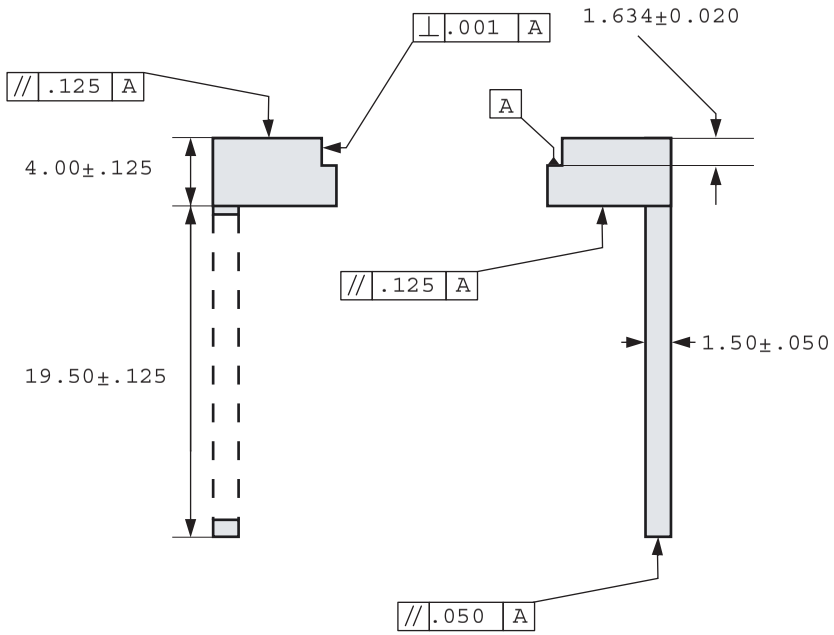

cross section AA

Base Cross Section	
Zimmerman	11 Aug 2003

D. MODAL AND STRESS ANALYSIS DIRECTORY

This appendix lists information regarding the final modal and static frame analysis files.

Tab. D.1: This is a file list of the final run Algor models as discussed in this dissertation, both static and vibrational models. These files can be accessed with user access to wave.umd.edu, and are located in the directory /data/3m/axl/Dissertation/algor_frame/. PDF output of mode shapes are available in: /data/3m/axl/Dissertation/figex/algor/modes/ and PDF outputs of static analyses are available in /data/3m/axl/Dissertation/figex/algor/static/.

Filename	Type	Constraints
ff2sph	Modal	All Edges
ff2sph_s	Static	All Edges
ff2sph_u	Modal	Only Base
ff2sph_r	Modal	Randomly Selected
ff2sph_e	Modal	One Edge

E. INSTRUMENTATION INFORMATION

This appendix collects schematics and other instrumentation information for instruments developed by the author that may be useful to other researchers, both in the Lathrop Lab and elsewhere.

E.1 Torque Transducer Schematics

The schematics for the wireless torque transmitter and its power supply are shown in Figs. E.1, E.2, and E.3. The home-made circuitry was constructed using point-to-point wiring on perf-board in a configuration that could plug in to the Arduino microcontroller board. Future versions of this device will be laid out on a printed circuit board, probably with multiple channels of acquisition addressed by the SPI bus protocol. Newer multi-channel ADC chips like the Analog Devices AD7606 may provide a good alternative to multiple one channel SPI-addressed converters.

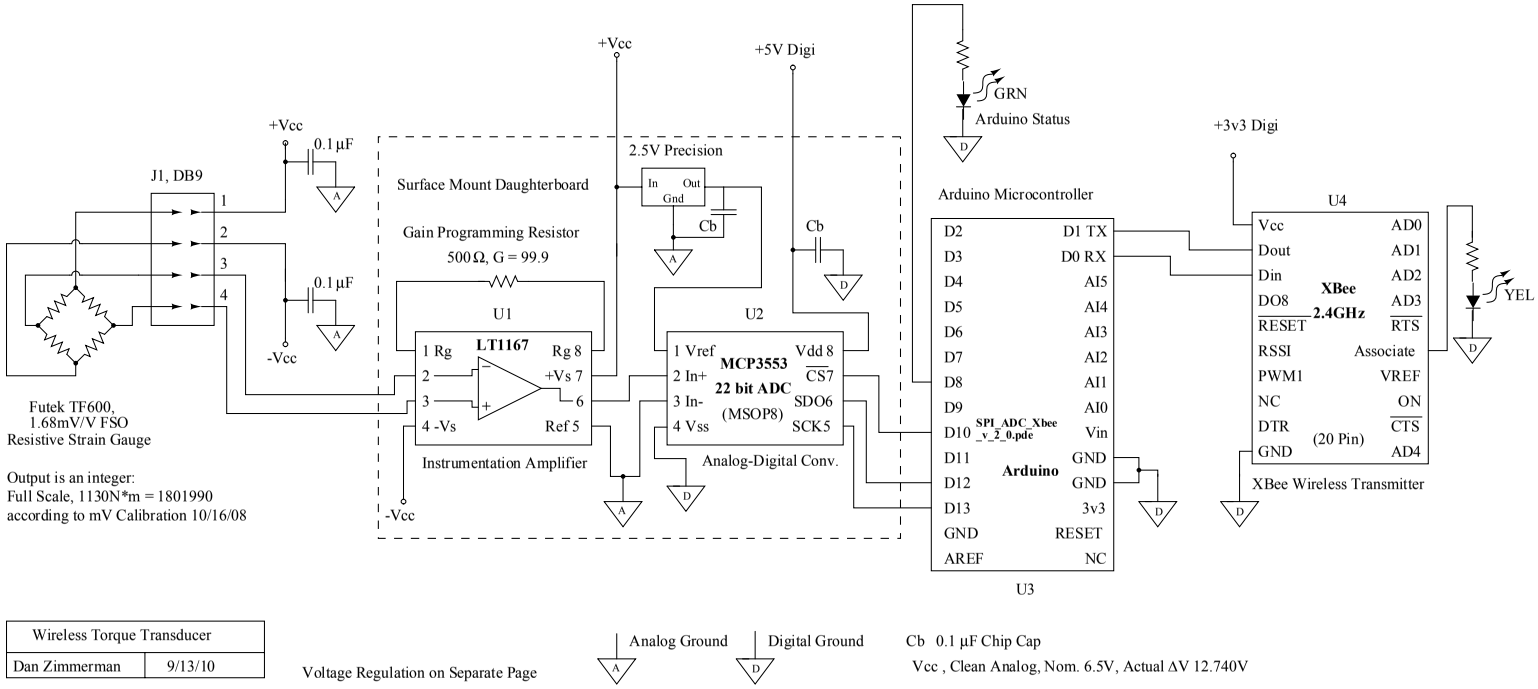

Fig. E.1: Schematic of the wireless torque transducer box, excluding voltage regulation/power conditioning circuitry. The strain gauge sensor is amplified by a Linear Technology LT1167 instrumentation amplifier of gain $\sim$ 100 and digitized with a Microchip MCP3553 22 bit ADC. The conversions are controlled by an Arduino microcontroller board running firmware written by the author, SPI_ADC_Xbee_v_2_0.pde, published below and available for download at **http://wave.umd.edu/axlcode/SPI_ADC_Xbee_v_2_0.pde** This code reads samples and transmits them in ASCII signed integer format via a Digi XBee 2.4GHz wireless serial connection to a computer in the lab frame.

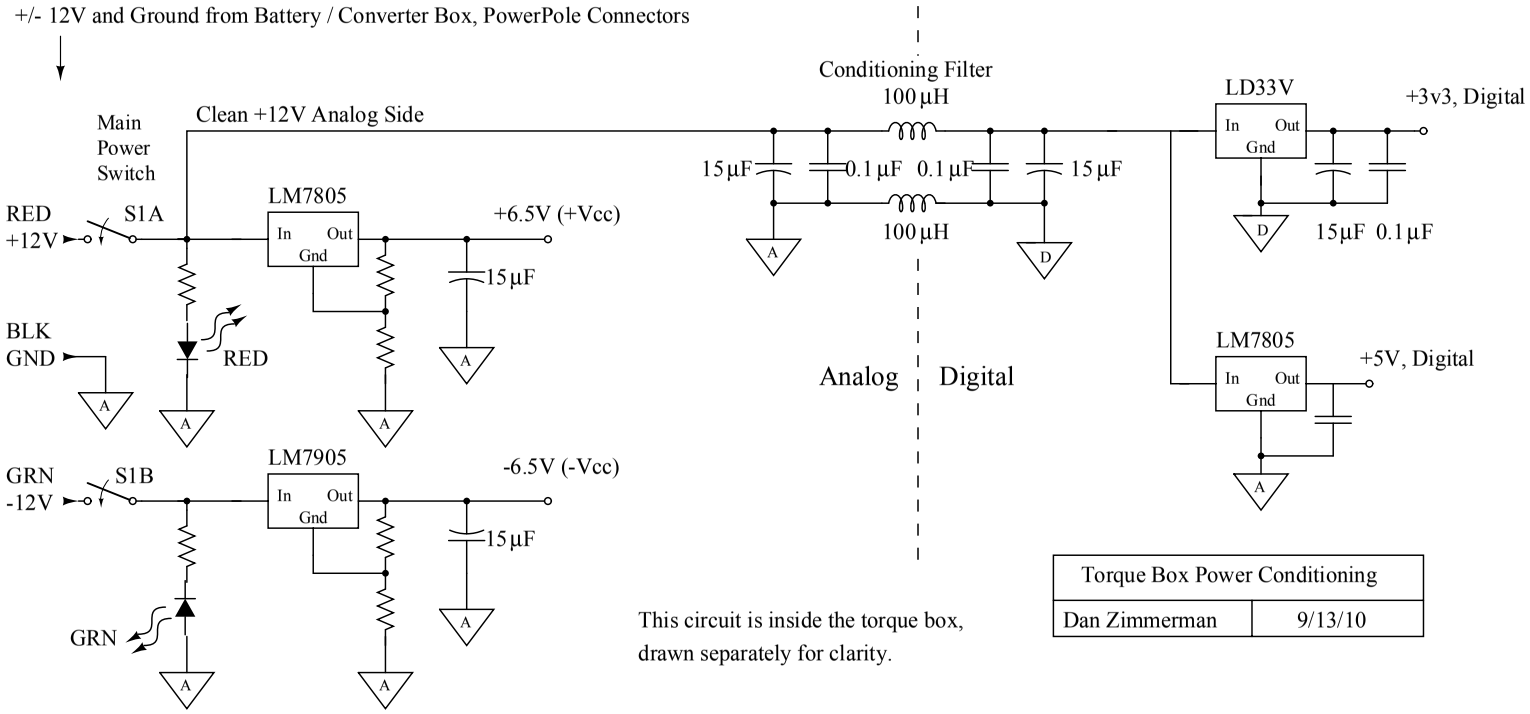

Fig. E.2: Torque box power conditioning. 7805 and 7905 linear regulators with voltage dividers (see datasheet) provide nominally $\pm 6.5V$ for the instrumentation amplifier and strain gauge excitation. A balanced-pi network filter separates analog and digital power and ground, allowing DC to pass but helping to keep digital pulses out of the sensitive millivolt-level analog circuitry. A 7805 regulator provides +5 V for the Arduino and an LD33V regulator provides +3.3 V for the XBee power supply. The Arduino has an on-board 3.3 V regulator, but it is insufficient to power the XBee.

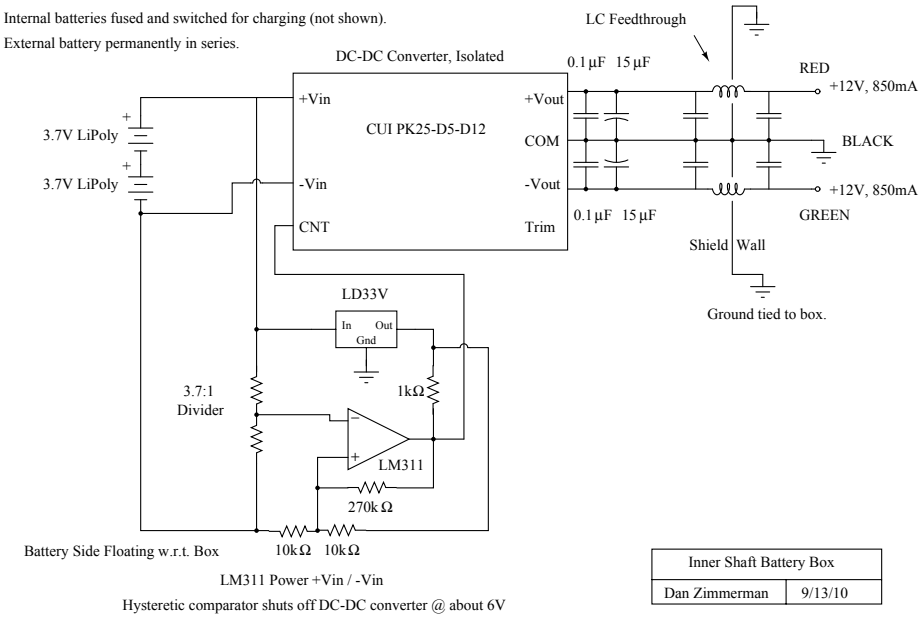

Fig. E.3: DC-DC converter to accept the 6 V to 8.3 V output of the lithium polymer battery pack and output $\pm 12\ V$ to power the torque sensor box. The comparator circuit is used to disable the DC-DC converter when the battery voltage drops below 6 V. Lithium polymer batteries do not survive deep discharge, and this is a simple protective circuit. Typically, the battery voltage rebounds a bit when load is removed, and the hysteresis built into this circuit is insufficient to keep the battery box off when the battery is just barely discharged to 6 V under load. However, large gaps and fluctuations appear in the acquired torque signal, signaling that the end of useful battery life has been reached, and the battery will not discharge below 6 V loaded in any case.

E.2 Resonant UVP Transformer

A resonant coupling ring arrangement was used early in the experiments for transferring the narrowband radio frequency pulses used in the ultrasound doppler velocimetry technique. A schematic and annotated photograph of the device are pictured in Fig. E.4. This system was adapted from a technique for coupling parallel-wire transmission line to a rotary antenna array found in an old American Radio Relay League antenna handbook [155]. This resonant coupling technique is currently enjoying something of a renaissance for "wireless power" delivery to small electronic devices [156, 157]. A significant amount of power may be transferred between electromagnetic resonators even with spacings of many resonator diameters. As the resonators are moved apart, however, more and more power is dissipated in the losses associated with large amounts of stored field energy. In the devices tested in our lab, we have always used close-coupling for best transfer efficiency, which should exceed 99% according to a LLNL NEC-2 finite element electromagnetic model. Reasonable results may be achieved with significantly wider ring spacing, however, if this is deemed necessary to accommodate the mechanical arrangement of a small experiment.

Ring size and geometry are not particularly critical, but will affect the capacitance required to resonate. We have implemented the with rings of 20 cm as well as the 45 cm diameter rings shown here. Both systems showed good results. The capacitors are selected by measuring or calculating the inductance of a single loop of the desired size and choosing $C = 1/((2\pi f_o)^2 L)$, with f_o the emission fre-

quency and L the loop inductance. Nearby metal reduces the inductance of the rings and affects tuning, but if loop inductance is measured *in situ*, this is not a serious problem. Because of the relatively loose coupling of the rings, this transformer provides a resistive impedance step up somewhere between 2:1 to 3:1 depending on the geometry.

However, we have found that the AC impedance[1] of a typical ultrasound transducer immersed[2] is not $50 + j0$, but typically somewhat lower and capacitatively reactive, $10 - j10$ for one example. So the impedance step-up is not a problem. For better impedance match, the ratio of the diameter of the rings could also be adjusted. The adjustable capacitors can be used to tune out residual reactance. A low cost MFJ Enterprises 259B impedance bridge is used for tuning the system to near 50Ω, as the resonant circuits are very sharp and tuning is critical. However, it should be possible to tune without an impedance bridge by tuning best echo signal if the capacitors are known to be approximately the right values. This circuit should be relatively noise immune with strong fields dropping off quickly, but devices and wiring that produce interfering energy in the range of the ultrasound emission frequency should be kept at least a few ring diameters away.

The system can be scaled down effectively for use in smaller experiments, where it might find maximum utility. However, some care should be used in capacitor

[1] The letter "j" is the engineering convention for $\sqrt{-1}$.

[2] A significant portion of the real part of the transducer electrical impedance is due to radiation. Impedance matching should be undertaken with the transducer immersed in the working fluid, or at least similar fluid.

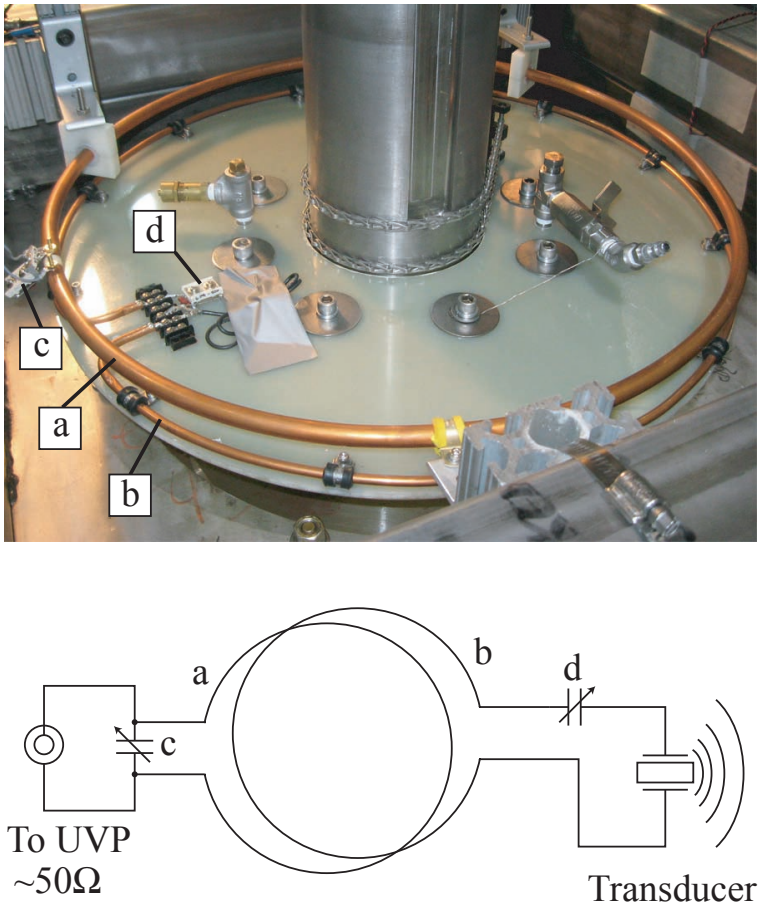

Fig. E.4: Annotated photograph and schematic of the resonant inductive coupling arrangement used to transfer 4 MHz signals into the rotating frame. A parallel (nearly) resonant circuit is connected to the ultrasound velocimetry unit via coaxial cable and a series (nearly) resonant circuit is connected to the ultrasound transducer. The photograph shows the physical layout of the system implemented on the three meter apparatus, with the lab-frame ring (a) and tuning capacitor (c) comprising the parallel resonant circuit connected to the UVP monitor and the rotating ring (b) and capacitor (d) connecting to the transducer in the rotating frame.

selection as the inductive reactance $X_L = 2\pi f_o L$ of the rings at the frequency of interest becomes small. Large capacitance will be needed, and dielectric losses might start to become an issue. Good radio-frequency capacitors should be chosen in any case, but the resistance of the capacitors will only cause significant losses when their reactance must be very large. For smaller devices (say, less than 10 cm for 4 MHz), heavy copper multi-turn inductors may be advantageous in this regard. When low-reactance rings are used, some parallel-connected fixed capacitors will probably be required, as variable capacitors of sufficient capacitance will not be available. The device used on the three-meter experiment uses a combination of fixed polystyrene and variable mica trimmer capacitors in parallel to provide sufficient capacitance with some tuning range.

E.3 CTA Circuit Board and Layout

The four-channel CTA circuit described in Section 3.5.4 was built with circuit boards made in house. Some circuits were made with double-sided board with a ground plane and others with single-sided. Neither construction seemed to have any significant advantage. Single-sided is therefore probably the recommended construction, as they are easier to etch, with no masking needed on the back. Boards were made using a toner-transfer process. Reversed board layout patterns are printed onto glossy paper, in this case a magazine cover, using a laser printer. The laser toner is then ironed on to a clean board. The board with paper is soaked in water, and the paper can be rubbed off leaving the toner behind. The laser toner is a

good resist for ferric chloride copper etchant, which is then used to etch the boards. The board foil pattern suitably reversed for toner transfer and a parts placement diagram are included below.

+
+
УЧЛСТУ
v3.0
+
+
УЧЛСТУ
v3.0

CTA Rev 3 Parts Placement Guide

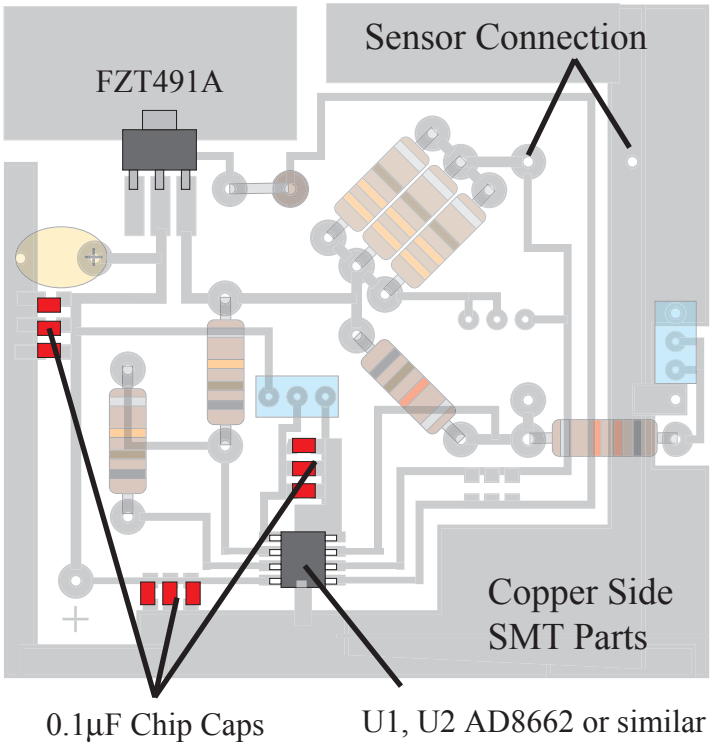

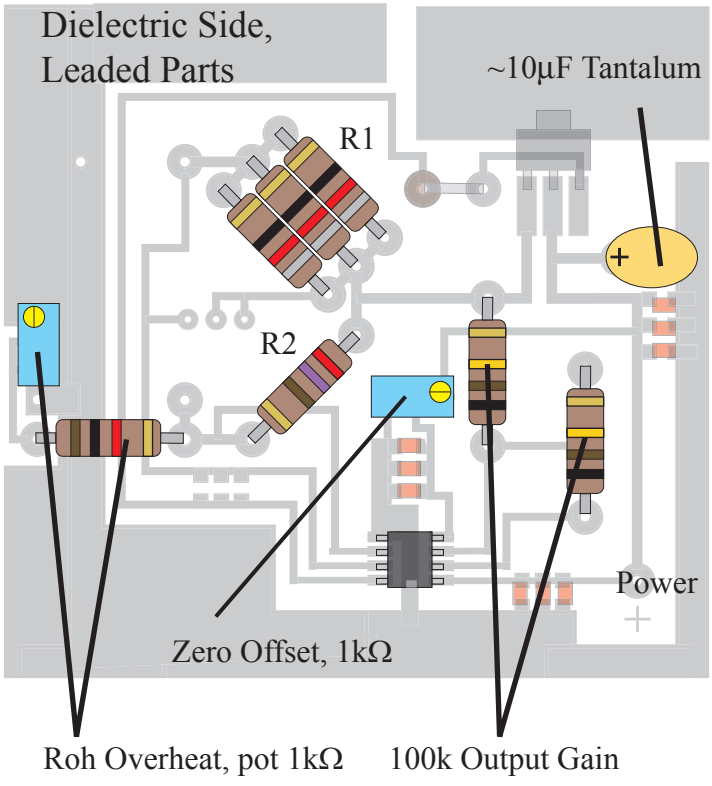

This view has resistors as built, R1 = 3x82Ω, R2 = 270Ω
Roh Fixed Portion 1kΩ, Output Gain 100kΩ

BIBLIOGRAPHY

[1] JF Lutsko and JW Dufty. Long-ranged correlations in sheared fluids. *Physical Review E*, 66(4, Part 1), OCT 2002.

[2] José M. Ortiz de Zárate and Jan V. Sengers. Nonequilibrium velocity fluctuations and energy amplification in planar couette flow. *Phys. Rev. E*, 79(4):046308, Apr 2009.

[3] D. B. Blum, S. B. Kunwar, J. Johnson, and G. A. Voth. Effects of nonuniversal large scales on conditional structure functions in turbulence. *Physics of Fluids*, 22(1):015107–+, January 2010.

[4] http://wmo.asu.edu/world-maximum-surface-wind gust. World wind speed record, 1996.

[5] Laura Messio, Cyprien Morize, Marc Rabaud, and Frederic Moisy. Experimental observation using particle image velocimetry of inertial waves in a rotating fluid. *Experiments in Fluids*, 44(4):519–528, APR 2008.

[6] H. P. Greenspan. *The Theory Of Rotating Fluids*. Cambridge monographs on mechanics and applied mathematics. Cambridge University Press, London, 1968.

[7] H. Poincaré. Sur l'Équilibre d'une masse fluide animée d'un mouvement de rotation. *Acta Mathematica*, 7(1):259–380, 1885.

[8] G. H. Bryan. The waves on a rotating liquid spheroid of finite ellipticity. *Phil. Trans. R. Soc. London A*, 180:187–219, 1889.

[9] M. D. Kudlick. *On transient motions in a contained, rotating fluid*. PhD thesis, Massachusetts Institute of Technology, February 1966.

[10] Keke Zhang, Paul Earnshaw, Xinhao Liao, and F. H. Busse. On inertial waves in a rotating fluid sphere. *Journal of Fluid Mechanics*, 437(-1):103–119, 2001.

[11] KK Zhang, XH Liao, and P Earnshaw. The poincare equation: A new polynomial and its unusual properties. *Journal Of Mathematical Physics*, 45(12):4777–4790, DEC 2004.

[12] Douglas H. Kelley, Santiago Andrés Triana, Daniel S. Zimmerman, and Daniel P. Lathrop. Selection of inertial modes in spherical couette flow. *Phys. Rev. E*, 81(2):026311, Feb 2010.

[13] D. H. Kelley, S. A. Triana, D. S. Zimmerman, B. Brawn, D. P. Lathrop, and D. H. Martin. Driven inertial waves in spherical couette flow. *Chaos*, 16:1105, December 2006.

[14] Douglas H. Kelley, Santiago Andres Triana, Daniel S. Zimmerman, Andreas Tilgner, and Daniel P. Lathrop. Inertial waves driven by differential rotation in a planetary geometry. *Geophysical and Astrophysical Fluid Dynamics*, 101(5-6):469–487, 2007.

[15] D. H. Kelley, S. A. Triana, D. S. Zimmerman, A. Tilgner, and D. P. Lathrop. Inertial waves driven by differential rotation in a planetary geometry. *Geophys. Astrophys. Fluid*, 101(5/6):469–487, 2007.

[16] M. Rieutord and L. Valdettaro. Inertial waves in a rotating spherical shell. *J. Fluid Mech.*, 341:77–99, 1997.

[17] M. Rieutord, B. Georgeot, and L. Valdettaro. Inertial waves in a rotating spherical shell: Attractors and asymptotic spectrum. *J. Fluid Mech.*, 435:103–144, 2001.

[18] A. Tilgner. Driven inertial oscillations in spherical shells. *Physical Review E*, 59(2):1789–1794, February 1999.

[19] M. Rieutord, B. Georgeot, and L. Valdettaro. Wave attractors in rotating fluids: A paradigm for ill-posed cauchy problems. *Phys. Rev. Lett.*, 85(20):4277–4280, Nov 2000.

[20] M. Rieutord and L. Valdettaro. Viscous dissipation by tidally forced inertial modes in a rotating spherical shell. *Journal Of Fluid Mechanics*, 643:363–394, JAN 25 2010.

[21] A. Tilgner. Zonal wind driven by inertial modes. *Phys. Rev. Lett.*, 99(19):194501, 2007.

[22] K. Zhang and X. Liao. A new asymptotic method for the analysis of convection in a rapidly rotating sphere. *J. Fluid Mech.*, 518:319–346, November 2004.

[23] Xinhao Liao and Keke Zhang. A new integral property of inertial waves in rotating fluid spheres. *Proceedings of the Royal Society A - Mathematical, Physical, and Engineering Science*, 465(2104):1075–1091, APR 8 2009.

[24] Xinhao Liao and Keke Zhang. A new legendre-type polynomial and its application to geostrophic flow in rotating fluid spheres. *Proceedings of the Royal Society A: Mathematical, Physical and Engineering Science*, 466(2120):2203–2217, August 2010.

[25] C.-G. Rossby. Relation between variations in the intensity of the zonal circulation of the atmosphere and the displacements of the semi-permanent centers of action. *J. Marine Res.*, pages 38–55, 1939.

[26] R E Dickinson. Rossby waves–long-period oscillations of oceans and atmospheres. *Annual Review of Fluid Mechanics*, 10(1):159–195, 1978.

[27] P. B. Rhines. Geostrophic turbulence. *Annual Review of Fluid Mechanics*, 11:401–441, 1979.

[28] YD Tian, ER Weeks, K Ide, JS Urbach, CN Baroud, M Ghil, and HL Swinney. Experimental and numerical studies of an eastward jet over topography. *Journal of Fluid Mechanics*, 438:129–157, JUL 10 2001.

[29] CN Baroud, BB Plapp, ZS She, and HL Swinney. Anomalous self-similarity in a turbulent rapidly rotating fluid. *Physical Review Letters*, 88(11), MAR 18 2002.

[30] CN Baroud, BB Plapp, HL Swinney, and ZS She. Scaling in three-dimensional and quasi-two-dimensional rotating turbulent flows. *Physics of Fluids*, 15(8):2091–2104, AUG 2003.

[31] CN Baroud and HL Swinney. Nonextensivity in turbulence in rotating two-dimensional and three-dimensional flows. *Physica D - Nonlinear Phenomena*, 184(1-4):21–28, OCT 1 2003.

[32] Peter L. Read, Yasuhiro H. Yamazaki, Stephen R. Lewis, Paul D. Williams, Robin Wordsworth, and Kuniko Miki-Yamazaki. Dynamics of convectively driven banded jets in the laboratory. *Journal Of The Atmospheric Sciences*, 64(11):4031–4052, NOV 2007.

[33] N Schaeffer and P Cardin. Rossby-wave turbulence in a rapidly rotating sphere. *Nonlinear Processes in Geophysics*, 12(6):947–953, 2005.

[34] F. H. Busse, K. Zhang, and X. Liao. On slow inertial waves in the solar convection zone. *Astrophys. J.*, 631:L171–L174, October 2005.

[35] N Schaeffer and P Cardin. Quasigeostrophic model of the instabilities of the stewartson layer in flat and depth-varying containers. *Physics Of Fluids*, 17(10), OCT 2005.

[36] A Barcilon and PG Drazin. Nonlinear waves of vorticity. *Studies In Applied Mathematics*, 106(4):437–479, MAY 2001.

[37] V. W. Ekman. On the influence of the earth's rotation on ocean-currents. *Arkiv foer matematik. astronomi o. fysik.*, 11, 1905.

[38] S Leibovich and S.K. Lele. The influence of the horizontal component of earths angular velocity on the instability of the ekman layer. *journal Of Fluid Mechanics*, 150(JAN):41–87, 1985.

[39] Denis Aelbrecht, Gabriel Chabert D'Hieres, and Dominique Renouard. Experimental study of the ekman layer instability in steady or oscillating flows. *Continental Shelf Research*, 19(15-16):1851 – 1867, 1999.

[40] Xinhao Liao, Keke Zhang, and Paul Earnshaw. On the viscous damping of inertial oscillation in planetary fluid interiors. *Physics of The Earth and Planetary Interiors*, 128(1-4):125 – 136, 2001.

[41] R. R. Kerswell. On the internal shear layers spawned by the critical regions in oscillatory ekman boundary layers. *J. Fluid Mech.*, 298:311–325, 1995.

[42] R. H. Kraichnan. Inertial ranges in two-dimensional turbulence. *Physics of Fluids*, 10:1417–1423, July 1967.

[43] Leslie M. Smith and Victor Yakhot. Bose condensation and small-scale structure generation in a random force driven 2d turbulence. *Phys. Rev. Lett.*, 71(3):352–355, Jul 1993.

[44] Z. Xiao, M. Wan, S. Chen, and G. L. Eyink. Physical mechanism of the inverse energy cascade of two-dimensional turbulence: a numerical investigation. *Journal of Fluid Mechanics*, 619(-1):1–44, 2009.

[45] J. Sommeria. Experimental study of the two-dimensional inverse energy cascade in a square box. *Journal of Fluid Mechanics*, 170(-1):139–168, 1986.

[46] Jerome Paret and Patrick Tabeling. Intermittency in the two-dimensionally inverse cascade of energy: Experimental observations. *Physics of Fluids*, 10(12):3126, 1998.

[47] L. M. Smith and Y. Lee. On near resonances and symmetry breaking in forced rotating flows at moderate rossby number. *J. Fluid Mech.*, 535:111–142, July 2005.

[48] James C. McWilliams, Jeffrey B. Weiss, and Irad Yavneh. Anisotropy and coherent vortex structures in planetary turbulence. *Science*, 264(5157):410–413, 1994.

[49] P. J. Staplehurst, P. A. Davidson, and S. B. Dalziel. Structure formation in homogeneous freely decaying rotating turbulence. *Journal of Fluid Mechanics*, 598:81–105, MAR 10 2008.

[50] C Morize, F Moisy, and M Rabaud. Decaying grid-generated turbulence in a rotating tank. *Physics Of Fluids*, 17(9), SEP 2005.

[51] Guillaume Roullet and Patrice Klein. Cyclone-anticyclone asymmetry in geophysical turbulence. *Phys. Rev. Lett.*, 104(21):218501, May 2010.

[52] RC Kloosterziel and GJF van Heijst. An experimental study of unstable barotropic vortices in a rotating fluid. *Journal of Fluid Mechanics*, 223:1–24, FEB 1991.

[53] D Sipp and L Jacquin. Three-dimensional centrifugal-type instabilities of two-dimensional flows in rotating systems. *Physics of Fluids*, 12(7):1740–1748, JUL 2000.

[54] R. C. Kloosterziel, G. F. Carnevale, and P. Orlandi. Inertial instability in rotating and stratified fluids: barotropic vortices. *Journal of Fluid Mechanics*, 583:379–412, JUL 25 2007.

[55] QN Chen, SY Chen, GL Eyink, and DD Holm. Resonant interactions in rotating homogeneous three-dimensional turbulence. *Journal Of Fluid Mechanics*, 542:139–164, NOV 10 2005.

[56] Fabian Waleffe. Inertial transfers in the helical decomposition. *Physics of Fluids A: Fluid Dynamics*, 5(3):677–685, 1993.

[57] P. A. Davidson, P. J. Staplehurst, and S. B. Dalziel. On the evolution of eddies in a rapidly rotating system. *Journal of Fluid Mechanics*, 557:135–144, JUN 25 2006.

[58] Itamar Kolvin, Kobi Cohen, Yuval Vardi, and Eran Sharon. Energy transfer by inertial waves during the buildup of turbulence in a rotating system. *Physical Review Letters*, 102(1), JAN 9 2009.

[59] L. M. Smith and F. Waleffe. Transfer of energy to two-dimensional large scales in forced, rotating three-dimensional turbulence. *Phys. Fluids*, 11:1608–1622, June 1999.

[60] G. P. Bewley, D. P. Lathrop, L. R. M. Maas, and K. R. Sreenivasan. Inertial waves in rotating grid turbulence. *Phys. Fluids*, 19(7):071701, 2007.

[61] M. D. Nornberg, H. Ji, E. Schartman, A. Roach, and J. Goodman. Observation of magnetocoriolis waves in a liquid metal taylor-couette experiment. *Physical Review Letters*, 104(7), FEB 19 2010.

[62] D. Schmitt, T. Alboussière, D. Brito, P. Cardin, N. Gagnière, D. Jault, and H. C. Nataf. Rotating spherical couette flow in a dipolar magnetic field: Experimental study of magneto-inertial waves. *J. Fluid Mech.*, 604:175–197, 2008.

[63] KP Bowman. Rossby wave phase speeds and mixing barriers in the stratosphere .1. observations. *Journal Of The Atmospheric Sciences*, 53(6):905–916, MAR 15 1996.

[64] Peter Haynes. Stratospheric dynamics. *Annual Review of Fluid Mechanics*, 37(1):263–293, 2005.

[65] I. I. Rypina, M. G. Brown, F. J. Beron-Vera, H. Koak, M. J. Olascoaga, and I. A. Udovydchenkov. On the lagrangian dynamics of atmospheric zonal jets and the permeability of the stratospheric polar vortex. *Journal of the Atmospheric Sciences*, 64(10):3595 – 3610, 2007.

[66] Lord Kelvin. Vibrations of a columnar vortex. *Phil. Mag.*, 10(155), 1880.

[67] Joseph Larmor. How the sun might have become a magnet. *Elec. Rev.*, 85:412, 1919.

[68] U. Christensen, D. Schmitt, and M. Rempel. Planetary dynamos from a solar perspective. *Space Science Reviews*, 144(1):105–126, 2009.

[69] G. Hulot, C. C. Finlay, C. G. Constable, N. Olsen, and M. Mandea. The magnetic field of planet earth. *Space Science Reviews*, 152(1-4):159–222, MAY 2010.

[70] Andrew Jackson, Art R. T. Jonkers, and Matthew R. Walker. Four centuries of geomagnetic secular variation from historical records. *Philosophical Transactions: Mathematical, Physical and Engineering Sciences*, 358(1768):957–990, 2000.

[71] Edward Bullard and H. Gellman. Homogeneous dynamos and terrestrial magnetism. *Philosophical Transactions of the Royal Society of London. Series A, Mathematical and Physical Sciences*, 247(928):213–278, 1954.

[72] Y. Ponty, J.-P. Laval, B. Dubrulle, F. Daviaud, and J.-F. Pinton. Subcritical dynamo bifurcation in the taylor-green flow. *Phys. Rev. Lett.*, 99(22):224501, Nov 2007.

[73] Agris Gailitis, Gunter Gerbeth, Thomas Gundrum, Olgerts Lielausis, Ernests Platacis, and Frank Stefani. History and results of the riga dynamo experiments. *Comptes Rendus Physique*, 9(7):721 – 728, 2008. Dynamo effect: experimental progress and geo- and astro-physical challenges / Effet dynamo : avances exprimentales et dfis go- et astrophysiques.

[74] Yu. B. Ponomarenko. Theory of the hydromagnetic generator. *Journal of Applied Mechanics and Technical Physics*, 14(6):775–778, 1973.

[75] R. Stieglitz and U. Müller. Experimental demonstration of a homogeneous two-scale dynamo. *Physics of Fluids*, 13:561–564, March 2001.

[76] M. Berhanu, R. Monchaux, S. Fauve, N. Mordant, F. Petrelis, A. Chiffaudel, F. Daviaud, B. Dubrulle, L. Marie, F. Ravelet, M. Bourgoin, Ph. Odier, J.-F. Pinton, and R. Volk. Magnetic field reversals in an experimental turbulent dynamo. *EPL*, 77(5), 2007.

[77] Romain Monchaux, Michael Berhanu, Sebastien Aumaitre, Arnaud Chiffaudel, Francois Daviaud, Berengere Dubrulle, Florent Ravelet, Stephan Fauve, Nicolas Mordant, Francois Petrelis, Mickael Bourgoin, Philippe Odier, Jean-Francois Pinton, Nicolas Plihon, and Romain Volk. The von karman sodium experiment: Turbulent dynamical dynamos. *Physics of Fluids*, 21(3), MAR 2009.

[78] GA Glatzmaier and PH Roberts. A 3-dimensional convective dynamo solution with rotating and finitely conducting inner-core and mantle. *Physics Of The Earth And Planetary Interiors*, 91(1-3):63–75, SEP 1995.

[79] Johannes Wicht and Peter Olson. A detailed study of the polarity reversal mechanism in a numerical dynamo model. *Geochem. Geophys. Geosyst.*, 5(3):Q03H10–, March 2004.

[80] U. Christensen, P. Olson, and G. A. Glatzmaier. Numerical modelling of the geodynamo: a systematic parameter study. *Geophysical Journal International*, 138:393–409, August 1999.

[81] Ulrich R. Christensen, Julien Aubert, and Gauthier Hulot. Conditions for earth-like geodynamo models. *Earth And Planetary Science Letters*, 296(3-4):487–496, AUG 1 2010.

[82] A. Tilgner. Precession driven dynamos. *Physics of Fluids*, 17(3):034104, 2005.

[83] PD Stein and HN Sabbah. Turbulent blood flow in the ascending aorta of humans with normal and diseased aortic valves. *Circ Res*, 39(1):58–65, 1976.

[84] E. Dekker. Transition between laminar and turbulent flow in human trachea. *J Appl Physiol*, 16(6):1060–1064, 1961.

[85] J C Wyngaard. Atmospheric turbulence. *Annual Review of Fluid Mechanics*, 24(1):205–234, 1992.

[86] TG Shepherd. Issues in stratosphere-troposphere coupling. *Journal Of The Meteorological Society Of Japan*, 80(4B):769–792, SEP 2002.

[87] Katepalli R. Sreenivasan and Brindesh Dhruva. Is there scaling in high-reynolds-number turbulence? *Progress of Theoretical Physics Supplement*, 130:103–120, 1998.

[88] E. Palmen and C.W. Newton. *Atmospheric Circulation Systems: Their Structure and Physical Interpretation*. Academic Press, 1969.

[89] Richard Grotjahn. *Global Atmospheric Circulations: Observations and Theories*. Oxford University Press, 1993.

[90] SE Larsen, HE Jorgensen, L Landberg, and JE Tillman. Aspects of the atmospheric surface layers on mars and earth. *Boundary-Layer Meteorology*, 105(3):451–470, DEC 2002.

[91] C. Guervilly and P. Cardin. Numerical simulations of dynamos generated in spherical couette flows. *Geophysical and Astrophysical Fluid Dynamics*, 104:221–248, 2010.

[92] Bruno Eckhardt, Siegfried Grossmann, and Detlef Lohse. Torque scaling in turbulent taylor-couette flow between independently rotating cylinders. *Journal of Fluid Mechanics*, 581:221–250, JUN 25 2007.

[93] B Dubrulle and F Hersant. Momentum transport and torque scaling in taylor-couette flow from an analogy with turbulent convection. *European Physical Journal B*, 26(3):379–386, APR 2002.

[94] Keke Zhang. On inertial waves in the earth's fluid core. *Geophysical Research Letters*, 19(8):737–740, April 1992.

[95] K Zhang. Spiraling columnar convection in rapidly rotating spherical fluid shells. *Journal of Fluid Mechanics*, 236:535–556, MAR 1992.

[96] JM Aurnou and PL Olson. Strong zonal winds from thermal convection in a rotating spherical shell. *Geophysical Research Letters*, 28(13):2557–2559, JUL 1 2001.

[97] J Aubert, D Brito, HC Nataf, P Cardin, and JP Masson. A systematic experimental study of rapidly rotating spherical convection in water and liquid gallium. *Physics of the Earth and Planetary Interiors*, 128(1-4):51–74, DEC 10 2001.

[98] E. Plaut, Y. Lebranchu, R. Simitev, and F. H. Busse. Reynolds stresses and mean fields generated by pure waves: applications to shear flows and convection in a rotating shell. *Journal of Fluid Mechanics*, 602:303–326, MAY 10 2008.

[99] Snellman, J. E., Käpylä, P. J., Korpi, M. J., and Liljeström, A. J. Reynolds stresses from hydrodynamic turbulence with shear and rotation. *Astronomy & Astrophysics*, 505(3):955–968, 2009.

[100] R. Hollerbach, M. Junk, and C. Egbers. Non-axisymmetric instabilities in basic state spherical couette flow. *Fluid Dyn. Res.*, 38:257–273, April 2006.

[101] P Wulf, C Egbers, and HJ Rath. Routes to chaos in wide-gap spherical couette flow. *Physics of Fluids*, 11(6):1359–1372, JUN 1999.

[102] K Stewartson. On almost rigid rotations. *Journal of Fluid Mechanics*, 3(1):17–26, 1957.

[103] K Stewartson. On almost rigid rotations 2. *Journal of Fluid Mechanics*, 26(Part 1):131–&, 1966.

[104] PS Marcus and LS Tuckerman. Simulation of flow between concentric rotating spheres 1: Steady states. *Journal of Fluid Mechanics*, 185:1–30, DEC 1987.

[105] F.P. Bowden and R.G. Lord. The aerodynamic resistance to a sphere rotating at high speed. *Proceedings of the Royal Society A - Mathematical and Physical Sciences*, 271:143–153, 1963.

[106] R Hollerbach, RJ Wiener, IS Sullivan, RJ Donnelly, and CF Barenghi. The flow around a torsionally oscillating sphere. *Physics of Fluids*, 14(12):4192–4205, DEC 2002.

[107] Y Kohama and R Kobayashi. Boundary layer transition and the behavior of spiral vortices on rotating spheres. *Journal Of Fluid Mechanics*, 137(DEC):153–164, 1983.

[108] R Hide and CW Titman. Detached shear layers in a rotating fluid. *Journal of Fluid Mechanics*, 29(Part 1):39–&, 1967.

[109] Rainer Hollerbach, Birgit Futterer, Tamar More, and Christoph Egbers. Instabilities of the stewartson layer: Part 2. supercritical mode transitions. *Theoret. Comput. Fluid Dynamics*, 18:197–204, 2004.

[110] H. C. Nataf, T. Alboussière, D. Brito, P. Cardin, N. Gagnière, D. Jault, J. P. Masson, and D. Schmitt. Experimental study of super-rotation in a magnetostrophic spherical couette flow. *Geophys. Astrophys. Fluid*, 100(4):281–298, 2006.

[111] H.-C. Nataf, T. Alboussière, D. Brito, P. Cardin, N. Gagnière, D. Jault, and D. Schmitt. Rapidly rotating spherical couette flow in a dipolar magnetic field: An experimental study of the mean axisymmetric flow. *Phys. Earth Plan. Int.*, 170:60–72, 2008.

[112] DR Sisan, N Mujica, WA Tillotson, YM Huang, W Dorland, AB Hassam, TM Antonsen, and DP Lathrop. Experimental observation and characterization of the magnetorotational instability. *Physical Review Letters*, 93(11), SEP 10 2004.

[113] Kenji Ohta, Kei Hirose, Masahiro Ichiki, Katsuya Shimizu, Nagayoshi Sata, and Yasuo Ohishi. Electrical conductivities of pyrolitic mantle and morb materials up to the lowermost mantle conditions. *Earth And Planetary Science Letters*, 289(3-4):497–502, JAN 31 2010.

[114] Emmanuel Dormy, Jean-Pierre Valet, and Vincent Courtillot. Numerical models of the geodynamo and observational constraints. *Geochem. Geophys. Geosyst.*, 1(10):–, October 2000.

[115] P. Olson. Gravitational dynamos and the low-frequency geomagnetic secular variation. *Proceedings of the National Academy of Sciences*, 104(51):20159–20166, December 2007.

[116] Warren C. Young. *Roark's Formulas for Stress and Strain.* McGraw Hill, 1989.

[117] Kelley. *Rotating, Hydromagnetic Laboratory Experiment Modelling Planetary Cores.* PhD thesis, University of Maryland, 2009.

[118] D. R. Sisan. *Hydromagnetic turbulent instability in liquid sodium experiments.* PhD thesis, University of Maryland, 2004.

[119] Nicholas L. Peffley, A. B. Cawthorne, and Daniel P. Lathrop. Toward a self-generating magnetic dynamo: The role of turbulence. *Phys. Rev. E*, 61(5):5287–5294, May 2000.

[120] Daniel P. Lathrop, Jay Fineberg, and Harry L. Swinney. Transition to shear-driven turbulence in couette-taylor flow. *Phys. Rev. A*, 46(10):6390–6405, Nov 1992.

[121] GS Lewis and HL Swinney. Velocity structure functions, scaling, and transitions in high-reynolds-number couette-taylor flow. *Physical Review E*, 59(5, Part B):5457–5467, MAY 1999.

[122] VT Roussinova, SM Kresta, and R Weetman. Resonant geometries for circulation pattern macroinstabilities in a stirred tank. *AICHE Journal*, 50(12):2986–3005, DEC 2004.

[123] Somnath Roy, Sumanta Acharya, and Michael D. Cloeter. Flow structure and the effect of macro-instabilities in a pitched-blade stirred tank. *Chemical Engineering Science*, 65(10):3009 – 3024, 2010.

[124] Pavel Hasal, Milan Jahoda, and Ivan Fořt. Macro-instability: a chaotic flow component in stirred tanks. *Philosophical Transactions of the Royal Society A: Mathematical, Physical and Engineering Sciences*, 366(1864):409–418, 2008.

[125] V. Lavezzo, R. Verzicco, and A. Soldati. Ekman pumping and intermittent particle resuspension in a stirred tank reactor. *Chemical Engineering Research & Design*, 87(4A, Sp. Iss. SI):557–564, APR 2009.

[126] F. Wendt. Turbulente strömungen zwischen zwei rotierenden konaxialen zylindern. *Ingenieur-Archiv*, 4(6):577–595, 1933.

[127] F. Ravelet, R. Delfos, and J. Westerweel. Influence of global rotation and reynolds number on the large-scale features of a turbulent taylor-couette flow. *Physics Of Fluids*, 22(5), MAY 2010.

[128] DP Lathrop, J Fineberg, and HL Swinney. Turbulent flow between concentric rotating cylinders at large reynolds number. *Physical Review Letters*, 68(10):1515–1518, MAR 9 1992.

[129] GJF van Heijst, RC Kloosterziel, and CWM Williams. Laboratory experiments on the tripolar vortex in a rotating fluid. *Journal of Fluid Mechanics*, 225:301–331, APR 1991.

[130] R Hollerbach. Instabilities of the stewartson layer part 1. the dependence on the sign of ro. *Journal of Fluid Mechanics*, 492:289–302, OCT 10 2003.

[131] E Dormy, P Cardin, and D Jault. Mhd flow in a slightly differentially rotating spherical shell, with conducting inner core, in a dipolar magnetic field. *Earth and Planetary Science Letters*, 160(1-2):15–30, JUL 1998.

[132] I. N. Beliaev, A. A. Monakhov, and I. M. Iavorskaia. Stability of spherical couette flow in thick layers when the inner sphere revolves. *Akademiia Nauk SSSR Izvestiia Seriia Fizicheskaia*, 13:9–15, November 1978.

[133] YN Belyaev, AA Monakhov, SA Shcherbakov, and IM Yavorskaya. Onset of turbulence in rotating fluids. *JETP Letters*, 29(6):295–298, 1979.

[134] MJ Schmeits and HA Dijkstra. Bimodal behavior of the kuroshio and the gulf stream. *Journal Of Physical Oceanography*, 31(12):3435–3456, DEC 2001.

[135] KR Sreenivasan, A Bershadskii, and JJ Niemela. Mean wind and its reversal in thermal convection. *Physical Review E*, 65(5, Part 2), MAY 2002.

[136] N Mujica and DP Lathrop. Hysteretic gravity-wave bifurcation in a highly turbulent swirling flow. *Journal of Fluid Mechanics*, 551:49–62, MAR 25 2006.

[137] F Ravelet, L Marie, A Chiffaudel, and F Daviaud. Multistability and memory effect in a highly turbulent flow: Experimental evidence for a global bifurcation. *Physical Review Letters*, 93(16), OCT 15 2004.

[138] A. de la Torre and J. Burguete. Slow dynamics in a turbulent von karman swirling flow. *Physical Review Letters*, 99(5), AUG 3 2007.

[139] J. F. Gibson, J. Halcrow, and P. Cvitanovic. Visualizing the geometry of state space in plane couette flow. *Journal of Fluid Mechanics*, 611:107–130, SEP 25 2008.

[140] Bruno Eckhardt, Holger Faisst, Armin Schmiegel, and Tobias M. Schneider. Dynamical systems and the transition to turbulence in linearly stable shear flows. *Philosophical Transactions of the Royal Society A - Mathematical Physical and Engineering Sciences*, 366(1868):1297–1315, APR 13 2008.

[141] Bjoern Hof, Jerry Westerweel, Tobias M. Schneider, and Bruno Eckhardt. Finite lifetime of turbulence in shear flows. *Nature*, 443(7107):59–62, SEP 7 2006.

[142] H Wedin and RR Kerswell. Exact coherent structures in pipe flow: travelling wave solutions. *Journal of Fluid Mechanics*, 508:333–371, JUN 10 2004.

[143] M. Burin, H. Ji, E. Schartman, R. Cutler, P. Heitzenroeder, W. Liu, L. Morris, and S. Raftopolous. Reduction of ekman circulation within taylor-couette flow. *Experiments in Fluids*, 40(6):962–966, 2006.

[144] Paoletti. Private communication.

[145] JC Wyngaard. Measurement of small-scale turbulence structure with hot wires. *Journal Of Physics E-scientific Instruments*, 1(11):1105–&, 1968.

[146] Arne V. Johansson and P. Henrik Alfredsson. Effects of imperfect spatial resolution on measurements of wall-bounded turbulent shear flows. *Journal of Fluid Mechanics*, 137(-1):409–421, 1983.

[147] C. Morize, M. Le Bars, P. Le Gal, and A. Tilgner. Experimental determination of zonal winds driven by tides. *Phys. Rev. Lett.*, 104(21):214501, May 2010.

[148] R Manasseh. Breakdown regimes of inertia waves in a precessing cylinder. *Journal Of Fluid Mechanics*, 243:261–296, OCT 1992.

[149] S. Lorenzani and A. Tilgner. Inertial instabilities of fluid flow in precessing spheroidal shells. *J. Fluid Mech.*, 492:363–379, October 2003.

[150] W. V. R. Malkus. Precession of the earth as the cause of geomagnetism. *Science*, 160(3825):259–264, April 1968.

[151] M. D. Nornberg, E. J. Spence, R. D. Kendrick, C. M. Jacobson, and C. B. Forest. Intermittent magnetic field excitation by a turbulent flow of liquid sodium. *Phys. Rev. Lett.*, 97(4):044503, Jul 2006.

[152] Romain Volk, Philippe Odier, and Jean-Francois Pinton. Fluctuation of magnetic induction in von karman swirling flows. *Physics of Fluids*, 18(8), AUG 2006.

[153] H. K. Moffatt. *Magnetic Field Generation in Electrically Conducting Fluids*. Camb, 1978.

[154] V. Noskov, R. Stepanov, S. Denisov, P. Frick, G. Verhille, N. Plihon, and J.-F. Pinton. Dynamics of a turbulent spin-down flow inside a torus. *Physics of Fluids*, 21(4):045108–+, April 2009.

[155] ARRL. *The A.R.R.L. Antenna Book, Tenth Edition*. The American Radio Relay League, 1964.

[156] Qiaowei Yuan, Qiang Chen, Long Li, and K. Sawaya. Numerical analysis on transmission efficiency of evanescent resonant coupling wireless power transfer system. *Antennas and Propagation, IEEE Transactions on*, 58(5):1751 –1758, may. 2010.

[157] Andre Kurs, Robert Moffatt, and Marin Soljacic. Simultaneous mid-range power transfer to multiple devices. *Applied Physics Letters*, 96(4):044102 – 044102–3, jan. 2010.